MULTISCALE MODELLING OF FLUID-IMMERSED GRANULAR MEDIA

Christian Paul André René Clément, M.Sci.

Thesis submitted to the University of Nottingham for the degree of Doctor of Philosophy

August, 2009.

Abstract

In this thesis we present numerical simulation studies of fluid-immersed granular systems using models of varying scales and complexities. These techniques are used to examine the effects of an interstitial fluid on the dynamics of dense granular beds within a number of vibrated systems.

After an introduction to the field of granular materials, we present the techniques used to model both the granular dynamics and the fluid flow. We introduce various multiscale techniques to couple the motion of the granular and fluid phases. An extensive comparison between these techniques is conducted for some well-known systems. The fluid-grain coupling techniques are applied to some larger systems in order to determine under what situations the approaches are most suitable.

An investigation concerning three-dimensional fluid-driven convection within vertically vibrated fluid-immersed granular beds is then presented. Here we observe granular piling and determine that this is a result of fluid-driven convective cycles within the bed which may be strengthened through the presence of wall friction. Our simulations capture this convective behaviour and lead to a detailed understanding of the mechanisms behind the phenomenon.

Under a wide range of conditions a system of fluid-immersed fine grains within a vibrated partitioned cell will transfer in their entirety into just one of the segments through a linking channel at the cell base. We perform an experimental and numerical study in order to understand the principle mechanisms behind the "partition instability". We determine that the instability arises due to the fluid experiencing less resistance to its motion when flowing through the shallower granular column during vibration. A simple analytical model is developed which captures this behaviour.

It is commonly known that large dense intruders may rise rapidly to the surface of a granular bed when subjected to a vertical vibrational force. We next present an experimental and numerical study to determine the principle mechanism associated when the granular bed is immersed in a fluid, the fluid-enhanced Brazil nut effect. Our key finding is that the behaviour of the intruder is sensitive to the detailed fluid and particle flow in its vicinity. An analytical approach is developed to model the rising of a dense intruder in a vibrating fluid-immersed porous bed.

Finally a brief study is presented into the behaviour of a vibrated system of fluid-immersed particles held within a zero-gravity environment. We conduct simulations which are able to reproduce the behaviour of a collection of particles suspended magnetically in a vibrating fluid.

Acknowledgements

I would now like to take the opportunity to thank some of the people who have helped and supported me throughout my research and made this doctorate possible. I am indebted to you all.

I would firstly like to thank my supervisor Mike for all of the guidance and educational discussions throughout my four years in the group. His input has been invaluable and through our interactions I have learnt to be rigorous and thoughtful as a scientist. I would also like to thank Peter for his input and enthusiastic contributions.

On a personal level I would like to thank my family: Elizabeth, Sebastian, Maria and Oscar, for all of their love. Without their support I would not be in the privileged position that I am today.

I would also like to thank Christina, Paul, Rhona, Helen and Matthew for their support. Christina's cakes have kept me going when Andrea's cooking was a hundred miles away!

I would like to thank my officemates and friends in particular Lui, Daphne, Dave, Pablo, Hector and Kathryn, who have helped keep me sane while I have probably sent them insane with my lame jokes! Our discussions on topics from economics through to philosophy have proved an excellent distraction from my research for many hours and have helped develop me into the person that I am today.

I would also like to thank Andrea, whose love and support has been unflinching these last four years. I love you more than anything and hope that I may somehow repay you in the future. I look forward to spending more time with you after what has been a difficult time for us both.

Lastly I would like to thank René and Neville, who both had a profound

impact on my values and me as a person. They will both be watching how my life twists and turns and I hope that they are proud of the decisions that I have made and achievements that I have accomplished so far. I think about you both very often. This thesis is dedicated to them.

Publications

The following paper has been published as a result of research presented in this thesis:

- C. P. Clément, H. A. Pacheco-Martinez, Michael R. Swift and P. J. King. *Partition instability in water-immersed granular systems*, Physical Review E **80**, 011311 (2009).

The following paper has been submitted as a result of research presented in this thesis:

- C. P. Clément, Michael R. Swift and P. J. King. *The fluid-enhanced Brazil nut effect*, submitted to Physical Review E.

The author has also collaborated on the following paper:

- P. J. King, P. López-Alcaraz, H. A. Pacheco-Martinez, C. P. Clément, A. J. Smith and Michael R. Swift. *Instabilities in vertically vibrated fluid-grain systems*, The European Physical Journal E **22**, 219-226 (2007).

Contents

Chapter 1

Introduction

This thesis concerns the behaviour of fluid-immersed granular beds subjected to vertical vibration for a variety of systems, in particular granular heaping, Faraday tilting, the "partition instability", the fluid-enhanced "Brazil nut" effect, and granular suspensions. This chapter provides a brief introduction to the field of Granular Dynamics and its wider importance and applications. We then follow with a brief description of granular systems which are coupled to the dynamics of a fluid. The chapter concludes with an outline for the remainder of the thesis.

1.1 Granular Systems

Granular materials are defined as large conglomerations of discrete macroscopic particles which are characterised by a loss of energy whenever they interact through collisions. If they are non-cohesive then the forces between them are only repulsive so that the shape of the material is determined by external boundaries and gravity. Such a definition describes a vast array of systems, from nuts or sugar granules contained in a jar to the huge piles of coal at power stations. Since granular systems are constantly in our lives, an understanding of their dynamical behaviour is of great importance, especially within industry. The pharmaceutical, agricultural and construction-based industries rely heavily on mixing and separation of a vast array of granular materials. The motivation for gaining a better understanding of these materials is high. For example, it is estimated that a high proportion of capacity of many industrial plants is wasted due to prob-

lems related to the transport of these materials (Ennis *et al.* 1994). A small improvement in efficiency due to a development of our understanding could have a significant impact on these industries.

Engineers have traditionally classified granular materials depending on their size; rubble is defined as being of greater size than >5 mm, grains have a generic size of 0.1–5 mm, powder 10–100 μm, superfine powder 1–10 μm and hyperfine powder which are otherwise known as latex spheres have a size of 0.1–1 μm. In this thesis, however, we only concern ourselves with grains since many of the dynamical behaviours and effects observed using these particles may be easily reproduced within both experiments and numerical computer simulations.

Despite the seemingly simple nature of granular materials, these materials behave differently from any of the other familiar forms of matter; they can be considered an additional state of matter in their own right. As we have already noted, the behaviour of granular systems are greatly affected by their internal collisions. A collection of grains are able to dissipate energy quickly through a large number of internal collisions so that an unagitated system with a large amount of internal energy will soon come to rest. It is observed that within multi-particle collisions energy is lost due to the inelasticity of collisions. An example of this dissipation may be seen if a bean bag is picked up and then dropped from a height of a few meters. In this instance we see that the bean bag does not bounce upon landing as all the kinetic energy is lost through millions of internal collisions between the beans.

Another important factor that contributes to the unique properties of granular materials is that ordinary temperature plays no role. On first inspection granular flows may be viewed favourably in comparison to a dense gas as they both consist of discrete particles with negligible cohesive forces between them. The energy scale of an ideal gas is k_BT while the relevant energy scale of our granular system is the potential energy mgd gained when a grain of mass m is raised by its diameter d in the Earth's gravitational field g. A simple comparison for a sand grain held at room temperature shows that this potential energy is 10^{12} times k_BT, which makes ordinary thermodynamic arguments for the treatment of granular materials irrelevant.

Granular materials are not solid, liquid or gas, yet they can behave like any of these states under the appropriate conditions. We find that when no energy is input into a granular system the particles will automatically settle into a solid state. If packed tightly enough the particles assume a "jammed state"; this occurs when the particles occupy a certain fraction of the overall bed volume. In this state the grains may support loading to the surface interface, as may be observed when a person walks along a beach of dry sand.

Those who have poured cereal into a breakfast bowl will also be aware that a collection of solid grains can behave like a fluid. Cereal "flows" out of the box and quickly forms the shape of the bowl upon relaxation. These "fluidised" states are achieved if the kinetic energy of the grains overcomes the inelastic losses sufficiently to allow the grains to flow. A characteristic of this state is that the grains have a lower packing fraction than in the jammed state.

If the packing fraction is reduced further the grains may even exhibit the properties of a gas. This may be achieved if the grains are shaken strongly within a cell such that the mechanical energy input into the system is high and the inelastic granular collisions are infrequent so that little energy is lost. For some further reading on granular systems we suggest the review articles by Jaeger (1996) and Kudrolli (2004).

The science of granular matter has a long history with many of the original insights made by engineers who considered how to treat these materials. Some of the original classical contributions were made in the 18th and 19th centuries. Amongst the first contributions were those made by Coulomb (1773) who proposed the idea of static friction and then Reynolds (1885) who introduced the ideas of bed dilation, which implies that a compacted granular material must expand in order for it to undergo any shear. More recently the topic has attracted condensed-matter physicists and other scientists, as well as engineers, who study complex systems and consider granular matter as a model of more complex materials. As an example of this sand-pile avalanches have been used as a macroscopic picture for the motion of flux lines in type-II superconductors (de Gennes 1966). It is the dynamical motion of grains, as in the systems first noticed by Faraday (1831), that this thesis is concerned with.

In this section we have introduced grains inhabiting dry systems. However, within the bulk of this thesis we are concerned with the dynamical behaviour of grains held within a fluid. We introduce such systems in the next section.

1.2 Fluid-Grain Systems

The majority of granular systems are affected in some way by the interstitial fluid in which they are immersed. The only exceptions to this are within experiments that are performed in a cell in which the fluid has been removed or in granular systems which exist outside the Earth's atmosphere like an asteroid belt. The effect of the fluid on the granular system depends on the size of the material. When the size of the body is substantial the fluid effects are known to be negligible, but for fine particles and powders ($\sim$10 μm) in air and particles ($\sim$1 mm) immersed in water, the effects of the fluid are appreciable.

Examples of fluid-immersed granular systems occur in many places in nature. These range from the creation of structures such as meanders and ox bow lakes in Brazil to the huge recurring sand dunes in the Sahara desert. Understanding the mechanics of sand-pile formation may even answer interesting questions as to why dunes have been discovered and continue to survive on the surface of Mars. There are also more dynamic fluid-immersed granular systems which society has a great incentive to understand better. These include the evolution of snow avalanches at ski resorts induced by strong winds and the more rare events of devastating tsunami's created by large sedimentations of rocks into the sea.

The size of the particles immersed in the fluid makes a great difference to the behaviour and hence its classification. As an example a collection of extremely fine particles, of size $<10^{-9}$ m, submerged in a liquid may dissolve to create an homogenous solution. These particles are able to change the dynamic properties of the fluid, including density and viscosity. When larger particles with sizes in the range 10^{-9}–10^{-6} m are submerged in a water-based fluid we create a colloid. These particles are suspended and dispersed evenly throughout the fluid. As the spheres suspended within the colloid are of similar scale to the fluid molecules the grains are thermally agitated by the fluid particles and experience Brownian

motion. Examples of colloids include mayonnaise and milk. If the size of the particles are increased further so that the diameters are in the range 10^{-6}–10^{-4} m then the particles do not dissolve and a heterogeneous solution like soup is created. If shaken vigorously the particles will disperse throughout the fluid; however, if left for a long period of time they will settle on the cell base. These particles are affected by macroscopic characteristics of the fluid such as density and viscosity. In this thesis the fluid-grain systems we are concerned with involve grain sizes in the range 10^{-4}–10^{-2} m. These particles demonstrate a wide variety of behaviours when immersed within fluids and are greatly affected by the fluid density and viscosity.

The field of fluid-immersed granular systems began in earnest when Faraday (1831) observed that a pile of granular material displays convection cycles and will sustain its own shape if vibrated on a flat surface. Faraday's questions about how fluids affect the dynamic behaviour of grains went largely unanswered for the next century. Over this period not much work was done on the field of fluid-immersed granular materials; however, it has been only been in the last two decades that the field has received a lot more interest. Recently such things as sedimentation, pattern formation, granular avalanches and segregation have all been and continue to be studied. With the advent of high-speed computers it is now possible to study these topics and understand the mechanisms in detail.

1.3 Thesis Outline

So far in this chapter we have given a brief introduction to two fields of study, namely dry granular systems and the special case of granular systems immersed in fluid. These fields permeate many aspects of our lives and, as a consequence, are of considerable interest. Due to the vastness and complexity of these fields we are only able to study a selection of fluid-immersed granular effects in which we try to determine the mechanisms which give rise to their behaviours.

I now give a brief outline of the remainder of this thesis and what each chapter will include.

The bulk of the research that I undertook involves simulating complex granu-

lar systems numerically on a computer. Thus the first part of this thesis, Chapter 2 and Chapter 3, is concerned with the development of my own code. We introduce several models and algorithms used to simulate systems of fluid-immersed granular beds. At the end of this part we perform a series of well-known numerical tests which assess the accuracy and efficiency of the models. These include determining the drag coefficient dependency on the Reynolds number for a falling sphere and measuring the pressure beneath a thrown granular bed over a single vibration cycle. The second part of the thesis, Chapter 4 and Chapter 5, involves applying several of the microscopic fluid-grain models to the study of the Faraday tilting and heaping effects in three dimensions and then to the "partition instability". We compare results when applying different simulation techniques and determine which approaches give the best results in each situation while simultaneously examining the dynamics of each effect. The third part of the thesis, Chapter 6 and Chapter 7, use one simulation technique to study the fluid-enhanced Brazil nut effect and zero-gravity fluid-immersed granular suspensions. The final chapter summarises the main conclusions from the thesis.

I now give a brief outline of what each chapter will include.

Chapter 2: Computational Techniques

Here we introduce a number of approaches that can be used to model computationally a system of fluid-immersed grains. The chapter begins by focusing on granular modelling techniques and then proceeds to give a detailed description of the Molecular Dynamics approach which we use throughout the course of this thesis. We then discuss the approach used to model the fluid. Here we use the governing equations of fluids, the Navier–Stokes equations, to solve the fluid motion on a spatially discretised Marker-and-Cell grid mesh using a fractional-time-step operator-splitting method otherwise known as the Projection Method. Later we bring these phases together and describe several different approaches to coupling the momentum transfer between the fluid and granular phases.

The first model described to resolve the fluid-grain coupling is an analytical model developed by Kroll which may be solved numerically to determine the flight of a porous bed within an incompressible fluid. The analytical Modified

Kroll model which is able to simulate granular beds thrown in dense fluids is also described. Two models are then outlined which are based on using empirically determined bed equations to resolve the fluid-grain coupling. These are the Simple Drag and Navier–Stokes models. The Navier–Stokes model is the first model we introduce which evaluates the fluid motion in addition to the granular motion. Within this model the grains are treated as local disturbances to the fluid flow and so the fluid resolution is determined on a scale larger than the size of the particles. We then describe two microscopic fluid-grain coupling models in which the fluid is resolved on a scale smaller than the size of the particles, such that fluid flow effects around the particles may be studied. These are the Particle Template and the Fluid Spring models. At the end of this chapter some simple comparisons between the fluid-grain coupling models are performed.

Chapter 3: Accelerated Systems

Within this chapter we consider how accelerated systems must be treated within our simulations. We then simulate thrown fluid-immersed granular beds to determine suitable parameters for our simulations. In the last part of the chapter a vibrated fluid-immersed bed is simulated and results are compared using the Modified Kroll, the Navier–Stokes, the Particle Template and the Fluid Springs models.

Chapter 4: Heap Formation

Here we present an investigation into three-dimensional heap formation using two of the fluid-grain coupling models, namely the Navier–Stokes and the Fluid Springs models. This chapter studies the mechanism through which a fluid-immersed granular bed will tilt and then maintain its shape through convection. The effects of friction-driven convection on this fluid-immersed granular system are also investigated. At the end of the chapter we simulate a fluid-immersed granular heap like that observed by Faraday (1831).

Chapter 5: Partition Instability

Here we investigate the "partition instability", where a system of fluid-immersed grains vibrated within a partitioned cell, connected by holes at the base and top, will spontaneously move into just one of the columns. We present an experimental and theoretical study of the process and propose a mechanism for the instability which is related to the fluid-driven convection mechanism discussed in the heaping chapter. At the end of the chapter we use this knowledge to propose a simple analytical model for the fluid-driven partition instability based on two coupled granular beds vibrated within an incompressible fluid.

Chapter 6: Fluid-Enhanced Brazil Nut Effect

Here we present an experimental and theoretical investigation of the fluid-enhanced Brazil nut effect where a large intruder rises to the surface of a bed of light host particles within a water-filled cell. Simulations are used to capture the behaviour first observed within experiments and also to investigate the rising mechanism. We show that when using a full microscopic fluid model, such as the Fluid Springs model, to simulate the Brazil nut effect the intruder rises but when using the Simple Drag model for the same system the Brazil nut does not rise. We are therefore able to show that the fluid and grain flow in close vicinity to the intruder are significant in the fluid-enhanced Brazil nut effect. At the end of the chapter we propose an analytical approach to model an intruder within a porous granular bed submerged in an incompressible fluid.

Chapter 7: Zero-Gravity Fluid-Immersed Granular Suspensions

Here we perform a brief theoretical investigation of a vibrated system of dense particles in a viscous fluid held in a weightless environment. The particles form thick granular layers, spanning the cross-section of the cell, perpendicular to the direction of the container vibrations. The effect is believed to arise due to steady streaming flows developing within the cell. Our simulations are able to capture similar effects observed in experiments.

Chapter 8: Conclusions

Here we review the concepts discussed in the previous chapters and propose some ideas for future work.

Chapter 2

Computational Techniques

In this chapter we describe the Molecular Dynamics method used to model granular interactions. The particle collision methods described are the Linear Spring-Dashpot scheme and Kuwabara and Kono's (1987) collision system.

We then introduce the fluid model for which the overall governing equations of fluid mechanics describe the fluid motion, namely the Navier–Stokes equations. The fluid algorithm is then described and the section is ended by simulating lid-driven Cavity Flow within a three-dimensional cell for which there are well-known results.

We then describe the way in which the fluid and granular motion may be coupled. We begin with the analytical Kroll model which considers the flight of a fluid-immersed porous bed in a vibrated cell. Models which operate within a Molecular Dynamics framework, including the Simple Drag model and the Navier–Stokes model are then described. The Navier–Stokes model is the first model we discuss which uses both Molecular Dynamics to describe the particle motion and the Navier–Stokes equations to model the fluid. In these models the particles are small compared to the fluid grid. Later we introduce a couple of microscopic fluid flow models, namely the Particle Template and Fluid Springs models, which model the fluid on a scale small compared to the particle size. We then perform some numerical tests with these fluid particle coupling models to examine the circumstances in which they are most suitable.

2.1 Particle Modelling

There are several different ways in which particle-particle interactions can be modelled. These methods fall into two main categories, hard-sphere and soft-sphere models.

The hard sphere (Event-Driven) approach is based on the idea that a collision between two grains is instantaneous, i.e. the collision time is zero $t_c = 0$. This means that two particles coming into contact will instantaneously collide. An efficient algorithm for this method was developed by Lubachevsky (1991), which is split into two parts. The first part uses an algorithm to determine when the next particle collision will be, given that we know the particle positions, velocities and all other dynamic characteristics of the particles (friction coefficient, coefficient of restitution etc.). All of the particles are then moved forward in time to when the collision occurs. The second part of the algorithm implements the collision dynamics for the particles in contact, so that the velocities are updated. This process then repeats itself ad infinitum. The Event-Driven model works well in dilute systems, such as gases, but fails in very dense systems. In highly populated granular regions the model breaks down as spheres come to rest and remain in contact with other spheres, effectively reducing the time between successive collisions to zero. The system slows dramatically as the event list increases to infinity. As our systems will often be densely packed another technique will be needed to resolve the particle interactions.

Stochastic approaches offer a very different way of modelling the particle interactions. Unlike the Event-Driven method the exact times and places of the particle collisions are not calculated, an example of this type of approach is the Direct Simulation Monte Carlo method which was first proposed by Bird (1994). This is another two-process simulation. Firstly the particles are assorted randomly into boxes and then set to move freely. Secondly, two particles, within a selection of boxes, are chosen to collide at random. The success of the collision is proportional to the relative velocity between the two particles. Extra parameters must be introduced since the colliding particles may not be in contact with each other. This method is often used in dilute systems to study thermodynamic limits, however, the method is not suitable for our simulations as microscopic

granular behaviour such as convection is not captured.

Soft particle techniques, as the name suggests, allow a slight overlap of the particles during collisions. The result of this is that the collision is not instantaneous and has a discrete time associated with it. When the particles collide, the interaction forces are a function of the collision overlap and collision velocity. Multiple particle collisions are also possible and the forces on the particles are determined by summing the individual collision forces. This type of technique is known as Molecular Dynamics (MD) and uses Newton's laws of motion as its foundations. MD manages to capture the essentials of particle collisions in a realistic manner and for this reason it is possible to apply it to a much wider class of systems (both rapid and slow flows) than hard-sphere models (rapid flows only). We describe the Molecular Dynamics technique in the following section. For a review of particle modelling techniques see the article by Herrmann (1997).

2.1.1 The Molecular Dynamics Technique

Modelling collisions between real particles is difficult, due to surface imperfections and the non-spherical nature of real grains. For ease, within this thesis we assume the particles are spherical. However, the modelling of realistic deformations during particle collisions is still considered to be much too complicated. For this reason we use the the MD technique in which the overlap of the two particles and the velocities are considered the most important quantities in determining the collision dynamics. The particles only interact when the overlap $\delta_n = (r_1 + r_2) - (\mathbf{r_1} - \mathbf{r_2}) . \hat{\mathbf{n}}$ is positive. Here $\hat{\mathbf{n}}$ is the unit vector connecting the centres of the two spheres and r_i and $\mathbf{r_i}$ are the particle radii and position vectors of particle i respectively. A schematic diagram of two colliding particles is shown in Figure 2.1.

We will be describing two soft-sphere techniques; the Linear Spring-Dashpot model and a second model that uses an elastic repulsive Hertzian contact force and a viscous dissipative force proposed by Kuwabara and Kono (1987).

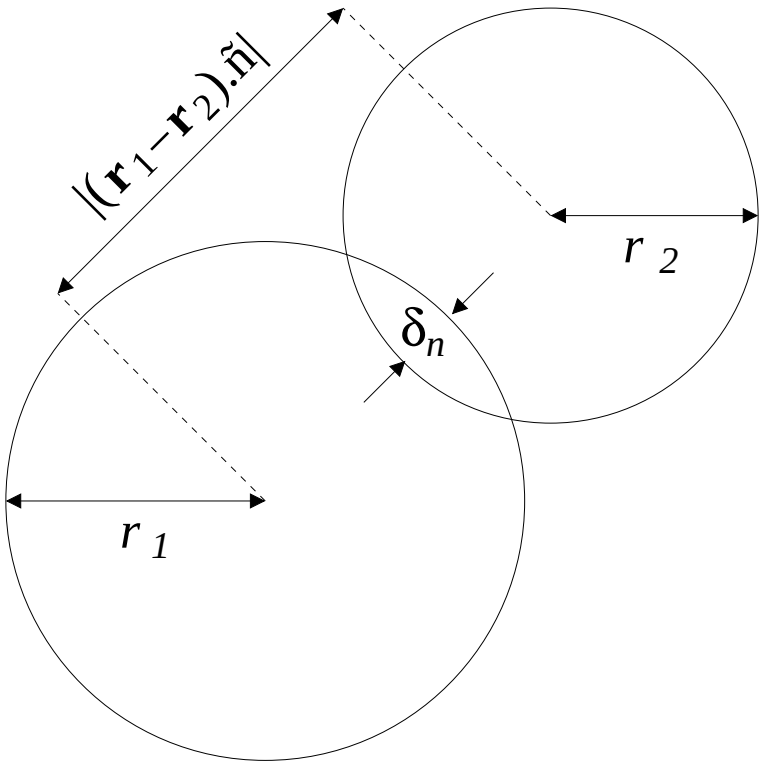

Fig. 2.1: Schematic diagram of two discs with different radii colliding. The overlap in this figure is exaggerated.

Linear Spring-Dashpot Model

The first force acting on particle 1 from 2 is an elastic repulsive force

$$\begin{aligned} \mathbf{F}_{el} &= -k_n\delta_0\left(\frac{\delta_n}{\delta_0}\right)^{\nu_c}\hat{\mathbf{n}} \quad \delta_n > 0 \\ &= 0 \qquad\qquad\qquad\quad \delta_n < 0. \end{aligned} \tag{2.1}$$

Here k_n is the elastic modulus and δ_0 is a normalisation constant dependent on the non-linearity ν_c and the number of dimensions. Using $\mathbf{F}_{el}$ on its own leads to elastic particle collisions in which no energy is lost during the interaction process. Most real collisions, however, lose energy and so we define a second dissipative force in the normal direction,

$$\mathbf{F}_{d1} = \gamma_n\dot{\delta_n}\left(\frac{\delta_n}{\delta_0}\right)^{\phi_c}\hat{\mathbf{n}}. \tag{2.2}$$

Here γ_n is a normal viscous dissipation coefficient and ϕ_c is another non-linearity parameter. $\dot{\delta_n}$ is the time derivative of δ_n also known as the relative collision velocity in the normal direction.

Both of these forces act along the line connecting the two particle centres, however, only frictionless spheres do not have forces acting in the tangential direction. For a lot of granular phenomenons it is necessary to include a sliding frictional force. Coulomb's criterion states that the restoring force is proportional to the normal force F_n and the coefficient of friction μ. Thus the frictional force becomes:

$$\mathbf{F}_{friction} = -\frac{\dot{\delta}_t}{|\dot{\delta}_t|}\mu F_n \hat{\mathbf{t}}, \tag{2.3}$$

where $\dot{\delta}_t$ is the relative velocity of the colliding particles in the tangential direction. $\hat{\mathbf{t}}$ is a unit vector in the collision frame perpendicular to $\hat{\mathbf{n}}$ which opposes the tangential relative velocity. F_n is calculated from the total instantaneous normal forces of the collision, $F_n = |\mathbf{F}_{el} + \mathbf{F}_{d1}|$. Rotational motion is not included within the collision model and is discussed at the end of the section.

All of the above forces are dependent on the instantaneous configuration of the granular particles. As the collision proceeds, the forces between the colliding pair will change as the relative velocities and overlap between the particles continuously evolve.

It is important to assign values to the dimensionless parameters, ν_c and ϕ_c, in equations 2.1 and 2.2, that have relevance to the type of system being modelled. In the elastic force equation, (2.1), if the non-linearity constant $\nu_c = 1$ then the particles interact by Hooke's law for springs. Thus k_n may alternatively be known as the spring constant. Equivalently, the dissipative force, (2.2), operates by checking relative velocities at the contacts and may be envisioned as resulting from dash-pots acting in the normal direction at the contact when $\phi_c = 0$. If we assign these values, we end up with the Linear Spring-Dashpot model (LSD) for particle-particle interactions.

We also consider another collision model which arises from the dimensionless parameters within equations 2.1 and 2.2 being set to $\nu_c = 3/2$ and $\phi_c = 1/2$. The resulting collision model is comprised of an elastic repulsive Hertzian force term and a viscous dissipative term. We describe it in more detail in the following section.

Hertzian Model

The first force in this model is an elastic Hertzian force term obtained when $\nu_c = 3/2$ is substituted into the elastic repulsive force equation 2.1. This term, when used independently of any dissipative term, is referred to as the Hertzian collision scheme. For our purposes we require a dissipative term such as that proposed by Kuwabara and Kono (1987), which we describe below. The elastic Hertzian force term may be given as

$$\mathbf{F}_{hz} = -\tilde{k}_n {\delta_n}^{3/2} \hat{\mathbf{n}}, \tag{2.4}$$

where $\tilde{k}_n$ is approximated using measurable properties of the particle:

$$\tilde{k}_n = \frac{4}{3}\sqrt{r_{eff}} E_{eff}. \tag{2.5}$$

Here r_{eff} and E_{eff} are functions of the radii and Young's Modulus' of the colliding particles otherwise known as the effective radius and effective Young's modulus. r_{eff} and E_{eff} may be calculated using:

$$r_{eff} = \frac{r_1 r_2}{r_1 + r_2} \tag{2.6}$$

and

$$\frac{1}{E_{eff}} = \frac{(1-\nu_1^2)}{E_1} + \frac{(1-\nu_2^2)}{E_2}, \tag{2.7}$$

where E_i and ν_i are the Young's Modulus and Poisson ratio of sphere i.

A dissipative force that compliments the Hertzian force term was suggested by Kuwabara and Kono (1987) and may be given as:

$$\mathbf{F}_{d2} = \tilde{\gamma}_n {\delta_n}^{1/2} \dot{\delta_n} \hat{\mathbf{n}}. \tag{2.8}$$

Here $\tilde{\gamma}_n$ is a normal viscous dissipation coefficient which is chosen so that the collision mimics real particle interactions.

As with the LSD model both $\mathbf{F}_{hz}$ and $\mathbf{F}_{d2}$ act along the line connecting the two particle centres. Friction may also be applied in the tangential direction by calculating $F_n = |\mathbf{F}_{hz} + \mathbf{F}_{d2}|$ and substituting this value into Coulomb's friction equation 2.3 (provided μ is non-zero). By combining equations 2.4 and 2.8 we obtain the Damped Hertzian (DH) collision model.

Throughout my simulations the particle rotations are not included. Particle rotations result from the torque applied by the tangential friction forces. However, even in the absence of fluid, the rotational energy of the particles is considerably lower than the translational kinetic energy (Luding 1995). This reduced rotational activity in combination with the damping effects that the fluid has on the rotation of immersed particles, allows particle rotation to be neglected from the simulations presented in this thesis. Modelling particle rotations also significantly increases the computing power required for negligible difference to overall results.

2.1.2 Equations of Motion

A method of evolving the particle motion is now required. MD is based around Newton's laws of motion, in particular Newton's second law of motion which is given by:

$$m\ddot{\mathbf{r}} = \mathbf{F}_{collision} + \mathbf{F}_{system}. \tag{2.9}$$

Here $\mathbf{r}$ is the position vector of the centre of the particle and m is its mass. $\mathbf{F}_{collision}$ is the force on the particle due to collisions with other particles and boundaries and $\mathbf{F}_{system}$ is the force on the particle due to all other external forces such as gravity, fluid drag and magnetic forces.

It is usually not possible to solve the equations of motion analytically and as a consequence we use numerical methods to discretise the temporal coordinates within equation 2.9. This allows us to determine approximately the trajectory of the particle so that if we know the dynamic properties of the particles at the current time t we may predict the position and velocity of the particle at time $t + \Delta t$. Here Δt is defined as the time-step between each simulation iteration. In this section we describe two methods by which the particle trajectories may be solved numerically in time, namely the Verlet and the "predictor-corrector" algorithms.

Verlet Algorithm

Newton's Second law is useful for determining the acceleration of the particle given the external forces acting upon it. However, to obtain an equation by which we are able to advance the particle positions from a current time of t to a

new time $t + \Delta t$ we must perform two Taylor expansions on the position vector $\mathbf{r}$, one going forward in time and one going backwards:

$$\begin{aligned} \mathbf{r}(t+\Delta t) &= \mathbf{r}(t) + \dot{\mathbf{r}}(t)\Delta t + \frac{1}{2}\ddot{\mathbf{r}}(t)(\Delta t)^2 + \frac{1}{6}\dddot{\mathbf{r}}(t)(\Delta t)^3 + \ldots \\ \mathbf{r}(t-\Delta t) &= \mathbf{r}(t) - \dot{\mathbf{r}}(t)\Delta t + \frac{1}{2}\ddot{\mathbf{r}}(t)(\Delta t)^2 - \frac{1}{6}\dddot{\mathbf{r}}(t)(\Delta t)^3 + \ldots . \end{aligned} \quad (2.10)$$

Here $\dot{\mathbf{r}}$, $\ddot{\mathbf{r}}$ and $\dddot{\mathbf{r}}$ are first, second and third time derivatives of the position vector, $\mathbf{r}$. The values $\dot{\mathbf{r}}$ and $\ddot{\mathbf{r}}$ are otherwise known as the velocity and acceleration. If we then sum these two equations and rearrange we obtain the Verlet equation (Allen and Tildesley 2000a):

$$\mathbf{r}(t+\Delta t) = 2\mathbf{r}(t) - \mathbf{r}(t-\Delta t) + \ddot{\mathbf{r}}(t)(\Delta t)^2 + O\left((\Delta t)^4\right). \quad (2.11)$$

Here we see that the first, $\dot{\mathbf{r}}(t)$, and third, $\dddot{\mathbf{r}}(t)$, time derivatives have been eliminated by summing the two Taylor expansions together. It is reasonable to ignore the Δt^4 and any higher-order terms since they are small. The Verlet equation tells us that if the current, $\mathbf{r}(t)$, and old, $\mathbf{r}(t-\Delta t)$, position vectors are known it is possible to determine the future position, $\mathbf{r}(t+\Delta t)$. The acceleration of each particle, $\ddot{\mathbf{r}}$, may be calculated using Newton's second law, equation 2.9, in which we determine the collisional and other system forces acting upon each particle and divide by the mass.

Verlet also developed a method of computing the particle velocities, which are most commonly used within MD to determine the dissipative force terms when a pair of particles collide inelastically. They are also important when coupling the motion of grains to the surrounding fluid, as discussed later in section 2.4. The velocities may be obtained from the formula

$$\mathbf{v}(t) = \frac{\mathbf{r}(t) - \mathbf{r}(t-\Delta t)}{\Delta t}. \quad (2.12)$$

This method for determining the future particle positions and the velocities, otherwise known as the Verlet algorithm, is a simple one stage process which requires only the old granular positions to be stored. It is otherwise a very fast method of evolving the particle trajectories.

Other particle trajectory methods include the "predictor-corrector" algorithm. This is different from the Verlet equation as it has several steps to determine the particle motion. We describe it here.

Predictor-Corrector Algorithm

The new positions, velocities and accelerations are predicted from their current values by performing Taylor expansions about time t:

$$\begin{aligned}
\mathbf{r}^p(t+\Delta t) &= \mathbf{r}(t) + \Delta t\dot{\mathbf{r}}(t) + \frac{1}{2}\Delta t^2\ddot{\mathbf{r}}(t) + \frac{1}{6}\Delta t^3\dddot{\mathbf{r}}(t) + \ldots \\
\dot{\mathbf{r}}^p(t+\Delta t) &= \dot{\mathbf{r}}(t) + \Delta t\ddot{\mathbf{r}}(t) + \frac{1}{2}\Delta t^2\dddot{\mathbf{r}}(t) + \ldots \\
\ddot{\mathbf{r}}^p(t+\Delta t) &= \ddot{\mathbf{r}}(t) + \Delta t\dddot{\mathbf{r}}(t) + \ldots \\
\dddot{\mathbf{r}}^p(t+\Delta t) &= \dddot{\mathbf{r}}(t) + \ldots .
\end{aligned} \tag{2.13}$$

The superscript marks that these are the "predicted" values, which will be "corrected" soon. The next stage of the algorithm involves determining the acceleration of the particles from the new positions, $\mathbf{r}^p$, using Newton's second law, equation 2.9. These may then be compared with the predicted accelerations from equation 2.13 to obtain the size of the error within the prediction step:

$$\Delta\ddot{\mathbf{r}}(t+\Delta t) = \ddot{\mathbf{r}}^c(t+\Delta t) - \ddot{\mathbf{r}}^p(t+\Delta t). \tag{2.14}$$

This error and the predicted values from equation 2.13 are used in a correction step. The idea being that the new "corrected" values are a better approximation to the true positions, velocities etc. These corrected values are calculated using

$$\begin{aligned}
\mathbf{r}^c(t+\Delta t) &= \mathbf{r}^p(t+\Delta t) + c_0\Delta\ddot{\mathbf{r}}(t+\Delta t) \\
\dot{\mathbf{r}}^c(t+\Delta t) &= \dot{\mathbf{r}}^p(t+\Delta t) + c_1\Delta\ddot{\mathbf{r}}(t+\Delta t) \\
\ddot{\mathbf{r}}^c(t+\Delta t) &= \ddot{\mathbf{r}}^p(t+\Delta t) + c_2\Delta\ddot{\mathbf{r}}(t+\Delta t) \\
\dddot{\mathbf{r}}^c(t+\Delta t) &= \dddot{\mathbf{r}}^p(t+\Delta t) + c_3\Delta\ddot{\mathbf{r}}(t+\Delta t).
\end{aligned} \tag{2.15}$$

Gear (1967) discussed the coefficients c_0, c_1, c_2, c_3 ... and found the best choice for optimum stability depended on the number of position derivatives and the order of the differential equations being solved. Note that here it is second-order since we use the second order time derivative of the position to compare between the predicted and corrected values in equation 2.14

The decision of which algorithm to use comes down to which method allows for the largest time-step and thus the fastest simulation speed. Both of these methods have similar errors associated with them, so choosing between them for

accuracy is trivial. The main difference is that the Verlet method is a one-step process, whereas Gear's predictor-corrector algorithm is made up of two steps and requires more data to be stored. Therefore, in all my simulations the Verlet method is implemented due to its simplistic nature.

The choice of time-step Δt is vital within collision dynamics. In an ideal system the time-step would be infinitely small so the collisions are resolved continuously rather than in small discrete steps. However, this is impossible due to the limited capacity of modern computers and entirely unnecessary as granular systems can run perfectly well for finite time-steps. The main priority of a successful algorithm is to duplicate the classical trajectory as closely as possible and to permit the use of a long time-step Δt. A limiting factor on the maximum size of Δt arises because a large time-step leads to excessive particle overlapping during collisions. This results in a net increase in the energy of the particles in a process which repeats itself until the simulation "blows up". For example, a system of elastic bronze particles with diameters 150 μm and spring constants k_n=3000 kg s^{-2} will experience large energy increases for time-steps $\Delta t > 1.5$ μs (Milburn 2006). A time-step therefore must be chosen so that each collision is resolved sufficiently but also allows the simulation to run as fast as possible.

Within both the LSD and DH contact models we may increase the simulation speed by modifying the spring constant k_n or $\tilde{k}_n$ within equations 2.1 and 2.4. A smaller spring will increase the collision duration and allow for a larger time-step. How this may be done is discussed in greater detail for the LSD model in the next section. It should be noted, however, that collision dynamics best mimic nature for a particular spring constant and so varying k_n or $\tilde{k}_n$ may lead to unrealistic particle interactions. For example, a small spring constant will lead to a large deformation of the granules.

2.1.3 Linear Spring-Dashpot Scheme

In the case of the LSD model it is possible to analytically solve the equations to determine the contact duration and the coefficient of restitution, e. This information is useful in simulations when choosing a suitable Δt and spring constant

k_n. The coefficient of restitution of two colliding particles is defined as the ratio of velocities before and after interaction and is expressed in the form

$$\mathbf{v}.\hat{\mathbf{n}} = -e\left(\mathbf{v}_0.\hat{\mathbf{n}}\right), \tag{2.16}$$

where $\mathbf{v}_0$ and $\mathbf{v}$ are the relative velocities of the interacting particles before and after collision. The collision dynamics can essentially be modelled as a harmonic oscillator with weak damping. Thus it is possible to determine analytically what the contact duration t_c and coefficient of restitution e of a particle collision are by using

$$t_c = \frac{\pi}{\omega}, \tag{2.17}$$

and

$$e = \exp\left(\frac{-\pi\eta_d}{\omega}\right). \tag{2.18}$$

Here ω is the angular frequency and η_d is a damping parameter. These may be calculated using:

$$\omega = \sqrt{{\omega_0}^2 - \eta_d^2}, \tag{2.19}$$

and

$$\eta_d = \frac{\gamma_n}{2m_{12}}. \tag{2.20}$$

Here m_{12} is the reduced mass defined as:

$$m_{12} = \frac{m_1 m_2}{m_1 + m_2}, \tag{2.21}$$

where m_i is the mass of particle i. ω_0 is the angular frequency without damping, which is a function of the spring constant, k_n, and the reduced mass:

$${\omega_0}^2 = k_n/m_{12}. \tag{2.22}$$

Here the spring constant k_n may be chosen so that realistic particle hardness and collision durations are achieved.

By using the above relations it is possible to determine analytically what viscous dissipation coefficient in equation 2.2 is necessary to obtain a specific value of e:

$$\gamma_n = \left(\frac{4m_{12}\, k_n\, \left(\ln\, e\right)^2}{\pi^2 + \left(\ln\, e\right)^2}\right)^{1/2}. \tag{2.23}$$

This is useful for computer simulations as we may chose e without concerning ourselves with the resulting damping parameter γ_n. Thus in our simulations we always chose a time-step such that $\Delta t < \frac{1}{10}t_c$. This way we ensure that our particle collisions are stable.

2.1.4 Particle Boundary Conditions

An important part of the system is what happens at the system boundaries. In our simulations it is possible to model either periodic boundaries or walls and each condition has useful applications. Periodic boundary conditions allow the particles to leave through one edge of the system and re-enter through the side directly opposite. Thus by using periodic boundary conditions we may reproduce the behaviour of very large systems whilst only actually modelling a very small one. In other scenarios it is necessary to insert walls, as very often we perform simulations which model real-world experiments. In an elastic collision between a particle and the wall, no momentum is passed to the wall and the particle rebounds with the same magnitude of velocity. The particle in effect behaves as if it has collided with an infinitely massive particle.

2.1.5 Molecular Dynamics Algorithm

So far we have shown how the collision forces between particles and boundaries are resolved. We now describe an algorithm which checks for collisions between particles within each time-step. This proceeds as follows:

a) We check whether there are any overlapping particles in the system. This is done by testing every possible pair of spheres to see if they lie within a distance $\delta_n < (r_1 + r_2)$ of each other. This condition ensures that collisions are resolved for overlapping particles only. If the system is not periodic the same checks are made with walls.

b) The collision forces and any other system forces acting upon each particle are evaluated. We then use Newton's second law, equation 2.9, to determine each particle's acceleration, $\ddot{\mathbf{r}}$.

c) Particle positions and velocities are updated using the Verlet algorithm equations 2.11 and 2.12.

However, this method is not the most efficient way of evolving a dense granular system. This is because at each time-step every particle checks with all other particles for collisions, regardless of position. This means that the same priority is given to checking for collisions between two spheres on opposite sides of the system and two particles in very close proximity. Clearly a far from efficient method. An approach designed to dramatically reduce the number of collision checks has been devised and is known as the "nearest neighbour" algorithm (Allen and Tildesley 2000b). Here the particles only check for overlap with other particles in close proximity and not with spheres long distances apart. The method consists of dividing the system into boxes and then separating the particles, depending on their positions, into these boxes. Two arrays are needed to order the checking of the collisions. One array is used to assign a "head" particle in each box and another is used to create a list which points to another particle in the box which has not yet been checked. Once a particle has checked for collisions with other particles in the box it inhabits, it then checks the surrounding boxes for collisions. As described in Section 2.1.2 a small time-step was chosen to resolve the particle collisions sufficiently. This means that the maximum distance moved by the particles within each time-step is many magnitudes less than the box sizes so that only the nearest neighbour boxes need to be checked for collisions. Figure 2.2 illustrates how a particle in box 12 will only have to make checks for collisions with four other boxes, namely 8, 13, 17 and 18. Following the same rules boxes 6, 7, 11, 16 will perform similar checks for collisions with particles inhabiting box 12. Figure 2.2 shows the case of a two-dimensional system, in which each box checks for collisions with 4 other boxes. Note that in a three-dimensional system because of the extra dimension we must check for collisions with 13 boxes.

This algorithm reduces the number of checks made from being proportional to N^2 down to order N, where N is the number of particles. The operation may be optimised further for faster simulations by varying the size of the "nearest neighbour" boxes. For optimal simulation efficiency boxes are reduced to roughly the size of the particle diameter. This way the particles only check for

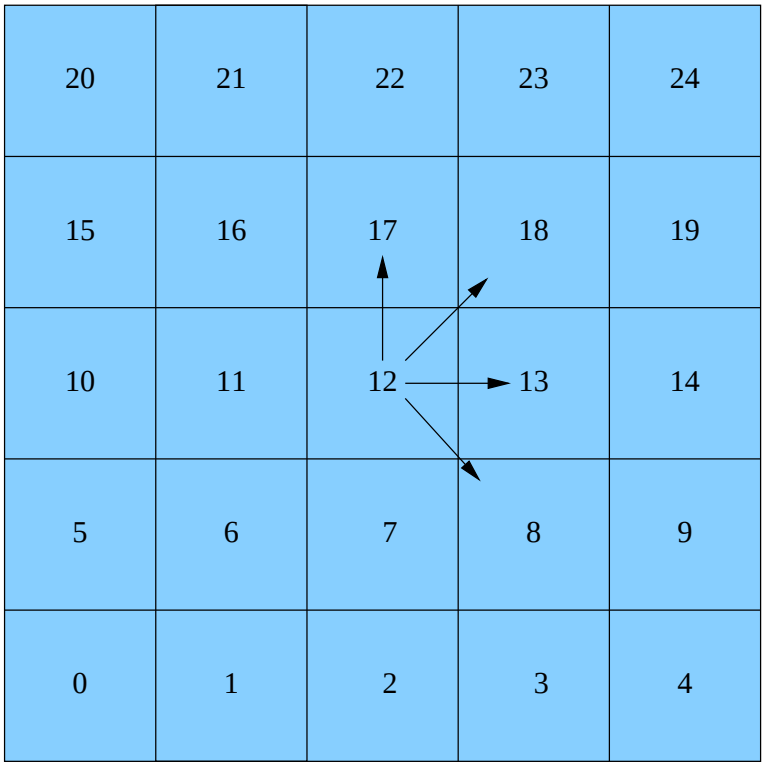

Fig. 2.2: Diagram displays how boxes are ordered in a two-dimensional system. The arrows illustrate how boxes check for collisions with other boxes in the nearest neighbour algorithm. Here a particle in box 12 checks for collisions with particles contained in boxes 8, 13, 17 and 18.

collisions within a small radius.

The granular algorithm may be summarised well in Figure 2.3. The repeatable part of this algorithm is performed every time-step.

2.1.6 Comparison of Soft-Sphere Techniques

In the final part of this section we perform a comparison between the soft-sphere collision models that are described in section 2.1.1. These are the Hertzian, the LSD and the DH models. We focus on stainless steel-stainless steel collisions, for which we are able to compare our soft sphere models to experimental results obtained by Stevens and Hrenya (2005). For these studies we place two grains, with bead properties as shown in Table 2.1, next to each other so that they are in contact but not overlapping. We then give both beads equal and opposite velocities in the direction of the other sphere so that the particle motion and collision axis are in the same plane. The only forces that act upon the particles

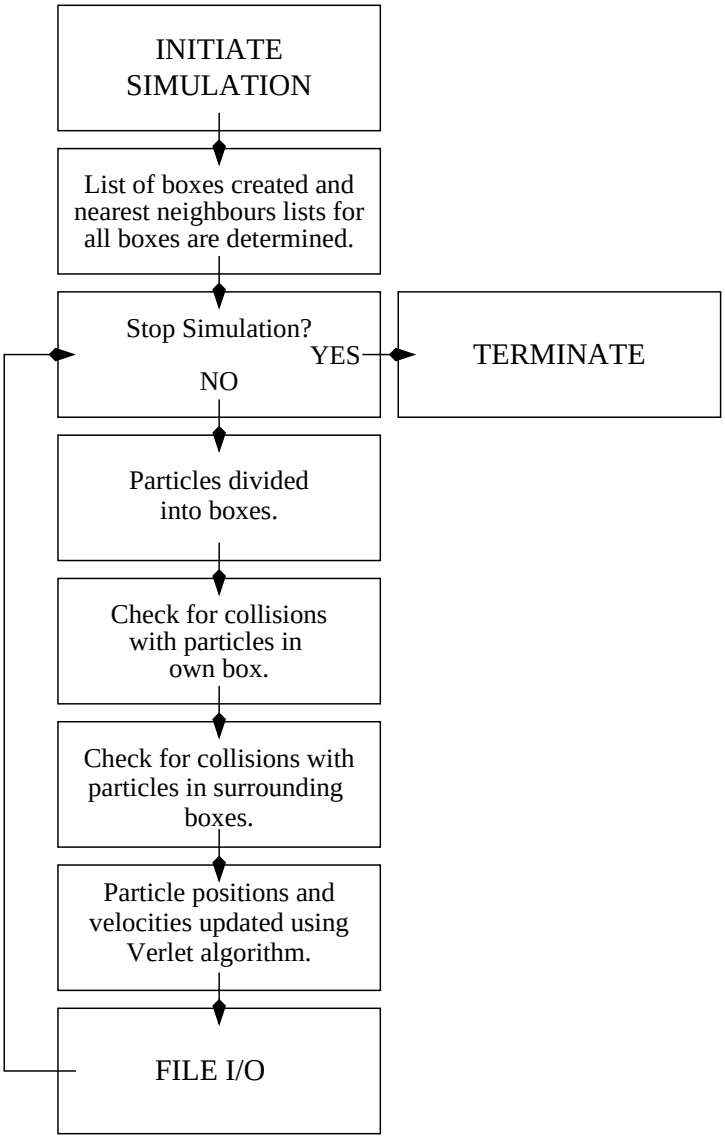

Fig. 2.3: Flow-chart showing the Molecular Dynamics algorithm for the particle model.

Parameter	*Value*
Grain density ρ_g	8030 kg m^{-3}
Radius r	1.27 cm
Young's modulus E	1.93×10^{11} kg m^{-1} s^{-2}
Poisson ratio ν	0.35

Table 2.1: Properties of the stainless steel particles used for testing different soft-sphere collision models.

Name	*Input 1*	*Input 2*
Hertz	$\tilde{k}_n = 1.942\times10^9$ kg s^{-2}	–
Linear Spring-Dashpot	$k_n = 5.160\times10^7$ kg s^{-2}	$\gamma_n = 5.58\times10^0$ kg s^{-1}
Damped Hertzian	$\tilde{k}_n = 1.942\times10^9$ kg s^{-2}	$\tilde{\gamma}_n = 3.41\times10^4$ kg s^{-1}

Table 2.2: The stainless steel parameters are chosen to match $e = 0.879$ and $t_c = 81.3$ μs at a relative impact velocity of $\delta_n = 0.84$ m s^{-1}. The bead properties in table 2.1 are used in equations 2.5 and 2.23 to determine the values of $\tilde{k}_n$ and γ_n. The other inputs are calculated numerically.

are collisional forces from the MD models. Each of the models require input parameters for the elastic and dissipative terms, which are chosen such that the values of the coefficient of restitution, e, and the collision duration, t_c, match experimental results for a particle velocity. The velocity is chosen to be in the middle of the impact velocity range that we study. The specific input values are shown in Table 2.2.

We do three specific behavioural comparisons between the soft-sphere models. These are; the normal force F_n vs the collision overlap δ_n shown in Figure 2.4, the coefficient of restitution e vs the relative impact velocity V_{imp} shown in Figure 2.5, and the duration of the collision, t_c, vs V_{imp} shown in Figure 2.6.

Figure 2.4 plots the predicted force against the particle overlap for our soft-sphere models at an impact velocity of $V_{imp} = 0.84$ m s^{-1}. In this graph, the trajectories for each particle collision form loops, the upper part of the loop representing the force profile as the particles move towards each other, whilst the

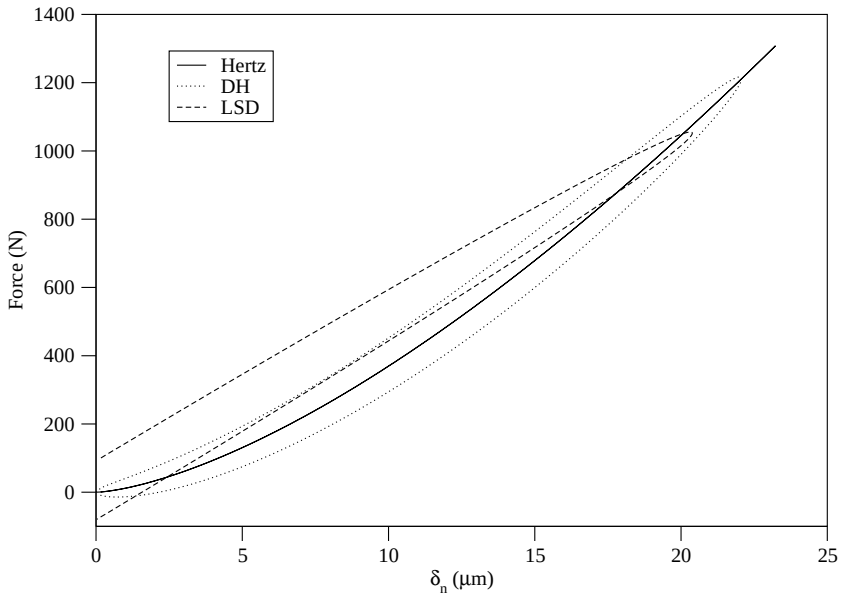

Fig. 2.4: Force profile over duration of collision as a function of the overlap. Diagram shows stainless steel system where input parameters were chosen to match $e = 0.879$ at an impact velocity of $\delta_n = 0.84$ m s^{-1}.

bottom part of the loop represents the force profile as the particles repel each other. The area enclosed within the curve is the total energy lost during the collision. As expected, the Hertzian contact model has identical approach and rebound curves as it is an elastic model with no energy lost during the collision. When examining the models qualitatively we find that the LSD model gives a non-zero force as the particle overlap tends to zero. This is repulsive in the approach phase and attractive in the rebound phase. We also find that the DH collision model displays an attractive force ($F < 0$) just before contact is lost between the particles at small values of the overlap δ_n. However, unlike the LSD model the force within the DH model does return to zero as $\delta_n \to 0$. This attraction occurs because the dissipative attractive forces are larger than the elastic repulsive forces for small overlaps as the particles move apart. Note that no cohesion between the particles occurs because as the particles slow down the elastic repulsive forces ensure that the particles remain repellent of one another. The attractive forces during collisions predicted by our MD models are unphysical, however, the effect is only slight and still allows for realistic overall collision dynamics (overlap, coefficient of restitution, collision duration) to be realised. In dense systems with large numbers of inelastic collisions this artefact of the collision schemes is

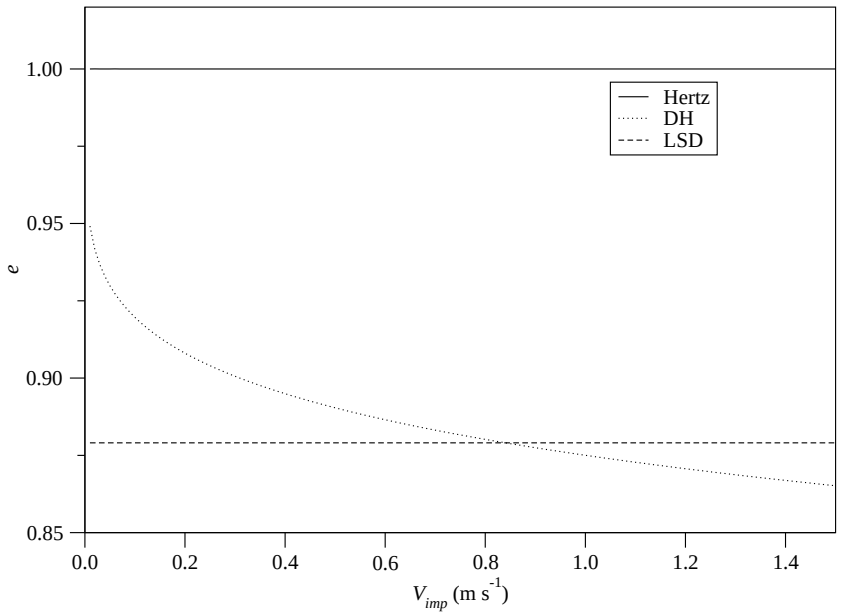

Fig. 2.5: Velocity dependence of the coefficient of restitution for stainless steel system using different MD models. Input parameters are chosen to match $e = 0.879$ at an impact velocity of $\delta_n = 0.84$ m s^{-1}.

completely unnoticed.

Figure 2.5 demonstrates the variation of the coefficient of restitution with the relative impact velocity for colliding stainless steel spheres. We find that when using the LSD and Hertzian models we obtain the same e regardless of the impact velocity. The experimental stainless steel collision data (Stevens and Hrenya 2005) gives a sloping downward trend which is best captured by the DH model. The coefficient of restitution is constant, $e = 1.0$ and $e = 0.879$, for all impact velocities when using the elastic Hertzian and LSD schemes respectively to model the steel particle collisions. In this test the DH model is able to mimic real collisions more accurately than the LSD and Hertzian models.

Figure 2.6 shows the effect of varying the impact velocity on the collision duration t_c for our stainless steel spheres. In real stainless steel particles collisions (Stevens and Hrenya 2005) t_c decreases as V_{imp} increases. This behaviour is best captured by the DH and Hertzian models. The LSD model gives a collision duration which is independent of the impact velocity and so does not capture the experimental collision dynamics as well.

In summary, within real stainless steel collisions (Stevens and Hrenya 2005) an increase in the impact velocity V_{imp} reduces the coefficient of restitution e and

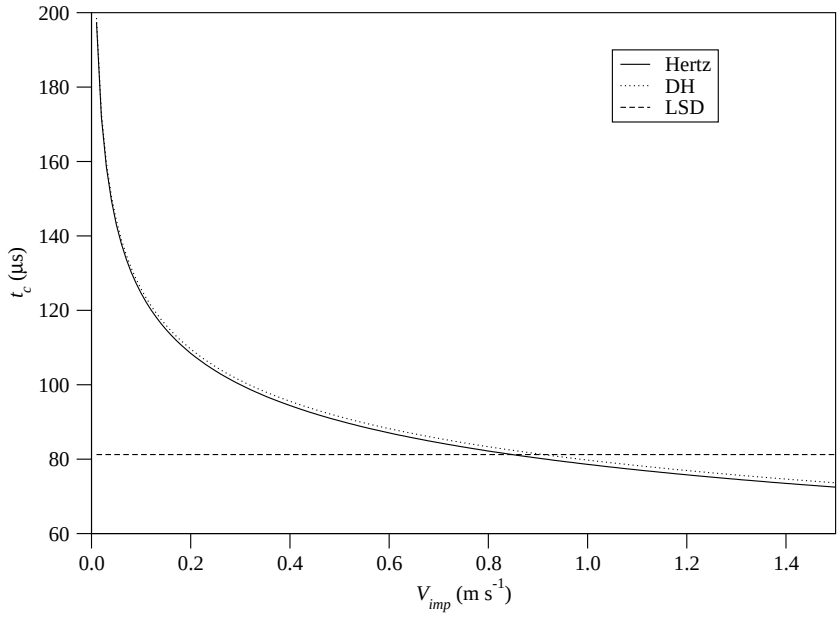

Fig. 2.6: Velocity dependence of the collision durations for stainless steel system using different MD models. Input parameters are chosen to match $e = 0.879$ at an impact velocity of $\delta_n = 0.84$ m s^{-1}.

collision duration t_c. Within our collision models e may be predicted to decrease (DH) or remain constant (LSD and Hertzian) as V_{imp} increases. The collision duration t_c may be predicted to decrease (DH and Hertzian) or remain constant (LSD) with increasing V_{imp}. Therefore the DH model developed by Kuwabara and Kono (1987) gives the best quantitative agreement with real collisions, with good agreement of the variation of t_c and e with impact velocity. This suggests the particle collisions operate within a viscoelastic regime for this range of V_{imp}. Thus in simulations where collision dynamics are important to the overall properties of the system, I will always use the DH model. The LSD model is still useful as it is easy to set up computationally.

If the spring constant is reduced, k_n and $\tilde{k}_n$, in both the LSD and DH collision models for fixed e we are able to substantially increase the collision duration as shown in Figure 2.7. With a longer collision duration it is possible to increase the time-step and hence speed up the simulation. However, the collisions only mimic real interactions for a particular set of parameters. Therefore by reducing k_n or $\tilde{k}_n$ the collision dynamics become less realistic as the collision overlap increases

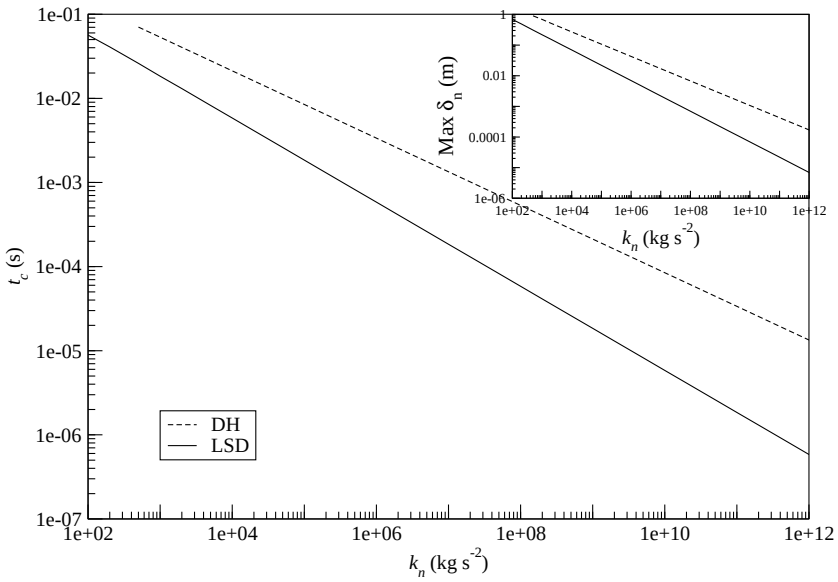

Fig. 2.7: The collision duration plotted as a function of the spring constant strength. The inset shows the maximum particle overlap as a function of the spring constant. The data from the Linear Spring-Dashpot model (solid-line) and the Damped Hertzian model (broken-line) are both plotted. Input parameters are chosen to match $e = 0.9$ at a relative impact velocity of $\delta_n = 1.0$ m s^{-1}.

at a similar rate to the collision duration (see Figure 2.7 inset). A realistic spring constant $\tilde{k}_n$ for the DH model may be predicted using equation 2.5, which uses measurable properties of the particles. Any $\tilde{k}_n$ less than this value will lead to larger deformations and unrealistic collision dynamics. In some simulations, however, it is possible to use the LSD and DH collision models with reduced spring constants. For example, in sedimenting beds where collisions are rare and do not affect the overall system properties, the LSD collision model may be implemented.

2.2 The Fluid Model

In this section we discuss the simulation method used to model the fluid. There are many different ways in which we may do this although the most popular modern methods predominantly fall into two groups. The first group involves discretising and solving fluid equations on a lattice while the second group of techniques involve modelling the fluid as a finite number of "particles" which move within a framework of various flow conditions.

One popular method used to simulate fluids, which falls into the first type of technique described above, involves the use of a lattice and is accordingly named the Lattice Boltzmann method. Here, instead of solving the governing equations of fluids, Navier–Stokes equations, the discrete Boltzmann equation is solved to simulate the flow of a Newtonian fluid. By simulating the interaction of a limited number of fluid "packets" on a triangular lattice the viscous flow behaviour emerges automatically from the flow and collision processes of the particles.

Some popular methods which fall into the second category include Dissipative Particle Dynamics (DPD) and Smoothed Particle Hydrodynamics (SPH) in which the fluid is modelled as fluid packets. These models apply short range forces between the fluid "particles" in such a way that the viscous flow behaviour is captured.

The approach that we use within this thesis falls into the first type of technique above and is based on spatially and temporally discretising the Navier–Stokes equations onto a staggered rectangular lattice. The Navier–Stokes equations describe the motion of fluid substances and are able to model the physics of a large variety of fluid phenomenon with high accuracy. We prefer this model as it is easy to code and the underlying domain is rectangular which enables the use of fast Fourier techniques within the fluid solver (see section 2.2.1). Questions also remain regarding the accuracy of the DPD and SPH models since they are essentially fitting their dynamics to match those of the Navier–Stokes equations. Models of this complexity are also unnecessary for the types of systems that we will be simulating in this thesis.

The Navier–Stokes equations, in an inertial frame of reference, may be given as:

$$\rho\left(\frac{\partial \mathbf{v}}{\partial t} + (\mathbf{v}.\nabla)\,\mathbf{v}\right) = -\nabla P + \eta\nabla^2\mathbf{v} + \rho\mathbf{f}. \tag{2.24}$$

Here $\mathbf{v}$, P and ρ are the fluid velocity, pressure and density. η is the dynamic viscosity and is related to the kinematic viscosity, ν, via the following equation:

$$\nu = \frac{\text{Dynamic Viscosity}}{\rho} = \frac{\eta}{\rho}. \tag{2.25}$$

The first and second terms in equation 2.24 are the unsteady and convective accelerations, which together are known as the material derivative. The unsteady

acceleration is the change in the fluid velocity with time, while the convective acceleration is the time independent acceleration of the fluid with respect to space. The third term is the pressure gradient term and the fourth is the viscous diffusion of momentum. **f** is the volume body force on the fluid and is usually equal to gravity or any other force on the fluid such as that from a magnetic field.

The Navier–Stokes equations are non-linear partial differential equations in most real situations. The only exception is the case of creeping flow where the Reynolds number is very low, i.e. $R_e \ll 1$. The Reynolds number is a dimensionless measure of the ratio of inertial forces to viscous forces, and consequently it quantifies the relative importance of these types of force for given flow conditions. It is typically defined as follows:

$$R_e = \frac{\text{Dynamic Pressure}}{\text{Shearing Stress}} = \frac{v_s L}{\nu}. \tag{2.26}$$

Here v_s is the mean fluid velocity and L is the characteristic length of the system.

The Navier–Stokes equations are derived by applying Newton's Second law to fluid motion and arise from the mass and momentum conservation equations for a fluid. The mass conservation equation may be given as:

$$\frac{\partial \rho}{\partial t} + \nabla.(\rho \mathbf{v}) = 0. \tag{2.27}$$

In this thesis we focus our attentions on incompressible fluids i.e. those fluids whose density does not alter in space and time ($\frac{\partial \rho}{\partial t} = 0$ and $\nabla \rho = 0$). By expanding equation 2.27 and substituting in the conditions for the density we obtain the incompressibility constraint:

$$\nabla.\mathbf{v} = 0. \tag{2.28}$$

2.2.1 The Fluid Algorithm

We now need to find a way of solving the Navier–Stokes equations such that we are able to apply it to a range of fluid flow problems within our simulations. One of the basic assumptions of the Navier–Stokes equations is that the fluid is continuous. However, the approach we use requires the Navier–Stokes equations to be spatially discretised so that local values of the fluid velocity and pressure are determined on a grid which covers the whole of the fluid system. We then use a

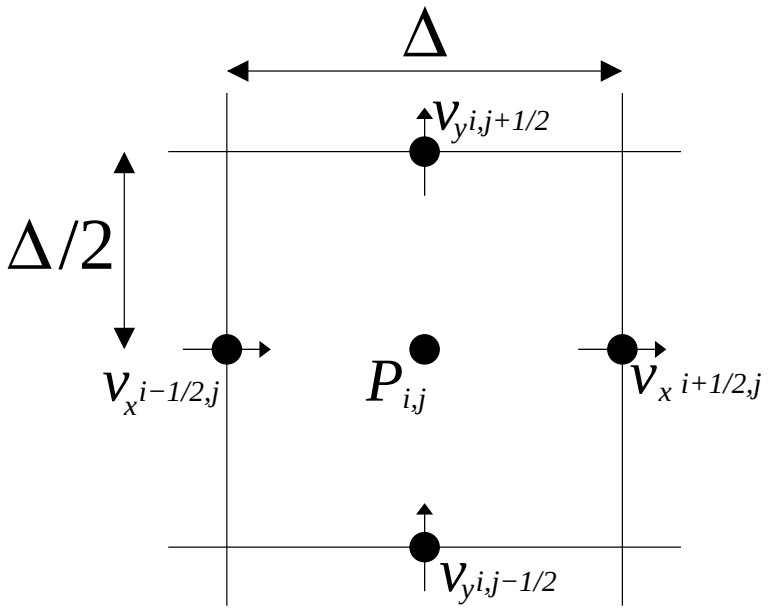

Fig. 2.8: Typical Marker-and-Cell (MAC) mesh in two dimensions, displaying the layout of velocities and pressure on the cell. Here $v_{x(i,j)}$ and $v_{y(i,j)}$ are the horizontal and vertical fluid velocities at position $(x, y) = ((i + 0.5)\,\Delta, (j + 0.5)\,\Delta)$, where $\mathbf{v} = v_x\mathbf{i} + v_y\mathbf{j}$.

projection method and proceed in time by using a fractional-time-step operator-splitting method (Chorin 1968). The grid we use for spatially discretising the Navier–Stokes equations 2.24 is a staggered Marker-and-Cell (MAC) mesh as shown in Figure 2.8 (Harlow and Welch 1965). It should be noted that the configuration of the single lattice grid cell shown in Figure 2.8 is part of a much larger mesh which spans the entire fluid system. The grid is configured so that the fluid pressure is determined within the centre of each cell, while the fluid velocities are calculated along the midpoint of each box edge. The fluid velocities are determined perpendicular to the surface of the mesh cell, so that the horizontal component of the velocities are calculated on the vertical edges of the cell and the vertical components of the velocities are calculated on the horizontal box edges. Constructing the grid in this way has several computational advantages over a standard grid system in which all of the fluid properties are determined upon the centres of each cell. This is because there are fewer numerical instabilities due to mesh decoupling within the staggered MAC mesh and it also exhibits greater accuracy.

Expanding equation 2.28 in two dimensions gives:

$$\frac{\partial v_x}{\partial x} + \frac{\partial v_y}{\partial y} = 0, \tag{2.29}$$

where v_i is the fluid velocity along the i–axis. If equation 2.29 is spatially discretised onto our staggered MAC grid in figure 2.8 we obtain:

$$\frac{v_x(i+1/2,j) - v_x(i-1/2,j)}{\Delta} + \frac{v_y(i,j+1/2) - v_y(i,j-1/2)}{\Delta} = 0 \tag{2.30}$$

This equation illustrates that the volume of fluid entering the cell through the side-walls must be equal to the volume of fluid leaving the cell. In essence no new fluid may be created or destroyed within each time-step.

The discretisation of the Navier–Stokes equations in time is explicit and first order. Index n refers to values at time, $t_n = n\Delta t$, and index $n+1$ to those at time $t_{n+1} = (n+1)\,\Delta t$. By discretising the Navier–Stokes equations 2.24 in time we obtain

$$\frac{\mathbf{v}_{n+1} - \mathbf{v}_n}{\Delta t} = -\left(\mathbf{v}_n.\nabla\right)\mathbf{v}_n - \nabla p_{n+1} + \nu\nabla^2\mathbf{v}_n + \mathbf{g}_n, \tag{2.31}$$

where $p = P/\rho$ and the fluid body force has been set equal to gravitational acceleration. The problem we now have is that at time t_n we know the fluid velocity field, $\mathbf{v}_n$, and the pressure field, p_n, but wish to determine the future fluid velocity and pressure fields, $\mathbf{v}_{n+1}$ and p_{n+1} using the time-discretised Navier–Stokes equations and the incompressibility constraint. We achieve this by employing an explicit fractional-time-step operator-splitting method which satisfies the incompressibility constraint in equation 2.28. Thus we introduce a provisional "velocity" $\mathbf{v}^*$ which has no physical meaning into equation 2.31, such that:

$$\frac{(\mathbf{v}_{n+1} - \mathbf{v}^*) - (\mathbf{v}_n - \mathbf{v}^*)}{\Delta t} = -\left(\mathbf{v}_n.\nabla\right)\mathbf{v}_n - \nabla p_{n+1} + \nu\nabla^2\mathbf{v}_n + \mathbf{g}_n. \tag{2.32}$$

Equation 2.32 is now split into two smaller equations which are mathematically equivalent to the single equation we started with:

$$\frac{\mathbf{v}^* - \mathbf{v}_n}{\Delta t} = -\left(\mathbf{v}_n.\nabla\right)\mathbf{v}_n + \mathbf{g}_n + \nu\nabla^2\mathbf{v}_n, \tag{2.33}$$

$$\frac{\mathbf{v}_{n+1} - \mathbf{v}^*}{\Delta t} = -\nabla p_{n+1}. \tag{2.34}$$

To obtain equations 2.33 and 2.34 an explicit method has been used, however, it is possible to use a semi-implicit method, which can allow for a larger time-step.

By taking the divergence of equation 2.34 and substituting in the incompressibility constraint, equation 2.28, we are able to eliminate the fluid velocity $\mathbf{v}_{n+1}$ to obtain the Poisson equation:

$$\frac{\nabla.\mathbf{v}^*}{\Delta t} = \nabla^2 p_{n+1}. \tag{2.35}$$

The steps above are often considered to be a projection of equations 2.33 and 2.34 onto a divergence free subspace of the velocity vector field. The pressure equation 2.35 is used to remove the "perpendicular" velocity components contained in $\mathbf{v}^*$, and thus the term "projection method" is often used to describe this process. The future fluid velocity, $\mathbf{v}_{n+1}$, has been eliminated from the two equations, 2.33 and 2.35 which allows us to solve these equations simultaneously. Firstly one obtains the virtual fluid velocity, $\mathbf{v}^*$, from equation 2.33 using the current values of the local fluid velocities. Then the future fluid pressure, p_{n+1}, are obtained by solving the diffusion equation 2.35 using a fast Fourier transforms (FFT) method (Frigo and Johnson 2005; Frigo and Johnson 2006). Using the fluid pressure field p_{n+1} and virtual fluid velocity field $\mathbf{v}^*$ within equation 2.34 it is then possible to compute the future fluid velocities $\mathbf{v}_{n+1}$. Thus the fluid model algorithm proceeds as follows:

a) The local fluid velocities and pressures are initially discretised onto the staggered MAC grid.

b) The "virtual" fluid velocities, $\mathbf{v}^*$, are calculated from equation 2.33, using the current local fluid velocities.

c) Input $\mathbf{v}^*$ into equation 2.35 to determine the fluid pressure field, p_{n+1}, either by the relaxation method or by using a FFT method.

d) Use the pressure p_{n+1} and the virtual fluid velocity $\mathbf{v}^*$ fields in equation 2.34 to calculate the new fluid velocity field, $\mathbf{v}_{n+1}$.

This algorithm can be repeated as required until a dynamic equilibrium is reached.

2.2.2 Fluid Boundary Conditions

An important consideration for the fluid system is what happens to the fluid flow at the boundaries. In this thesis the boundaries are treated as solid walls which

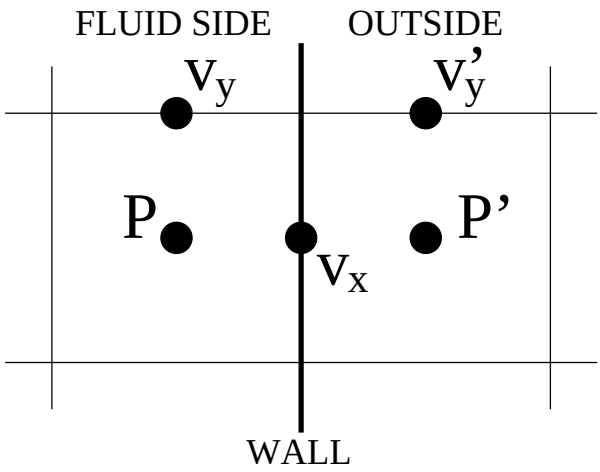

Fig. 2.9: Field variables near a wall.

fluid is unable to flow through, however, as with the granular system, periodic conditions are also possible. The boundaries are positioned on the edge of the Eulerian cells such that only horizontal fluid velocities lie on the vertical wall boundaries and only vertical fluid velocities lie on the horizontal wall boundaries. In three dimensions a similar arrangement occurs for the front and back boundaries. Figure 2.9 shows this arrangement for a two-dimensional system near a wall. A rigid wall can be of two types, a no-slip and a free-slip surface, depending on the type of boundary properties required. A no-slip surface is one in which there is zero fluid velocity on the wall, while a free-slip boundary is one in which the fluid just has zero velocity normal to the surface. The no-slip boundaries mimic real systems best and can be imagined conceptually as the outermost "particles" of fluid nearest the wall sticking to the surface. The free-slip surface can be used to represent a plane of symmetry or moving surface. We impose no-slip boundary conditions for the majority of this thesis.

The fluid boundary conditions are enforced by imposing rules on the fluid flow and pressure variables within the cells adjacent to the wall. Figure 2.9 shows a sample two-dimensional system of the important fluid flow and pressures on either side of a solid boundary necessary for enforcing the conditions. In a real system, fluid is unable to escape through the boundary walls. Thus the fluid velocity across the vertical wall is set to zero, i.e. $v_x = 0$. For a no-slip wall the boundary condition tangential to the wall is set to $v'_y = -v_y$. This condition forces the fluid flowing vertically to zero on the boundary as the wall lies on the

midpoint of these velocities. The corresponding free-slip condition is $v'_y = v_y$. Analogous conditions are applied on all other walls. The pressure condition for vertical walls may be derived as $P' = P$, while for horizontal walls an extra term is introduced to enforce the hydrostatic pressure condition $P' = P + g\Delta$. The boundary conditions on the fluid are usually sufficient to enforce no-slip conditions. This means that in our code the pressure condition is not required to resolve the fluid algorithm. These boundary conditions are enforced during each time-step.

2.2.3 Cavity Flow

As a minor digression we may use the fluid model to simulate lid-driven cavity flows. This fluid problem is possibly the most studied area of computational fluid dynamics and is often used as a benchmark problem for testing numerical methods for accuracy and efficiency. This study gives us an opportunity to discuss some other important aspects of viscous fluid regimes.

The properties of the cavity flow problem are characterised by its Reynolds number, given by

$$R_e = \frac{U.L}{\nu}, \tag{2.36}$$

where U and L are the characteristic velocities and lengths of the system. The Reynolds number, R_e, gives us an indication as to which viscous regime the fluid system lies in.

An important consideration for the simulation is what time-step, Δt, we should use within the fluid model. The larger the time-step Δt the faster the simulation will run, however, if the time-step is too large errors accumulate and the fluid becomes unstable. By performing an error analysis (Anderson 1995) on the time and space discretised Navier–Stokes equations in D dimensions Anderson was able to derive two conditions for the fluid time-step:

$$\Delta t \leq \frac{1}{2D}\frac{\rho\Delta^2}{\eta} \tag{2.37}$$

and

$$\Delta t < \frac{\Delta}{Dv_{\max}}. \tag{2.38}$$

Parameter	*Value*
Time-step Δt	10^{-6} s
Cavity size (x–axis)	10 mm
Cavity size (y–axis)	10 mm
Lattice spacing Δ	50 μm
u_{shear}	0.1–1.0 m s^{-1}
Fluid density ρ	1000 kg m^{-3}
Dynamic viscosity η	10^{-3} kg m^{-1} s^{-1}
R_e	1000–10000

Table 2.3: Parameters for lid-driven cavity flow system.

If the time-step does not obey the inequalities 2.37 and 2.38 then the error becomes progressively larger and will quickly cause the numerical solution to "blow up".

We now return to our lid-driven cavity problem where we set up a two-dimensional cell completely filled with water of density $\rho = 1000$ kg m^{-3} and viscosity 1×10^{-3} kg m^{-1} s^{-1}. We impose free-slip boundary conditions on the top surface which moves with velocity u_{shear} from left to right. No-slip boundary conditions are imposed on the bottom and two side walls. The rest of the cavity parameters are shown in table 2.3. The fluid in the cell initially begins stationary. After a few seconds the flow becomes steady and a large vortex is created within the cavity. Figure 2.10 shows the streamfunction contours within the cavity for Reynolds numbers of $R_e = 1000$, $R_e = 5000$ and $R_e = 10000$ which are determined when the shear velocity and cell length are used within equation 2.36. The streamfunction, ψ, allows us to plot the flow streamlines which are defined as the family of curves instantaneously tangent to the flow vectors for incompressible fluids. The streamfunction may be calculated using the relation:

$$d\psi = -v_y dx + v_x dy. \tag{2.39}$$

Figure 2.10 shows how for each Reynolds number a large vortex forms which dominates the centre of the cavity. Several secondary vortices also form in the corners of the cell, in particular in the top left corner and in both corners at the

bottom of the cell. The fluid in the main vortex moves around in a clockwise motion, whilst the secondary vortices move anti-clockwise, in the opposite direction to the main flow. In Figure 2.10(a) we see that, for $R_e = 1000$, there are two auxiliary vortices in both corners at the bottom of the cavity with fluid flow moving in an anticlockwise direction. In Figure 2.10(b) as the Reynolds number increases to $R_e = 5000$, we observe that the two bottom vortices become larger while an extra anti-clockwise flowing vortex develops in the top left. In Figure 2.10(c), for $R_e = 10000$, all of the secondary vortices grow larger and an extra vortex develops in the bottom right which flows in a clockwise direction. Figure 2.10 shows that as R_e is increased the trend is for the secondary vortices to grow and for new ones to develop.

In Figures 2.11 and 2.12 we measure the velocity profiles of the cavity. We calculate the normalised v_x and v_y velocities along a vertical and horizontal line through the centre of the cavity and plot them in Figures 2.11 and 2.12 respectively. The area on either side of the lines are equal due to fluid incompressibility. As R_e increases the maximum velocities occur nearer the boundaries and the velocity profile becomes more linear across the cell. Our results agree well with the comprehensive simulations carried out by Erturk (2005).

We now move onto describing the methods through which the fluid and granular phases may be coupled. One way in which this is possible is through the analytical Kroll model which may be solved numerically to determine the flight of a fluid-immersed porous granular bed within a vibrating cell. This can be used as a comparison to some of the microscopic fluid-grain coupling techniques introduced later.

2.3 The Kroll Model

We have already separately described how we model granular and fluid systems in sections 2.1 and 2.2 respectively. To simulate a coupled system of fluid-immersed grains we must develop a technique that models the momentum transfer between the fluid and grains both accurately and efficiently. There are many different methods in which we may model the fluid and grains interactions, however, before

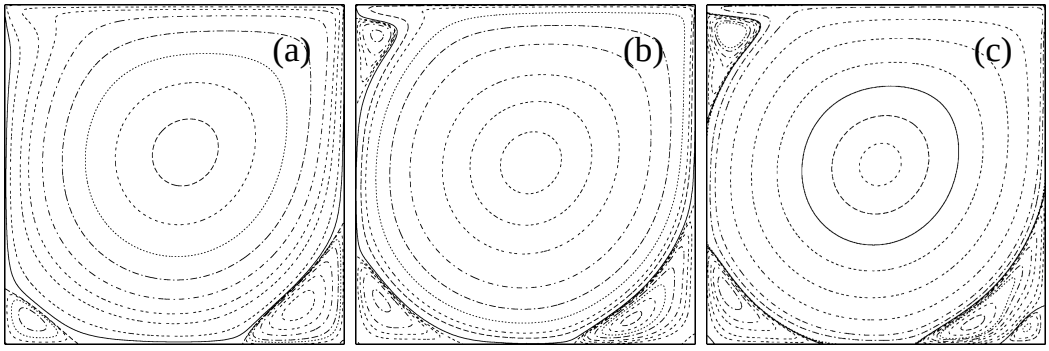

Fig. 2.10: Streamfunction contours within a two-dimensional lid-driven cavity flow system for Reynolds numbers (a) 1000, (b) 5000 and (c) 10000. The system parameters are shown in Table 2.3.

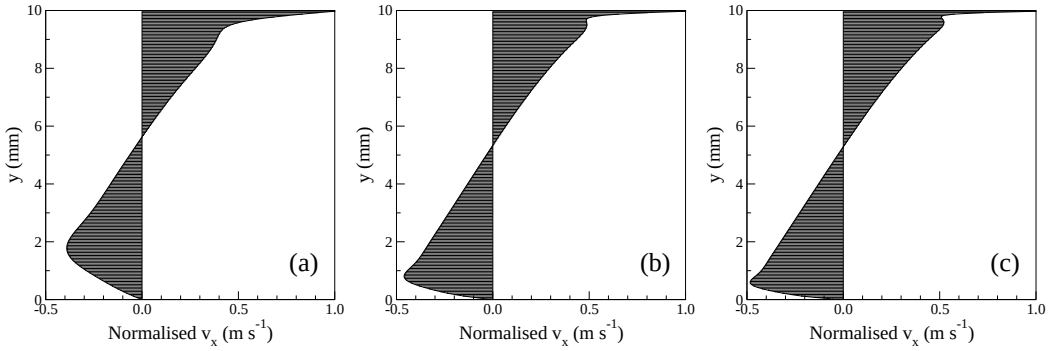

Fig. 2.11: The normalised v_x velocity profile along a vertical line passing through the centre of the cavity for Reynolds numbers of (a) 1000, (b) 5000 and (c) 10000 within the two-dimensional lid-driven cavity flow system.

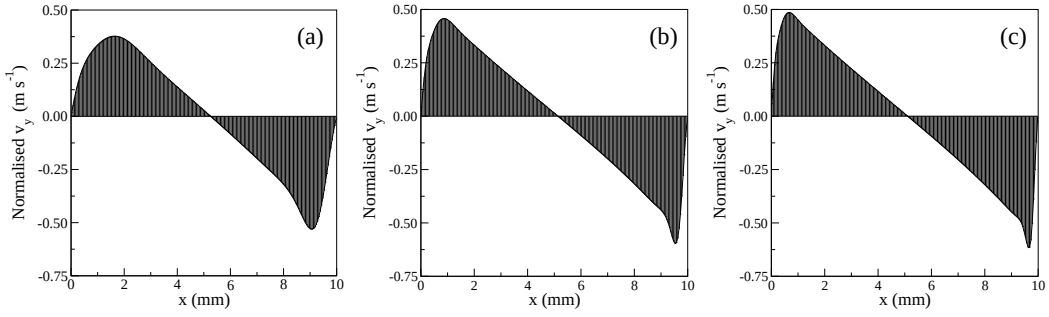

Fig. 2.12: The normalised v_y velocity profile along a horizontal line passing through the centre of the cavity for Reynolds numbers of (a) 1000, (b) 5000 and (c) 10000 within the two-dimensional lid-driven cavity flow system.

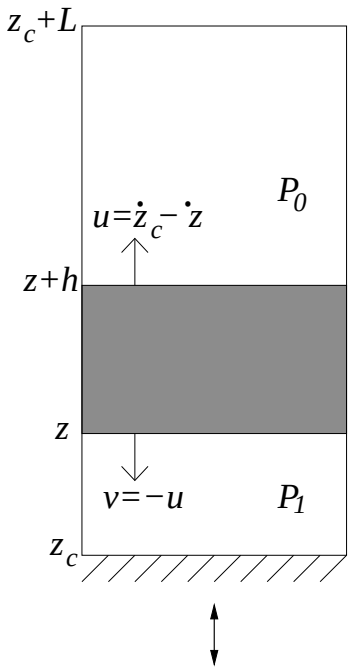

Fig. 2.13: Schematic diagram of porous bed within a vibrating cell.

we describe any of them we introduce the analytical Kroll model. This approach predicts the flight of a fluid-immersed porous granular bed in a vibrated cell and produces results very comparable to those measured within experiments. Later we introduce a modified version of the Kroll model which accounts for the presence of a dense fluid.

The Kroll model (1954) is a theoretical numerical technique which is useful in determining the bed flight of a porous bed in a vibrated system. In this method the bed of particles are assumed to behave as a porous plug, which does not dilate during flight. The fluid is treated as massless and incompressible, such that as the cell is vibrated the bed lifts from the cell base and fluid flows downwards through the bed to occupy the space beneath. A schematic representation of this setup may be seen in Figure 2.13.

The vibration of the cell is considered to be sinusoidal with maximum amplitude A_0 and frequency f such that the position of the cell base z_c may be obtained using:

$$z_c = A_0 \sin(\omega t) + A_0. \tag{2.40}$$

The speed of vibration is therefore

$$\dot{z}_c = A_0 \omega \cos(\omega t) \tag{2.41}$$

and the acceleration is

$$\ddot{z}_c = -A_0\omega^2 \sin(\omega t). \tag{2.42}$$

Here $\omega = 2\pi f$ is the angular frequency. When describing vibrating systems an important parameter is the dimensionless maximum acceleration, Γ. This parameter is the ratio of the maximum vibrational acceleration to the gravitational acceleration g and is given by:

$$\Gamma = \frac{A_0\omega^2}{g}. \tag{2.43}$$

If $\Gamma > 1$ then in the early part of the cycle, when the cell is simultaneously moving upwards and decelerating, the bed of particles will lift off from the base. This occurs when the cell accelerates downwards faster than the gravitational acceleration. Thus we may determine the phase angle of take-off, θ_{to}, as:

$$\theta_{to} = \frac{180}{\pi} \sin^{-1}\left(\frac{1}{\Gamma}\right). \tag{2.44}$$

After take-off the granular bed is moving relative to the cell and so fluid moves through the bed into the space beneath in order to conserve volume. Due to fluid motion through the bed the particles experience a drag force.

We define z as the position of the lower edge of the granular bed in the laboratory frame so that the acceleration of the bed, $\ddot{z}$, can be determined by applying Newton's laws of motion to the bed when in flight:

$$hA(1-\phi)\rho_g \ddot{z} = -hA(1-\phi)\rho_g g - A(P_0 - P_1). \tag{2.45}$$

Here ρ_g is the density of the grains and h and A are the height and cross-sectional area of the bed. P_0 and P_1 are the pressure above and below the bed respectively. The porosity, ϕ, of the bed, is defined as the ratio of fluid within a given volume and is calculated using:

$$\phi = 1 - \frac{\text{Volume occupied by spheres}}{\text{Total volume of bed}}. \tag{2.46}$$

In the Kroll model the porosity is assumed to be unchanged throughout the bed flight. On the right hand side of equation 2.45 the first term is a gravitational acceleration term and the second is an acceleration term due to the pressure drop

across the bed. By dividing equation 2.45 by the mass of the grains $hA\left(1-\phi\right)\rho_g$ we may simplify the bed acceleration to:

$$\ddot{z} = -g - \frac{\nabla P}{\rho_g \left(1-\phi\right)}. \tag{2.47}$$

To determine the bed acceleration $\ddot{z}$ the pressure gradient across the bed, ∇P, must be evaluated. It is possible to model ∇P approximately using an empirical equation such as Darcy's law (1856).

Darcy's law relates the pressure drop to the fluid flow through a dense porous medium:

$$\mathbf{v} = -\frac{\kappa}{\eta}\nabla P \tag{2.48}$$

Here κ is the permeability of the bed and $\mathbf{v}$ is superficial velocity, which is defined as the volumetric flow rate per unit area with respect to a static bed of grains. For the specific case of a porous bed of spherical particles with porosity ϕ moving in one dimension the equation becomes:

$$-\nabla P = \frac{180\eta\left(1-\phi\right)^2}{d^2\phi^3}v. \tag{2.49}$$

If we define the velocity of the bed in the frame of reference of the cell as $u = \dot{z} - \dot{z}_c$, then the superficial velocity of the fluid with respect to the bed becomes $v = -u$. We then substitute Darcy's law into equation 2.47 and rearrange to obtain a first-order differential equation describing the flight of the bed:

$$\dot{u} + \gamma u + g + \ddot{z}_c = 0. \tag{2.50}$$

Here $\gamma = \frac{180\eta(1-\phi)}{d^2\rho_g\phi^3}$ depends on the bed equation used to determine the pressure drop across the bed (Section 2.4.4). This model, however, does not consider the fluid density and the upthrust resulting from the vibrating fluid within the cell. When the fluid has a low density like air, we may use the Kroll model with confidence, however, when the fluid is dense like water the Kroll model loses validity. Thus a numerical model which accounts for a dense fluid is necessary to successfully model these systems. This leads us to describe the Modified Kroll model.

2.3.1 The Modified Kroll Model

If the density of the fluid, ρ, is considered and we examine the pressure across the three phases of the vibrated system; above, within and below the bed during flight we are able to obtain the equation of motion (Smith *et al.* 2005):

$$\dot{u}\left(1+\frac{\rho\left(1-\phi\right)}{\rho_g\phi}\right)+\frac{\rho_g-\rho}{\rho_g}\left(g+\ddot{z}_c\right)+\gamma u=0. \tag{2.51}$$

Here γ takes the same form as in the Kroll model such that $\gamma=\frac{180\eta(1-\phi)}{d^2\rho_g\phi^3}$ and is again dependent on the bed equation used to determine the pressure drop across the bed (Section 2.4.4).

The two differences between equations 2.50 and 2.51 are the added mass correction, which appears in the first term of equation 2.51, and the buoyancy correction, which appears in the second term. If the density of the fluid is reduced towards zero, $\rho\rightarrow 0$, equation 2.51 tends towards equation 2.50. This shows that in low density limits the Kroll model is a valid approach for bed flight analysis.

The Kroll and Modified Kroll (MK) models are able to accurately reproduce experimental data and so may be used for comparisons against other fluid-grain models. However they are not good on their own for thorough fluid-grain analysis as granular micro-behaviour is not considered.

2.4 Fluid-Grain Coupling with Bed Equations

We now describe several fluid-grain models in which the grains are modelled within the framework of the Molecular Dynamics technique. There are several methods of doing this that are easy to code including the Pressure model, the Simple Drag model, the Resistor Network model and the Navier–Stokes model, however, some of these are either too simplistic or do not offer sufficient fluid detail for our purpose.

There are three types of models that we focus on in this thesis. The first are models in which the particles experience the fluid but the fluid does not experience the particles, namely the Simple Drag model. The second are models in which the particles experience the fluid and the fluid experiences the particles, namely the Navier–Stokes model. Here the grains are small in comparison to the

size of the fluid grid and require the use of bed equations to couple the fluid grain motion. The third type are models in which the particles and fluid experience each other and the grains are large in comparison to the fluid grid, so that the fluid is everywhere, including "inside" the particles. The two models we describe of this kind are the Particle Template model and the Fluid Springs model. The methods by which the fluid and grains are coupled are very different for each model approach. The first coupling technique requires a fluid drag force term to be applied explicitly onto the particles, while the models with bed equations treat the grains as local disturbances to the fluid motion. In the models in which fluid is everywhere the particles encapsulate a large number of fluid grid points. The fluid is then forced to match the motion of the particle in which it is immersed. The first approach we describe in the next section is the Simple Drag model which is the most basic fluid-grain coupling model that we report in this thesis and is a model in which the grains move within a homogeneous background fluid and experience a drag force, the form of which is based on the empirical bed equations.

The second approach we describe which requires a bed equation is the Navier–Stokes algorithm. This approach includes the governing equations of fluids, the Navier–Stokes equations, to resolve the fluid motion and MD to model the particle motion. A momentum transfer term is used to couple the two phases together, the form of which is also dependent on the empirical bed equation used. There have been several bed equations developed which estimate the pressure drop as fluid flows through a densely packed porous granular bed. We describe the bed equations in more detail in section 2.4.4.

2.4.1 The Simple Drag Model

The essence of the Simple Drag (SD) model is that the granular bed particles interact, according to MD technique, and then experience a drag force due to the presence of an homogeneous background fluid. We treat the fluid as a single entity which moves with the cell so that its velocity relative to the container is zero.

To find the force on a single particle, we first consider the force acting on the

whole of the bed. In the limit of steady flow one can show that the force on the bed is:

$$\mathbf{F}_{bed} = V\left(-\nabla P\right). \tag{2.52}$$

Here V is the total volume of the fluid and grains within the bed and ∇P is the pressure gradient across the bed. The average force on each particle may be determined by dividing the total force on the bed, from equation 2.52, by the number of grains contained within the bed, N, so that we obtain:

$$\mathbf{F}_{Drag} = \frac{\mathbf{F}_{bed}}{N}. \tag{2.53}$$

The number of particles N may be estimated by dividing the volume of grains within the bed by the volume of a single particle V_p, such that $N = (1-\phi)\,V/V_p$. Substituting this relation into equation 2.53 gives

$$\mathbf{F}_{Drag} = \frac{V_p\left(-\nabla P\right)}{1-\phi}. \tag{2.54}$$

The pressure gradient across the bed, $-\nabla P$, is determined using an empirical bed equation such as Darcy's (1856)

$$-\nabla P = \frac{180\eta\left(1-\phi\right)^2}{d^2\phi^3}\mathbf{V}_0, \tag{2.55}$$

where $\mathbf{V}_0$ is the superficial velocity and d is the average diameter of the particles in the bed. We usually assume a constant porosity across the bed corresponding to a random packing fraction $\phi = 0.42$, however, it is possible to calculate local porosities so that the drag force may be applied more accurately. $\mathbf{F}_{Drag}$ is applied explicitly onto all the particles in a manner as to oppose the direction in which the particle is moving.

We also apply a buoyancy and gravitational force explicitly onto the particles as this information is not obtained from the fluid pressure gradient in equation 2.54. The buoyancy force is equal to the the weight of the volume of fluid displaced by the particle and is applied in an upward direction

$$\mathbf{F}_{buoyoncy} = \rho V_p \mathbf{g}, \tag{2.56}$$

where $\mathbf{g}$ is the gravitational acceleration.

Thus the overall equation of motion for the particles within the SD model may be given by

$$m\ddot{\mathbf{r}} = \mathbf{F}_{collision} + \mathbf{F}_{Drag} + V_p\left(\rho - \rho_g\right)\mathbf{g}, \tag{2.57}$$

where $\mathbf{F}_{collision}$ are the forces on the particles due to collisions with walls and with other particles.

In the next section we describe the other model which uses bed equations, namely the Navier–Stokes model.

2.4.2 The Navier–Stokes Algorithm

The Navier–Stokes (NS) model is based on an additional momentum transfer term within the Navier–Stokes equations which couples the fluid to the granular motion. An associated drag force which conserves momentum is also applied onto the grains. The coupling force term for the NS model is derived by combining the momentum conservation equations for the fluid and the granular bed. We are able to derive a modified version of the Navier–Stokes equations which include a momentum transfer term, β', between the fluid and grains:

$$\frac{\partial \mathbf{v}}{\partial t} + \mathbf{v}.\nabla\mathbf{v} = -\nabla p + \nu\nabla^2\mathbf{v} + \mathbf{g} - \frac{\beta'}{\phi\rho}. \tag{2.58}$$

Here $p = P/\rho$. It is possible to estimate β' by applying equation 2.58 to steady one-dimensional fluid flow through a porous plug of porosity ϕ. In this situation the unsteady and convective acceleration, and the diffusive terms become zero. Neglecting gravity, we obtain:

$$-\nabla p = \frac{\beta'}{\phi\rho}. \tag{2.59}$$

In such a system it is possible to use an empirical bed equation such as Darcy's law (equation 2.55) to estimate the pressure gradient. Thus an approximation to the momentum transfer term is obtained:

$$\beta' = \frac{180\eta\left(1-\phi\right)^2}{d^2\phi^2}\mathbf{V}_0. \tag{2.60}$$

The superficial velocity with respect to the static bed $\mathbf{V}_0$ is calculated using $\mathbf{V}_0 = \phi\left(\mathbf{v} - \mathbf{u}\right)$. Here $\mathbf{v}$ is the internal fluid velocity and $\mathbf{u}$ is the local grain

velocity. The internal fluid velocity refers to the actual speed with which the fluid flows through the bed. Thus we obtain:

$$\beta' = \frac{180\eta\left(1-\phi\right)^2}{d^2\phi}\left(\mathbf{v}-\mathbf{u}\right). \tag{2.61}$$

Therefore using Darcy's law we obtain the fluid momentum equation:

$$\frac{\partial \mathbf{v}}{\partial t} + \mathbf{v}.\nabla\mathbf{v} = -\nabla p + \eta\nabla^2\mathbf{v} + \mathbf{g} - \beta\left(\mathbf{v}-\mathbf{u}\right), \tag{2.62}$$

where $\beta = \frac{180\eta(1-\phi)^2}{\rho d^2\phi^2}$. When using different bed equations, such as Ergun's or Di Felice's (see section 2.4.4), the form of β will change.

Due to the presence of grains the incompressibility constraint becomes:

$$\nabla.\left(\phi\mathbf{v} + \left(1-\phi\right)\mathbf{u}\right) = 0. \tag{2.63}$$

As we did within the fluid algorithm in Section 2.2.1 we introduce the fictitious velocity component, $\mathbf{v}^*$, into the time-discretised momentum transfer equation. We use the projection method to split equation 2.62 into two equations which are then solved simultaneously:

$$\frac{\mathbf{v}^* - \mathbf{v}_n}{\Delta t} = -\mathbf{v}_n.\nabla\mathbf{v}_n + \nu\nabla^2\mathbf{v}_n + \mathbf{g}_n - \beta\left(\mathbf{v}_n - \mathbf{u}\right), \tag{2.64}$$

$$\frac{\mathbf{v}_{n+1} - \mathbf{v}^*}{\Delta t} = -\nabla p_{n+1}. \tag{2.65}$$

These are similar to equations 2.33 and 2.34 but with an extra fluid momentum term. Taking the divergence of equation 2.65 and using the modified incompressibility constraint, equation 2.63, we obtain the second-order pressure solver equation:

$$\nabla^2 p_{n+1} = \frac{\frac{1}{\phi}\left[\nabla\phi.\left(\mathbf{v}^*-\mathbf{u}\right) + \left(1-\phi\right)\nabla.\mathbf{u}\right] + \nabla.\mathbf{v}^*}{\Delta t}. \tag{2.66}$$

We find that the Navier–Stokes algorithm is similar to the fluid model algorithm described in section 2.2.1. The main difference is that the momentum transfer field, $\beta\left(\mathbf{v}-\mathbf{u}\right)$, must be determined on the MAC grid mesh in order to calculate the virtual velocity $\mathbf{v}^*$ in equation 2.64. The virtual velocity field values $\mathbf{v}^*$ are then substituted along with the local grain velocities $\mathbf{u}$ into equation 2.66 and is solved using FFT methods to obtain the updated pressure field, p_{n+1}. It is then possible to obtain the new velocities at time $t_{n+1} = \left(n+1\right)\Delta t$ by substituting the pressure field, p_{n+1}, back into equation 2.65.

2.4.3 Granular Techniques

In the NS model algorithm, the dynamic granular properties, ϕ and $\mathbf{u}$, are introduced. To evolve the fluid-grain phases these particle attributes need to be resolved onto the same grid as the fluid properties. One method of accomplishing this is using the grid-mapping technique, where the properties of each grain are interpolated onto the staggered MAC mesh. The properties of each grain are smoothed onto the four nearest fluid grid points (eight points in three dimensions) using a bilinear interpolation technique. We are then able to determine the momentum transfer term $\beta(\mathbf{v}-\mathbf{u})$ on each grid point in equation 2.64.

If the particle position is given by (x, y) the kernel, s_i, used to interpolate the particle attributes onto one of the nearest grid points with position (x_i, y_i) may be calculated using:

$$s_i(\mathbf{r}-\mathbf{r}_i) = \left(1-\frac{|x-x_i|}{\Delta}\right)\left(1-\frac{|y-y_i|}{\Delta}\right) \tag{2.67}$$

where

$$\sum_i^{2^D} s_i = 1 \tag{2.68}$$

and

$$|x-x_i|, |y-y_i| < \Delta. \tag{2.69}$$

Here D is the number of dimensions and Δ is the length of the grid cell. Figure 2.14 shows the area-weighted form of the kernel in two dimensions. The granular attributes contributions to each lattice position are proportional to the area of the rectangle opposite the lattice point. For example in Figure 2.14 the kernel for point (x_1, y_1) may be evaluated by calculating the normalised area of the shaded region.

We showed in Section 2.2.1 that fluid velocity components are staggered on the MAC grid, such that the horizontal component of the fluid velocity exists on the vertical walls and the vertical components exist on the horizontal walls of the cells. When determining the momentum transfer each component of the grain velocity must be smoothed onto the same grid-point as the corresponding component of the fluid velocity. Thus for each dimension that our simulations are modelled in, a new set of kernels must be evaluated. Similarly the local porosities

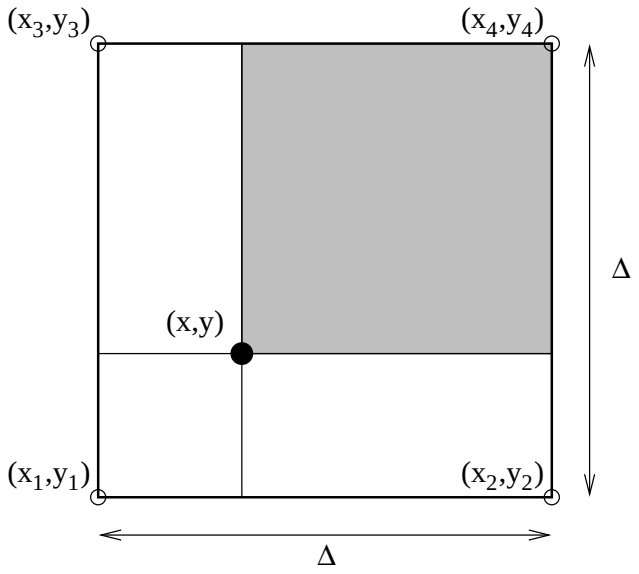

Fig. 2.14: Bilinear interpolation in two dimensions of a particle's properties smoothed onto the four nearest fluid grid-points. Here the shaded region shows the area-weighted form of the kernel for the lattice point (x_1, y_1).

are also evaluated on each fluid lattice point. The arrangement of the staggered grids in two dimensions is shown in figure 2.15. Here a particle situated in the top right of the lattice cell has its attributes smoothed onto two different sets of grid-points corresponding to the x and y components of the velocities.

Using this smoothing process one ends up with a staggered grid with the local grain velocities and bed porosities, as well as the fluid velocities, defined upon it.

2.4.4 Empirical Bed Equations

In fluid dynamics, bed equations are phenomenologically derived constitutive equations that describe steady fluid flow through a porous bed of grains. So far we have used only Darcy's law to determine the momentum transfer term, β, however, it is possible to utilise other bed equations in the SD and NS models.

Darcy's law, equation 2.49, gives a linear relationship between the flow rate and the pressure gradient. This relation is predominantly used for low fluid flow velocities as it loses validity at higher flow rates in dense granular beds. Ergun (1952) determined experimentally a bed equation which included a Darcy like term and a term proportional to the square of the fluid velocity. Ergun's equation

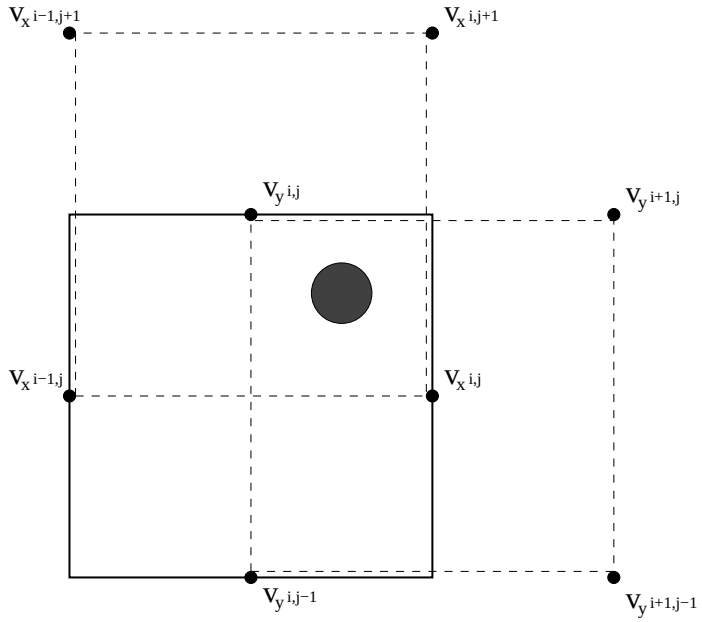

Fig. 2.15: Arrangement of staggered grids for a two-dimensional system. The fluid velocities are shown as an indication of which component of the grain attributes are interpolated onto each grid-point. Here the horizontal grain velocities are interpolated onto the v_x points and the vertical velocities onto the v_y points.

is expressed as:

$$-\nabla P = \left[\frac{150\eta\left(1-\phi\right)^2}{d^2\phi^3} + \frac{1.75\rho\left(1-\phi\right)|\mathbf{V}_0|}{d\phi^3}\right]\mathbf{V}_0. \tag{2.70}$$

Ergun's empirical bed equation was derived for densely packed beds and is unable to accurately model dilute beds as well, i.e. $\phi > 0.8$. Wen and Yu (1966) proposed a relationship valid in fluid regions with a low granular content which can be given as:

$$-\nabla P = \frac{3}{4}\frac{\left(1-\phi\right)\rho C_d}{\phi d}\phi^{-2.65}|\mathbf{V}_0|\mathbf{V}_0. \tag{2.71}$$

Here C_d is the fluid drag coefficient for a single particle which can be calculated using:

$$C_d = \left[0.63 + \frac{4.8}{R_{ep}^{0.5}}\right]^2. \tag{2.72}$$

The particle Reynolds number, R_{ep}, is not to be confused with the fluid Reynolds number from equation 2.36 and is dependent on the superficial fluid velocity, $\mathbf{V}_0$, so that:

$$R_{ep} = \frac{d|\mathbf{V}_0|}{\nu}. \tag{2.73}$$

When using a combination of Ergun, and the Wen and Yu relationships there is a discontinuity in the pressure gradient. Di Felice (1994) proposed an empirical relationship which agreed with both Ergun's equation in dense regions and Wen and Yu's equation in the dilute range. Di Felice's equation is given as:

$$-\nabla P = \frac{3}{4}\frac{(1-\phi)\,\rho C_d}{\phi d}\phi^{-\chi}|\mathbf{V}_0|\mathbf{V}_0, \tag{2.74}$$

where χ is flow dependent and is given as:

$$\chi = 3.7 - 0.65\exp\left[-\frac{(1.5-\log_{10}R_{ep})^2}{2}\right]. \tag{2.75}$$

The choice of bed equation depends largely on the system in question. The Ergun equation is very simple computationally, whereas Wen and Yu's, and Di Felice's are more complex and require greater computational power. Di Felice's equation is valid over a wider range of porosities than the other bed equations, and thus can be used in simulations where there exists both dilute and dense granular beds. We note that in a vibrated cell the bed equations may not be completely accurate as they are empirical fits to steady flow through a bed of grains. However, in this thesis we simulate systems with low f and Γ so the associated errors should be small. Throughout the course of this thesis the choice of bed equation will always be specified wherever used.

2.4.5 Drag Force

We have shown how the fluid experiences the particle motion in the form of an additional momentum transfer term in the NS equation 2.62. However, to conserve momentum within the system an equal and opposite force to that applied to the fluid must be applied to the particles. This force is applied explicitly onto the particles at the same time as when the fluid velocities are updated. The form described here is similar in form to that used in the SD model in Section 2.4.1:

$$\mathbf{F}_{Drag} = \frac{\frac{1}{6}\pi d^3\,(-\nabla P)}{1-\phi}. \tag{2.76}$$

We obtain the pressure gradient, ∇P, across the bed from one of the empirical bed equations described in section 2.4.4. To find the local porosity, ϕ, and the pressure gradient ∇P on the position of the particle we use a bilinear interpolation technique described in section 2.4.3.

2.5 Fluid Grain Template Models

In the previous sections we introduced the Simple Drag and Navier–Stokes models which use empirical bed equations to couple the fluid and grains interactions. The bed equations require a fluid regime in which the MAC grid mesh is of a much greater size than the particles. As the fluid resolution is low we are unable to investigate microscopic fluid behaviour around the grains. Therefore in this section two models are introduced in which the fluid grid is small in relation to the particle size, namely the Particle Template (PT) and the Fluid Springs (FS) models. These two models share similar features as neither use empirical bed equations to determine the momentum transfer between the two phases. Instead the models define the size of the grains on a scale much larger than the MAC grid so that the fluid is everywhere including "inside" the particles. The fluid grid-points encapsulated by the particles are forced, via different methods, to share the same velocity as the particle. The particles also experience an effective "drag force" from the fluid to resist the motion of the particles. The PT model sets the velocities of the encapsulated fluid points to be equal to the particle covering them. A fluid drag force is then applied onto the particle by calculating the volume integral of the stress-tensor divergence over all the encapsulated fluid grid-points. The momentum transfer in FS model is based on imaginary "springs" exerting equal and opposite forces between the fluid and grains so that the motion of the two phases converges.

We note that, in the models detailed in this section, no external vibration is applied to the cell. Therefore in all equations of motion the cell is held stationary. We consider the special situation of a fluid-grain system in an accelerated frame of reference in section 3.1.

We describe these two models in more detail in the following sections. We begin with the Particle Template model.

2.5.1 Particle Template Model

The PT model involves creating a template which is the same size and shape as the moving particle. Each template is superimposed onto the MAC grid points

that are covered by the immersed body. The fluid points that lie within the template are then forced to have the same velocity components as the moving particle (Ristow 1996; Ristow 1997; Kalthoff *et al.* 1997).

The fluid is governed by the Navier–Stokes equations

$$\frac{\partial \mathbf{v}}{\partial t} + (\mathbf{v}.\nabla)\,\mathbf{v} = -\frac{1}{\rho}\nabla P + \nu\nabla^2\mathbf{v} + \mathbf{g}, \tag{2.77}$$

where P is the pressure of the fluid in the reference frame which is stationary with respect to the cell. Since we are dealing with an incompressible fluid the continuity equation is:

$$\nabla.\mathbf{v} = 0. \tag{2.78}$$

As with the NS model we use the projection method to solve the fluid equations. We discretise and then introduce an intermediate virtual fluid velocity, $\mathbf{v}^*$, to split equation 2.77 into two new equations as follows:

$$\frac{\mathbf{v}^* - \mathbf{v}_n}{\Delta t} = -(\mathbf{v}_n.\nabla)\,\mathbf{v}_n + \nu\nabla^2\mathbf{v}_n + \mathbf{g}_n, \tag{2.79}$$

$$\frac{\mathbf{v}_{n+1} - \mathbf{v}^*}{\Delta t} = -\frac{1}{\rho}\nabla P_{n+1}. \tag{2.80}$$

Once the intermediate fluid velocity, $\mathbf{v}^*$, has been calculated, the particle template is placed over the velocity field. We then replace the velocities of the intermediate fluid velocity grid-points $\mathbf{v}^*$ encapsulated by the particle template with the velocity of the particle. This acts to enforce the no-slip boundary condition around each template. Figure 2.16 shows this schematically in two dimensions. All the fluid points within the particle boundary that have their velocities set to that of the templates are coloured black whilst the fluid points outside the particle are coloured white.

By taking the divergence of equation 2.80 and substituting the continuity equation 2.78 into the resulting expression we obtain the following Poisson equation:

$$\nabla^2 P_{n+1} = \frac{\rho}{\Delta t}\nabla.\mathbf{v}^*. \tag{2.81}$$

We solve this equation using either the relaxation method or the FFT approach to find the new pressure field P_{n+1}. This pressure field is then used within 2.80 to update the new fluid velocity field, $\mathbf{v}_{n+1}$.

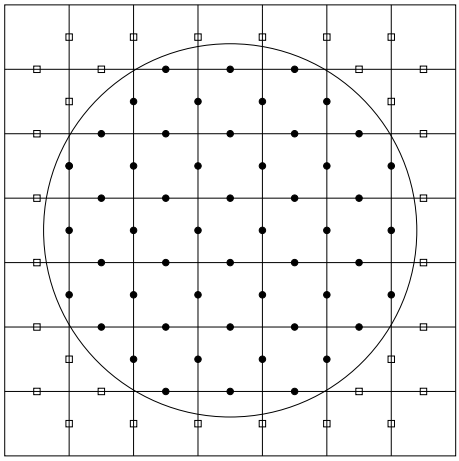

Fig. 2.16: Schematic drawing of template upon staggered grid. Filled circles represent the fluid points contained within the template which have their velocity replaced with that of the particle. Points outside the template are shown as empty squares.

The corresponding fluid force on the particle is calculated by evaluating a volume integral over the template of the divergence of the stress-tensor given by:

$$\mathbf{F}_f = \int_V -\nabla P + \eta \nabla^2 \mathbf{v} \; dV. \tag{2.82}$$

The fluid force acting on the particle, given in equation 2.82, captures both the viscous drag forces and the buoyancy forces which are experienced by the immersed particle.

The equation of motion of a particle in the laboratory reference frame is therefore:

$$m\ddot{\mathbf{r}} = \mathbf{F}_f + \mathbf{F}_c + m\mathbf{g}, \tag{2.83}$$

where m and $\ddot{\mathbf{r}}$ are the mass and acceleration of the particle respectively and $\mathbf{F}_c$ is the total force due to collisions with other particles and walls. The collision forces can be modelled using either the LSD or the DH models, described in detail in section 2.1.

For the particle motion to remain accurate and stable the template associated with each particle must encapsulate a large number of lattice points. This is because as the template moves across the lattice both the number of the grid points covered by the particle and the positions of the grid points in relation to

the particle vary. If the template contains only a few lattice points this has a significant effect on the integration of the stress-tensor.

The Particle Template method is very effective when studying fluid flow patterns around a small number of grains, i.e. less than ten spheres. For a high level of accuracy each particle must cover a large number of fluid grid points which requires the use of a small lattice spacing compared to the size of the particle. Due to the limits of modern computers, the largest size of the MAC grid mesh that we may simulate is restricted. The dilemma is that to study a large number of particles we must reduce the number of fluid grid-points covered by each particle, which reduces the accuracy of any results attained.

One approach that is stable when fewer lattice points are covered by each particle is the Fluid Springs model (Fogelson and Peskin 1988; Glowinski *et al.* 1999; Glowinski *et al.* 1999; Glowinski *et al.* 1999). As with the PT model the fluid is defined on a grid with lattice spacing much smaller than the size of the particle. However, the model differs in that on each grain we create a template of grid-points which moves with the particle. This grid is the same size and shape as the fluid grid mesh so that there are always a constant number of points on each template during the simulation. For each lattice point on the template, we predict the difference in the future fluid and grain paths and then correct the motion using damped "springs". These springs force the two phases to converge so that the fluid grid-points encapsulated by the immersed spheres share the same velocity as the particle that embodies them.

This method combines both sufficient computational accuracy with numerical efficiency and allows the study of several thousand, in principle arbitrarily shaped, interacting particles. The method we use and now describe is detailed by Höfler and Schwarzer (2000), which follows a similar method used by Fogelson and Peskin (1988).

2.5.2 Fluid Springs Model

The model can be separated into three parts; firstly the fluid equations, secondly the motion of the suspended particles, and thirdly their mutual coupling. Afterwards we summarise the FS model algorithm. The first two sections I have

discussed previously but will include here for completeness. The main difference between this model and the PT model is the coupling between the two phases which is discussed here in detail.

Fluid

Our starting point is the Navier–Stokes force equations describing the motion of a Newtonian fluid with inertia:

$$V\rho\frac{\partial \mathbf{v}}{\partial t} + V\rho\left(\mathbf{v}.\nabla\right)\mathbf{v} = -V\nabla P + V\eta\nabla^2\mathbf{v} + V\mathbf{f}. \tag{2.84}$$

Here V, ρ and η denote the fluid volume, density and dynamic viscosity. $\mathbf{v}$ and P are the fluid velocity and pressure, respectively, and $\mathbf{f}$ is a volume force term. If we divide each term by the mass of the fluid ρV we obtain:

$$\frac{\partial \mathbf{v}}{\partial t} + \left(\mathbf{v}.\nabla\right)\mathbf{v} = -\nabla p + \nu\nabla^2\mathbf{v} + \frac{1}{\rho}\mathbf{f}. \tag{2.85}$$

Here $p = P/\rho$ and $\nu = \eta/\rho$ are the reduced pressure and kinematic viscosity respectively. We do not consider the time independent gravity contribution to $\mathbf{f}$ explicitly, but cancel it against the hydrostatic pressure and omit both terms from equation 2.85. The corresponding buoyancy forces will be taken into account explicitly in the equations of motion of the suspended particles. As usual the liquid is considered as incompressible, i.e. $\nabla.\mathbf{v} = 0$, however, this is not a necessary condition for the coupling technique.

Again the incompressibility technique is satisfied via an explicit fractional-time-step operator-splitting method. By introducing a "virtual" velocity, $\mathbf{v}^*$, in order to split the one velocity equation 2.85 into two, we obtain:

$$\frac{\mathbf{v}^* - \mathbf{v}_n}{\Delta t} = -\left(\mathbf{v}_n.\nabla\right)\mathbf{v}_n + \nu\nabla^2\mathbf{v}_n + \frac{1}{\rho}\mathbf{f}_n, \tag{2.86}$$

$$\frac{\mathbf{v}_{n+1} - \mathbf{v}^*}{\Delta t} = -\nabla p_{n+1}. \tag{2.87}$$

Here the subscript n and $n+1$ denote the values at $t_n = n\Delta t$ and $t_{n+1} = (n+1)\,\Delta t$ respectively.

Taking the divergence of equation 2.87 and substituting the incompressibility constraint eliminates $\mathbf{v}_{n+1}$ leaving:

$$\nabla^2 p_{n+1} = \frac{\nabla.\mathbf{v}^*}{\Delta t}. \tag{2.88}$$

The fluid equations must be solved subject to the boundary and initial conditions implied by the confining geometry, in our case a quadrilateral volume, which is either limited by fixed walls on which no-slip conditions hold or periodically repeated in space.

One fluid time-step consists of first computing the virtual velocity $\mathbf{v}^*$ from equation 2.86, which provides the information for the source terms of the pressure equation 2.88. The pressure values are then substituted into equation 2.87 to calculate the updated velocities $\mathbf{v}_{n+1}$. Finally the boundary conditions are applied to the fluid motion to ensure no-slip conditions.

Particle-Fluid Coupling

The method that we detail here manages to enforce the no-slip boundary, which is the main challenge facing any method that couples the particle and fluid motion. Instead of implementing the no-slip boundary conditions by modifying coefficients of the discretised system or employing grid adaptivity as in finite-volume or finite element techniques, we use the body-force term in the Navier–Stokes equations to implement constraints acting on the fluid such as to mimic the presence of rigid particles at appropriate regions in the flow. These regions move as the particle moves across the grid and contain sufficiently many grid-points in order to represent the geometry of the physical particles. Since the lattice points are fixed in space, but the particles move, the association of grid-points to particle representing regions will change in the course of the simulation.

In more detail, the computation of the motion of a physical particle i is decomposed into two contributions. A moving liquid volume element V_i of the same shape as the particle makes up the first contribution. We imagine this particle moving within the rest of the fluid, just as if it were a solid particle of fluid density ρ with mass $M_i^f = V_i\rho$. In my simulations I only model spherical objects, however, as will become clear this approach is not limited to regular disks or spheres.

The second contribution is a particle template that also has the shape of the rigid physical particle, but it carries the mass M_i^t. These values complement the contribution of the fluid particle as their sum are equal to the mass of the physical

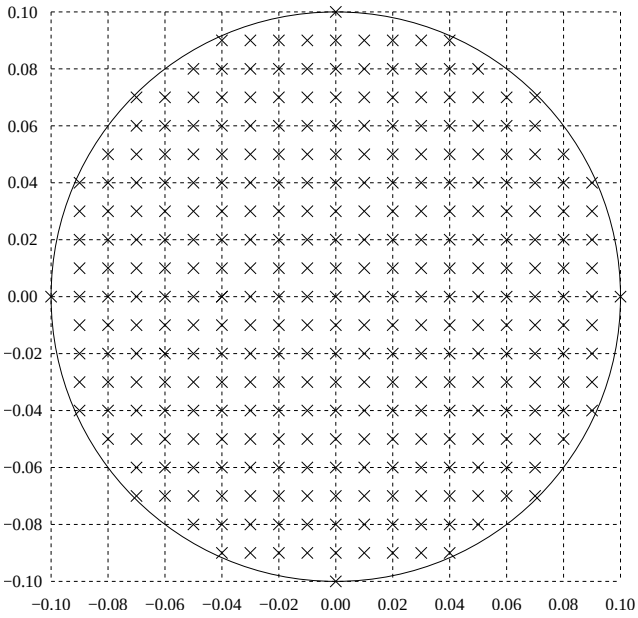

Fig. 2.17: Cross-section of a sphere illustrating a typical configuration of reference points $\mathbf{r}_{ij}^r$ on a particle template i in two dimensions. The template has radius 100 mm with a reference point spacing of 10 mm. All crosses illustrate coordinates of $\mathbf{r}_{ij}^r$ vectors which are relative to the centre of mass of sphere located at $(0.0, 0.0)$.

particle i, i.e, $M_i = M_i^f + M_i^t$.

We must now describe how to achieve rigid coupling between the template and the associated fluid element. We first describe the template which requires the introduction of n_i reference positions $\mathbf{r}_{ij}^r, j = 1, ..., n_i$ distributed over the volume of template i. The $\mathbf{r}_{ij}^r$ are vectors relative to the centre of mass of template i. The density and location of the tracers should in general be chosen such that the number of fluid lattice cells contained within the template volume should equal the controlling number of tracers. Therefore the spacing between lattice points should resemble the MAC grid so that each tracer controls a fluid of volume Δ^D, where D is the number of dimensions. Figure 2.17 shows a typical configuration of reference points for a particle of radius $R = 100$ mm and constant reference point spacing of $\Delta = 10$ mm. The radial density of reference points n_r is defined as:

$$n_r = \frac{R}{\Delta}. \tag{2.89}$$

In Figure 2.17 the radial density n_r is equal to 10. The higher the value of n_r the better the reference points approximate the shape of the immersed particle. The spatial coordinates, $\mathbf{x}_{ij}^r$, associated with each reference point, change only due to

the movement and rotation of the rigid template such that:

$$\mathbf{x}_{ij}^{r}\left(t\right)=\mathbf{x}_{i}\left(t\right)+\mathbf{O}_{i}\left(t\right).\mathbf{r}_{ij}^{r}, \tag{2.90}$$

where $\mathbf{O}_i$ is a matrix describing the instantaneous orientation and $\mathbf{x}_i$ is the position of the centre of mass of the template. In two dimensions $\mathbf{O}_i$ is obtained by forming the rotation matrix associated with one angular degree of freedom of the particle. In three dimensions we can use quaternions to represent the particle orientation and compute the rotation matrix $\mathbf{O}_i$.

Associated with each reference position is a tracer $\mathbf{x}_{ij}^{m}, j=1,...,n_i$ which tracks the motion of the fluid so that

$$\dot{\mathbf{x}}_{ij}^{m}=\mathbf{v}\left(\mathbf{x}_{ij}^{m}\right). \tag{2.91}$$

Here $\dot{\mathbf{x}}_{ij}^{m}$ is defined as the velocity of fluid at the position $\mathbf{x}_{ij}^{m}$. Therefore on every reference point we are able to determine the velocity of the template $\dot{\mathbf{x}}_{ij}^{r}$ and the fluid $\dot{\mathbf{x}}_{ij}^{m}$.

Now we are able to obtain an explicit numerical scheme for the computation of the force density $\mathbf{f}$ constraining the fluid motion as follows. This part of the algorithm works by predicting the difference in the future fluid and template paths and then correcting the motion using a damped "spring" which forces the two phases to converge.

We define $\boldsymbol{\epsilon}_{ij}$ as the difference between the positions of the particle i and fluid tracer elements j at future time $t+\Delta t$ and $\dot{\boldsymbol{\epsilon}}_{ij}$ as the difference in the respective velocities at future time $t+\Delta t$. Both $\boldsymbol{\epsilon}_{ij}$ and $\dot{\boldsymbol{\epsilon}}_{ij}$ assume that the fluid and template velocities do not change over the following time-step. Therefore we obtain:

$$\boldsymbol{\epsilon}_{ij} = \dot{\mathbf{x}}_{ij}^{m}\Delta t-\dot{\mathbf{x}}_{ij}^{r}\Delta t, \tag{2.92}$$

$$\dot{\boldsymbol{\epsilon}}_{ij} = \dot{\mathbf{x}}_{ij}^{m}-\dot{\mathbf{x}}_{ij}^{r}. \tag{2.93}$$

We then generate an additive contribution $\mathbf{f}_{ij}$ to the force density in the fluid which tends to drive the fluid tracer back to the reference position and diminish the relative velocity between the particle and fluid tracer element. The fluid-template rigid coupling force acting on each reference point is given by:

$$\mathbf{f}_{ij}^{r}=-k_i\boldsymbol{\epsilon}_{ij}-2\gamma_i\dot{\boldsymbol{\epsilon}}_{ij}, \tag{2.94}$$

where k_i is a "spring" constant and γ_i a damping constant. k_i must be chosen large enough so that $|\boldsymbol{\epsilon}_{ij}| \ll \Delta$ holds at all times. Similarly, the dissipation controlled by γ_i must be small enough to be negligible against the external physical sources of energy dissipation. To determine $\mathbf{f}^n$ in equation 2.86 the fluid-template rigid coupling forces $\mathbf{f}_{ij}^r$ are interpolated from the template reference points onto the four nearest MAC grid points (eight in three dimensions). The kernels used to interpolate the rigid coupling force onto the fluid lattice points are given in section 2.4.3.

In order to estimate the largest spring constant k_i we can use for a given time-step Δt we consider a couple of masses connected by a linear spring. The two masses being a fluid element $\Delta M_f = \rho \Delta^D$ and the mass of the particle template $M_i^t = M_i - M_i^f$. By calculating the reduced mass of the particle template and fluid element:

$$M_r = \frac{M_i^t \Delta M_f}{M_i^t + \Delta M_f}, \tag{2.95}$$

we may obtain a time scale of oscillation for the coupling,

$$T_{coupling} = 2\pi \sqrt{\frac{M_r}{n_i k_i}}. \tag{2.96}$$

We achieve stability when $\Delta t = C_s t_{coupling}$ and C_s is a coupling coefficient that determines the ratio of time-steps to the timescale of the coupling oscillation. Thus k_i may be calculated using:

$$k_i = {C_s}^2 \times 4\pi^2 \frac{M_r}{n_i \Delta t^2}. \tag{2.97}$$

If γ_i is chosen so that its value is close to the aperiodic damping of the particle template, it is able to eliminate small but unphysical oscillations of the particles. In the case of fixed tracer positions we obtain $\gamma_i = \sqrt{k_i} M_t$. In three dimensions the value of γ is less important and it is possible to use $\gamma = 0$.

Particle Motion

The constraint force distribution that we have imposed on the fluid to guarantee quasi-rigid fluid motion must be cancelled by applying equal and opposite forces on the particles to ensure momentum is conserved. Therefore via Newton's laws the "spring" associated with each reference-point-tracer pair exerts an equal and

opposite force to $\mathbf{f}_{ij}^r$ from equation 2.94 onto the template so that:

$$\mathbf{F}_{ij} = k_i \boldsymbol{\epsilon}_{ij} + 2\gamma_i \dot{\boldsymbol{\epsilon}}_{ij}. \tag{2.98}$$

Here $\mathbf{F}_{ij}$ is the force acting on particle template i at the location of reference point j. To find the total force on the template we sum $\mathbf{F}_{ij}$ over all reference points j.

Gravity and buoyancy must be taken into account in an explicit force, $\mathbf{F}_i^s$, defined on the particle:

$$\mathbf{F}_i^s = -M_i \mathbf{g} + \rho V_i \mathbf{g} = (\rho - \rho_g) V_i \mathbf{g}, \tag{2.99}$$

where ρ_g is the particle density and V_i is the volume (or area in two dimensions). We define the force contributions from collisions with all other particles and with the walls as $\mathbf{F}_i^c$.

Therefore the equation of motion of the particle template is:

$$M_i \ddot{\mathbf{r}} = \mathbf{F}_i^s + \mathbf{F}_i^c + \sum_j \mathbf{F}_{ij}. \tag{2.100}$$

Verlet's equations, which are based on Newton's laws of motion, are then used to update the positions and velocities of the particles (see section 2.1.2).

Summary

To summarise, the modelling of a rigid heavy particle requires the "freezing" of the region of fluid occupying the space of the particle. This region is then coupled to a particle template whose dynamical properties supplement those of the fluid in such a fashion that the coupled system behaves just as the modelled particle would.

The algorithm that we use within each time-step of the FS model simulations proceeds as follows. First we calculate the fluid, $\dot{\mathbf{x}}_{ij}^r$, and template velocities, $\dot{\mathbf{x}}_{ij}^m$, for each reference point. We then calculate the predicted difference in the positions and velocities between the fluid and template, $\boldsymbol{\epsilon}_{ij}$ and $\dot{\boldsymbol{\epsilon}}_{ij}$, at time $t+\Delta t$ using equations 2.92 and 2.93. We then correct the motion using equation 2.94 which determines the constraint-forces, $\mathbf{f}_{ij}^r$, on each template reference point. The constraint-force distribution is then imposed on the fluid grid via a bilinear

interpolation technique. Equation 2.86 is used to evaluate the intermediate fluid velocity field, $\mathbf{v}^*$, which make up the source terms of the diffusion equation 2.88 to give the new pressure field. We then evaluate the new fluid velocity field using equation 2.87. An equal and opposite force from the constraint forces is applied to the particle template using equation 2.98. The collisional, gravitational and buoyancy forces acting on the particle are all calculated and the motion of the particles can be stepped forward in time using Verlet's method.

Figure 2.18 illustrates, as a flow chart, the sequence of steps that must be performed at each time-step in the simulation.

2.6 Numerical Results

In the following sections we will perform some numerical simulations to compare and test some of the models described earlier in the chapter. In particular we will focus on the application of the Navier–Stokes, the Particle Template and the Fluid Springs models to a series of well known tests. Throughout this section we focus on the selection of the coupling coefficient C_s, from equation 2.97, within the FS model as varying C_s can significantly affect the strength of the coupling between the fluid and template. If C_s is small then the constraint forces associated with each reference point are weak and the velocity of the fluid does not converge to the velocity of the immersed particle. In extreme cases of $C_s \ll 1$ there is little fluid and grain coupling and the particles behave as if they are in a vacuum. Conversely if C_s is "large" then the coupling is unstable.

We also consider the radial reference point density n_r as it was observed in Figure 2.17 that the larger n_r is, the better the template reference points approximate the shape of the immersed body. However, increasing n_r slows the computer simulations and limits the potential size of the systems we wish to model. A good starting point is to investigate a falling cylinder within a box.

2.6.1 Falling Cylinder

In this section we simulate a falling cylinder in a two-dimensional cell using the PT and FS models. The orientation of the cylinder is fixed, with the axis which

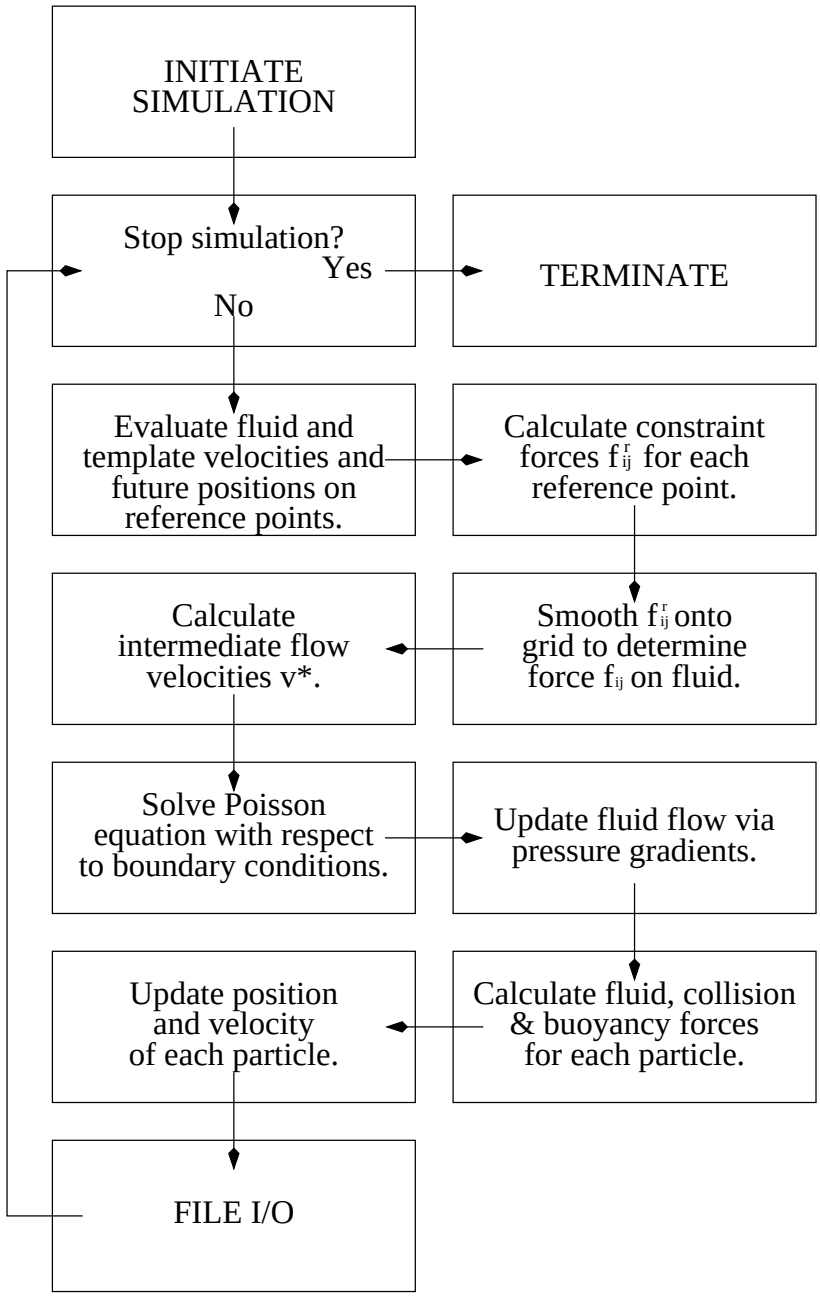

Fig. 2.18: Flow-chart for the Fluid Springs model algorithm.

Parameter	*Value*
Cylinder density ρ_g	1100 kg m^{-3}
Cylinder radius r	0.5–2.0 cm
Cell size (x–axis)	10.0 cm
Cell size (y–axis)	30.0 cm
Fluid density ρ	1000 kg m^{-3}
Fluid viscosity η	0.01 kg m^{-1} s^{-1}
Time-step Δt	100 μs
Lattice spacing Δ	78.125–2500 μm
n_r	2–64
C_s	0.01–1.00

Table 2.4: Table of simulation parameters for the falling cylinder problem.

runs through the cylinders length, being aligned (along the z–axis) constantly perpendicular to the two axes under consideration.

The density of the cylinder is set to be greater than that of the fluid, so that under the influence of gravity it will fall through the liquid, increasing its speed until viscous forces balance the gravitational pull. At this point the cylinder is said to have reached its terminal velocity.

In the first part of this section we investigate the effect of varying the fluid coupling coefficient, C_s, for a falling cylinder with a large radial reference point density n_r when just using the FS model. We set up a cylinder of diameter 1 cm and density $\rho_g = 1100$ kg m^{-3} in a fluid-filled cell. The fluid lattice spacing is $\Delta = 156.25$ μm so that $n_r = 32$. The fluid has the same density as water, i.e. $\rho = 1000$ kg m^{-3} but is ten times as viscous so that $\eta = 0.01$ kg m^{-1} s^{-1}. The other variables are summarised in table 2.4.

Figure 2.19 plots the vertical velocity of the cylinder against time for C_s values spanning the range 0.01–1.00. When the particle is released, the particle accelerates under the influence of gravity. The particle motion is opposed by the buoyancy force which is constant and the viscous drag force. For low velocities the particle velocity increases linearly as the viscous drag is low. As the velocity

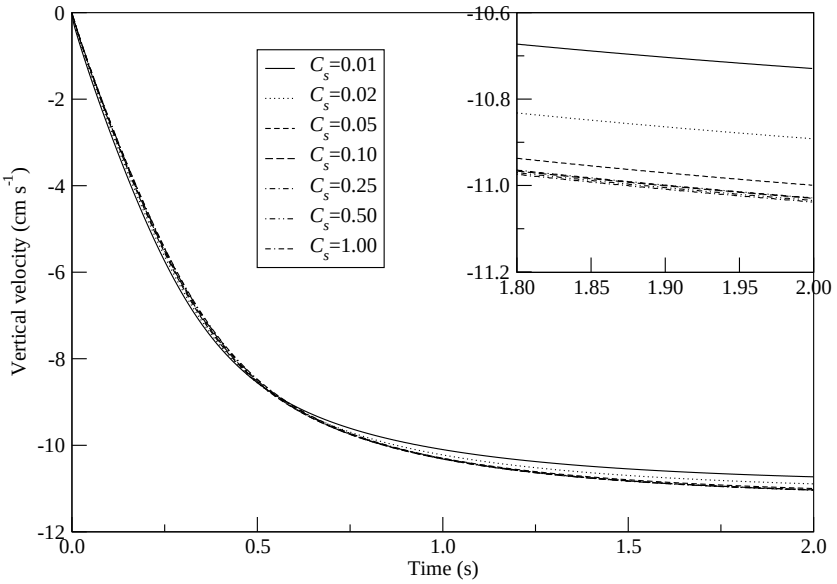

Fig. 2.19: Vertical velocity plotted against time for a cylinder of diameter 1 cm and radial lattice density $n_r = 32$ using the FS model. Each line corresponds to a different C_s value. The insert is a close up of the end point of the runs.

increases the viscous drag forces increase and slow the acceleration of the cylinder. Eventually the viscous fluid drag and the gravitational forces acting on the particle are equal as the cylinder reaches its terminal velocity. The insert in Figure 2.19 shows that the terminal velocity of the cylinder is approximately constant in the range $C_s = 0.25$–1.00. Counter-intuitively as the coupling coefficient C_s is reduced towards 0.01 the terminal velocity reduces also. Above $C_s > 1.0$ the fluid-grain coupling becomes unstable. The overall dispersion of velocities is very low which shows that for large n_r varying the fluid-grain coupling coefficient does not greatly affect the terminal velocity.

When simulating systems containing just a single particle, a large radial reference point density of $n_r = 32$ is acceptable as the overall fluid lattice is unlikely to be very large. If we extended this simulation to several hundred spheres in three dimensions with the same radial reference point density we would require a huge MAC grid mesh. However this is inefficient and unnecessary as for a reduced n_r we may still obtain accurate and stable results. The second test in this chapter involves varying the radial reference point density, n_r, for falling cylinders using both the PT and FS models. We fix the cylinder to a diameter of 1 cm and vary the lattice spacing in the range $\Delta = 78.125$–2500 μm so that $n_r = 2$–64. In the

FS model C_s is fixed to 0.5. The system parameters are again summarised in Table 2.4.

Figures 2.20 and 2.21 plot the vertical velocities of the falling cylinders against time for the PT and FS models. The different curves correspond to n_r in the range 2–64. We find that for large n_r the velocity curves agree very well between the two models, as both have similar terminal velocities. However, as n_r is reduced the terminal velocities of the cylinders decrease and there is less agreement between the models. As n_r decreases, the drag force experienced by the cylinder increases due to the reference points over-estimating the size of the cylinder. Also as n_r is reduced the cylinder velocity curves become more jagged due to lattice effects. These effects are especially prominent in the PT curves (Figure 2.20). This is because, in the PT model, as the cylinders fall the number of lattice points encapsulated by the cylinder and positions of these lattice points relative to its centre of mass constantly change. Whereas, in the FS approach the number and positions of points relative to the template are fixed.

The velocity curves obtained using the FS model have less dispersion between the terminal velocities than those obtained using the PT model. We also find that the curves converge to a common solution for a lower radial point density of $n_r \approx 8$ within the FS model compared to $n_r \approx 32$ in the PT model. The FS model, therefore, produces smoother and more accurate results for lower n_r than the PT model.

Within an infinite fluid the terminal velocity of the cylinders is a function of the size of the cylinder, however, in a confined geometry, the width of the cell plays an important role. If a single falling cylinder has its diameter increased whilst all other parameters remained unchanged, the terminal velocity will increase. However, for larger cylinders the drag increases as the fluid finds it increasingly difficult to squeeze past the particle.

To test how the geometry affects the cylinders within each of the PT and FS models we plot the terminal velocities of a range of falling cylinder systems against the value D/L. This is a ratio of the cylinder diameter to cell width. In these simulations we fix the constraint force coefficient C_s in the FS model to 0.5 and use a large reference point density of $n_r = 32$ in both models. The simulation

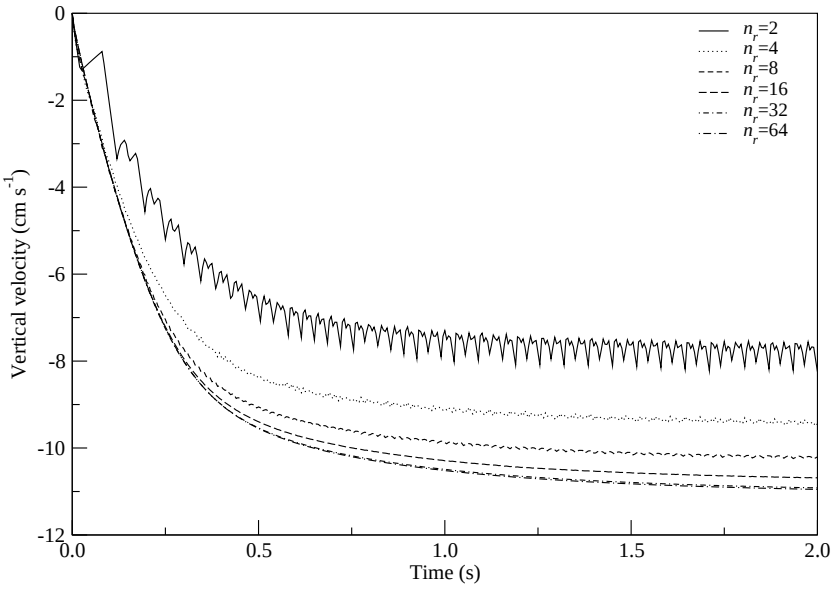

Fig. 2.20: Vertical velocity against time for a cylinder of diameter 1 cm for a range of fluid lattice sizes and radial densities n_r. Fluid and particle coupling is modelled using the Particle Template model.

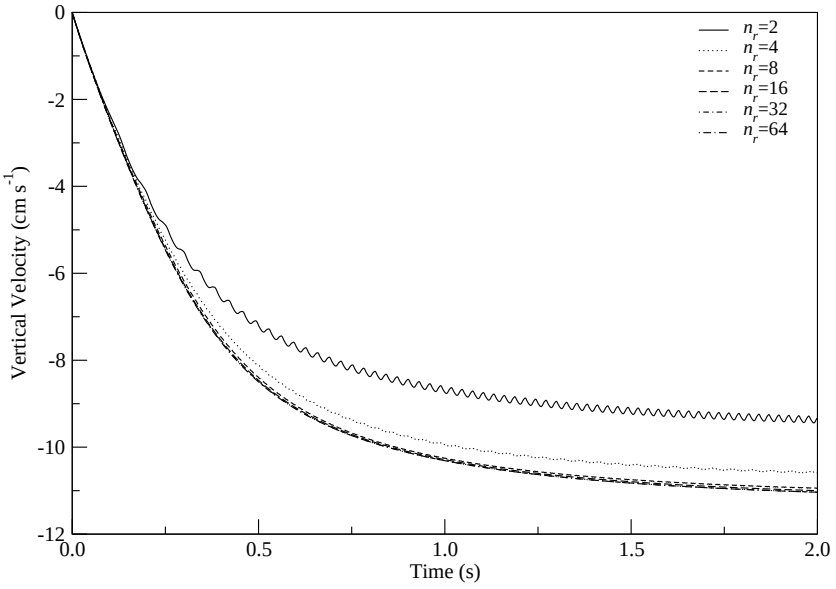

Fig. 2.21: Vertical velocity against time for a cylinder of diameter 1 cm for a range of fluid lattice sizes and radial densities n_r. Fluid and particle coupling is modelled using the Fluid Springs model.

Parameter	*Value*
Cylinder density ρ_g	1100 kg m^{-3}
Cylinder diameter D	1.0–4.0 cm
Cell size (x–axis)	5–20 cm
Cell size (y–axis)	30 cm
Fluid density ρ	1000 kg m^{-3}
Fluid viscosity η	0.01 kg m^{-1} s^{-1}
Time-step Δt	100 μs
Lattice spacing Δ	156.25 μm
n_r	32
C_s	0.5

Table 2.5: Table of simulation parameters for the Ristow test problem.

parameters for both models are summarised in Table 2.5 and the resulting data is shown in Figures 2.22 and 2.23. Curves of quadratic least squares are fitted to the terminal velocity data sets, $v_t(D/L)$, for fixed cylinder diameters over the range of D/L values. By extrapolating the curves to zero, $D/L \to 0$, the terminal velocities, $v_t^\infty(D)$, for an infinite fluid system may be approximated. Each set of data may then be normalised using its infinite fluid system velocity, $v_t^\infty(D)$, to give the function:

$$f(D/L) = \frac{v_t(D/L)}{v_t^\infty(D)}. \tag{2.101}$$

For larger D the function $f\,(D/L)$ may be approximately linear with D/L, however, some curves, particularly $D = 1.0$ cm, are often approximated better with quadratic equations of the form:

$$f(D/L) \approx 1 - c_1\frac{D}{L} - c_2\left(\frac{D}{L}\right)^2. \tag{2.102}$$

Figures 2.24 and 2.25 display the normalised terminal velocities for cylinders diameters $D = 1.5$–4.0 cm using the PT and FS models. The solid lines in these figures are quadratic least square fits to all of the shown data points, the form of which are shown in equation 2.102. For the PT model the quadratic coefficients are $c_1 = 0.922$ and $c_2 = 0.237$, while for the FS model they are $c_1 = 0.878$ and

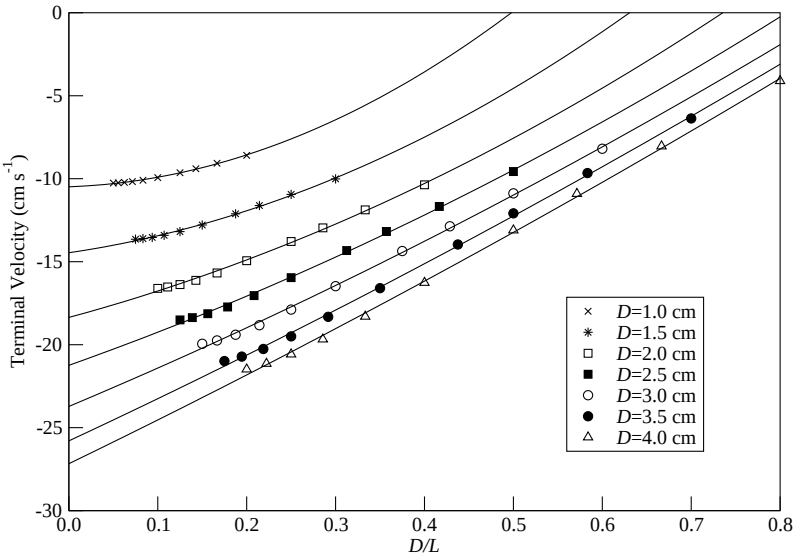

Fig. 2.22: Terminal velocity plotted against ratio of the cylinder diameter to the width of the cell D/L for the Particle Template model. From the top line down the curves correspond to diameters of, 1.0 cm, 1.5 cm, 2.0 cm, 2.5 cm, 3.0 cm, 3.5 cm and 4.0 cm. The solid lines are quadratic fits to the data.

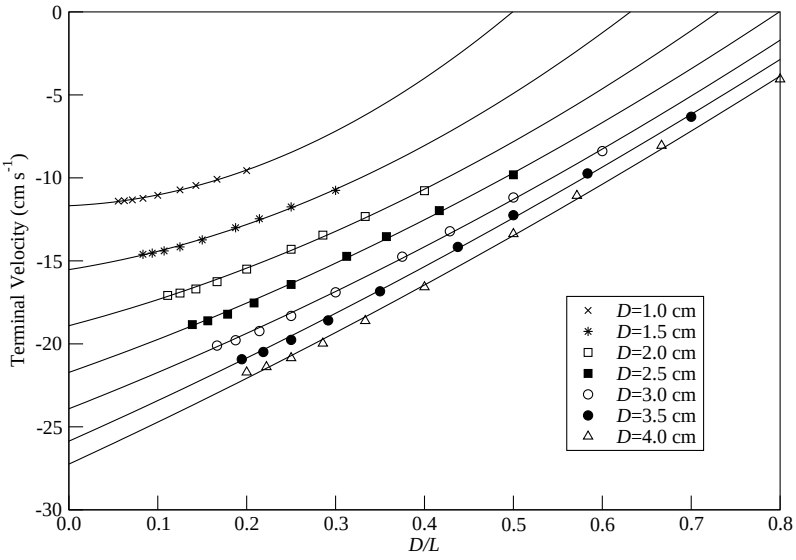

Fig. 2.23: Terminal velocity plotted against ratio of the cylinder diameter to width of the cell D/L for the Fluid Springs model. From the top line down the curves correspond to diameters of, 1.0 cm, 1.5 cm, 2.0 cm, 2.5 cm, 3.0 cm, 3.5 cm and 4.0 cm. The solid lines are quadratic fits to the data.

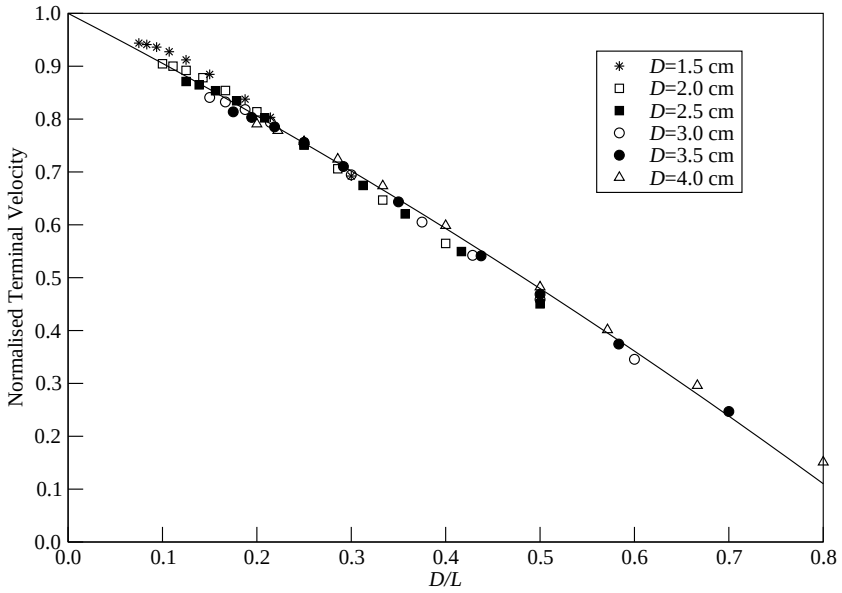

Fig. 2.24: Normalised terminal velocity plotted against ratio of the cylinder diameter to the width of the cell D/L for Particle Template model. Solid line is quadratic least squares fit to all the data shown with equation $f(x) = 1 - 0.922(\frac{D}{L}) - 0.237(\frac{D}{L})^2$.

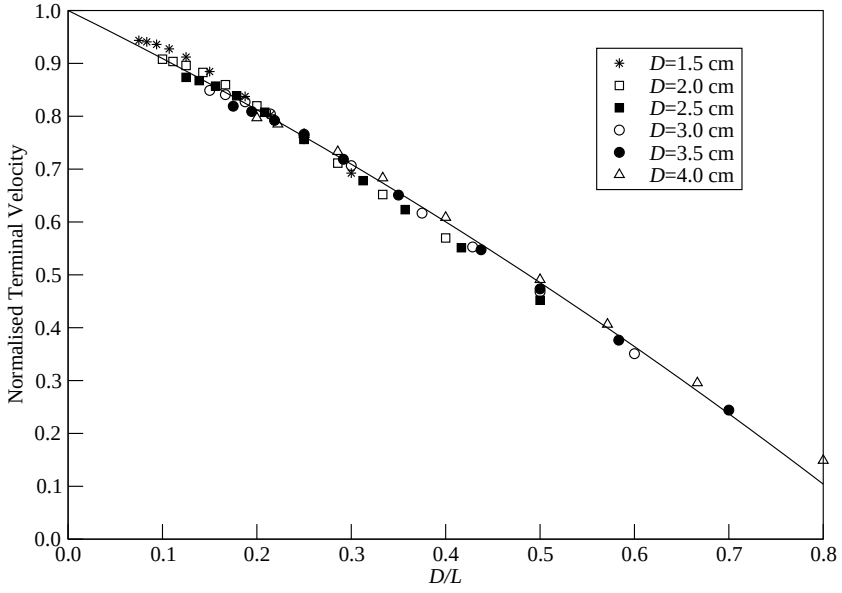

Fig. 2.25: Normalised terminal velocity plotted against ratio of the cylinder diameter to the width of the cell D/L for Fluid Springs model. Solid line is quadratic least squares fit to all the data shown with equation $f(x) = 1 - 0.878(\frac{D}{L}) - 0.302(\frac{D}{L})^2$.

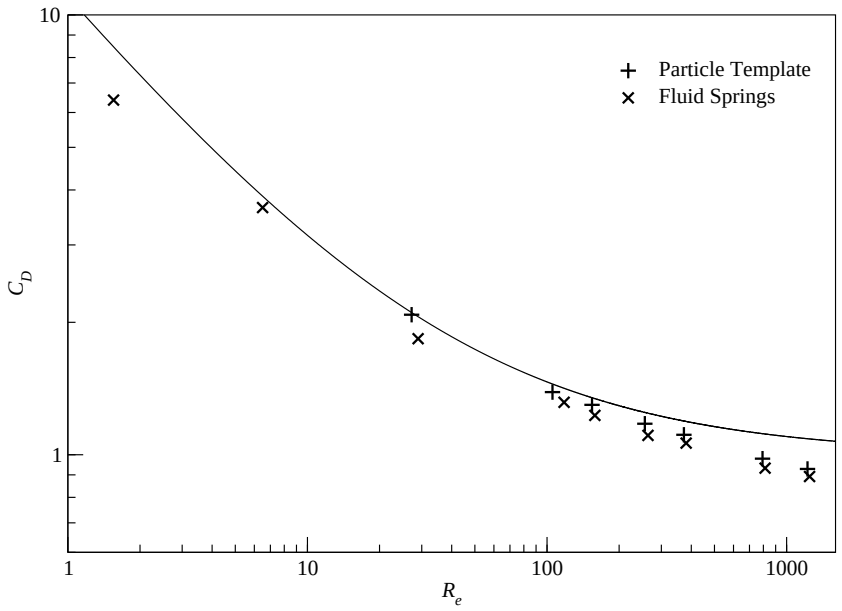

Fig. 2.26: The drag coefficient C_D as a function of the Reynolds number for a cylinder falling through viscous water. Data from the Particle Template model (pluses) and from the Fluid Springs model (stars) are shown. The solid line is the empirical curve, $C_D \approx 1 + \frac{10}{R_e^{2/3}}$, proposed by White (1991) for a falling cylinder.

$c_2 = 0.301$. These results are both in good agreement with those reported by Ristow (1997):

$$f\,(D/L) \approx 1 - 1.14\frac{D}{L}. \tag{2.103}$$

We note that the agreement between Figures 2.24 and 2.25 is so strong that on first impression the figures appear identical, however they do in fact show different data.

Drag Curve

Figure 2.26 plots the drag coefficient, C_D, against the Reynolds number R_e for a single falling cylinder using both the PT and FS models. We determine the characteristic Reynolds number of this system using

$$R_e = \frac{U\,2R}{\nu}, \tag{2.104}$$

while the usual definition of C_D is

$$C_D = \frac{\text{Drag Force}}{\frac{1}{2}\rho U^2(\text{Projected Area})}. \tag{2.105}$$

Here the projected area for the cylinder is the area normal to the particle motion. We determine the drag force when the cylinder has reached its terminal velocity so that the viscous drag and gravitational forces are equal. Therefore the characteristic velocity U is the terminal velocity of the cylinder in an infinite system, v_∞. For a cylinder of volume $\pi R^2 L_c$ the drag coefficient is evaluated using:

$$C_D = \frac{(\rho_g - \rho)\,\pi R^2 L_c g}{\frac{1}{2}\rho {v_\infty}^2\,(L_c 2R)} = \frac{\rho_g - \rho}{\rho}\frac{\pi R g}{{v_\infty}^2}. \tag{2.106}$$

We have chosen the radial reference point density n_r to be 32 for both the PT and FS models and $C_s = 0.5$ within the FS model. The mass of the cylinder is varied from ρ_g = 1000.1–10000 kg m^{-3} while the box width is fixed to 10 cm. The remaining parameters are as in Table 2.5. To determine v_∞ the terminal velocities are corrected using our quadratic fits from equation 2.102. The solid line in Figure 2.26 is an empirical curve to experimental data proposed by White (1991) which is given by:

$$C_D \approx 1 + \frac{10}{R_e^{2/3}}. \tag{2.107}$$

The fluid flow around the particle is steady for systems with a Reynolds number below $R_e \approx 230$ (Chen *et al.* 1995). Above this Reynolds number the fluid flow around the particle becomes increasingly unsteady. Figure 2.26 shows that the simulations agree well with experimental data and are able to capture the drag coefficient in the transition from steady to unsteady flow.

In the next section we extend our study from a single falling particle to the sedimentation of an entire bed of grains.

2.6.2 Sedimenting Cylinders

We now consider the case of multiple cylinders falling in a fluid-filled two-dimensional cell. These simulations serve as a useful comparison between the NS, PT and FS models. Here we simulate the motion of 200 sedimenting cylinders of diameter 2 mm in a large square cell of side length 44 mm. The fluid lattice spacing is Δ = 0.1 mm in the PT and FS models and Δ = 4.4 mm in the NS model so that the fluid resolution is 44 times greater in the PT and FS models than in the NS model. We introduce the LSD model to treat collisions as they are not significant to the system behaviour. We also set C_s to 0.5 in the FS model. The

Parameter	*Value*
Number of particles	200
Cylinder diameter	2 mm
Cylinder density ρ_g	1050 kg m^{-3}
Fluid density ρ	1000 kg m^{-3}
Fluid viscosity η	1×10^{-2} kg m^{-1} s^{-1}
e	0.9
K	1000 kg s^{-2}
Cell size (x–axis)	44 mm
Cell size (y–axis)	44 mm
Δ (NS model)	4.4 mm
Δ (PT & FS models)	0.1 mm
Δt	10^{-4} s

Table 2.6: Table of simulation parameters for sedimenting cylinders.

parameters shared by each system are shown in Table 2.6. At $t = 0$ s the sedimenting particles are stationary and positioned in a lattice like arrangement. To induce some interesting sedimentation configurations these particles were given small dispersions around the rigid lattice positions.

Figure 2.27 shows the initial configuration of grains for the three models at $t = 0$ s. The particles are released and Figures 2.28, 2.29 and 2.30 show the positions of the particles and instantaneous fluid flows within the NS, PT and FS model at times, t, of 1.5 s, 3.0 s and 4.5 s. Due to the low fluid resolution within the NS model simulations we find that a couple of channels of very fast falling cylinders form. This is very different to the PT and FS model simulations, whose flow patterns in Figures 2.29 and 2.30 agree very well with each other. We see that the grains fall together at approximately the same rate with several channels of faster flowing fluid forming briefly. Due to the higher fluid resolution the PT and FS models are able to mimic sedimenting systems more realistically.

The histories of the averaged vertical and horizontal translational cylinder velocities and positions for the three models are shown in Figure 2.31. Good

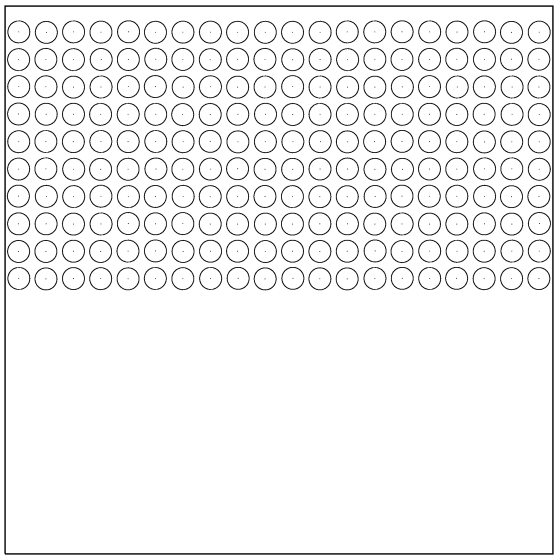

Fig. 2.27: Sedimentation of 200 fluid-immersed cylinders. Here the initial starting positions for the cylinders are shown.

agreement is achieved between the three models. For further information on sedimenting beds see the thesis by Kuusela (2005).

So far we have only considered two-dimensional systems. In the next section we simulate a falling sphere in three dimensions and determine the corresponding drag curve.

2.7 Falling Sphere

We now consider the case of a falling sphere in three dimensions. Here we study the dependence of the drag coefficient on the Reynolds number for the PT and FS models and compare to well known empirical results. These simulations are similar to those simulations performed in two dimensions to obtain Figure 2.26.

We drop a sphere of diameter 10 mm in a cell of width 50 mm filled with fluid of density 1000 kg m^{-3} and viscosity $1{\times}10^{-2}$ kg m^{-1} s^{-1}. The lattice spacing is $3.125{\times}10^{-4}$ m so that there are $n_r = 16$ reference points across each particle. The mass of the sphere is varied from $\rho_g = 1100$–10000 kg m^{-3} so that the sphere falls with a range of speeds.

Figure 2.32 plots the drag coefficient, C_D, against the Reynolds number R_e for a single falling sphere using both the PT and FS models. The characteristic

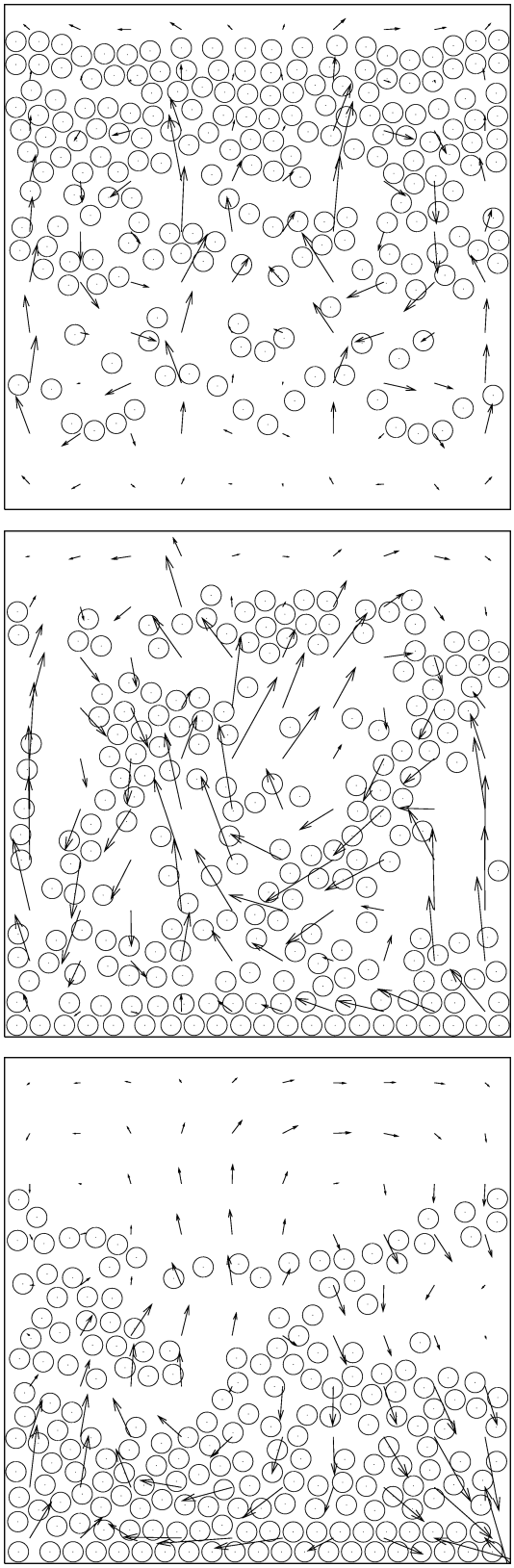

Fig. 2.28: Sedimentation of 200 cylinders using the Navier–Stokes model. From top to bottom the plots are at $t = 1.5$ s, $t = 3.0$ s and $t = 4.5$ s. The vectors in this plot show the instantaneous fluid velocities and have been scaled by a factor 0.5 for visual purposes. This means that if unchecked the fluid "particles" would move these distances in 0.5 s. As a reference the length of the cell is 44 mm.

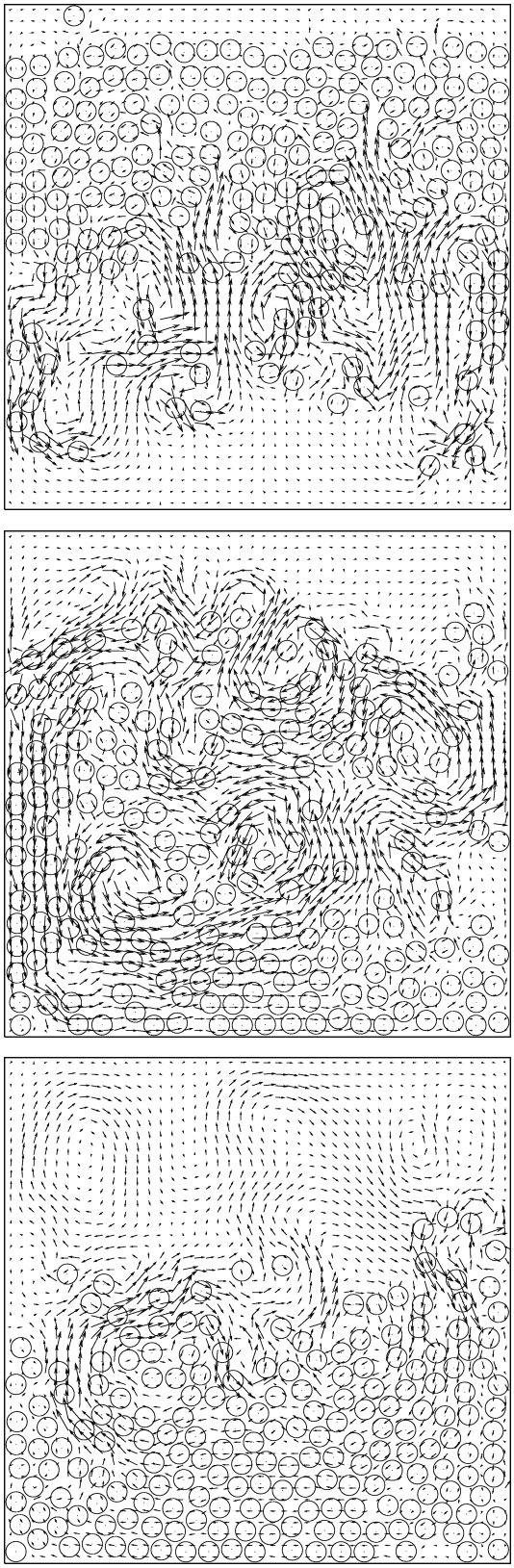

Fig. 2.29: Sedimentation of 200 cylinders using the Particle Template model. From top to bottom the plots are at $t = 1.5$ s, $t = 3.0$ s and $t = 4.5$ s. The vectors in this plot show the instantaneous fluid velocities and have been scaled by a factor 0.05 for visual purposes. This means that if unchecked the fluid "particles" would move these distances in 0.05 s. As a reference the length of the cell is 44 mm.

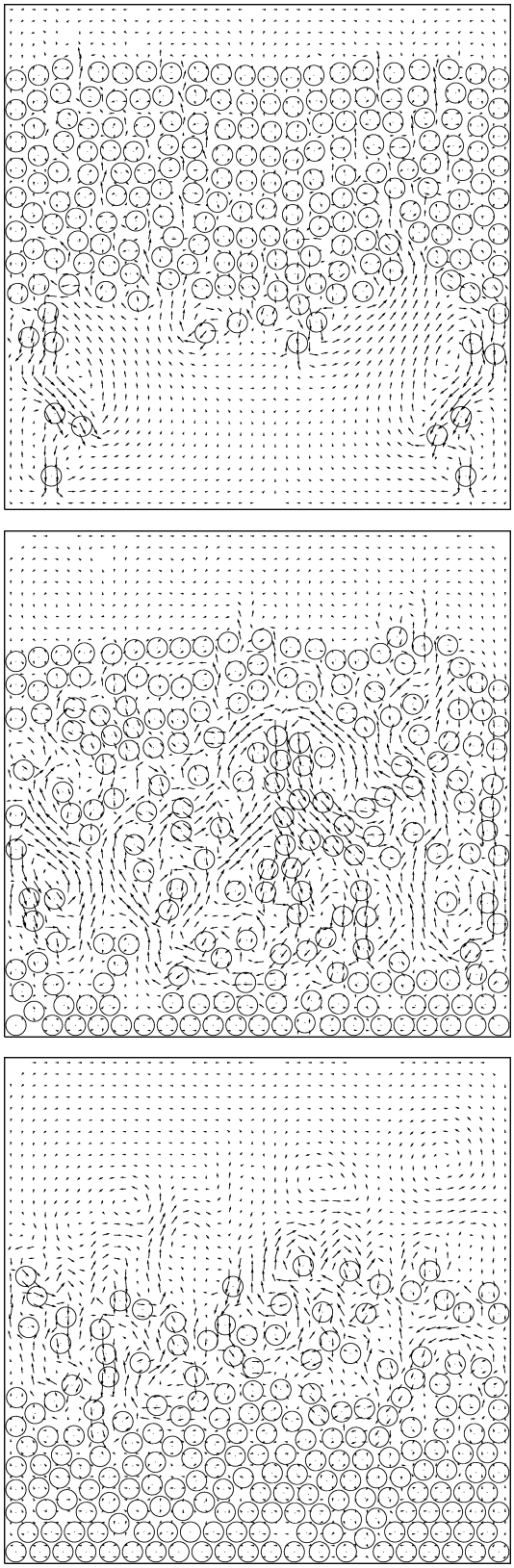

Fig. 2.30: Sedimentation of 200 cylinders using the Fluid Springs model. From top to bottom the plots are at $t = 1.5$ s, $t = 3.0$ s and $t = 4.5$ s. The vectors in this plot show the instantaneous fluid velocities and have been scaled by a factor 0.05 for visual purposes. This means that if unchecked the fluid "particles" would move these distances in 0.05 s. As a reference the length of the cell is 44 mm.

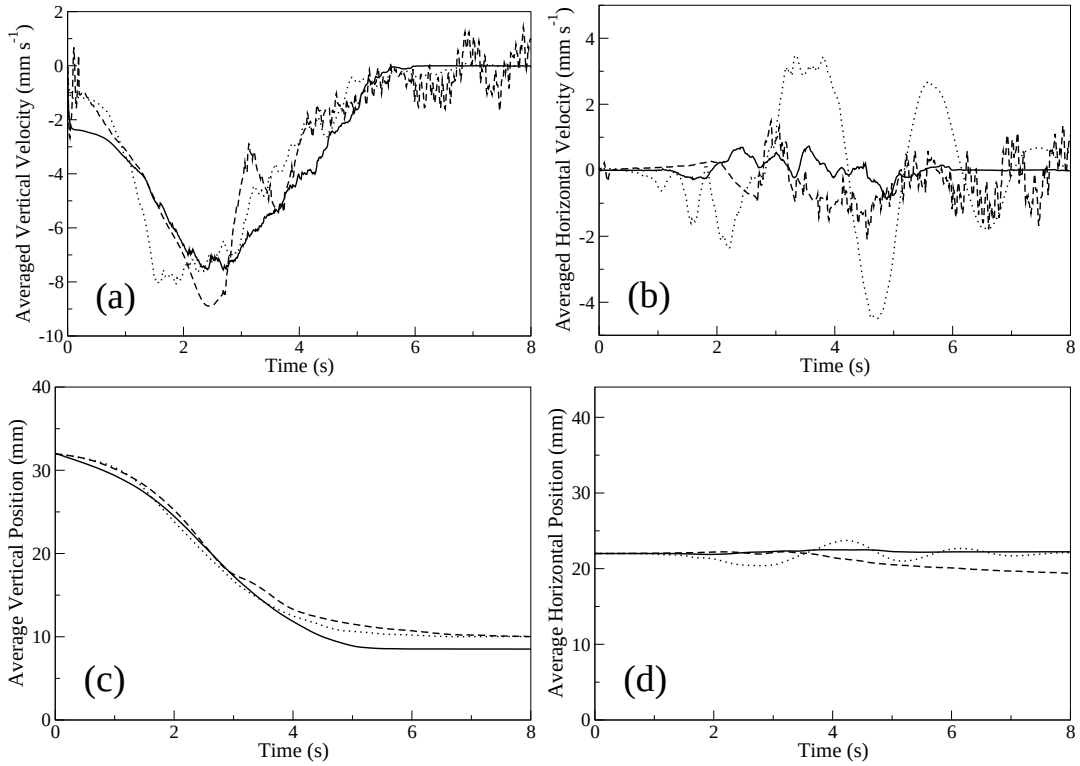

Fig. 2.31: Bed data for 200 sedimenting cylinders when using different fluid-grain coupling models. The (a) average vertical bed velocity and the (b) average horizontal bed velocity are both plotted against time t. Similarly the (c) average vertical position of the bed and the (d) average horizontal position of the bed are plotted against time t. The curves correspond to the Navier–Stokes model (dashed lines), the Particle Template model (dotted lines) and the Fluid Springs model (solid lines).

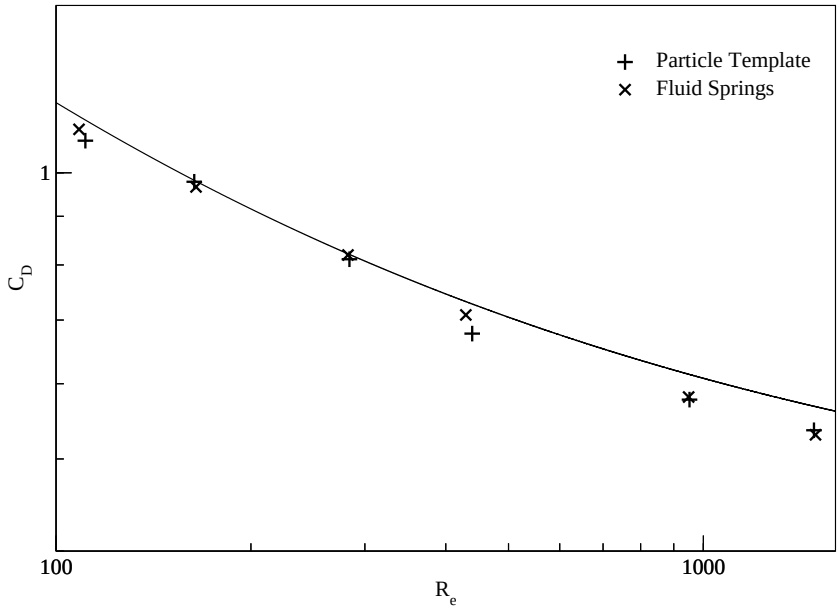

Fig. 2.32: The drag coefficient C_D as a function of the Reynolds number for a sphere falling through viscous water. Data from the Particle Template model (pluses) and from the Fluid Springs model (stars) are shown. The solid line is the empirical curve $C_D \approx \frac{24}{R_e} + \frac{6}{1+\sqrt{R_e}} + 0.4$ proposed by White (1991) for a falling sphere.

Reynolds number R_e of this system and the drag coefficient C_D are determined using equations 2.104 and 2.105 respectively. The solid line in Figure 2.26 is an empirical curve for a falling sphere proposed by White (1991) and is given by:

$$C_D \approx \frac{24}{R_e} + \frac{6}{1+\sqrt{R_e}} + 0.4. \tag{2.108}$$

We see that Figure 2.32 shows excellent agreement between the two models and the empirically determined curve. Thus the simulations are again able to capture the transition from unsteady to steady flow regimes.

2.8 Lubrication

In this section we give a brief introduction into lubrication and then discuss whether viscous forces are captured by the FS model.

Lubrication forces arise from fluid being squeezed between two close solid surfaces. These hydrodynamic viscous forces initially received considerable attention in tribology in the late 1970's, where tribology is the study of interacting surfaces in relative motion. Later Davis (1986) obtained both analytical and numerical

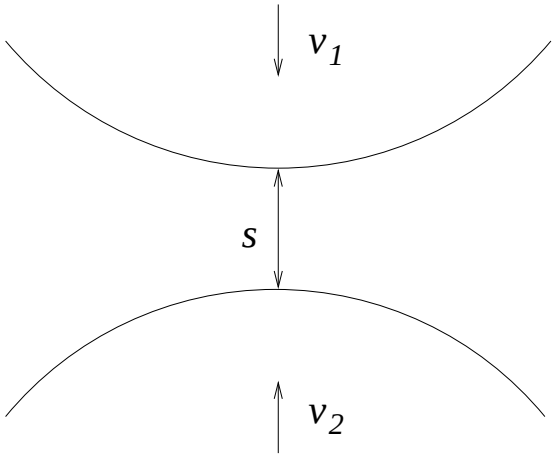

Fig. 2.33: Schematic representation of two approaching spherical particles in a viscous fluid.

solutions for collisions between two spheres surrounded by thin isoviscous liquid layers. The form of the force often used in simulations without lubrication is detailed by Lian *et al.* (2001) and Zhang *et al.* (2005).

Figure 2.33 shows a schematic representation of two approaching fluid-immersed particles. The particles have radii r_1 and r_2 and positions $\mathbf{r}_1$ and $\mathbf{r}_2$ and approach each other with velocities $\mathbf{v}_1$ and $\mathbf{v}_2$. Figure 2.33 introduces the quantity s which is defined as the smallest gap between the two particle surfaces. The gap, s, and relative velocity v_{12} between the particles are calculated using

$$s = (\mathbf{r}_1 - \mathbf{r}_2) \cdot \hat{\mathbf{n}} - (r_1 + r_2)\,, \tag{2.109}$$

and

$$\frac{ds}{dt} = -(\mathbf{v}_1 + \mathbf{v}_2) = \mathbf{v}_{12}, \tag{2.110}$$

where $\hat{n}$ is a unit vector connecting the centre of the two particles. For a fluid-grain system without any lubrication forces the hydrodynamic viscous force, $\mathbf{F}_L$, may be introduced and implemented through the well known equation (Davis *et al.* 1986; Lian *et al.* 2001):

$$\mathbf{F}_L = -\frac{6\pi\eta r^{*2}}{s}\mathbf{v}_{12}. \tag{2.111}$$

The force opposes the direction of relative particle motion and is dependent on the fluid viscosity, η, the effective particle radius, r^*, and the gap between the surfaces s. The effective radius r^* is related to the radii of the two approaching

spheres by the following expression:

$$\frac{1}{r^*} = \frac{1}{r_1} + \frac{1}{r_2}. \tag{2.112}$$

In the case of a sphere of radius r_1 colliding with a wall we assume $r_2 = \infty$ such that $r^* = r_1$.

The force $\mathbf{F}_L$ is applied over a limited range of s values because as, $s \to 0$, an unphysical infinite lubrication force results, otherwise known as "Stokes paradox". Thus a lower limit for the gap over which the force is effective s_{min} is introduced. The minimum gap s_{min} over which the force is applied is ambiguous and is thought to mainly depend on the roughness of the particle surface preventing s approaching zero. However, even for perfectly smooth particles a minimum molecular distance of $s_{min} = 4{\times}10^{-10}$ m due to molecular repulsion will remain when the surfaces make "physical" contact. An upper limit s_{max} below which the force is significant is also applied. This is assumed to be smaller than the particle radius of the order $0.1r^* - r^*$. In reality lubrication is a long range force, however applying the force over a large range of s dramatically reduces simulation speeds. The s range, therefore, over which the lubrication force is effective is limited. Due to the individual nature of each system the gaps s_{min} and s_{max} are at best empirical fits. The use of $\mathbf{F}_L$ allows the modelling of viscous damped collisions more closely, although not with 100% accuracy.

We now test if there are any hydrodynamic viscous forces present when the FS model is used to model the fluid-grain coupling. We do this by colliding a single spherical particle with a solid surface in a water-filled cell and recording the particle velocity before and after the collision. Since the particle will slow regardless of whether the wall is present due to fluid drag we also compare our results to the situation where the particle moves through the fluid without colliding with any surface.

We set up a cell of horizontal cross-section $L_x \times L_y = 3.625$ mm$\times$3.625 mm and height $L_z = 14.5$ mm which is filled with water of density $\rho = 1000$ kg m^{-3} and viscosity $\eta = 1{\times}10^{-3}$ kg m^{-1} s^{-1}. A single particle of density $\rho_g = 4500$ kg m^{-3} and radius $r_I = 362.5$ μm is then inserted into the cell and given an initial velocity of v_0. The particle then moves downwards along the z–axis of the cell until it collides with the bottom wall. Gravity is neglected from the

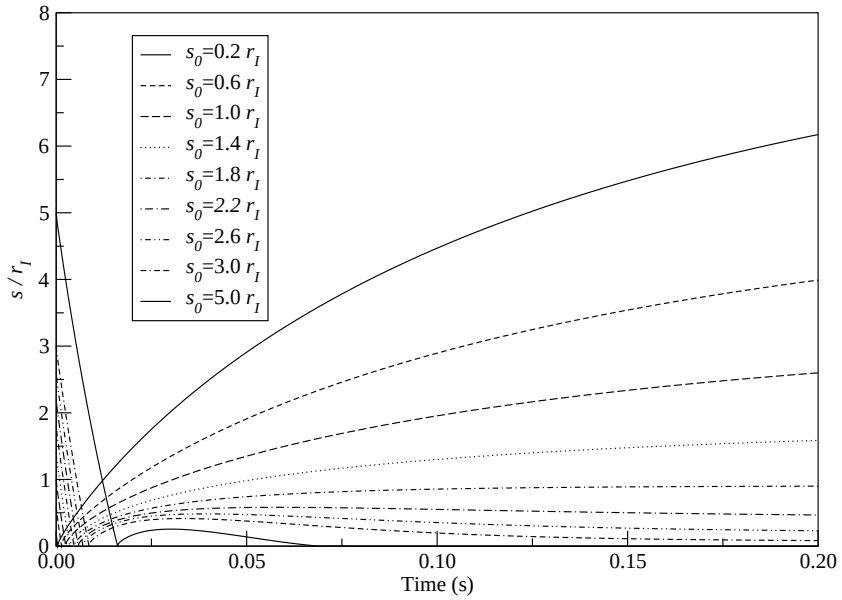

Fig. 2.34: s/r_I plotted against time t for a particle approaching and colliding with a solid wall. The particle initially starts a gap $s_0 = 0.2r_I$–$5.0r_I$ from the wall.

system so that the particle experiences only viscous and collisional forces. The particle collisions are elastic so that if the same particle collided with the wall in a vacuum the coefficient of restitution e would be 1.0. This allows us to isolate the hydrodynamic effect of fluid being squeezed between the surfaces during collisions. When the particle is initially released within the cell it loses a significant amount of its velocity within just a few time-steps. This is because the fluid surrounding the particle is initially stationary and the microscopic fluid flow fields which allow fluid to flow past the particle take a few time-steps to develop.

Figure 2.34 plots the scaled gap $s/r_I = (z_I - r_I)/r_I$ between the particle and the wall against time t. Here z_I is the vertical position of the intruder within the cell. The particle is given an initial velocity in each run of $v_0 = 0.26$ m s^{-1} and is released from a range of initial gaps $s_0 = 0.2r_I$–$5.0r_I$. After a few time-steps the particle velocity v_I settles to approximately 0.14 m s^{-1}. We find that the further away the particle begins from the wall the lower the intruder's speed is on impact due to fluid drag slowing the particle.

Figure 2.34 shows that for small initial separations $s_0 \leq 1.4 \times r_I$ the particle collides with the wall and then moves away. The particle loses some velocity in the collision and then continues to decelerate due to fluid drag until it stops completely at an equilibrium distance s_{eq} from the wall. We find that as the

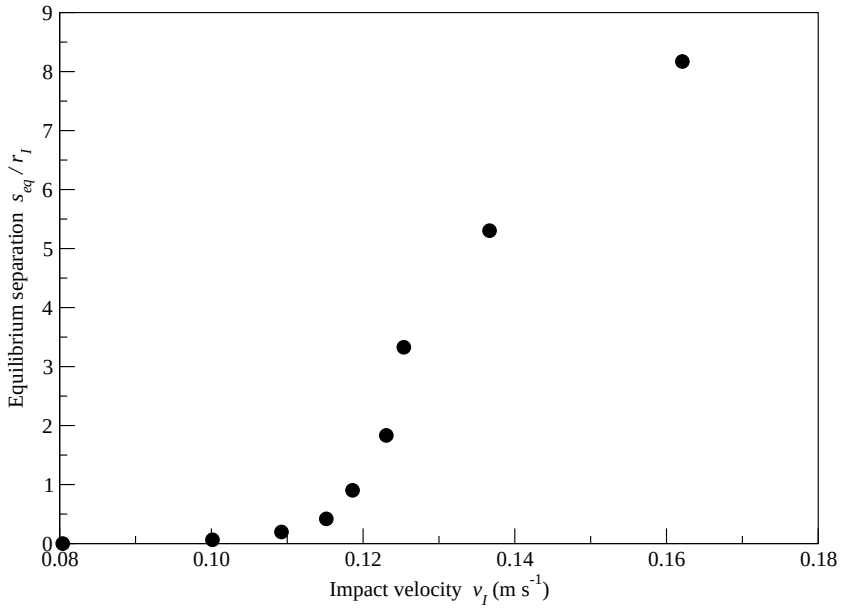

Fig. 2.35: The equilibrium distance s_{eq}/r_I as a function of impact velocity v_I for a particle approaching and colliding with a solid.

initial distance s_0 increases the intruder speed on impact decreases and as a result s_{eq} reduces. As s_0 increases further to $1.8r_I$ the equilibrium distance s_{eq} reduces also, however, the particle behaves differently to those in earlier runs. Here the intruder initially moves away from the wall and decelerates until it is stationary, the particle then moves slightly back towards the wall before stopping completely. These "oscillations" continue to become stronger so that as s_0 is increased to $3.0r_I$ the final resting position of the particle s_{eq} gets closer to the wall. Similar oscillations have been observed in the analytical study of colliding spheres (Davis *et al.* 1986). As s_0 is increased to $5.0r_I$ the oscillations become so large that the particle's final position is touching the wall having initially moved away. Figure 2.34 shows that if the particle initially stops within $s = r_I$ of the wall it experiences an attractive force which causes it to move back towards the wall.

Figure 2.35 plots the scaled equilibrium distance s_{eq}/r_I against the collision impact velocity v_I for the particles from Figure 2.34. As v_I is increased in the range $0.08 \rightarrow 0.12$ m s^{-1} there is only a small increase in s_{eq} from $0.0 \rightarrow\sim r_I$. Between $v_I = 0.12$ m s^{-1} and $v_I = 0.13$ m s^{-1} the equilibrium distance increases rapidly. Above $v_I > 0.13$ m s^{-1} the equilibrium distance s_{eq} increases less quickly

so that an s-curve is created by the data. Figure 2.35 shows that if the particle is to "escape" the wall after collision it must have an impact velocity v_I above ~ 0.12 m s^{-1}. In the impact velocity range 0.08–0.12 m s^{-1} the particle experiences damped oscillations until it stops. This oscillating behaviour is due to the lubrication forces experienced by the particle when in close contact with the wall. The particle motion is damped due to fluid friction as it is squeezed back and forth between the two surfaces.

Below $v_I = 0.08$ m s^{-1} the equilibrium separation is $s_{eq} = 0.0$. If the only fluid drag force experienced by the particle was proportional to its velocity, as with Stokes Drag, we would expect the separation curve in Figure 2.35 to equal zero only when the impact velocity is zero. This shows that the particle experiences a further hydrodynamic drag force which has a significant impact on the collision dynamics.

To determine the effect of the walls we measure the coefficient of restitution e for the particle-wall collisions using the expression:

$$v = -ev_I. \tag{2.113}$$

Here v_I and v are the velocities of the sphere before and after the collision. We wish to measure how much the thin fluid layer between the surfaces has on the velocity by calculating the coefficient of restitution. To do this we measure the particle velocity as it moves towards and away from the wall at a fixed distance s from the wall. We record the velocities for a range of gaps $s = 0.05r_I - 0.50r_I$ and plot the results in Figure 2.36.

Figure 2.36 plots e as a function of the distance from the wall that the initial and final velocities are measured. The results are obtained for a particle with an initial gap of $s_0 = r_I$ from the wall. We observe that for small s the restitution coefficient is close to unity since the collision with the wall is elastic. As the gap s increases e reduces rapidly until $s \approx 0.5r_I$ where the coefficient of restitution is approximately 0.1.

The problem with measuring e in this way is that the particle has to move through the fluid to where the initial and final velocities are recorded. During this time the particle is also slowed due to viscous fluid forces. This makes it difficult to determine whether the particle is slowing due to lubrication or fluid

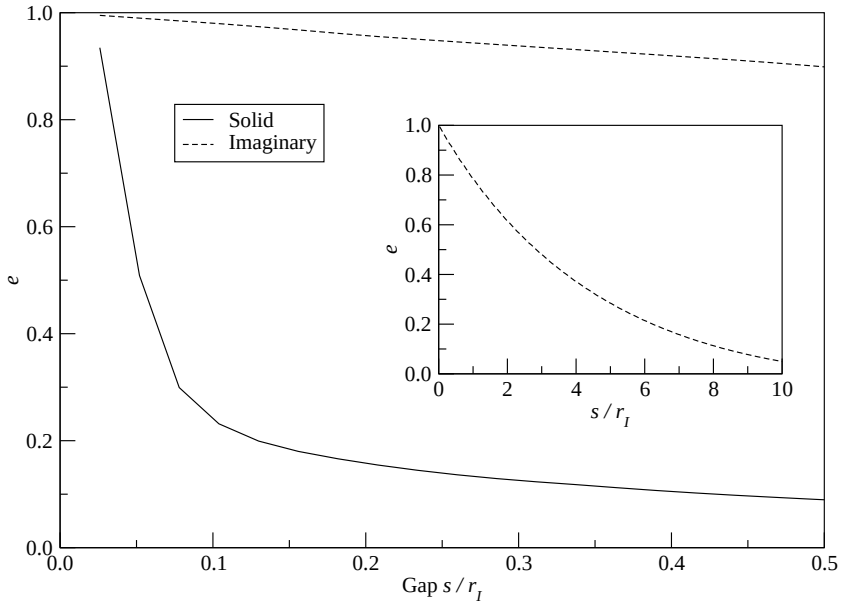

Fig. 2.36: e as a function of the gap s/r_I that the velocities, v_I and v, are measured. The particle collides with a solid wall (solid-line) and an imaginary wall (dashed-line). e is calculated over a range spanning $s = 0 - 0.5r_I$, while the insert shows the imaginary wall data plotted over a range of $s = 0 - 10r_I$.

drag effects. For this reason we have measured the input and output velocities of the particle moving past an imaginary wall and then calculated e in the same way as we did for the particle-wall collisions. By making this comparison we are able to isolate the effect of the wall on the particle velocity. The simulation is set up so that the particle collides with the imaginary wall with the same velocity as it did for the real one. The results of both the real and imaginary wall simulations are plotted Figure 2.36. The results from the collisions with the imaginary wall, in the inset, show that e reduces over a large s range. For the same range that the real wall collisions are measured e reduces to just 0.9. This shows that the effect of fluid drag over a range this small is minimal, which means that the majority of the particle slowing is due to lubrication effects. When $s = 0.5r_I$ the restitution coefficient is still reducing faster than for the equivalent velocity in the imaginary wall simulations. This shows that the lubrication forces are effective over a range greater than $s = 0.5r_I$ within our simulations.

The quantitative comparison between the FS model simulations and experiments is difficult. This means that the choice of coefficient of restitution e in fluid-immersed particle collisions is somewhat arbitrary. For consistency with our

other models we therefore include a coefficient of restitution e which will further dampen particle collisions in our FS model simulations.

2.9 Computation

All of the codes used within this thesis were developed from scratch using C programming language. The code was compiled using Gnu library and some further optimisation tools. The simulations were all submitted to the High Performance Computing (HPC) facility at the University of Nottingham and were run on single compute nodes. The nodes within the HPC facility are split into five separate clusters. The executable files of our codes are submitted to just one of the clusters each time in a task array format. All of the clusters contain nodes with a minimum CPU performance of 2.2×AMD Opteron 2.2 GHz single core and a minimum RAM of 2 GB.

All of the simulations in the following chapters yielded results within timescales of a few days to a maximum of two weeks.

2.10 Summary

In this chapter we have described the simulation methods used to model our fluid-grain systems. The first part of the chapter was concerned with outlining the MD technique used to model the grains. Within this section we described the contact forces we may use including the LSD and DH contact force models. We then performed some comparisons to show under what conditions each model is best suited. We showed that to achieve realistic collisions the DH model allowed for the largest time-step and thus the best computational efficiency. If contact forces do not affect the system behaviour then LSD contact forces are suitable. We then briefly discussed the approach used to model the fluid. This approach was based on spatially discretising the governing equations of fluids, the Navier–Stokes equations, on a staggered MAC mesh and solving using the projection method with suitable boundary conditions.

We then discussed several approaches in which we may couple the granular and fluid phases. The first model we described is the analytical Kroll model. This

model considers the forces experienced by a porous granular bed when shaken in an air-filled cell. We manage to determine an equation of motion for the flight of the bed. To determine the flight of a body within a dense fluid we modify the Kroll model to include buoyancy and added mass corrections within the flight equation. Both of these models capture fluid-immersed granular bed behaviour very accurately despite modelling the bed as a porous body. We then described two models which use empirical bed equations to couple the fluid and grain phases. The first model uses MD to determine the particle interactions and couples the fluid and grain phases using a drag force based on a bed equation. This force is applied explicitly onto the grains so that it opposes the direction of particle motion. The model is appropriately named the Simple Drag model. The second model modifies the Navier–Stokes equations for incompressible fluids to include a term, based on a bed equation, which estimates the momentum transfer between the fluid and grain phases. The resulting model, which is called the NS model, reproduces the effects of a fluid-immersed granular bed where the grains are individually modelled using MD.

We then introduce two models in which the fluid grid is small in relation to the particle size. These two models share common features as neither use bed equations to determine the momentum transfer between the fluid and grains. Instead the forces are determined through a template. The first model we described was the PT model where the particles' motions are determined individually using MD and the fluid is solved using the Navier–Stokes equations. In order to couple the fluid and grain motion the fluid lattice points immersed within the particle are forced to share the same velocity as the particle while the corresponding force on the particle is calculated by taking an integral of the stress-tensor divergence over the template. The second model we describe is the FS model. This model differs from the PT model in that on each grain we create a template of grid-points which moves with the particle. For each lattice point on the template, we predict the difference in the future fluid and grain paths and then correct the motion using an imaginary damped spring which forces the two phases to converge.

The second half of this chapter was concerned with comparing the models and determining under which conditions they were most suitable. We found that

in two dimensions the FS model was stable and able to achieve more accurate results with fewer lattice points contained within its volume than for the same parameters in the PT model. In the last part of the chapter we observed that the FS model is able to capture lubrication effects that arise when fluid is squeezed from between two close surfaces.

Chapter 3

Accelerated Systems

In this chapter we discuss fluid-immersed granular beds which are subjected to vertical vibrations. First, we consider how to treat the vibrations within our simulations in the simplest way possible. We then simulate a fluid-immersed packed bed as it is thrown from a surface using the Fluid Springs model. These results are compared with the Modified Kroll model so that we may determine which simulation parameters work best. In the last part of the chapter we simulate a thrown granular bed and compare results obtained using four models detailed in Chapter 2, namely the Modified Kroll (MK), the Navier–Stokes (NS), the Particle Template (PT) and the Fluid Springs (FS) models.

3.1 Treatment of Vibrated Systems

So far we have only considered sedimentation, where the fluid-grain system is held stationary; however, in this thesis we will be simulating several *vibrated* granular systems. Thus, to make our simulations easier to compute, we must consider how to treat a vibrated cell of fluid-immersed grains in the simplest possible way. For the majority of systems with which we are concerned, the fluid and grains are constantly excited through vibration; however, in order to keep the simulations as simple as possible we change the reference frame from that of the laboratory to that of the cell, which allows simpler computation of the no-slip boundary conditions at the walls and on the particles themselves. As a consequence we must include an acceleration term in the equation of motion for the particles,

which will be equal and opposite to the acceleration of the cell in the reference frame of the laboratory. The equation of motion for a single particle, equation 2.9, is therefore modified to become

$$m\ddot{\mathbf{r}} = \mathbf{F}_{collision} + \mathbf{F}_{system} - m\mathbf{a}(t), \tag{3.1}$$

where $\mathbf{a}(t)$ is the time-dependent acceleration of the cell as observed in the frame of reference of the laboratory. The particle position $\mathbf{r}$ is now taken to be in the reference frame of the vibrating cell. $\mathbf{F}_{collision}$ and $\mathbf{F}_{system}$ are the collisional forces and any other system forces experienced by the particles respectively.

We must also consider how the hydrostatic pressure gradient force acting on the fluid-immersed particles is modified within the vibrating cell. The hydrostatic pressure within the fluid will oscillate with the vibration of the cell and may be given as

$$\nabla P_{hydrostatic} = \rho \mathbf{g}', \tag{3.2}$$

where $\mathbf{g}'$ is the "modified" gravity and is obtained using:

$$\mathbf{g}' = \mathbf{g} - \mathbf{a}(t), \tag{3.3}$$

where $\mathbf{g}$ is the gravitational acceleration. Thus, to account for the cell accelerations, the fluid motion equations for the PT model, equation 2.77 and the NS model, equation 2.62, are modified so that $\mathbf{g}$ is replaced by $\mathbf{g}'$. The fluid motion equation in the FS model may be modified but it is not necessary as the fluid drag force on the particles are not determined through the hydrostatic fluid pressure.

Within the remainder of this chapter we consider the properties of a thrown fluid-immersed granular bed.

3.2 Thrown Beds

So far we have only simulated a single falling sphere in three dimensions (section 2.7). However, in this section we consider a three-dimensional fluid-immersed granular bed system within an oscillating cell. We have two specific objectives for the thrown bed simulations. These are: to find suitable simulation parameters for the FS model, and to compare simulation results obtained with the MK, NS,

PT and FS models. To our knowledge the PT and FS models have not previously been used to simulate vibrating densely-packed granular beds.

3.2.1 Fluid Springs Model

We first focus on finding parameters that allow for accurate and efficient simulations within the FS model. In section 2 we simulated two-dimensional systems using a large value of the radial reference point density n_r. However, extending these simulations into three dimensions for the same n_r can result in an extremely large MAC grid, which is computationally very time consuming to simulate. Thus we wish to find parameters for three-dimensional simulations which produce accurate results in an efficient and stable manner. We found in the previous section that for large n_r the PT and FS models gave convergent results, but as n_r was reduced the results produced with the FS model were more accurate (see Figures 2.20 and 2.21). Therefore we simulate a vibrated system of densely-packed fluid-immersed grains with the radial density of reference points n_r reduced to 3. A three-dimensional template of radial reference point density $n_r = 3$ contains approximately as many reference points as a two-dimensional template of $n_r = 6$.

We model 600 water-immersed spherical particles in a cell vibrated vertically along the z–axis. Gravity acts along this axis also. The particles within the bed are either glass or bronze and have a 10% dispersion in diameters to prevent crystallisation. The grain interactions were modelled using the LSD collision model with a large spring constant and the vessel was given periodic boundary conditions along the x–axis and y–axis so that wall effects do not affect the flight of the grains. The remaining simulation parameters are given in Table 3.1.

Within each simulation, the particles are initially set up in a lattice-like arrangement throughout the cell and then allowed to settle under the influence of gravity. Once the grains are at rest the cell is shaken to remove transient effects with a trajectory of

$$z_c = A \sin(\omega t) . \tag{3.4}$$

Here z_c is the position of the cell base and A and ω are the vibration amplitude and angular frequency respectively. After the bed has been vibrated for a second both the base pressure and the gap between the bottom edge of the bed and the

Parameter	*Value*
Number of particles	600
Particle diameter	630–770 μm
Glass density ρ_{glass}	2500 kg m^{-3}
Bronze density ρ_{bronze}	8900 kg m^{-3}
K	3000 kg s^{-2}
e	0.2
Fluid density ρ	1000 kg m^{-3}
Fluid viscosity η	8.91$\times$10^{-4} kg m^{-1} s^{-1}
Cell size (x–axis)	4 mm
Cell size (y–axis)	4 mm
Cell size (z–axis)	30 mm
C_s	0.1–2.0
Δt	10^{-5} s
f	20 Hz
Γ	2.0

Table 3.1: Simulation parameters used to model a fluid-immersed granular bed held in a vibrated cell.

cell base are measured. The data is then averaged over 40 cycles. Each vibration cycle begins at a phase angle of $\theta = 0°$, which corresponds to when the cell is moving upwards with maximum velocity $\dot{z}_c = A\omega$.

Figure 3.1 plots the pressure and gap curves for vibrated water-immersed glass and bronze beds over the course of a single vibration cycle. The various dashed curves correspond to C_s values spanning 0.1–2.0 while results from the MK model, which have been shown to agree well with experimental results (López-Alcarez 2007), are plotted as a solid line. Ergun's bed equation 2.70 has been used to couple the fluid and grain motion within the MK model. Figures 3.1(a) and 3.1(b) show the pressure curves for the glass and bronze beds with the additional hydrostatic pressure due to oscillation effects removed. Figures 3.1(c) and 3.1(d) show the gap between the bottom edge of the bed and the cell base for the

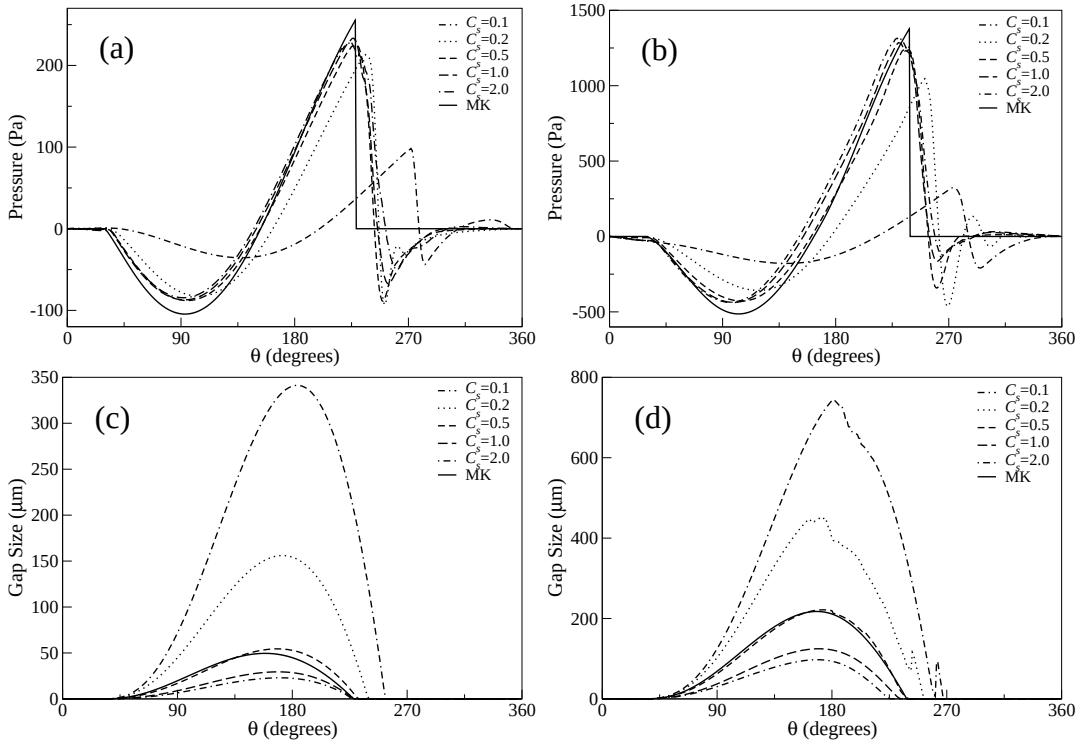

Fig. 3.1: Pressure and flight curves obtained from a thrown water-immersed granular bed system. The system was modelled using the Fluid Springs model for C_s values in the range 0.1–2.0 for a system with $n_r = 3$. All results are averaged over 40 cycles. The system was shaken with vibration parameters $f = 20$ Hz and $\Gamma = 2.0$. Plots (a) and (b) show the measured base pressures with the additional hydrostatic pressure due to oscillation effects removed. Plots (c) and (d) show the gap between the base of the cell and the lowest edge of the bed. The left plots are for a system of glass particles with density 2500 kg m^{-3}, and the right plots are for a system of bronze particles with density 8900 kg m^{-3}. The solid lines are results from the theoretical Modified Kroll model.

glass and bronze beds also. Figures 3.1(c) and (d) show that the granular bed is thrown and lands within each vibration cycle. As the bed is thrown in the early part of the cycle, incompressible fluid flows downwards through the bed. Later in flight, as the bed lands, fluid flows upwards through the beds and an overpressure develops. The pressure curves in Figure 3.1 converge for C_s values in the range 0.5–2.0 and that these curves demonstrate excellent agreement with the MK model. For C_s values below 0.5 the shapes of the pressure curves are severely altered and agreement with the MK model worsens.

Figures 3.1(c) and 3.1(d) show that as C_s reduces the maximum heights that the beds are thrown increases. This is because as C_s reduces the fluid-grain coupling weakens and the grains experience less drag from the fluid and so are thrown higher. For both glass and bronze beds the strongest agreement between the FS and MK models is when $C_s = 0.5$. The value of C_s may be determined empirically in this way for different fluid-grain systems.

3.2.2 Comparison between Models

We now perform the same thrown bed simulations using the MK, NS and PT models in addition to the FS model. Ergun's empirical bed equation 2.70 has been used implement the coupling between the fluid and grain phases in the MK and NS models. As in Section 3.2.1 we measure the pressure across the bed and the gap evolution over the course of a vibration cycle. Within both the PT and FS models we set n_r to 3, while in the FS model we set $C_s = 0.5$ for the glass and bronze systems. The remaining parameters for the models are summarised in Table 3.1. Figure 3.2 shows the pressure and height curves for a water-immersed bed of glass and bronze particles.

Figure 3.2 shows excellent agreement between the MK, NS and FS models. However, we find that the PT model is unable to model the pressure and thrown heights of the bed accurately. Therefore, when we wish to simulate dense granular beds in three dimensions with a microscopic fluid model we chose the FS model rather than the PT model.

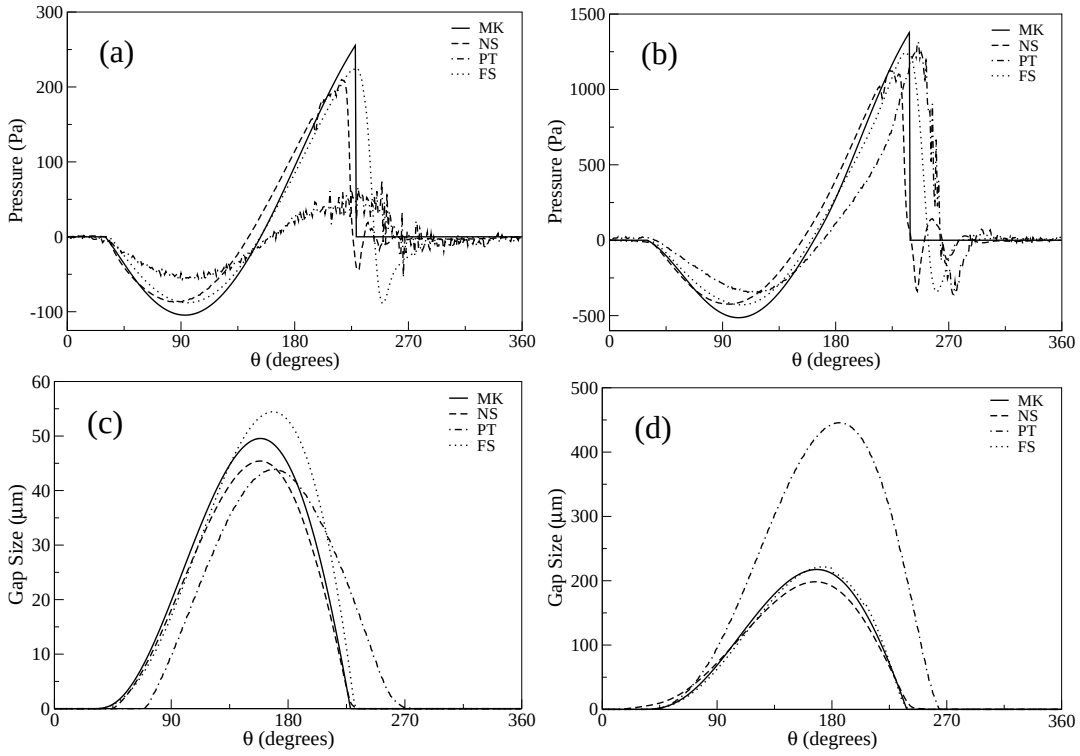

Fig. 3.2: Pressure and flight curves obtained from a thrown water-immersed granular bed system. All results are averaged over 40 cycles. The system was shaken with vibration parameters $f = 20$ Hz and $\Gamma = 2.0$. Plots (a) and (b) show the measured base pressures with the additional hydrostatic pressure due to oscillation effects removed. Plots (c) and (d) show the corresponding gaps between the base of the cell and the lowest edge of the bed. The left plots are for a system of glass particles of density 2500 kg m^{-3} and the right plots are for bronze particles of density 8900 kg m^{-3}. The curves correspond to the Modified Kroll (solid-line), the Navier–Stokes (dashed-line), the Particle Template (dotted-line) and the Fluid Springs (dot-dashed-line) models. In the Fluid Springs model $C_s = 0.5$ for both the glass and bronze beds.

3.3 Summary

Within this chapter we studied fluid-immersed granular beds subjected to vertical oscillations. The fluid and grains were both simulated in three dimensions. We initially observed that the FS model was able to model the behaviour of a thrown bed. This showed that the FS method was able to model fluid flowing through packed beds in an unsteady flow regime.

Later in the chapter we simulated a thrown bed using four models described in Chapter 2. Here we found that the NS and FS models could capture the behaviour of a thrown porous bed accurately while the PT model was unable to do so for the same parameters. We found that the NS model simulations were able to capture the behaviour of the thrown bed despite using Ergun's empirical bed equation which was developed for steady flow through packed granular beds.

In the next chapter we extend our simulations to investigate the phenomena of heap formation.

Chapter 4

Heap Formation

In this chapter we study convection within a fluid-immersed granular bed held in a vertically vibrated cell. We compare results obtained using the Simple Drag (SD), the Navier–Stokes (NS) and the Fluid Springs (FS) models. The chapter begins by demonstrating wall-driven convection effects using the SD model. We then show that convection is enhanced when the hydrostatic fluid motion is modelled using the NS and FS models. Our principle finding is that convection is a fluid-driven effect which is enhanced by the presence of some wall friction. At the end of the chapter we simulate the formation of a heap in three dimensions.

4.1 Introduction

A granular bed resting on a horizontal surface may gain energy if the surface is vibrated either by periodic tapping or by continuous sinusoidal oscillations. The grains will leave the plane if the maximum acceleration of the boundary is greater than gravity. The granular temperature of the bed of grains decreases mainly through inelastic collisions with other particles contained in the bed. If during one vibration cycle, more energy is fed into a granular bed through mechanical agitation than is lost through energy dissipation, the bed is able to flow like a fluid and is said to be "fluidised".

Faraday (1831) noted that fine particles may spontaneously form conical piles when placed on an oscillating horizontal surface. Grains are said to "avalanche" down the pile surface, the shape of the pile being maintained by movement of

grains upwards through the bed due to air flow. Likewise, within a vertically vibrated cell, a body of grains that form a pile within the centre of the cell may be observed to "Faraday tilt" (Pak *et al.* 1995). Here the granular bed symmetry is broken and the pile migrates to one edge of the box so that the bed slopes downwards across the cell and grains cascade down the top surface to be replenished by grains moving upwards within the bed.

Faraday tilting is a well-known effect for fine granular beds in air and is caused by the influence of the horizontal component of the fluid flow, set up once any deviation from horizontal symmetry occurs (Leaper *et al.* 2005; Thomas *et al.* 2000; Thomas and Squires 1998). The mechanism for tilting within a two-dimensional water-immersed bed is described in full by Milburn *et al.* (2005). As the bed of grains are thrown from their supporting platform, fluid is drawn through the bed to fill the void below. The fluid will prefer to flow through the shallower parts of the bed so any asymmetry within the bed leads to preferential fluid flow through the regions with least resistance, i.e. the shallowest parts of the bed. The resulting horizontal fluid flow beneath the bed whilst it is still in flight is directed towards any deeper regions of the bed. This flow carries grains with it causing the deeper regions of the bed to become more pronounced. As the asymmetry grows so does the preferential path of the fluid flow through the bed leading to an increasingly tilted configuration. One finds that the tendency for Faraday tilting is stronger at lower frequencies and at lower amplitudes of vibration. This tendency extends to higher frequencies for finer and deeper beds (Milburn *et al.* 2005).

The chapter is organised as follows. Firstly we simulate a vibrated fluid-immersed granular bed within a walled cell with varying wall friction to induce convection within the bed. In this first case the fluid-grain coupling is modelled using the SD model (Biswas *et al.* 2003). We then simulate the same system using two models which include hydrodynamic information about the fluid and grain motion, namely the NS and FS models. We show that both of these models are able to capture Faraday tilting. The results obtained with each model are then compared. To our knowledge this is also the first time the NS and FS models have been used to model three-dimensional fluid-grain systems. At the end of the

chapter we simulate a "Faraday heap" using the FS model.

4.2 Quantifying Convection

The convective flow needs to be quantified. We use a similar measure to the one used by Taguchi (1991). In order to measure the strength of the flow of convection, we introduce the cell-to-cell flow **J**. This field may be calculated in three dimensions; however, in our simulations we construct a cell with greatest dimensions along the x and z axes. The vibrations and gravity also act along the z–axis. The other cell length (y–axis) is approximately $\sim$7 particles deep and so little convection occurs in this direction. Thus the majority of convective motion is in the x–z plane and so we divide the whole space into two-dimensional cells of $\Delta \times \Delta$ squares. The positions of the particles are measured at the beginning of each cycle ($\theta = 0°$) which corresponds to when the granular bed sits on the base of the cell and the vibrating vessel moves upwards with maximum velocity $\dot{z}_c = A\omega$. The recording times occur at times $t = nT$, where n is an integer and T is the period of vibration. At the end of each cycle of vibration the distance that each particle has moved over the course of that cycle is calculated. We then attribute half of the displacement of each particle to the cell that the particle has come from and half to the cell that the particle currently resides in. If, after one vibration, the particle has remained in the same cell, then all the displacement is attributed to that cell. The convective motion may be averaged over many cycles to give the average convective behaviour of the system. We define the displacement convective field, **J**, as

$$\langle \mathbf{J}(X,Y) \rangle = \left\langle \frac{1}{2} \sum_i \left[\left(\delta_i(X,Y;t) + \delta_i(X,Y;t-T) \right) \left(\mathbf{r}_i(t) - \mathbf{r}_i(t-T) \right) \right] \right\rangle_t , \tag{4.1}$$

where $\mathbf{r}_i$ is the position of the particle i and $\delta_i(X,Y;t) = 1$ when particle i resides in the cell with integer labels X and Y at time t. This means that cell (X,Y) spans the space $X\Delta < x < (X+1)\Delta$ and $Y\Delta < y < (Y+1)\Delta$, where x and y are the horizontal and vertical coordinates respectively.

An overall measure of the convection may be determined by summing the

displacement field over all cells. Thus:

$$J = \left(\sum_{X,Y} |\mathbf{J}(X,Y)|^2 \right)^{\frac{1}{2}}. \tag{4.2}$$

4.3 Simple Drag System

We begin our studies by simulating 2500 spherical bronze particles immersed in water in a vibrating sealed cell using the SD model to couple the fluid and grain motion. Our aim is to see whether convection occurs within a fluid-immersed granular bed when using a model in which the fluid is homogeneous and is not affected by the presence of particles.

The grains are immersed in water with density $\rho = 1000$ kg m^{-3} and viscosity $\eta = 1{\times}10^{-3}$ kg m^{-1} s^{-1}. The fluid drag force, $\mathbf{F}_{Drag}$, experienced by the grains takes the form:

$$\mathbf{F}_{Drag} = \frac{V_p(-\nabla P)}{1-\phi}, \tag{4.3}$$

where V_p is the volume of the particle and ϕ is the bed porosity. Since we are dealing with a densely packed granular bed we can determine the pressure gradient across the bed, $-\nabla P$, using Ergun's empirical bed equation (Ergun 1952) (See section 2.4.4):

$$-\nabla P = \left[\frac{150\eta(1-\phi)^2}{d^2\phi^3} + \frac{1.75\rho(1-\phi)|\mathbf{V}_0|}{d\phi^3} \right] \mathbf{V}_0. \tag{4.4}$$

Here d is the average particle diameter and $\mathbf{V}_o$ is the superficial velocity with respect to the container. The porosity across the bed is given a constant value of $\phi = 0.42$ corresponding to the grains being randomly packed.

The bronze particles have densities $\rho_g = 8900$ kg m^{-3} and diameters 700 μm with a 10% dispersion in size to avoid crystallisation in the presence of cell oscillations, the equation of motion of a particle of density ρ_g and mass $m = \rho_g V_p$ in the SD model becomes

$$m\ddot{\mathbf{r}} = \mathbf{F}_{Collision} + \mathbf{F}_{Drag} + V_p(\rho - \rho_g)\mathbf{g}', \tag{4.5}$$

where $\mathbf{r}$ is the particle position in the frame of reference of the moving cell and $\mathbf{g}'$ is the modified gravity. $\mathbf{g}'$ is applied in the vertical direction (z–axis) and is

Parameter	*Value*
Number of particles	2500
Particle density ρ_g	8900 kg m^{-3}
Particle diameter d	700 μm
K	1500 kg s^{-2}
e	0.2
μ	0.2
μ_W	0.0–1.0
Fluid density ρ	1000 kg m^{-3}
Dynamic viscosity η	10^{-3} kg m^{-1} s^{-1}
Time-step Δt	10^{-5} s
Cell size (x–axis)	20 mm
Cell size (y–axis)	5 mm
Cell size (z–axis)	20 mm
f	10–30 Hz
Γ	3.0

Table 4.1: Parameters for tilting simulations using the Simple Drag model.

the sum of gravity, $\mathbf{g}$, and the acceleration of the system, $\mathbf{a}(t)$, such that:

$$\mathbf{g}' = \mathbf{g} - \mathbf{a}(t)\,. \tag{4.6}$$

The model is described in greater detail in section 2.4.1.

In the simulation the particles are initially placed randomly within the box in such a way as to ensure that none of the particles are overlapping. The box is held stationary and the particles are allowed to settle under the influence of gravity onto the cell base. Both box vibration and the coupling force between the fluid and grains are then initiated. We fix the dimensionless acceleration constant to $\Gamma = 3.0$ and vary the wall friction coefficient μ_W in the range 0.0–1.0 for three different frequencies of f = 10, 20 and 30 Hz. As $\Gamma > 1$ the granular bed is thrown and lands during each vibration cycle. The simulation parameters for this system are summarised in Table 4.1.

Figure 4.1 shows snapshots of the time evolution of the granular bed vibrated

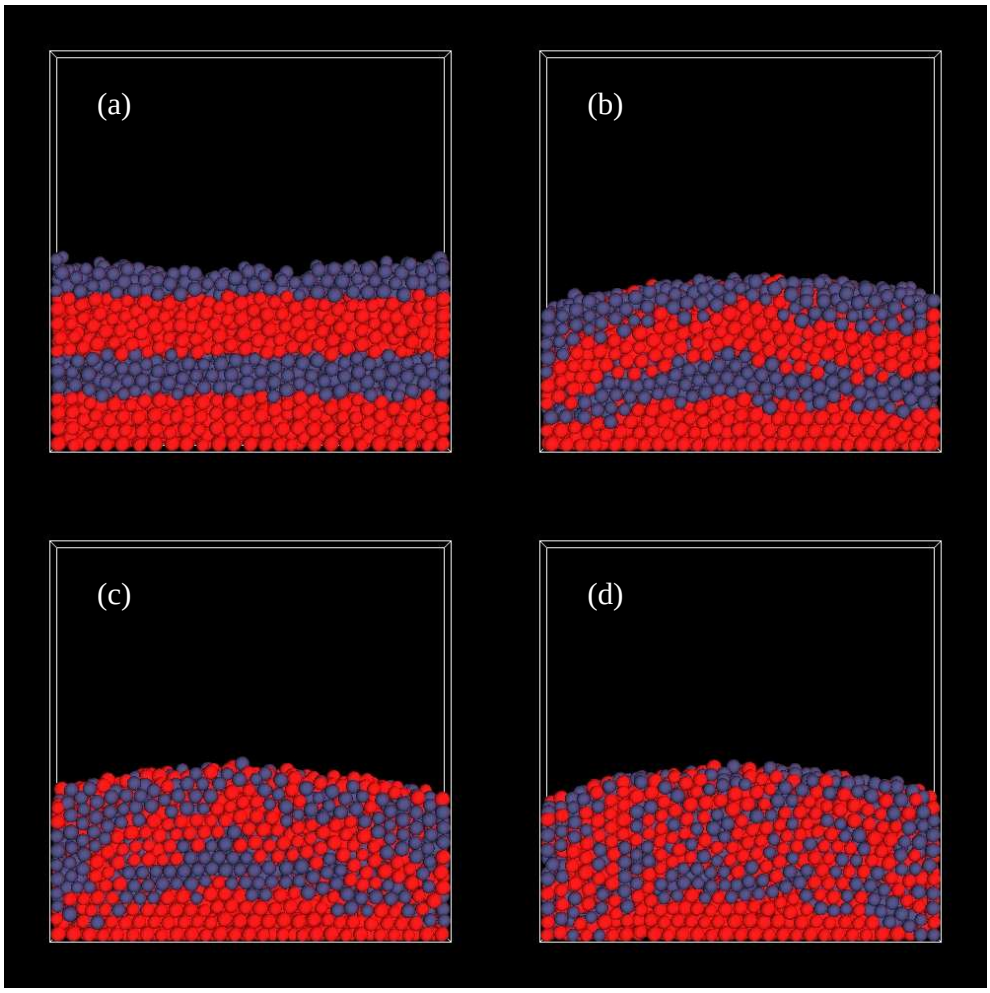

Fig. 4.1: Evolution of 2500 water-immersed bronze particles shaken with vibration parameters $f = 10$ Hz and $\Gamma = 3.0$ with a wall friction parameter of $\mu_W = 1.0$. Snapshots are taken at (a) $t = 0$ s, (b) $t = 10$ s, (c) $t = 40$ s and (d) $t = 150$ s. Fluid and grain interactions are modelled using the Simple Drag model. The grains are coloured for visual purposes only.

with parameters $f = 10$ Hz and $\Gamma = 3.0$ for a wall friction value of $\mu_W = 1.0$. All of the images are displayed in the x–z plane as this is where the majority of the convection occurs. In the y–z plane the particles move in a random manner so that there is no noticeable convection. The bronze particles have been coloured in layers as a visual aid so that the behaviour of the bed may be monitored. Figure 4.1(a) shows that the granular bed surface is initially level. However, as the simulation proceeds a domed surface soon develops in the middle of the box, as seen after $t = 10$ s in Figure 4.1(b). The grains from within the bulk of the pile then begin to break through the bed surface while the top layer of grains

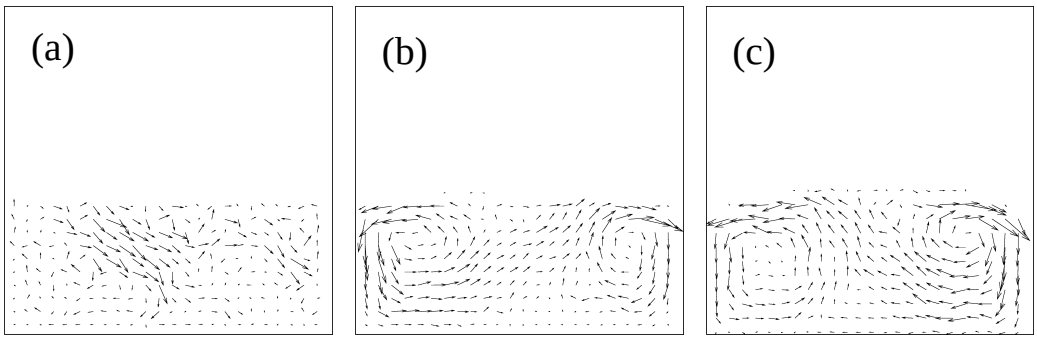

Fig. 4.2: Convection flow diagrams for a walled system without a microscopic fluid model. Fluid and grain motion is coupled using the Simple Drag model. From left to right the diagrams correspond to wall friction coefficients of (a) $\mu_W = 0.0$, (b) $\mu_W = 0.6$ and (c) $\mu_W = 1.0$ vibrated at $f = 10$ Hz and $\Gamma = 3.0$. Within each plot the arrows show the distance and direction that the grains would move in (a) 80 s, (b) 25 s and (c) 20 s. As a reference of scale the length of the cell wall is 20 mm.

cascade down the heap slopes towards the container walls. Figure 4.1(c) shows that at $t = 40$ s the grains that have previously avalanched down the bed slope now move downwards parallel to the side walls. After 150 s the bulk of grains in the bed have been mixed, apart from a small region of grains in the bottom centre of the box which remains largely untouched.

The size and shape of the pile is sustained by two convective cycles which rotate in opposite directions to each other. Within both convective cycles, grains on the top surface initially avalanche down the domed surface and then continue downwards once they have reached the side walls. From the bottom edges of the cell the grains move inwards. The cycle is completed as grains move upwards through the bulk of the bed and emerge through the domed surface.

The convection cycles can be seen more clearly in Figure 4.2 for wall friction values of $\mu_W = 0.0$, 0.6 and 1.0 and vibration parameters $f = 10$ Hz and $\Gamma = 3.0$. The figure shows the average granular displacement field over the course of a vibration cycle **J**. The data is obtained after $t = 20$ s once the convective motion is established within the bulk of the bed. Only the granular motion is shown as the SD model does not capture hydrodynamic fluid flow.

Figure 4.2 shows that as μ_W is increased, the granular convective flow increases also. In Figure 4.2(a) when $\mu_W = 0.0$ the grains move very little. This state may

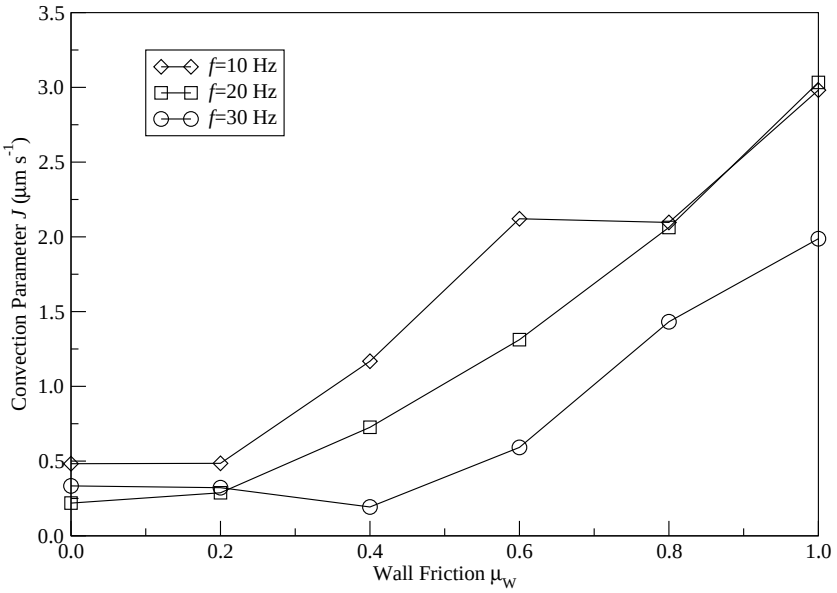

Fig. 4.3: The variation of the convection parameter J with the wall friction μ_W when using the Simple Drag model to couple the fluid and grain interactions. The symbols correspond to frequencies of $f = 10$ Hz (diamonds), $f = 20$ Hz (squares) and $f = 30$ Hz (circles). The solid lines connecting the data points are for visual purposes only. All results were obtained for $\Gamma = 3.0$.

be regarded as a control and illustrates how densely packed particles vibrated in a frictionless cell may move randomly. In Figure 4.2(b) the wall friction is increased to $\mu_W = 0.6$ and we see that the grains have organised themselves into two convective cells which both move upwards through the centre of the heap and downwards at the box edges. In Figure 4.2(c) the wall friction is increased to $\mu_W = 1.0$ and the convective pattern and granular flow strengthens further. In Figure 4.2 we notice that the least granular motion is in the bottom centre of the box.

As μ_W is increased for fixed f and Γ the granular convection increases and the domed surface becomes more pronounced. This is illustrated further in Figure 4.3 which plots the convection parameter J calculated using equation 4.2 against μ_W for frequencies $f = 10$, 20 and 30 Hz. Here all convection data was collected and averaged for 30 s of real time. The points are joined up for visual purposes only.

Figure 4.3 shows how J varies with wall friction μ_W and frequency f when the fluid and grains are coupled using the the SD model. As μ_W increases the convec-

tion parameter J increases for all our frequency curves. In the range $\mu_W = 0.0$–0.2 convection J remains approximately constant for all the frequency curves; however, above $\mu_W = 0.2$ the convection increases almost linearly. The presence of wall friction is, therefore, the major driving factor of convection within the SD model simulations. Secondly, we notice that as the frequency f increases the convection decreases. This is because at lower frequencies a greater amount of energy is input into the bed. The convection process arises because the particles experience differential drag dependent on their positions within the bed and hence they follow different paths. We find that those particles nearest the walls experience increased drag due to wall friction and are therefore not thrown as high. The particles nearest the walls are forced downwards and underneath the thrown bed so that convection cycles are created, a process which is often referred to as wall-driven convection (Zeilstra *et al.* 2008). Without wall friction there is only granular motion due to random granular interactions.

4.4 Microscopic Fluid Models

We now wish to perform similar simulations for two of the microscopic fluid models described previously in Section 2.1: the Navier–Stokes model and the Fluid Springs model. The results obtained with these models are compared with each other and against those obtained using the SD model in the previous section.

The simulation parameters used in the NS and FS model simulations are shown in Tables 4.2 and 4.3. The fluid and grain motion within the NS model simulations are coupled using the empirical bed equation developed by Ergun (1952) and shown in equation 4.4. The simulations are set up and initiated in exactly the same way as they were for the SD model in the previous section. Here the grains are allowed to settle solely under the influence of gravity until they rest on the base of the cell. Once the grains are at rest, the cell vibrations and the fluid-grain coupling are turned on.

Figures 4.4 and 4.5 are made up of a series of snapshots illustrating the evolution of the NS and FS model simulations respectively using vibrational parameters $f = 10$ Hz and $\Gamma = 2.0$. Both figures show that the granular beds within

Parameter	*Value*
Number of particles	2500
Particle density ρ_g	8900 kg m^{-3}
Particle diameter d	700 μm
Spring constant K	1500 kg s^{-2}
e	0.2
μ, μ_W	0.2
Fluid density ρ	1000 kg m^{-3}
Dynamic viscosity η	1×10^{-3} kg m^{-1} s^{-1}
Lattice spacing Δ	1.66×10^{-3} m
Time-step Δt	10^{-5} s
Cell size (x–axis)	20 mm
Cell size (y–axis)	5 mm
Cell size (z–axis)	20 mm
f	10–30 Hz
Γ	1.5–4.0

Table 4.2: Parameters for tilting simulation using the Navier–Stokes model.

Parameter	*Value*
Number of particles	2500
Particle density ρ_g	8900 kg m^{-3}
Particle diameter d	700 μm
Spring constant K	1500 kg s^{-2}
e	0.2
μ, μ_W	0.2
Fluid density ρ	1000 kg m^{-3}
Dynamic viscosity η	1×10^{-3} kg m^{-1} s^{-1}
Lattice spacing Δ	116.7×10^{-6} m
n_r	3
C_s	1.5
Time-step Δt	10^{-4} s
Cell size (x–axis)	20 mm
Cell size (y–axis)	5 mm
Cell size (z–axis)	20 mm
f	10–30 Hz
Γ	1.5–4.0

Table 4.3: Parameters for tilting simulation using the Fluid Springs model.

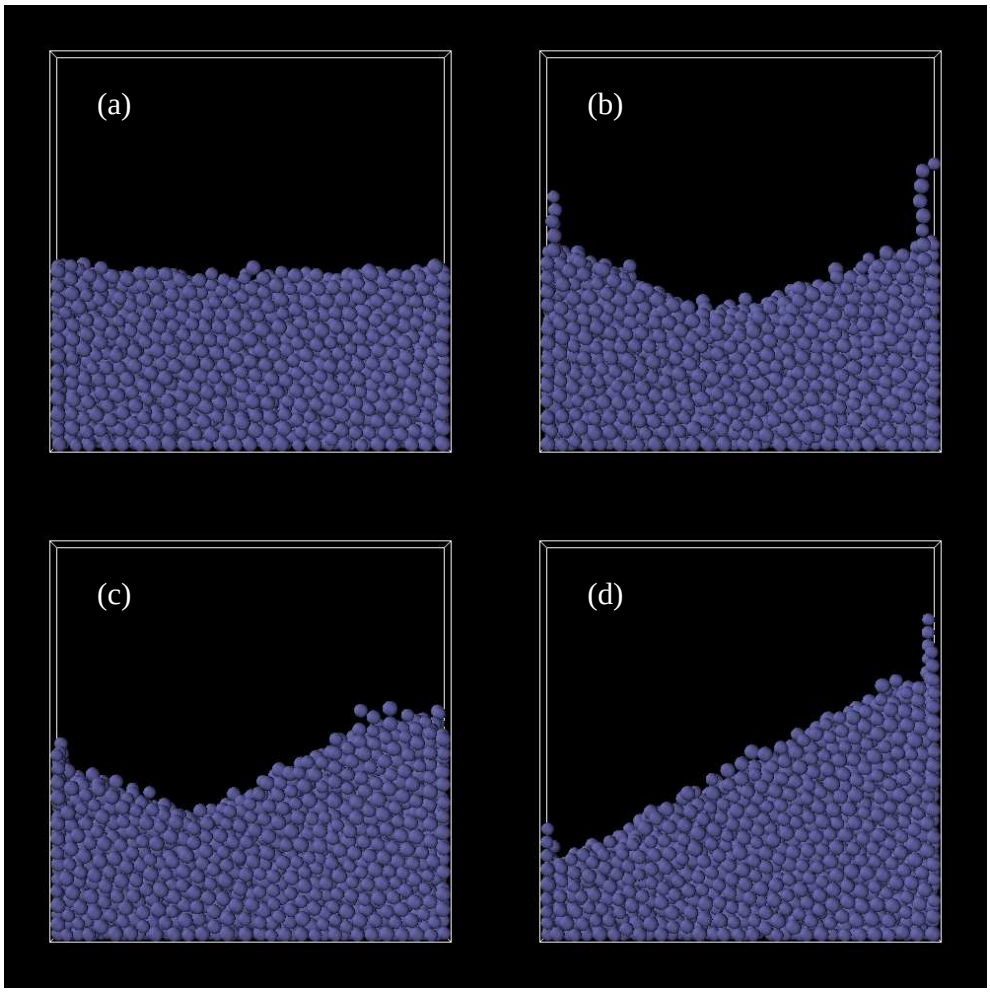

Fig. 4.4: Evolution of 2500 water-immersed bronze particles shaken with vibration parameters $f = 10$ Hz and $\Gamma = 2.0$. Snapshots are taken at (a) $t = 0$ s, (b) $t = 3$ s, (c) $t = 6$ s and (d) $t = 11$ s. Fluid and grain interactions are modelled using the Navier–Stokes model.

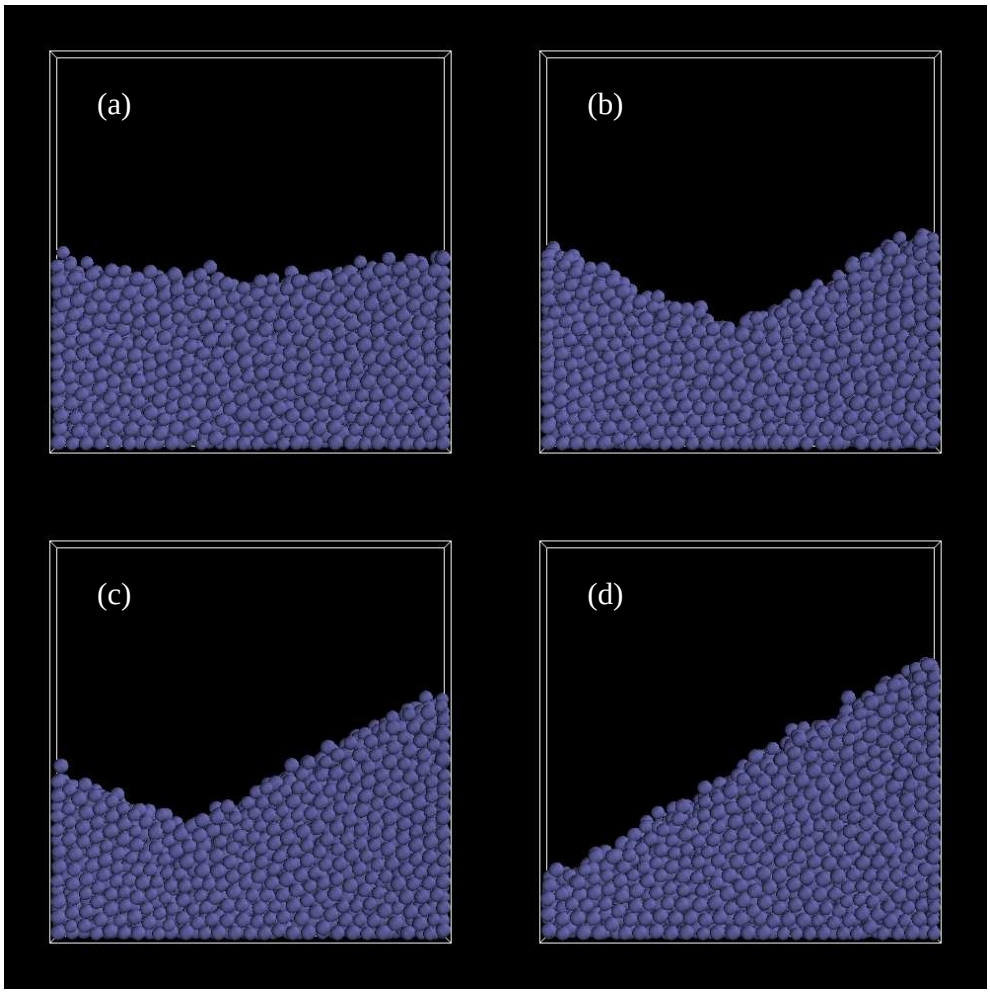

Fig. 4.5: Evolution of 2500 water-immersed bronze particles shaken with vibration parameters $f = 10$ Hz and $\Gamma = 2.0$. Snapshots are taken at (a) $t = 0$ s, (b) $t = 3$ s, (c) $t = 6$ s and (d) $t = 11$ s. Fluid and grain interactions are modelled using the Fluid Springs model.

each simulation ultimately form a tilt which spans the entire width of the container. These "Faraday tilts" prove to be very stable and once formed remain in these configurations for the duration of timescales available to our computer simulations.

Figure 4.4 shows how the tilt develops when the fluid and grain coupling is modelled using the NS model. Figure 4.4(a) shows the initial system configuration at $t = 0$ s. Here the granular bed begins level. Once the system has started vibrating the grains begin to build up at the box edges. Hence two tilts develop which both slope downwards from the cell walls towards the middle of the box as observed in Figure 4.4(b). As the NS model simulations progress any slight size inequalities between the two piles at the cell edges leads to one of the piles growing and the other reducing in size. The configuration is observed in Figure 4.4(c) where grains begin to congregate nearest the right wall. The transferring of grains from the smaller tilt to the larger tilt continues so that eventually one of the piles becomes so large that it spans the entire width of the box. We observe this after $t = 11$ s in Figure 4.4(d). We also notice that short columns of particles a single grain in width form near both walls. This is an artefact of the low fluid resolution and no-slip boundary conditions being insufficient to force particles in this orientation apart.

Similar behaviour is observed when using the FS model in Figure 4.5. Here the snapshots are taken at the same moments in real time as those from the NS model (Figure 4.4). Again, two piles develop and compete for space within the cell. Eventually one pile dominates and that ends up spanning the entire width of the container.

The diagrams within Figures 4.4 and 4.5 are very similar despite being produced by two models with very different fluid resolutions and fluid-grain coupling methods. The main difference we find in the figures is that there are no single particle columns near the walls within the FS model.

The results obtained with the NS and FS models are in stark contrast to those obtained when the SD model is used to couple the fluid and grain motion. When using the SD model friction-driven convection leads to the grains forming a domed surface in the box centre which slopes downwards towards the cell edges

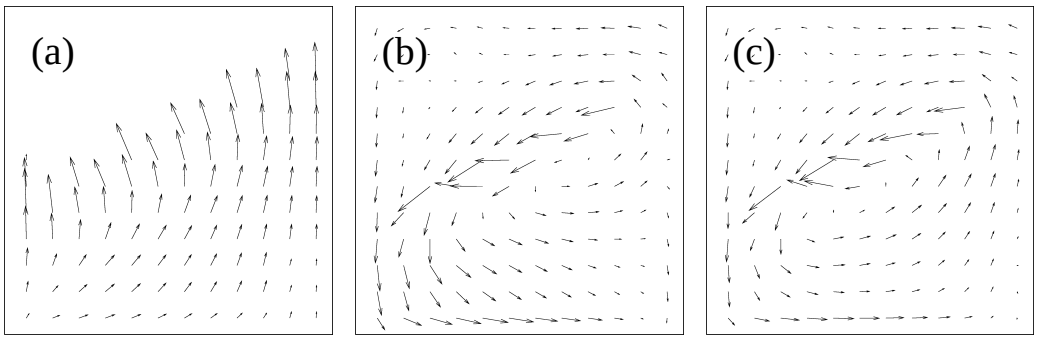

Fig. 4.6: Flow diagrams for 2500 water-immersed bronze particles shaken with vibration parameters of $f = 10$ Hz and $\Gamma = 2.0$. Plots show the (a) grain motion, (b) fluid motion and (c) combined granular and fluid motion for the Navier–Stokes model simulations in the frame of reference of the vibrating cell. The cycle phase is $\theta = 135°$ and the arrows show the distance the grains or fluid would move in 0.02 s. As a reference of scale the length of the cell is 20 mm.

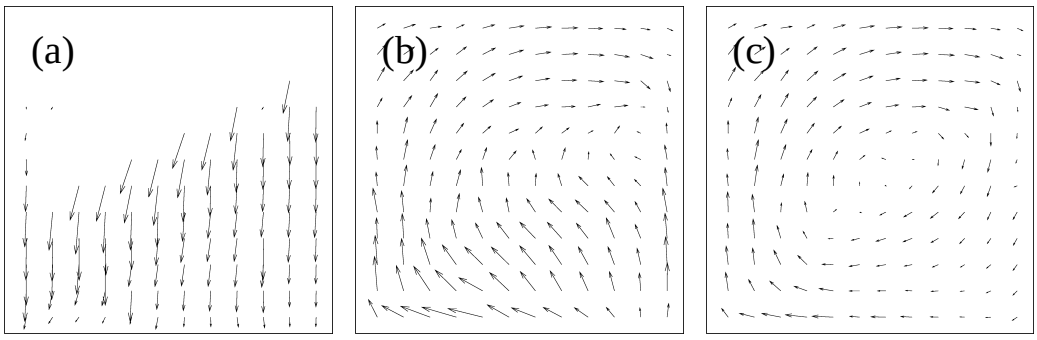

Fig. 4.7: Flow diagrams for 2500 water-immersed bronze particles shaken with vibration parameters of $f = 10$ Hz and $\Gamma = 2.0$. Plots show the (a) grain motion, (b) fluid motion and (c) combined granular and fluid motion for the Navier–Stokes model simulations in the frame of reference of the vibrating cell. The cycle phase is $\theta = 225°$ and the arrows show the distance the grains or fluid would move in 0.02 s. As a reference of scale the length of the cell is 20 mm.

(Figure 4.1). In the NS and FS models there is substantially more grain motion and instead the particles form tilts which span the width of the cell, as in Figures 4.4 and 4.5.

Figures 4.6, 4.7, 4.8 and 4.9 show vector plots of the granular flow, fluid flow and combined granular and fluid motion once the tilt has been fully established for the NS and FS models at two stages within the vibration cycle. Figure 4.6

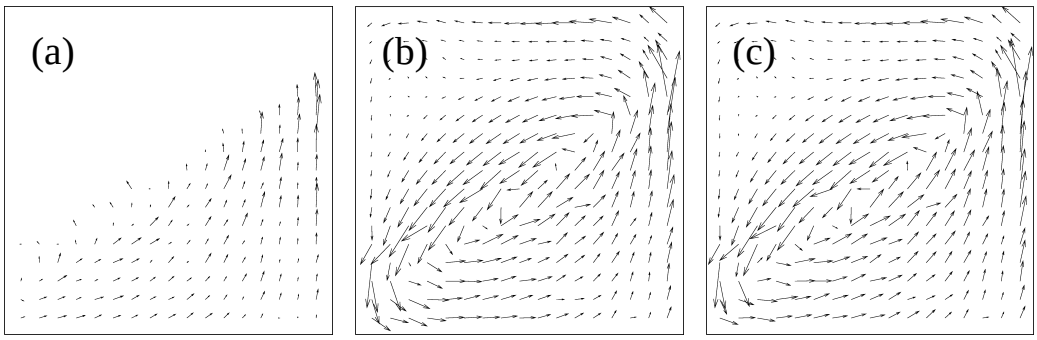

Fig. 4.8: Flow diagrams for 2500 water-immersed bronze particles shaken with vibration parameters of $f = 10$ Hz and $\Gamma = 2.0$. Plots show the (a) grain motion, (b) fluid motion and (c) combined granular and fluid motion for the Fluid Springs model simulations in the frame of reference of the vibrating cell. The cycle phase is $\theta = 135°$ and the arrows show the distance the grains or fluid would move in 0.02 s. As a reference of scale the length of the cell is 20 mm.

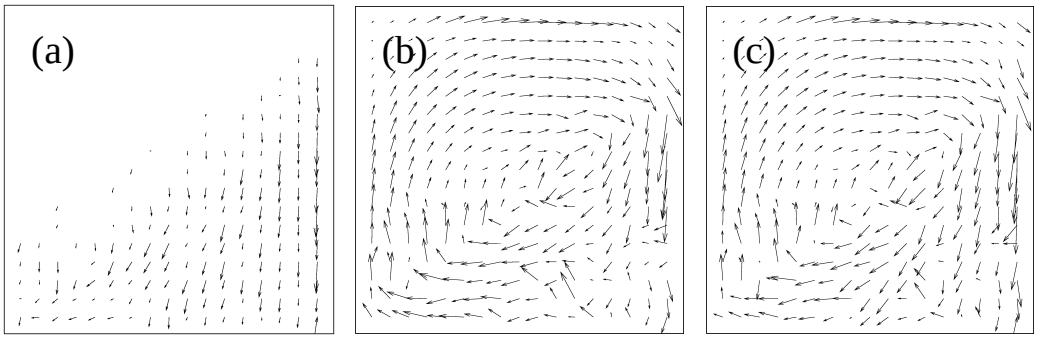

Fig. 4.9: Flow diagrams for 2500 water-immersed bronze particles shaken with vibration parameters of $f = 10$ Hz and $\Gamma = 2.0$. Plots show the (a) grain motion, (b) fluid motion and (c) combined granular and fluid motion for the Fluid Springs model simulations in the frame of reference of the vibrating cell. The cycle phase is $\theta = 225°$ and the arrows show the distance the grains or fluid would move in 0.02 s. As a reference of scale the length of the cell is 20 mm.

shows the flow within the cell at a phase angle of $\theta = 135°$, corresponding to the point in the cycle when the grains are thrown and are moving upwards relative to the container. Figure 4.7 shows the flow at $\theta = 225°$, when the grains are are moving downwards relative to the container. Both of these figures have been produced using the NS model. From left to right the figures show the granular flow, the fluid flow and the combined granular and fluid flow. All the data has

		Granular (mm s^{-1})	Fluid (mm s^{-1})	Combined (mm s^{-1})
$\theta = 135°$	NS	49.8	44.0	34.6
	FS	18.8	42.1	42.5
$\theta = 225°$	NS	84.4	62.8	25.4
	FS	35.9	51.3	49.7

Table 4.4: Typical speeds of the grains, fluid and combined granular and fluid flow at a position of $x = 10$ mm and $y = 5$ mm in the bed. The flows are obtained using the Navier–Stokes and Fluid Springs model simulations.

been averaged over one second of real time. To obtain the combined granular and fluid flow we perform a weighted sum of fluid velocities, $\mathbf{v}$, and the grain velocity data $\mathbf{u}$ at each fluid grid-point using the formula:

$$\mathbf{w} = \phi\mathbf{v} + (1 - \phi)\mathbf{u}, \tag{4.7}$$

where $\mathbf{w}$ is the combined grain and fluid velocity and ϕ is the fluid porosity.

Similarly figures 4.8 and 4.9 show the flow vector fields for the FS model at phase angles of $\theta = 135°$ and $\theta = 225°$ respectively. To obtain the three flow vector fields we use a different process to that used to obtain the NS model flows. This is because within the FS model the "fluid" flow contains information about both the grains and fluid as wherever the particles overlap the lattice grid the fluid and grain velocities converge. This is explained in detail in Section 2.5.2. To obtain the grain velocities we search the fluid lattice in our simulations to determine whether a grid point is occupied by a particle. When averaged one obtains the granular flow vector field and, from the unoccupied lattice sites the fluid flow vector field is obtained.

To compare the two models we also measure typical speeds within the grain and fluid phases from each set of simulations. The measurements are taken half way along the base and a quarter of the way up the cell so that the speeds are determined within the bed at approximate coordinates of $x = 10$ mm and $y = 5$ mm. The results are shown in table 4.4.

Figures 4.6, 4.7, 4.8 and 4.9 show that there is good agreement between the NS and FS models in both the thrown and landing phases of the cycle with

only slight differences in some of the flow directions. Table 4.4 shows that the granular flow in the NS model is approximately 2.5 times greater than those in the FS model, while the fluid and combined flows are comparable.

We believe that these slight differences in the flow could arise because the NS model essentially models the granular bed as a porous plug. Therefore as the granular bed is thrown fluid passes through the grains to fill the void beneath. Whereas, in the FS model the particle motion is imposed onto the fluid lattice. This means that on the lattice sites not occupied by particles the fluid moves in a similar direction to the particles.

Therefore convection is observed within both the NS and FS models. As another test we use the models to measure the pressure underneath the bed during the cycle.

Pressure Curves

Figures 4.10 and 4.11 plot the pressure drop ΔP across the bed at the bottom of the cell against the phase angle θ. The pressure drop data is recorded once the tilt is fully established and spans the entire box. The various curves correspond to different positions along the cell base and are labelled as percentages of the total cell width. The pressure curves are measured beginning on the side of the box with the lowest bed height. The data is averaged over 100 vibration cycles.

In both Figures 4.10 and 4.11 the pressure drop across the bed, ΔP, is equal to 0 Pa until the bed is thrown from the cell base. At this point an underpressure, $\Delta P < 0$ Pa, develops as fluid is forced to flow through the bed to fill the gap below. Later in the cycle as the bed falls, an overpressure, $\Delta P > 0$ Pa, develops as fluid passes upwards through the bed. This becomes stronger and peaks as the bed lands, after which there is a sharp reduction in the pressure until $\Delta P = 0$ Pa is reached at the end of the vibration cycle. The different curves in Figures 4.10 and 4.11 show that, when moving along the base towards where the bed depth is greatest, both the underpressure in the early part and the overpressure in the later part of the cycle are greater than for the shallower part of the tilting bed. Therefore we see that a pressure gradient develops along the cell base.

This pressure gradient may be predicted from Kroll's model (1954) which

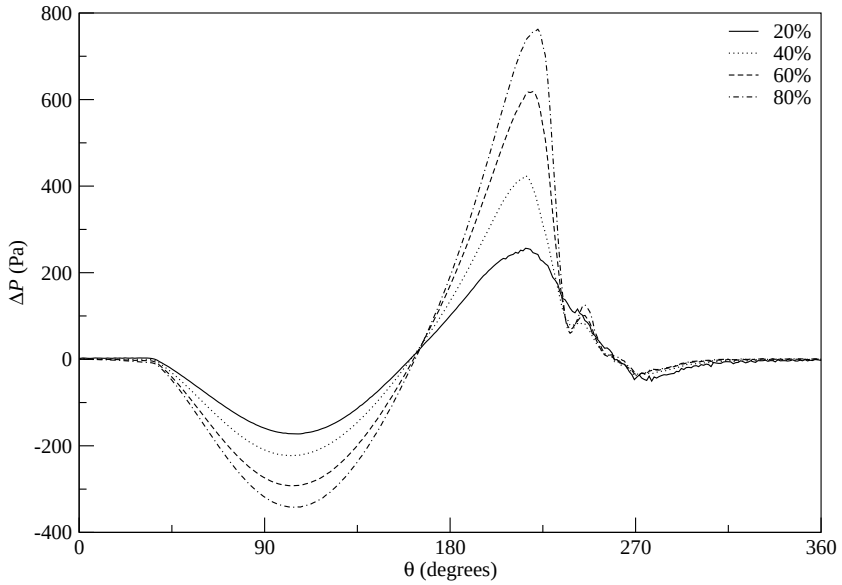

Fig. 4.10: ΔP as a function of phase angle θ for vibration parameters of $f = 10$ Hz and $\Gamma = 2.0$. The curves correspond to pressure measurements taken at different points along the base (measured from the edge with lowest bed depth), i.e. 20% along the base (solid-line), 40% (dotted-line), 60% (dashed-line) and 80% (dot-dash-line). The fluid and grains were coupled using the Navier–Stokes model.

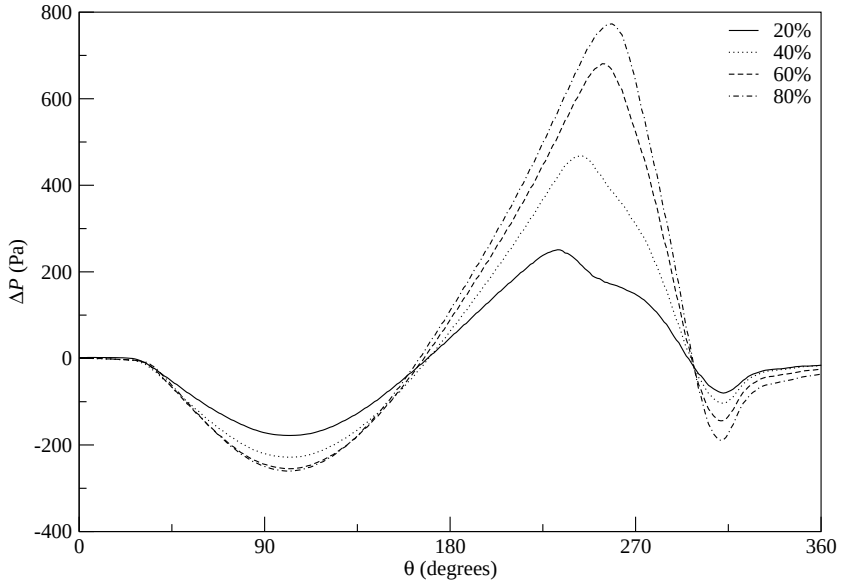

Fig. 4.11: ΔP as a function of phase angle θ for vibration parameters of $f = 10$ Hz and $\Gamma = 2.0$. The curves correspond to pressure measurements taken at different points along the base (measured from the edge with lowest bed depth), i.e. 20% along the base (solid-line), 40% (dotted-line), 60% (dashed-line) and 80% (dot-dash-line). The fluid and grains were coupled using the Fluid Springs model.

states that the pressure drop is proportional to the height of the bed and the fluid velocity

$$\Delta P = Khv. \tag{4.8}$$

The pressure gradient drives the fluid towards the deeper part of the bed early in the vibration cycle and then towards the shallow part of the bed in the later part. The fluid flow accelerates grains so that particles move towards the deeper part of the bed in the early part of the cycle and then later when the flow reverses the particles decelerate. Therefore the pressure gradient along the base drives the convection and tilt creation. As soon as the bed surface is uneven fluid passes through the bed region with least resistance, i.e. the shallower sections, and then moves beneath the bed towards the region with greatest depth dragging grains with it. The convective motion is self-enforcing because as the tilt becomes larger the preferential paths through the shallower regions strengthen.

When comparing the pressure drop data in Figures 4.10 and 4.11, obtained using the NS and FS models respectively, we observe that all of the corresponding curves between the figures share approximately the same peak in the overpressures. However, the lowest underpressures are only shared for the shallower parts of the bed (20% and 40%) but not for deeper parts of the bed (60% and 80%) where the NS model peaks are up to 50% greater than the FS model peaks. We also notice that the shape of the curves are slightly different, with the FS model curves peaking at a slightly later phase angle and then returning to zero slower than in the NS model simulations. There is also a greater underpressure when the bed lands within the FS model simulations.

We note that when the Modified Kroll (MK) model (described in section 2.3.1) is used to determine the base pressure of the same system the peak overpressure is $\Delta P = 912$ Pa while the lowest underpressure is $\Delta P = -353$ Pa. To calculate these pressure peaks the average height of the bed, $h = 8.74$ mm, and average bed porosity, $\phi = 0.45$, were used. By studying the pressure curves in Figures 4.10 and 4.11 we see that the pressure peaks produced with the MK model are greater than all of those produced by the NS and FS models. This suggests that the fluid convection dramatically reduces the peak pressures produced within tilted beds. The enhanced fluid flow through the shallower sections of the bed during

bed motion substantially reduces the scale of the pressure drops across the deeper parts of the bed.

Convection Parameter

We now study the effect of varying the vibrational parameters on the convection parameter J for the NS and FS model respectively. Figures 4.12 and 4.13 plot the convection parameter J against Γ for frequencies of $f = 10$, 20 and 30 Hz. The convection parameter is plotted on a logarithmic scale as the convection varies over a large range. The results obtained by the two microscopic fluid models are very similar. Both models illustrate that for fixed f as Γ increases convection increases also (moving along the curves in Figures 4.12 and 4.13). Additionally the figures show that if Γ is fixed and the frequency is increased J is reduced (moving between the curves in Figures 4.12 and 4.13). Comparing these results to those obtained with the SD model in Figure 4.3 we observe that convection is approximately 400–2000 times greater when using a microscopic fluid model.

4.4.1 Wall Friction

In this section the microscopic fluid models have shown that convection is greatly influenced by the presence of a hydrostatic fluid as illustrated by comparing Figures 4.12 and 4.13 to Figure 4.3. We have also found that convection is strengthened if either Γ increases or f decreases. In Section 4.3 the same system was simulated using the SD model and it was found that wall friction, μ_W, greatly affected the total convection J. Figure 4.3 showed that as $\mu_W \to 0$ convection is substantially reduced until eventually the only grain motion is through random inter-grain interactions. We now perform similar tests using the microscopic fluid models to see what affect varying the wall friction has on fluid convection J.

Figures 4.14 and 4.15 plot the convection parameter J against wall friction μ_W when using the NS and FS models respectively. The cell is shaken with three different vibration frequencies, $f = 10$, 20, and 30 Hz for a vibration amplitude corresponding to $\Gamma = 3.0$. Figure 4.14 shows that for each frequency curve within the NS model simulations the general trend is that J increases slowly as μ_W increases, however, for much of the curves J remains reasonably constant. The

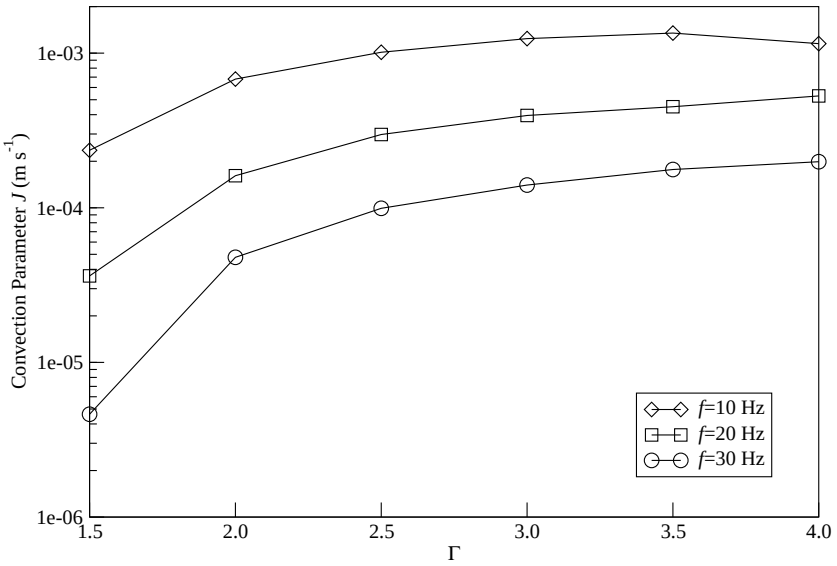

Fig. 4.12: The convection parameter J as a function of Γ when using the Navier–Stokes model to couple the fluid and grain interactions. The different lines correspond to frequencies of $f = 10$ Hz (diamonds), $f = 20$ Hz (squares) and $f = 30$ Hz (circles).

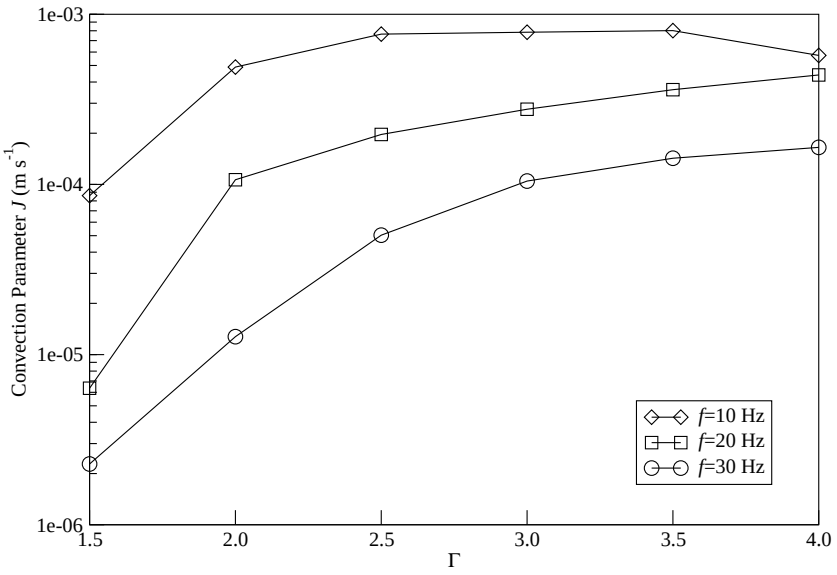

Fig. 4.13: The convection parameter J as a function of Γ when using the Fluid Springs model to couple the fluid and grain interactions. The different lines correspond to frequencies of $f = 10$ Hz (diamonds), $f = 20$ Hz (squares) and $f = 30$ Hz (circles).

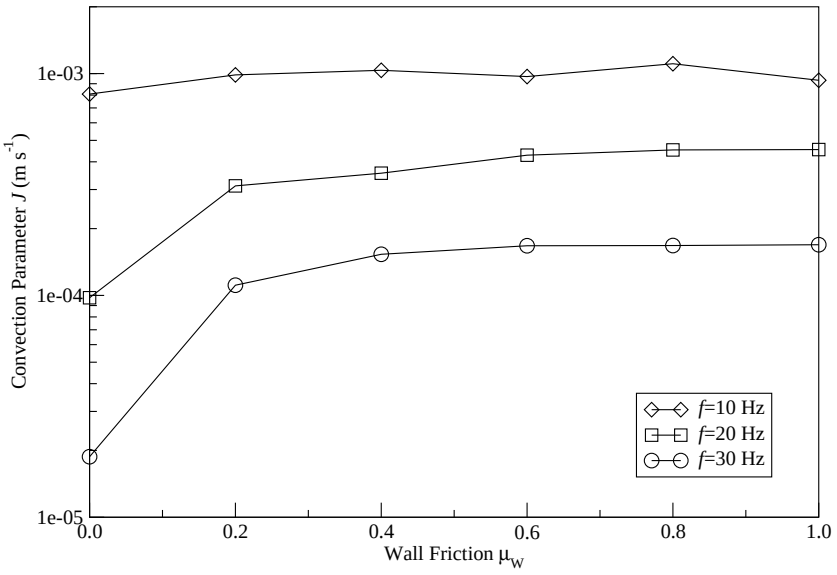

Fig. 4.14: The convection parameter J as a function of the wall friction μ_W when 2500 water-immersed bronze particles are shaken with a vibration amplitude corresponding to $\Gamma = 3.0$. The fluid and grain interactions are coupled using the Navier–Stokes model. The different lines correspond to frequencies of $f = 10$ Hz (diamonds), $f = 20$ Hz (squares) and $f = 30$ Hz (circles).

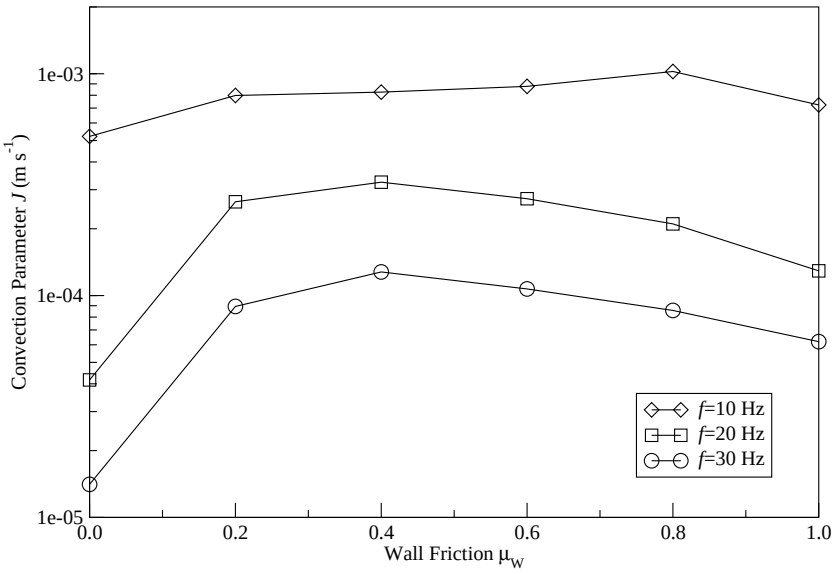

Fig. 4.15: The convection parameter J as a function of the wall friction μ_W when 2500 water-immersed bronze particles are shaken with a vibration amplitude corresponding to $\Gamma = 3.0$. The fluid and grain interactions are coupled using the Fluid Springs model. The different lines correspond to frequencies of $f = 10$ Hz (diamonds), $f = 20$ Hz (squares) and $f = 30$ Hz (circles).

only anomalies are when $\mu_W = 0.0$ for $f = 20$ Hz and 30 Hz where we find the convection is significantly less.

Similar results are obtained to those in Figure 4.14 when using the FS model. In Figure 4.15 we observe that the convection increases as wall friction increases until $\mu_W = 0.4$, at which point J peaks in the $f = 20$ Hz and $f = 30$ Hz curves. After this point J reduces slightly as $\mu_W \to 1.0$. The convection when $f = 10$ Hz is roughly constant as μ_W is increased. Therefore, the $f = 10$ Hz curves are approximately the same in both models, however, the $f = 20$ Hz and 30 Hz curves are slightly different with the convection reducing in the FS model for friction greater than $\mu_W > 0.4$.

Overall Figures 4.3, 4.14 and 4.15 show that the effect of increasing μ_W on the convection is very different when using microscopic fluid models to when the SD model was used. Figure 4.3 showed that when using the SD model as μ_W is reduced towards 0.0 convection decreases and the motion consists primarily of random granular interactions. However, Figures 4.14 and 4.15 show that when using a microscopic fluid model as μ_W is reduced towards 0.0 J reduces but there is still a significant amount of convection. The amount of convection present within the NS and FS models is still several magnitudes stronger than that found in the SD model. Therefore convection is primarily a fluid-driven effect, which is enhanced by the presence of some wall friction.

In the next section we test whether convection is affected by the presence of the walls by simulating a fluid-immersed granular heap on a vibrating surface.

4.4.2 Heaps

In all the systems we have simulated so far the cells have had walls. Here we test whether the convection process is affected by the removal of the walls. We simulate 4000 water-immersed bronze particles within a large vibrating cell, with periodic boundary conditions on the side walls so that any particles which exit through one edge of the box reappear on the opposite edge. Similarly the fluid velocity is periodic in space so that on opposite walls the fluid flow is equal:

$$\mathbf{v}_{[0,y]} = \mathbf{v}_{[L_x,y]} \tag{4.9}$$

and

$$\mathbf{v}_{[x,0]} = \mathbf{v}_{[x,L_y]}. \tag{4.10}$$

Here L_i is the length of the cell along the i–axis. The cell has cross-section $L_x \times L_y = 32.7$ mm$\times$32.7 mm and height $L_z = 9.8$ mm. Compared to the tilting simulations the horizontal cross-section of the container has been extended. This is so that grains are no longer forced to remain in contact with the boundaries. Instead the grains are able to form a heap in the middle of the cell base. The fluid and grain interactions are modelled only with the FS model in this simulation.

Due to the difficulties of simulating large MAC grids, the axis along which gravity and the cell oscillations are applied (z–axis) is reduced. This limits the vibration amplitudes that are possible as a large Γ leads to grains coming into contact with the top surface of the cell during flight. If the pile is thrown with too much energy, the pile is destroyed upon landing. Therefore the box is vibrated with a low vibration amplitude corresponding to $\Gamma = 1.5$. As the simulations are very computer intensive the particles begin as a pile.

Figure 4.16 shows the evolution of the heap. The grains are initially dropped from a lattice configuration into a small cell which sits in the centre of our large cell. The cell is fluid-less and has an area a quarter of the size of the large cell. This initial configuration is shown in Figure 4.16(a). Here the grains are falling into the cell which sits in centre of the box. The walls of the cell are not shown so that we may view the grains.

Once the grains have relaxed the cell walls are removed so that the grains spread out within the large cell. This "invisible" cell enables us to begin the simulation with a granular pile already formed. Once the grains have settled the fluid drag forces and cell oscillations are initiated. Figure 4.16(b) shows that at $t = 0$ s the majority of grains make up the bulk of a pile; however, there are still many particles spread across the cell. As the cell is vibrated the pile increases slightly in height and many of the loose grains are pulled towards the pile. After $t = 10$ s there is a clear heap and only a few grains are not contained within the pile, as shown in Figure 4.16(c). This behaviour is a result of fluid being pulled upwards and then downwards through the bed as the granular pile is thrown. The fluid motion leads to large convective cycles forming within the bed

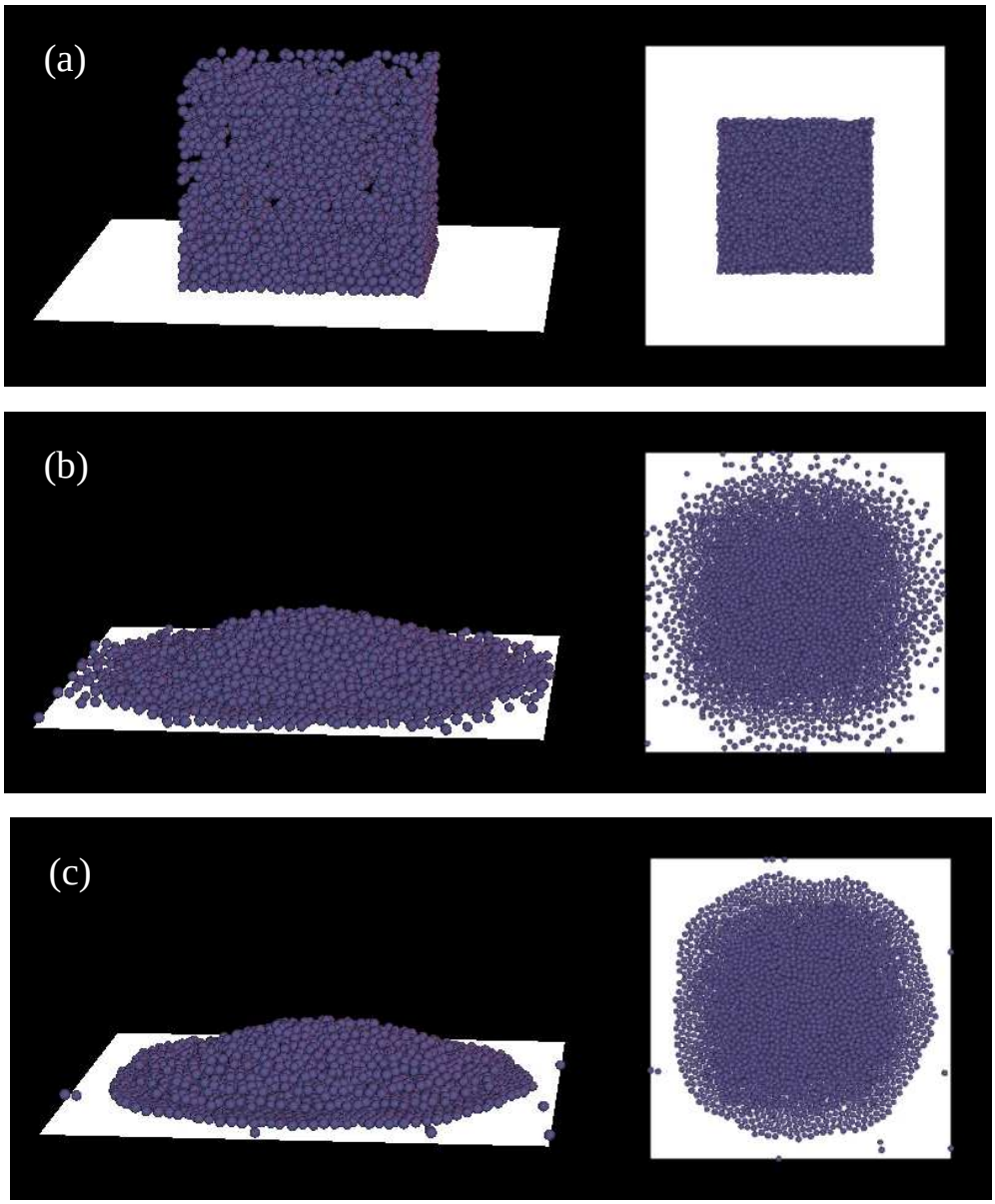

Fig. 4.16: Evolution of 4000 water-immersed bronze spheres of diameter 700 μm shaken sinusoidally with vibration parameters of $f = 10$ Hz and $\Gamma = 1.5$. Only the cell base is shown here for visual purposes and the fluid and grain interactions are modelled using the Fluid Springs model. Figure (a) shows the grains as they initially settle within an imaginary container. Figures (b) and (c) show the granular heap at times $t = 0$ s and $t = 10$ s. The images on the left are a side-view of the cell while the images on the right give a view of the cell from above.

which strengthens the heap shape and height. As the granular heap is thrown upwards there is significant resistance to the fluid passing through the pile to the area beneath. The fluid experiences less resistance if it moves beneath the bed from the heap edges. This motion drags loose grains inwards so that the pile is strengthened and grows in height. As the bed lands the pile spreads out slightly and the loose grains decelerate. After a while all of the grains are contained within the pile and there is a clear heap boundary. These simulations reproduce some of the early heaping phenomena observed by Faraday (1831).

4.5 Summary

We found in our SD model simulations the main driver of convection was wall friction. However, when using a microscopic fluid model such as the NS or FS models a granular tilt develops as a result of the fluid passing through the bed region where it experiences least resistance. We found that "fluid-driven" convection occurred in the NS and FS model simulations regardless of the wall friction μ_W. To check that the presence of walls did not influence convection we simulated a granular pile in a wall-less cell which showed that a pile is maintained and strengthened by the fluid-driven convection. We conclude that "Faraday tilting" is a fluid-driven effect that may be strengthened by the presence of wall friction.

When studying the "Faraday tilting" effect the NS and FS models give similar results and are very comparable. However, for ease of use and speed the NS model is preferred. We note that the FS model was able to capture all of the behaviour of the tilting simulations that the NS model captured despite not using any empirical bed equations to couple the fluid and grain motion. The FS model also did not have any noticeable boundary effects which we saw in the NS model simulations which manifested itself in unrealistic particle columns at the wall edges.

Chapter 5

Partition Instability

Under a wide range of conditions a system of fluid-immersed fine grains within a vibrated partitioned cell will transfer in their entirety into just one of the segments through a linking channel at the cell base. In this chapter we perform a thorough experimental and numerical study of the "partition instability" in order to understand the mechanism for this behaviour. Numerical simulations are first carried out using the Navier–Stokes model which incorporates a bed equation to couple the fluid and grain motion and then later simulations using the Fluid Springs model are undertaken. At the end of the chapter an analytical approach is proposed to model the fluid-driven partition instability based on two coupled granular beds vibrated within an incompressible fluid.

5.1 Introduction

It is commonly observed that a system of grains under vertical vibration exhibits spatial instabilities (van der Weele 2008). In particular grains held in a space which is partitioned into segments linked by connecting holes may move into just one segment, the phenomenon of the "partition instability" (Akiyama and Shinomura 1991; Akiyama and Shinomura 1993; Akiyama *et al.* 2001; Chen and Wei 1998; Eggers 1999; Maeno 1996; van der Meer *et al.* 2002; Ohtsuki *et al.* 1998; van der Weele *et al.* 2001). There are a number of quite distinct physical mechanisms leading to this behaviour.

The inelastic nature of granular materials has been shown to provide a mecha-

nism for the partition instability (Eggers 1999). Within a collection of kinetically active grains, dense regions will experience frequent dissipative collisions and the grains there will lose energy more rapidly than those in less dense regions. The system will spontaneously condense in the more dense regions which become even more dense as they rapidly lose energy. This is the phenomenon of inelastic collapse (Goldhirsch and Zanetti 1993; McNamara and Young 1994). Related behaviour of this type is dramatically displayed by grains held in a vertically vibrated box which is divided by a vertical partition either of finite height or containing a small elevated hole (Eggers 1999; van der Meer *et al.* 2002; van der Weele *et al.* 2001). If there are more grains on one side of the partition, then those grains will experience greater dissipation and be less kinetically active; they will bounce less high than those on the other side of the partition where there are fewer grains. This disparity in kinetic activity may cause a net flow of grains over the partition, or through the hole, from the minority side to the majority side. Under suitable conditions of vibration all of the grains may move to one side of the partition (Eggers 1999; van der Meer *et al.* 2002; van der Weele *et al.* 2001). For an illustration of Eggers' collapse see Figure 5.1. Similar behaviour has also been observed within vibrated granular mixtures. Furthermore, for particular vibratory conditions, this instability may lead to periodic oscillatory motion of the grains from one side to the other (Hou *et al.* 2008; Lambiotte *et al.* 2005; Viridi *et al.* 2006).

In this chapter we study a second mechanism which can give rise to a spatial instability, namely, the interaction between fine grains and a background fluid. This process may be illustrated for a fluid-immersed granular bed within a vertically vibrating partitioned cell with two connecting holes, one at the top and one at the bottom of the cell. Under vibration the granular bed spontaneously moves into just one of the segments via a gradual transfer of grains through the connecting hole at the base of the cell.

Ohtsuki *et al.* (1998) studied one such system consisting of fine grains in air vibrated within a partitioned cell. They observed that the presence of air influences the height difference between the beds on either side of the cell. Chen and Wei (1998) have suggested that this height difference may be due to the air-

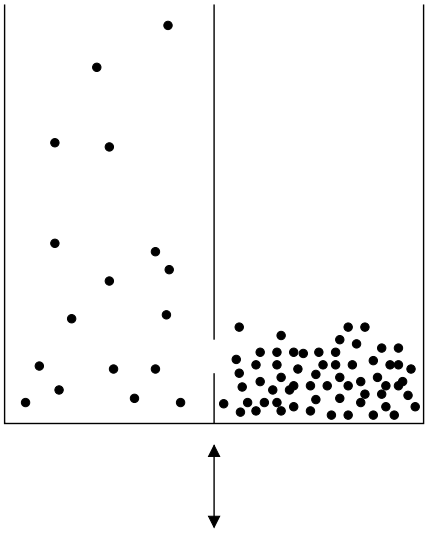

Fig. 5.1: Schematic illustration of inelastic collapse experiments performed by Eggers (1999). Here a vertically vibrated cell is partitioned into two equal sized segments with a small hole connecting the two halves. Grains, represented here as black dots, initially begin equally distributed between the two columns. When vibrated dense regions will experience frequent inelastic collisions and will lose energy more rapidly than less dense regions. As a result the granular temperature within the dense regions reduces and these grains will spontaneously condense. Inelastic collapse follows as the granular temperature of the dense regions reduces so that they become even denser. Depending on where the hole in the partition is situated it is possible for all the grains to eventually occupy just one column.

driven mechanism of Pak *et al.* (1995), used to explain Faraday heaping (1831). Akiyama *et al.* (1991) have carried out a detailed study of the influence of air on the behaviour of vertically vibrated grains in a symmetrically partitioned box. Unfortunately, the granular convection allowed by their wide box dimensions may well have contributed to the complex phenomena which they observed.

Here, we present an experimental and computational study of a water-immersed bed of barium titanate spheres vibrated within a partitioned cell in which the two identical columns are linked by two holes, one at the base and, importantly, a further hole in the partition, positioned well above the grains to allow fluid circulation. The two columns are of restricted horizontal dimensions to reduce the effects of tilting and of convection currents. Over a range of frequencies and amplitudes of vibration we observe that the granular bed spontaneously moves into one of the columns, so that few grains occupy the opposing column.

The use of a fluid such as water offers a number of advantages for investigating partition instabilities. Firstly, water enables larger particles to be used, making the observation of the granular dynamics considerably simpler than for air. For non-turbulent fluid flow, the effects of fluid drag on the granular dynamics scale approximately as $\rho_g d^2/\eta$, where ρ_g is the density of the granular material, d is the grain diameter and η is the dynamic viscosity of the surrounding fluid (Leaper *et al.* 2005). This expression is a measure of the dissipation of fluid velocity and must be matched between different systems to ensure the acceleration affects are similar. At 20^oC, water is about 50 times more viscous than air. This suggests that similar effects may be observed in water for particles $\sim$7 times larger in diameter than for the equivalent behaviour exhibited by fine particles in air.

The increased damping provided by a liquid such as water (Gondret *et al.* 2002) reduces the granular temperature of a thrown bed maintaining the porosity, ϕ, closer to the value appropriate to a random packing of spheres. This makes comparison with the theory which we will develop later more straightforward than would be the case for a fluid such as air. Finally, the use of water eliminates the effects of static electricity which often slow and otherwise modify the dynamics of dry granular systems when they are shaken vigorously for long periods, particularly within an insulating box (Leaper *et al.* 2005).

Our studies begin with observations of the "partition instability" within experiments.

5.2 Experimental Methods

All of our experiments were performed in collaboration with Hector Pacheco-Martinez, who is also studying within Nottingham University's Granular Dynamics Group. To conduct the experiments a water-tight partitioned cell was constructed from PMMA, a cross-section of which is shown schematically in Figure 5.2. The cell is divided into two columns of identical dimensions by a central partition, each column being 90 mm high and 10 mm$\times$10 mm in horizontal cross section. The columns are linked by a gap at the bottom of the central partition, spanning the depth of the cell from front to back. The gap is 4 mm high and 10

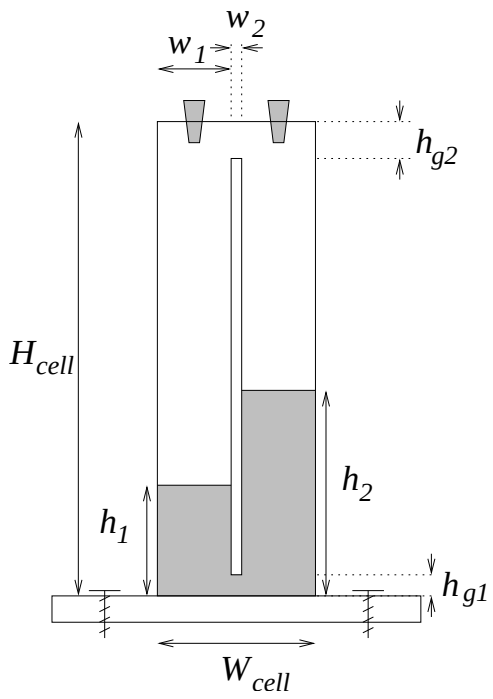

Fig. 5.2: Schematic representation of experimental setup. The partition cell is fixed to a stand which is screwed onto a pair of vibrating loudspeakers. The granular bed is shown as a shaded region within the cell, while the bungs, which ensure that no air bubbles enter the cell, are highlighted at the top of the cell. The values of the cell dimensions highlighted here are given in table 5.1.

mm in depth while the partition is 2 mm thick. A further substantial 7 mm gap spanning the depth of the cell at the top of the partition allows the free flow of fluid between the two columns in a region above the grains.

The experiments have been performed using spherical barium titanate grains of density 4500 kg m^{-3} and diameters spanning the range 600–850 μm to avoid gross crystallisation effects. The grains are inserted into the cell through one of two upper holes. The cell is then filled with water of density 1000 kg m^{-3} and viscosity $\eta = 8.91\times10^{-4}$ kg m^{-1} s^{-1}, which has been pumped prior to experiments to remove dissolved air. The cell is shaken to release any air bubbles trapped within the grains and then refilled and sealed. The total number of grains is such that $h_1 + h_2 = 40$ mm and they are distributed between the two columns so that the beds are given an initial height difference of $h_2 - h_1 = 4$ mm. Here h_i is the height of the granular bed within column i, as shown in Figure 5.2. The experimental parameters are summarised in table 5.1.

During experiments the cell is vibrated sinusoidally with frequency f on a

Parameter	*Value*
Particle density	4500 kg m^{-3}
Particle diameter	600–850 μm
Total bed height $h_1 + h_2$	40 mm
Fluid density ρ	1000 kg m^{-3}
Dynamic viscosity η	8.91×10^{-4} kg m^{-1} s^{-1}
Cell size (x–axis) W_{cell}	22 mm
Cell size (y–axis)	10 mm
Cell size (z–axis) H_{cell}	90 mm
w_1	10 mm
w_2	2 mm
h_{g1}	4 mm
h_{g2}	4 mm
f	15 Hz
Γ	2.25–3.50

Table 5.1: Parameters for experimental partition system.

loudspeaker in a direction $\pm 0.2^o$ off vertical (Leaper *et al.* 2005). The motion is monitored using cantilever capacitance accelerometers which display the dimensionless maximum acceleration Γ. A photograph of the experimental setup illustrating how the partitioned cell is fixed to the speaker is shown in figure 5.3.

Vibration is applied and the height of the granular columns in the right and left segments are studied as a function of the total time of vibration, the heights being measured through the use of a high speed camera. This camera, usually operated at 1000 frames per second, also allows the study of granular motion within each cycle.

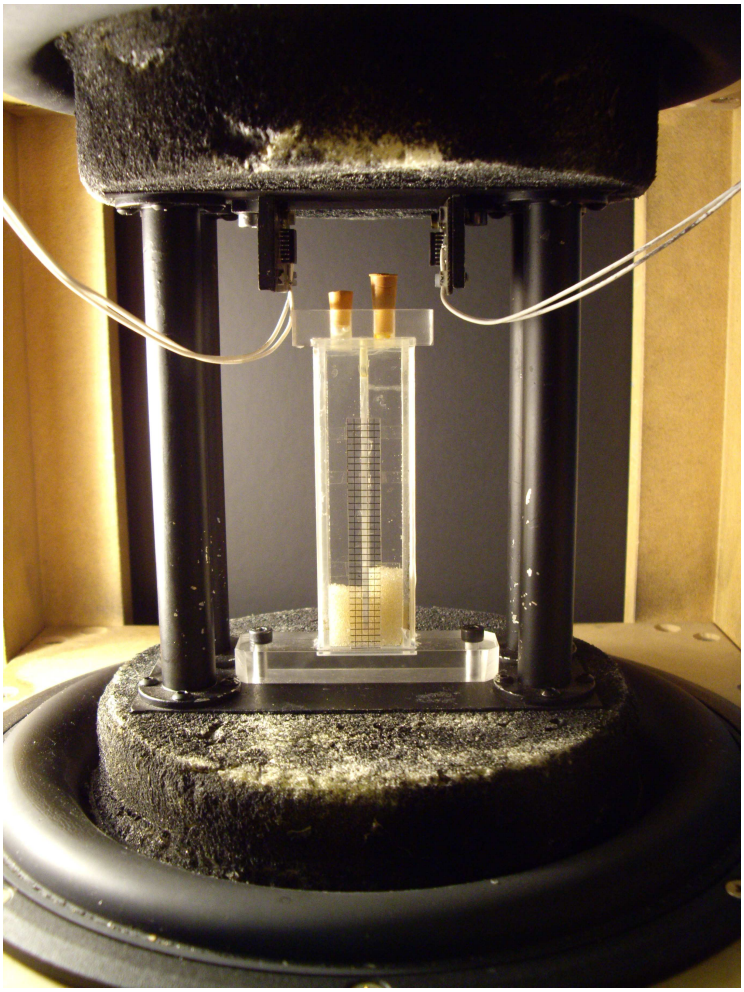

Fig. 5.3: Photograph of experimental setup. Here the partitioned cell is screwed to the loudspeaker. A signal generator (not seen here) produces a sinusoidal signal of desired frequency and is fed into the loudspeaker via an amplifier. Above the cell are the capacitance cantilever accelerometers, which monitor the vibrational motion of the loudspeakers. The white wires connect the accelerometers to a digital voltmeter which displays the maximum acceleration output in the form of Γ.

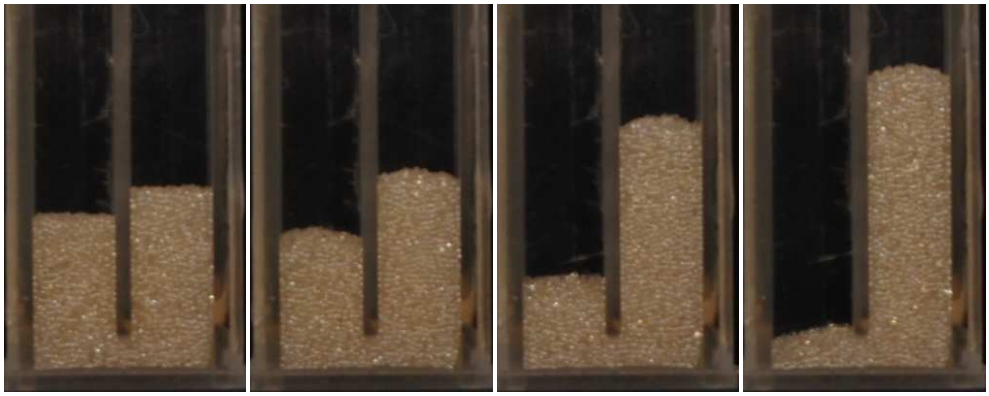

Fig. 5.4: Snapshots from experiments illustrating the time-evolution of water-immersed barium titanate particles of diameter 700 μm shaken within the partitioned cell for vibration parameters of $f = 15$ Hz and $\Gamma = 2.5$. Here the grains are given a small initial difference in the heights. As the cell is vibrated the particles migrate into the right-hand column.

5.3 Experimental Results

As the system is vibrated we find that over time the particles migrate through the lower hole from the shallower bed into the taller bed. Eventually almost all the grains occupy just one of the columns, with only a small percentage of grains inhabiting the gap and the base of the opposite column. Figure 5.4 illustrates this motion within the partitioned cell for vibration parameters of $f = 15$ Hz and $\Gamma = 2.5$. By analysing footage from a high speed camera we have observed in detail the motion of grains between columns within each cycle. In the first part of the cycle the grains are thrown and particles are drawn from the shallower to the deeper bed whilst both beds are in flight. In the second part of the cycle as the two beds land a smaller number of particles are forced back towards the shallower bed. On average we find that the motion of grains is greater during flight than on landing, thus the particles gradually migrate from the shallower to the deeper granular bed. Eventually the flow of grains moving backwards and forwards between the columns evens out so that there is no net granular movement over the vibration cycle and the system is said to be in "dynamic equilibrium". This means that, over the course of one cycle, the grains move from the shallower towards the deeper granular bed at the same rate as particles move from the deeper to the shallower bed. Thus if we were to take a snapshot of the system once

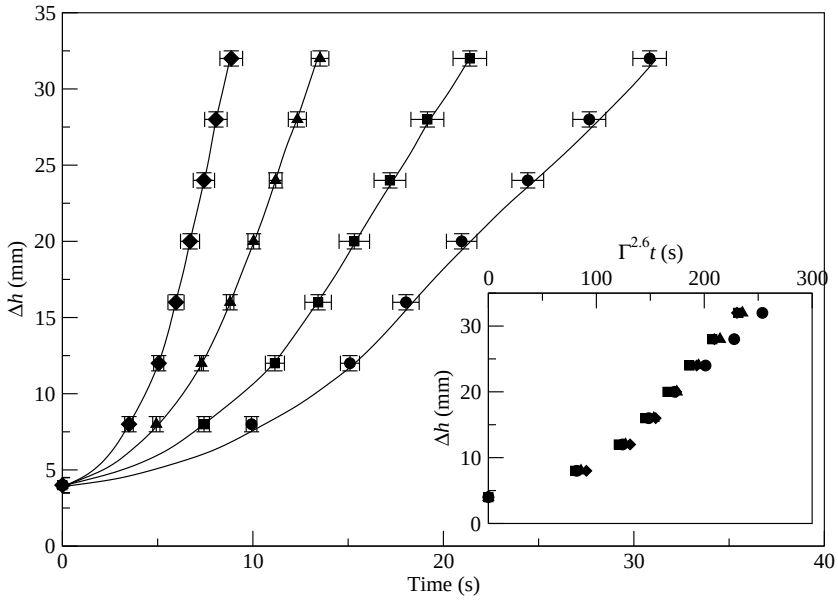

Fig. 5.5: The variation in height difference Δh as a function of time for a system of barium titanate grains fully immersed in water. The cell was vibrated at $f = 15$ Hz and vibration amplitudes corresponding to, from right to left, $\Gamma = 2.25$ (circles), $\Gamma = 2.50$ (squares), $\Gamma = 3.00$ (triangles) and $\Gamma = 3.50$ (diamonds). The inset shows that the data can be collapsed onto a single curve, as described in the text.

each cycle the overall arrangement of the granular beds would appear unchanged, however, the motion of grains within each cycle may still be substantial.

We define $\Delta h = |h_1 - h_2|$ as the magnitude of the difference in height between the two granular columns. Figure 5.5 plots Δh against time, t, for water-immersed barium titanate vibrated at $f = 15$ Hz with vibrational accelerations in the range $\Gamma = 2.25$–3.50. The error bars were obtained from averaging the data sets over 10 independent runs. Figure 5.5 shows that the transfer of grains into the deeper bed initially accelerates as Δh increases and then continues at an almost constant rate until nearly all the grains are in the deeper bed. Subsequently the net transfer of grains decelerates until a steady state is reached in which a small number of grains move backwards and forwards between the two columns. The last experimental points plotted are at $\Delta h = 32$ mm as beyond this point the results become erratic and difficult to measure.

Unsurprisingly as Γ is increased the total time taken for the grains to migrate into one column reduces due to the increased amount of mechanical energy within the beds driving the grain transfer process. The inset to Figure 5.5 shows that

the data for different values of Γ can be collapsed onto a single curve when plotted against a rescaled time t/τ, where $\tau = 100\Gamma^{-2.6}$ s. This strong dependence on Γ results from the non-linear flight dynamics of the bed within the fluid and the variation of bed porosity with vibratory conditions.

We note that, when experiments are performed with the gap through the partition at the top of the cell sealed, there is no transfer of grains from the shallower to the deeper granular bed. In fact if vibrated for a long period of time the granular beds then end up of equal height.

5.4 Simulations

To gain insight into the physical mechanisms which lead to the instability formation, and in order to be able to study features not readily accessible from experiment, we have also carried out numerical simulations. Initially we tried to simulate the partition instability using a particle fluid model in which the grains operate in a MD framework, the fluid motion is governed by the Navier–Stokes equations and the fluid particle coupling is introduced through the use of an empirical bed equation (Kuipers *et al.* 1993). Models of this type have been used effectively to simulate Faraday tilting (see Chapter 4) and the separation of a binary mixture (van Gerner *et al.* 2007; Milburn *et al.* 2005). Using these models we were able to simulate the partition instability, but as we see in Section 5.4.1 we were unable to obtain agreement with certain aspects of our experimental results. As a result for the majority of this chapter we employ an alternative simulation approach, the Fluid Springs (FS) model, which is described in detail in Section 2.5.2. This model uses a fluid grid lattice small in scale compared to the size of the particles and does not use bed equations to couple the fluid and grain interactions.

Within this section we present results obtained using the Navier–Stokes (NS) model and show the limitations of using an approach based on bed equations. We then present simulation results for the same system using the FS model. In the last part of the section we compare the use of the NS and FS models when simulating the Partition Instability.

Parameter	*Value*
Number of particles	2700
Particle density	4500 kg m^{-3}
Particle diameter	600–850 μm
Young modulus E	6.7×10^{10} kg m^{-1} s^{-2}
Poisson ratio σ	0.30
μ, μ_W	0.52
Total bed height $h_1 + h_2$	40 mm
Fluid density ρ	1000 kg m^{-3}
Dynamic viscosity η	1×10^{-3} kg m^{-1} s^{-1}
Lattice spacing Δ	2 mm
Cell size (y–axis)	2.5 mm
Δt	10^{-5} s
f	15 Hz
Γ	2.25–3.50

Table 5.2: Parameters for the partition instability simulations when using the Navier–Stokes model. The cell parameters are the same as those found in table 5.1 except for the "front to back" cell depth along the y–axis.

5.4.1 Navier–Stokes Model

We begin by using the NS model to simulate a two column system similar to the experimental setup described in section 5.2. Each column has the same width and height as in experiment, 10 mm and 90 mm respectively, while the depth of the cell is reduced to 2.5 mm for computational speed. The connecting gaps between the two columns at the base and top of the cell both have a width of 2 mm and respective heights of 4 mm and 7 mm. We use 2700 barium titanate particles of density $\rho_g = 4500$ kg m^{-3} and diameters in the range 600–850 μm to prevent crystallisation. The particles are distributed throughout the partitioned cell and then allowed to settle under the influence of gravity. As the grains settle the cell is not vibrated and the particles do not experience any fluid drag forces. At rest the total height of both columns is 40 mm and as with the experimental

system the initial height difference is set to $h_2 - h_1 = 4$ mm. The cell is vibrated sinusoidally at $f = 15$ Hz over several Γ values.

The particle interactions are modelled using the Damped Hertzian (DH) model described in section 2.1.1. The DH model best replicates the contact forces experienced by real particle interactions. This is important within the partition instability simulations as the effect on the dynamics and overall timescales of the grain "hardness" can be significant. Coulomb friction between particles is also included. Here the coefficient of friction μ was chosen to be 0.52 which was determined experimentally from angle of repose measurements.

The fluid and grain coupling interactions are modelled using Di Felice's empirical bed equation (1994), given in equation 2.74 by:

$$-\nabla P = \frac{3}{4}\frac{(1-\phi)\,\rho C_d}{\phi d}\phi^{-\chi}|\mathbf{V}_0|\mathbf{V}_0. \tag{5.1}$$

Here ϕ is the bed porosity, d is the average particle diameter, C_d is the fluid drag coefficient, χ is a flow dependent variable and $\mathbf{V}_0$ is the superficial fluid velocity through the bed (for more information see section 2.4.4). Di Felice's bed equation is an empirical fit to the pressure drop experienced by steady flow through a porous granular bed in both low and high porosity regimes. The simulation parameters are given in table 5.2, while the cell dimensions in table 5.1, apart from the y–axis length, are still relevant.

Figure 5.6 plots Δh against time t when the water-immersed barium titanate particles are vibrated at $f = 15$ Hz for four vibrational accelerations in the range $\Gamma = 2.25$–3.50. The plot shows that as the partition cell is vibrated the grains move towards the bed of greater depth until virtually all the grains occupy just one of the cell columns. The rate of grain transfer increases with Δh in an exponential-like manner until the grains abruptly reach equilibrium at $\Delta h \approx 40$ mm. As was observed in experiments Figure 5.6 shows that as Γ is increased the total time that the system takes to reach equilibrium decreases. In the early stages of the simulation the Γ curves are almost indistinguishable. This means that once the grains have transfered into one column the total span of the curves is very low.

These characteristics are very different to the experimental results in Figure 5.5 where the grain transfer process initially accelerated and then proceeded lin-

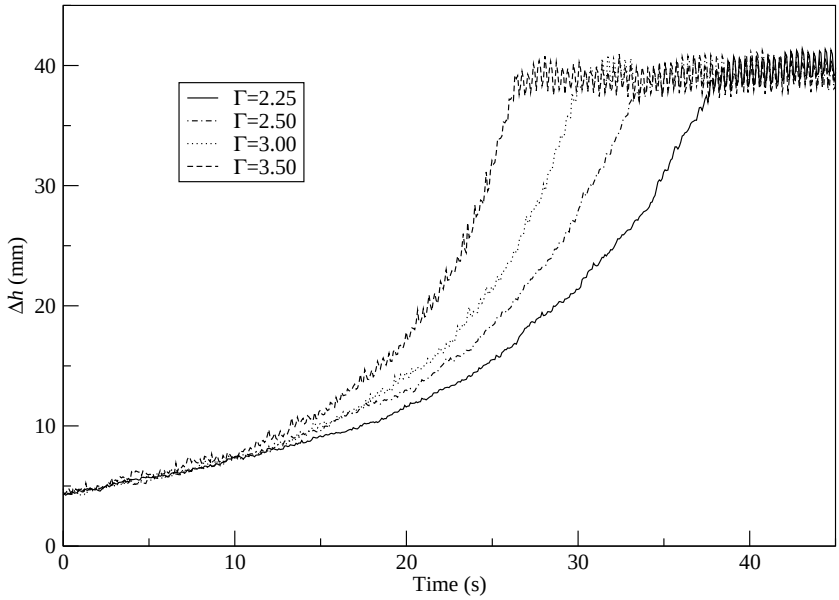

Fig. 5.6: The height difference Δh plotted against time t for 2700 water-immersed barium titanate particles vibrated in a partitioned cell at $f = 15$Hz for Γ in range of 2.25–3.50. Fluid grain interactions are modelled using the Navier–Stokes model.

early before slowing at the end. Despite both the experiments and the NS model simulations accelerating with increasing Δh the shape of the curves are markedly different. In the simulations we find that Δh reaches equilibrium very abruptly, with little slowing in the grain transfer process while in experiments Δh increases linearly until $\Delta h \approx 32$ mm after which it slows more steadily towards equilibrium. We also find that within experiments the curves are more distinguishable and span a greater amount of time.

We find that the NS model simulations are unable to accurately model the dynamics of the partition instability. This is because the fluid and grains are coupled using bed equations which are empirical fits to experimental data for steady fluid flow passing through a porous granular bed. They were not developed to model oscillatory fluid flow through systems of complex geometries. We have observed that the NS model is unable to model the fluid and grain flow within the lower channel in a realistic manner. Instead we find that the granular beds in each column behave independently. The majority of grain motion is in the vertical direction and large gaps appear beneath each bed with little horizontal motion through the gap. This is very different to experiments where hardly any gap develops beneath the granular bed during flight and there is significant

Parameter	*Value*
Number of particles	2700
Particle density	4500 kg m^{-3}
Particle diameter	600–850 μm
Young modulus E	6.7×10^{10} kg m^{-1} s^{-2}
Poisson ratio σ	0.30
μ, μ_W	0.52
Total bed height $h_1 + h_2$	40 mm
Fluid density ρ	1000 kg m^{-3}
Dynamic viscosity η	10^{-3} kg m^{-1} s^{-1}
Lattice spacing Δ	120.83×10^{-6} m
Cell size (y–axis)	2.5 mm
n_r	3
C_S	1.8
Δt	1×10^{-4} s
f	15 Hz
Γ	2.25–3.50

Table 5.3: Parameters for the partition instability simulations when using the Fluid Springs model. The cell parameters are the same as those found in table 5.1 except for the "front to back" cell depth along the y–axis.

horizontal granular motion through the bottom channel. In experiments we find that the grains firstly move towards the deeper bed and then, as the grains land, towards the shorter bed so that the horizontal granular motion through the lower channel is comparable to the vertical motion of the beds.

It is this partial coupling of the fluid and grains within the gap which explains why the behaviour of the NS model system in Figure 5.6 is so different to the experimental data in Figure 5.5. This leads us to simulating the partition instability using the FS model, which we do in the following section.

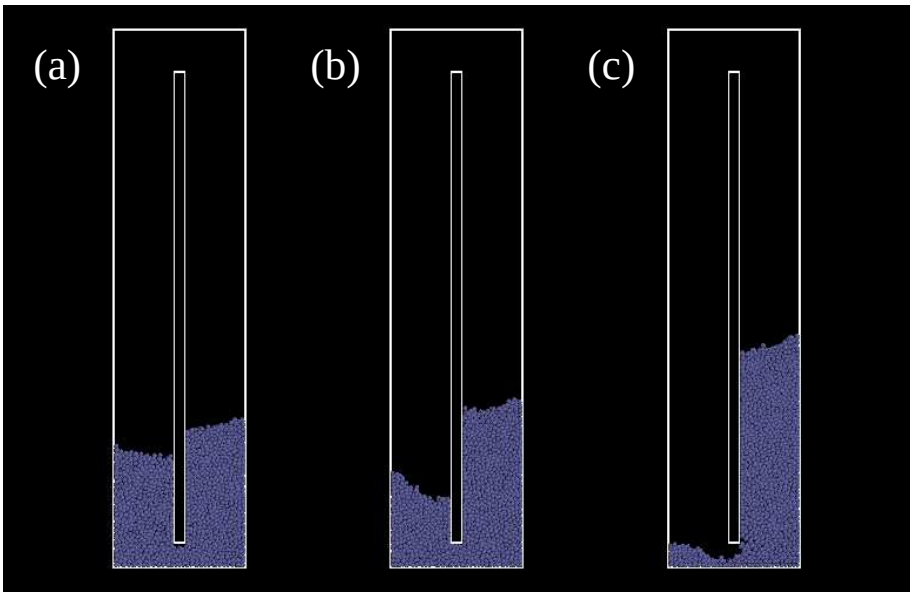

Fig. 5.7: Snapshots from simulation showing the time evolution of 2700 water-immersed barium titanate particles of diameter 600–850 μm vertically vibrated within the partitioned cell at $f = 15$ Hz and $\Gamma = 2.5$. The timings are a) $t = 0$ s, b) $t = 10$ s and c) $t = 25$ s.

5.4.2 Fluid Springs Model

We now simulate the partition instability using FS model simulations. In the same way as we did for the NS model the particle interactions are modelled within an MD framework using the DH collision model. The fluid is modelled using the global equations for fluids, namely the Navier–Stokes equations. The momentum transfer between the particles and fluid is modelled using the method detailed in section 2.5.2. One requirement of the FS model is that the particles are large in comparison to the fluid lattice grid. Thus the grid spacing Δ is set to 120.83×10^{-6} m such that there are 6 lattice points across each particle diameter and the radial reference point density is $n_r = 3$. As in the NS model the particles are initially distributed throughout the partitioned cell which is held stationary as the grains are allowed to settle under the influence of gravity. Once the particles are settled on the base of the partitioned cell the vibrations begin. The simulation parameters are summarised in table 5.3, while the cell dimensions may be found in table 5.1 except for the "front to back" cell depth which was again reduced to 2.5 mm.

Figure 5.7 shows the evolution of the partition instability for $\Gamma = 2.5$ at times

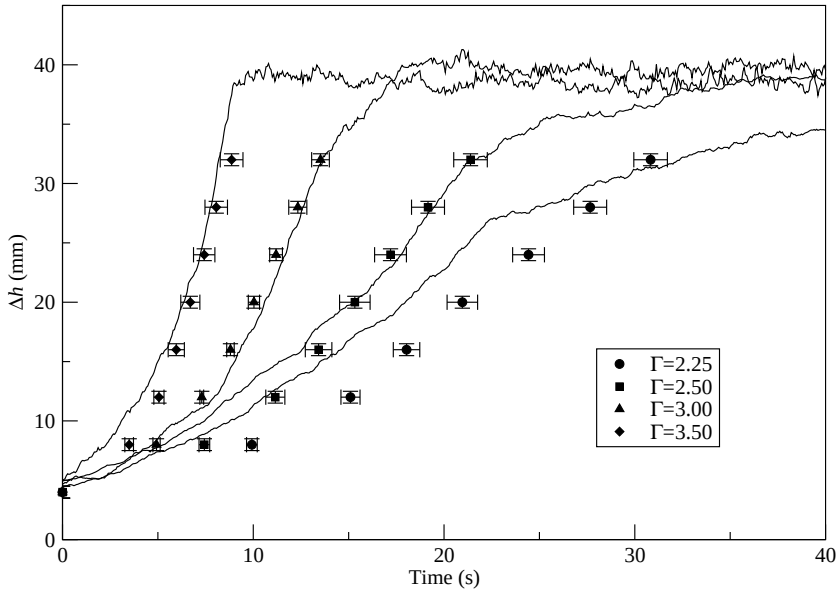

Fig. 5.8: Variation of Δh with time, t at $f = 15$ Hz. Solid curves from right to left are for $\Gamma = 2.25$, 2.5, 3.0 and 3.5. The experimental data has also been plotted for comparison.

of $t = 0$ s, 10 s and 25 s. The columns are given an initial height difference of $\Delta h = 4$ mm as in experiments. At $t = 10$ s the grains have appreciably transfered into the right hand column and by $t = 25$ s almost all of the grains in the left hand column have moved through the gap in the base into the right hand column. At this point the columns are in dynamic equilibrium.

Figure 5.8 plots Δh against time for vibration parameters $f = 15$ Hz and $\Gamma = 2.25$, 2.50, 3.00, 3.50 for the FS model simulations. We have also included the results from experiments within the figure. Here we see that the agreement between simulation and the experimental results is very good, except at the lowest value of Γ used, 2.25. For this value of Γ the agreement is not as good, which we believe is due to the fact that in the experiments the barium titanate grains are slightly non-spherical and tend to jam within the gap. At low Γ there is not enough agitation to maintain the smooth flow of grains found at higher Γ. Figure 5.8 also shows how as Γ is increased the time taken to reach the equilibrium height reduces as was the case in experiments.

In the next section we briefly study the main differences observed when the NS and FS models simulate the partition instability.

5.4.3 Comparison between Microscopic Fluid Models

In this section we compare simulation results obtained using the NS and FS models. Figure 5.8 showed that we are able to achieve excellent agreement between the FS model and the experiments. However, earlier in Figure 5.6 we saw that the NS model failed to capture the qualitative behaviour of the partition instability observed in experiments. We propose that this is because the NS model is unable to capture the fluid-grain coupling behaviour within the gap.

In Figure 5.9 we show the granular motion within the partition instability at four points within the vibration cycle; $\theta = 0°$, $90°$, $180°$ and $270°$. Here, the granular beds within the NS model are thrown significantly higher than the beds in the FS model. The behaviour of the granular beds when using the FS model simulations agrees better with what has been observed within experiments, where very little gap develops beneath the coupled beds during flight. No figure of the experiment has been included due to the quality of images achieved with the high speed camera.

Given the good agreement between the FS model simulations and experiments we will now use simulations alone to investigate in detail the instability mechanism. In the next section we study flow data through the columns and the connecting channel to develop our understanding of the partition instability effect.

5.5 Flow Graphs

Within this section we investigate the partition mechanism through data obtained from the FS model simulations. Figures 5.10 and 5.11 compare the granular flow within each column and the fluid flow within each column respectively. Both figures show data for one cycle of vibration after $t = 1$ s for vibrational parameters $f = 15$ Hz and $\Gamma = 2.5$. In these figures a positive value of the flow means that the fluid or grains were flowing upwards through the column.

Figure 5.10 shows that grains within each column experience upward motion in the early part of the cycle and then downward motion in the later part. The grains within the shallow bed are thrown upwards with a much smaller velocity than

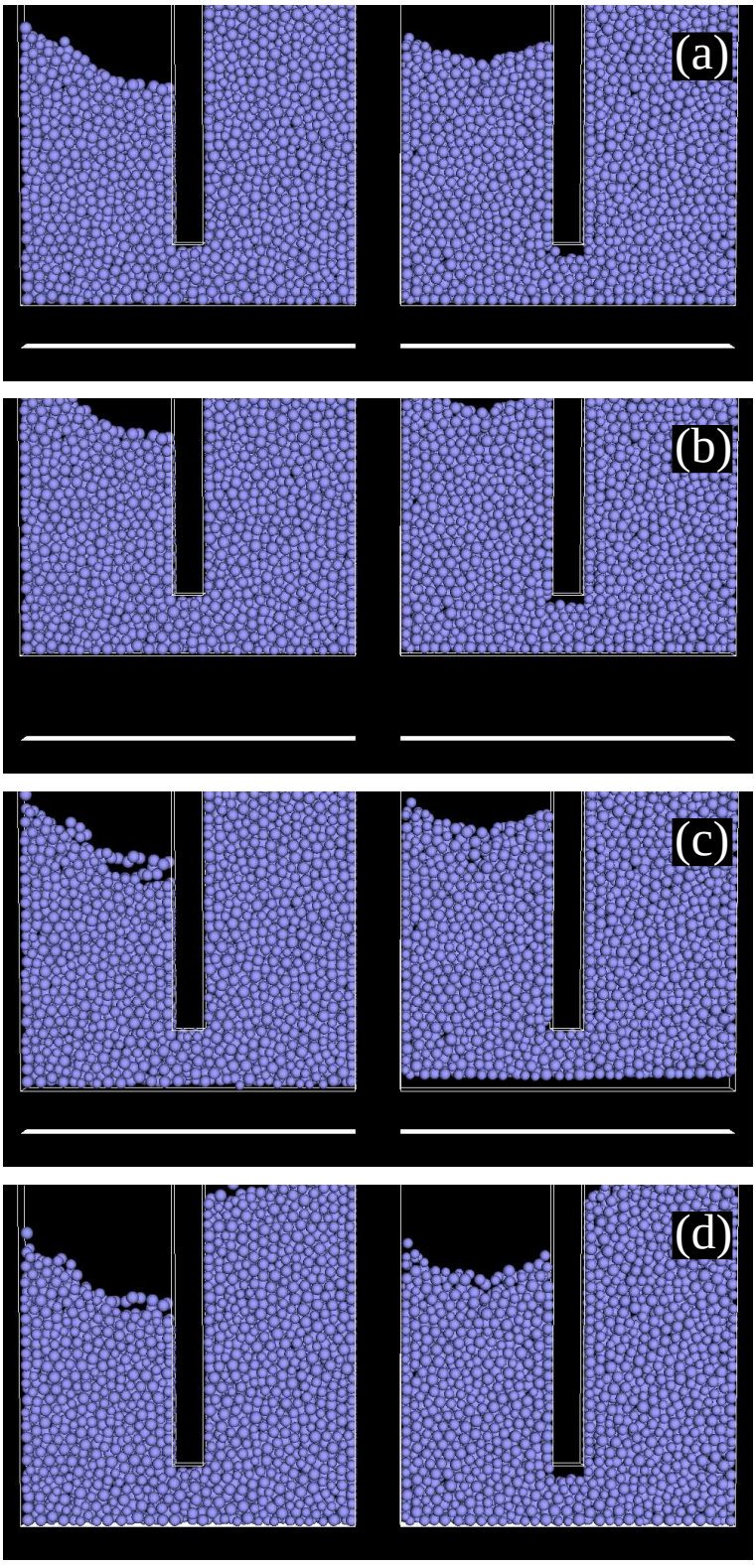

Fig. 5.9: One cycle of vibration for the granular bed within the partitioned cell when shaken with vibration parameters of $f = 15$ Hz and $\Gamma = 2.5$. The bed on the left was modelled using the Fluid Springs model while the bed on the right was modelled using the Navier–Stokes model. The figures correspond to (a) $\theta = 0°$, (b) $\theta = 90°$, (c) $\theta = 180°$ and (d) $\theta = 270°$.

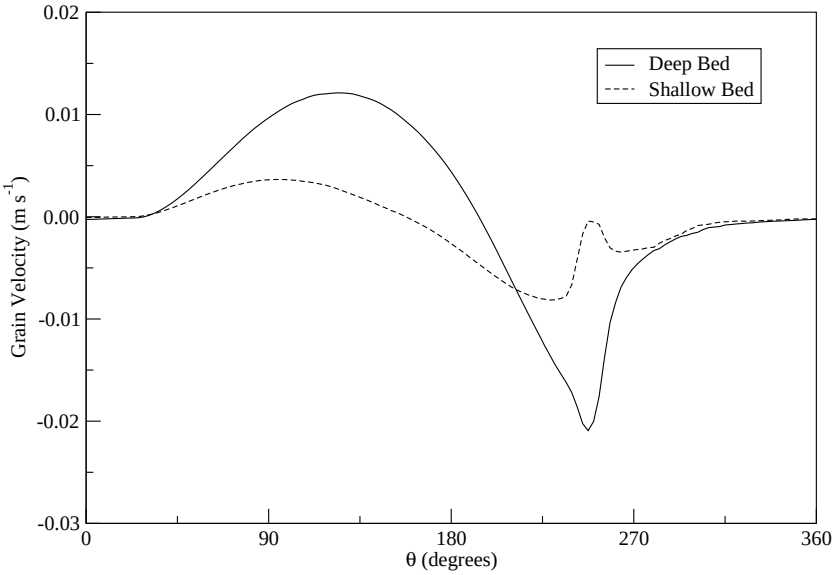

Fig. 5.10: The grain velocities within each column plotted against the phase angle θ. The data shows a vibration cycle after $t = 1$ s when shaken with vibration parameters of $f = 15$ Hz and $\Gamma = 2.5$. The simulations were performed using Fluid Springs model.

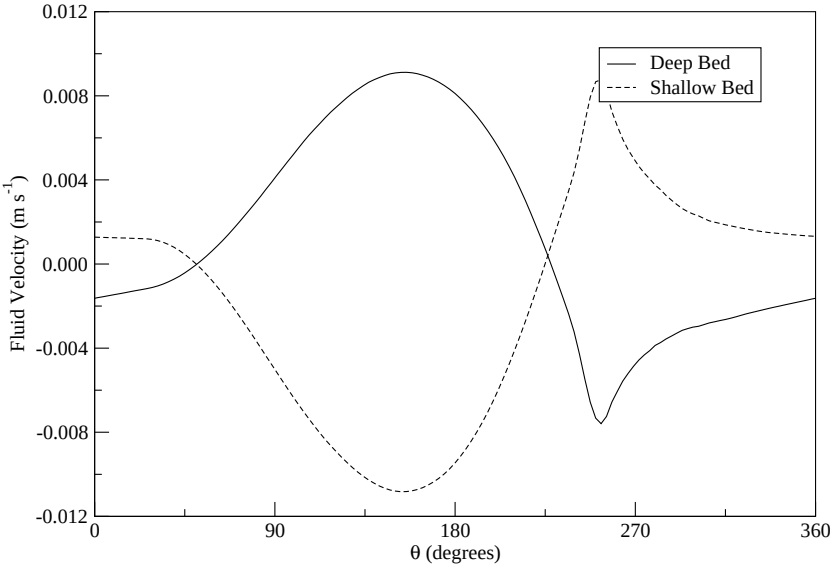

Fig. 5.11: The fluid velocities within each column plotted against the phase angle θ. The data shows a vibration cycle after $t = 1$ s for vibration parameters $f = 15$ Hz and $\Gamma = 2.5$. The simulations were performed using Fluid Springs model.

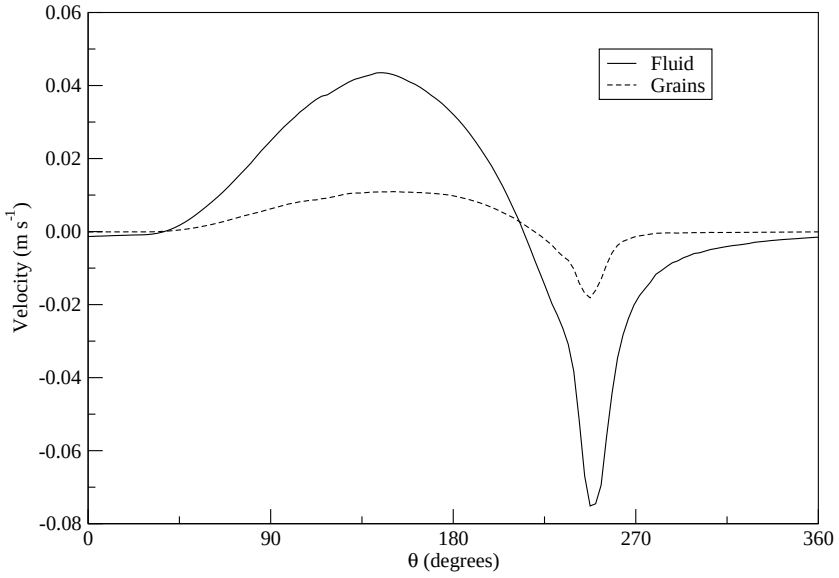

Fig. 5.12: The fluid and grain velocities through the lower connecting channel within the partitioned cell plotted against the cycle phase. The data shows the vibration cycle at $t = 1$ s for vibration parameters $f = 15$ Hz and $\Gamma = 2.5$.

those within the deeper column. Both beds decelerate during flight, however, the shallower bed decelerates at an earlier stage than the deeper bed. This leads to the shallower bed falling and landing before the deeper bed. As the shallower bed lands it experiences a sharp upward acceleration in the grain motion at $\theta \approx 240°$. This corresponds to the moment the deep bed lands and pushes grains through the gap back towards the shallower bed. The average velocity remains negative, however, as the majority of grains are still falling. The granular motion towards the shallow bed occurs as the deep bed collapses. As the deep bed motion slows rapidly the shallow bed is able to resume its falling motion. Figure 5.10 shows that the average downward granular motion continues despite the beds having already landed (after $\theta = 270°$). This corresponds to the beds expanding during flight and taking time to land.

The motion of the beds may be explained by interpreting Figure 5.11 which follows the motion of the fluid within each column over the course of a cycle. Here we see the fluid flows through the shallow column with similar behaviour to what was observed within a single column thrown bed system (see Section 3.2). In the early part of the cycle the bed is thrown upwards and fluid flows downwards through the bed. Later in the cycle the bed falls and fluid flows upwards through

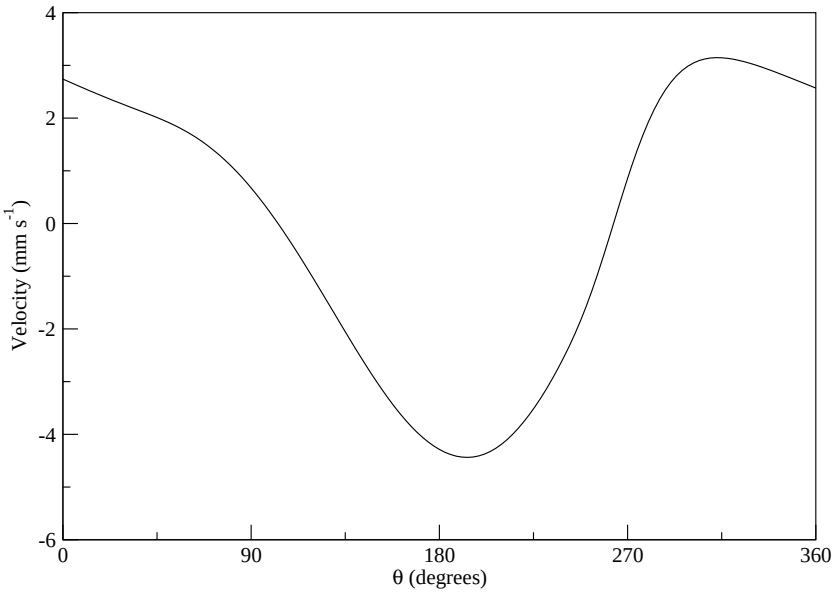

Fig. 5.13: The fluid flow velocity through the upper connecting channels plotted against the phase angle θ. The data shows a vibration cycle after $t = 1$ s for vibration parameters of $f = 15$ Hz and $\Gamma = 2.5$.

the bed to occupy the space above. This is in contrast to the fluid flow observed within the column containing the deep bed. Here the fluid flows in the opposite direction to the fluid within the shallow column. Instead we find that the fluid flow in the deeper bed column moves in the same direction as the deep granular beds. Therefore as the beds are thrown the fluid exerts a greater amount of drag on the shallower bed than on the deeper bed. Hence, the shallower bed is not thrown as high and lands before the deep bed as observed in Figure 5.10.

Figure 5.12 shows the flow of the fluid and grains through the bottom connecting channel over the course of a cycle early in the transfer process. In this graph a positive value indicates flow towards the deep bed. In the early part of the cycle as the beds are thrown both the fluid and grains flow towards the deep bed. In the later part of the cycle, as both beds land, the fluid and grains accelerate sharply towards the shallow bed. Over the course of a vibrational cycle the granular flow is approximately proportional to the fluid flow. We also notice that in the early part of the cycle the grain motion slightly lags that of the fluid as the grains are accelerated by the fluid flow.

Finally, we plot the fluid flow through the upper connecting channels over the course of a cycle after $t = 1s$. This flow is shown in Figure 5.13. As with earlier

figures a positive value in this graph indicates flow towards the deep bed. The flow through the upper channel is made up entirely of fluid. In the early part of the cycle the flow in the upper connecting channel moves towards the deep bed. As the beds are thrown, fluid in the upper channel is drawn towards the shallow bed. Later in the cycle, as the beds land the fluid then moves towards the deeper column. We note that if the top channel is sealed then there is no transfer of grains through the lower channel. This shows that the fluid flow through the top hole is significant within the transfer process.

5.6 Instability Mechanism

We now consider the possible mechanism for the partition instability. Two limiting cases can readily be described. In the first, the resistance to fluid flow through the bottom gap far exceeds that through either bed. Under vibration each granular column is thrown independently and will develop an under-pressure proportional to its height. The pressure drop under the deeper bed early in flight will be greater than beneath the shallower bed causing grains to move in the direction of the deeper bed. Later in flight the changing pressure reduces the particles' velocities but is not sufficient to reverse the direction of grain motion. A second possibility is that the coupling between the two columns is such that the resistance to fluid flow through the lower hole is far less than that through either bed. Both columns experience a common under-pressure which can only be achieved if more fluid flows through the shallower bed rather than through the deeper bed. This fluid flow also transports grains towards the deeper granular column.

In order to test which, if either, mechanism is dominant we determine from simulation the pressure beneath each column for vibrational parameters $f = 15$ Hz and $\Gamma = 2.5$. Figures 5.14 (a) and (b) show the pressure drop ΔP across the bed on each side of the partition at times $t = 10$ s and $t = 30$ s. The inset in Figure 5.14 (a) shows the variation of h_2/h_1 with time t. The variation of pressure throughout a cycle shows that ΔP is approximately the same on both sides of the partition. For example, by $t = 30$ s the height ratio is $h_2/h_1 \approx 15$ while the ratio

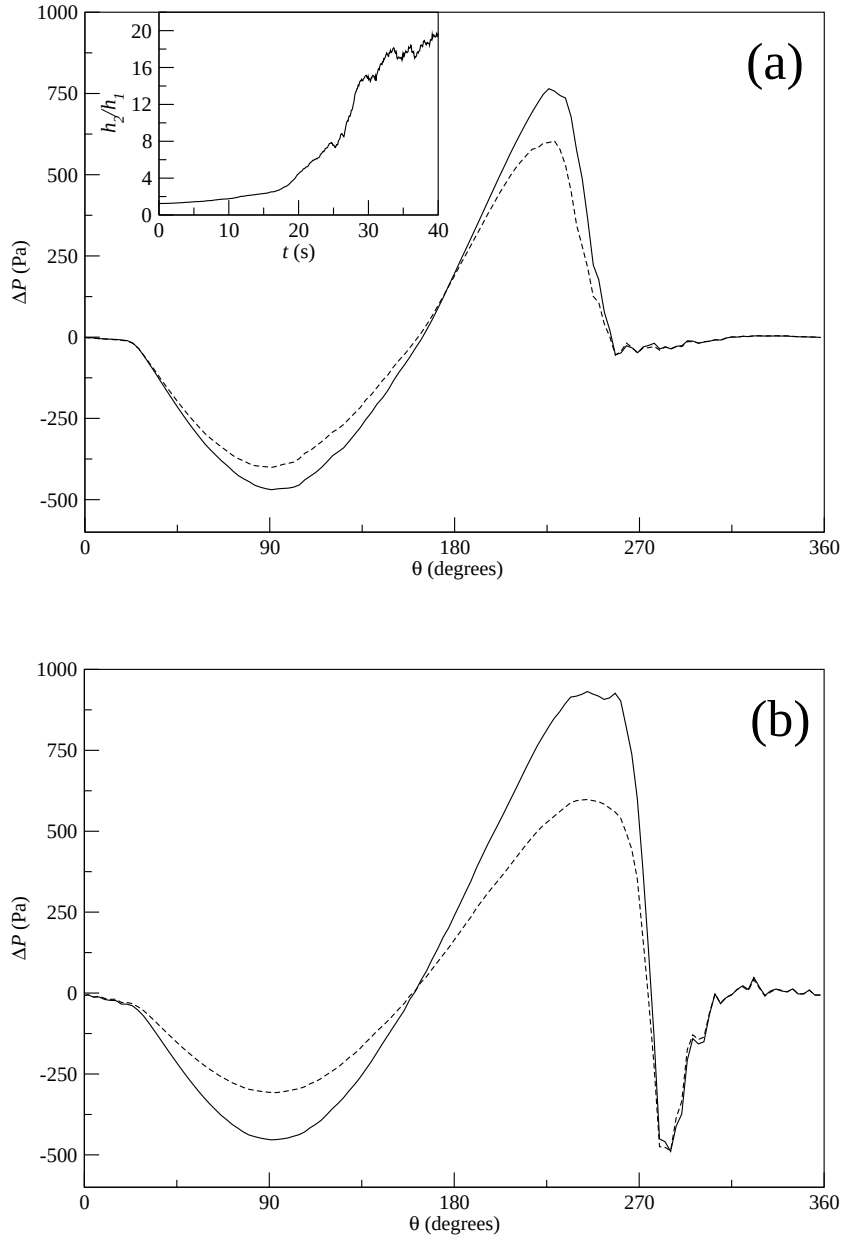

Fig. 5.14: Under-pressure drop across the bed on each side of the partition plotted against the phase angle θ for the deep column (solid-line) and the shallow column (dashed-line) for vibration parameters $f = 15Hz$ and $\Gamma = 2.5$. The top figure is at $t = 10$ s and the bottom figure is at $t = 30$ s. The data was averaged over 5 cycles. The insert in the top figure shows the height ratio h_2/h_1 against time, t.

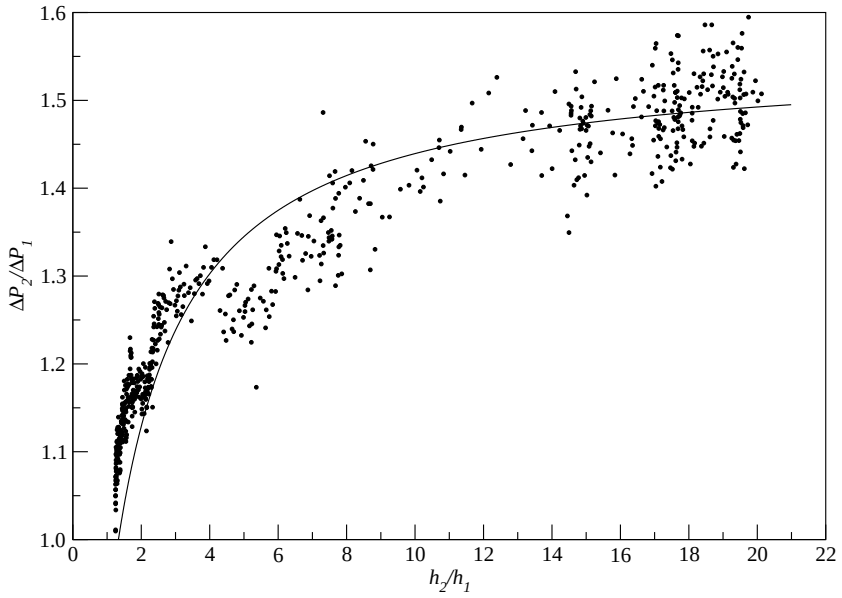

Fig. 5.15: Ratio of pressure drops, $\Delta P_2/\Delta P_1$, as a function of the height ratios h_2/h_1. The solid line is a guide to the eye.

of pressures on the two sides $\Delta P_2/\Delta P_1$ is only 1.5. Furthermore, the pressure curves throughout a cycle on either side of the partition can be scaled onto each other. Figure 5.15 plots the ratio of pressure drops, $\Delta P_2/\Delta P_1$, across each bed against the ratio of the heights of the two bed depths, h_2/h_1, as grains move from one column to the other. The figure shows that as h_2/h_1 increases $\Delta P_2/\Delta P_1$ only increases slowly and eventually levels at approximately 1.55 as h_2/h_1 reaches 21. These results show that, for our experimental geometry, the resistance to fluid flow through the bottom gap is low, the second scenario described previously. In the next section we propose an analytical model based on the Kroll model which captures this mechanism.

5.7 Coupled Column Kroll Model

In this section we propose a semi-analytical approach to model the transfer of grains between two coupled columns, namely the Coupled Column Kroll model. The approach we use is based on the numerical Kroll model described in section 2.3. We extend these ideas to the present experimental situation, that of two coupled columns, an arrangement shown schematically in figure 5.16 where the variables and parameters of the two columns are labelled 1 and 2.

In essence the two granular beds are treated as independent porous beds which interact when fluid flows between the columns through the bottom channel. The resistance to the flow through the bottom channel is much smaller than through either column so we may reasonably approximate that there is no resistance to flow. In reality, however, the flow does experience a resistance due to the presence of grains in the channel. As there is no resistance to flow in our analytical model the pressure is equal across the base for the entire flight duration.

We suppose that the two beds experience under-pressures ΔP_1 and ΔP_2 when in flight which may be related to the fluid flow through each bed such that we have $\Delta P_1 = h_1 K_1 v_1$ and $\Delta P_2 = h_2 K_2 v_2$. Here v_i is the fluid flow through column i, defined as the volumetric flow rate per unit area and K_i is the permeability of bed i. The permeability is a measure of the ability of a porous material to transmit fluids. It is dependent on the size and shape of the particles and how densely packed they are. The pressure ratio consequently satisfies

$$\frac{\Delta P_2}{\Delta P_1} = \frac{h_2 K_2 v_2}{h_1 K_1 v_1}. \tag{5.2}$$

As noted above this pressure ratio is approximately constant throughout the transfer process. For simplicity we fix $\Delta P_2/\Delta P_1 = 1.0$. Consequently the pressure drop across each bed is proportional to its depth. The small variation of the pressure ratio with height, shown in Figure 5.15, can be included in the analytical model by using a best fit to the simulated data. However, such variation does not significantly change the predicted dependence of Δh on t.

Note that were the two columns to be connected by a long tube, this condition would be replaced by $\Delta P_2/\Delta P_1 = h_2/h_1$. In this limit the resistance to flow through the gap is high and the two beds are assumed to be thrown independently.

During bed flight there will be a movement of fluid, at velocity v, through the lower coupling hole. The fluid flow being driven by the different fluid flows through each bed. No pressure resistance developes as the instantaneously moves through the gap to no re For this motion to occur there must be a corresponding flow through the upper hole, high in the partition. Using variables $u_1 = \dot{z}_1 - \dot{z}_c$ and $u_2 = \dot{z}_2 - \dot{z}_c$, conservation of fluid volume requires that

$$u_1 + v_1 = -A_r v = -u_2 - v_2, \tag{5.3}$$

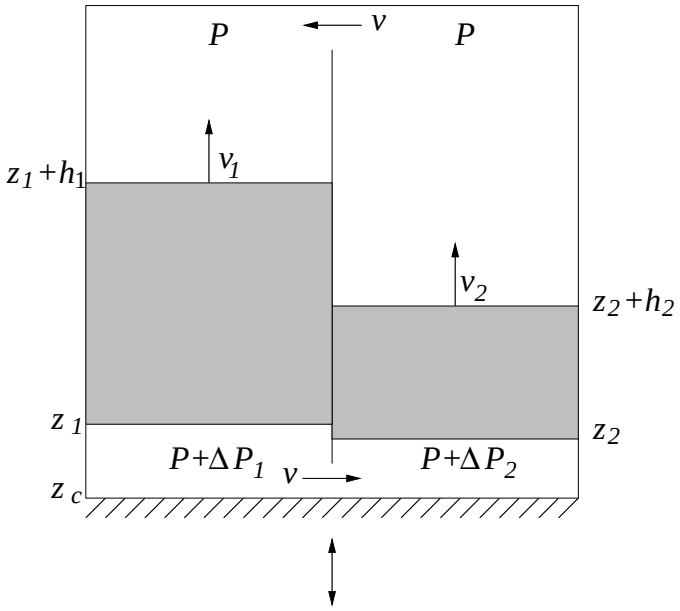

Fig. 5.16: Representation to illustrate how the pressure, the positions of the bed and fluid velocities are defined within a two column system. Here v_i are defined as the superficial fluid velocities. The arrows show the direction of up and define our instantaneous fluid direction, meaning flow can be in the opposite direction.

where A_r is the ratio of the cross-sectional areas of the channels to the lower coupling hole. Applying Newton's laws to the two beds as before we obtain

$$\dot{u}_1 + g = K_1' v_1 - \ddot{z}_c \tag{5.4}$$

and

$$\dot{u}_2 + g = K_2' v_2 - \ddot{z}_c. \tag{5.5}$$

While both beds are in flight Equations 5.2, 5.3, 5.4 and 5.5 may be solved to find u_1, u_2, v_1 and v_2. Using these values, v may be obtained from Equation 5.3. To solve these equations K_i' was based on Ergun's equation and obtained using

$$K_i'(u_i) = \frac{180\,(1-\phi)\,\eta}{\phi^3 \rho_g d^2} + \frac{1.75\rho}{\phi^3 \rho_g d}|u_i|. \tag{5.6}$$

It is found that the two strongly coupled beds do not follow the same flight path and that one lands before the other. We suppose that grains only move through the lower channel from one column to the other while both beds are in flight. As a simple approximation we suppose that the velocity of grains through the bottom gap u is obtained using

$$u = cv\Gamma \tag{5.7}$$

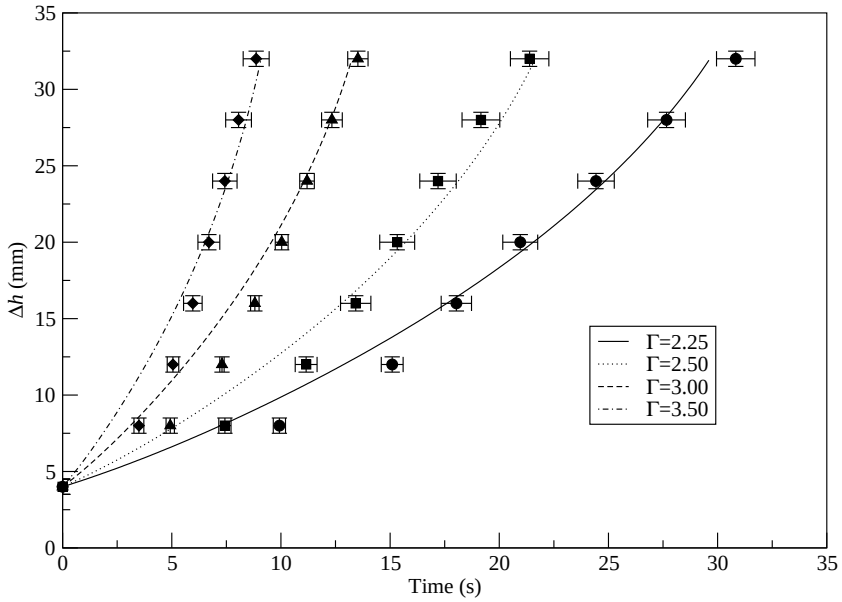

Fig. 5.17: The height difference Δh plotted against t using experimental data and results obtained with the Coupled Column Kroll model. The cell was vibrated at $f = 15$ Hz and amplitudes in the range $\Gamma = 2.25$–3.50.

where c is a constant fitting parameter. The net transfer of grains during a cycle is assumed to be proportional to the volume flow of fluid through the hole and how strongly the bed is fluidised by the vibration. This assumption is reasonable as Figure 5.12 demonstrates. This model has been implemented numerically.

Figure 5.17 shows a comparison between the experimental data and the Coupled Column Kroll model. Here the single fitting parameter c has been chosen to be 0.019. The analytical model provides a good fit to the experimental data. However, it is unable to accurately capture the final stage of the grain transfer when the rate begins to slow. As in experiment, the Coupled Column Kroll model data can be collapsed onto a single curve by rescaling time by $\tau = 100\Gamma^{-2.6}$ s.

The analytical model enables us to better understand the mechanism which drives the grain transfer. When the beds are thrown, an under-pressure develops across the base of the cell and thus fluid flows downwards through the beds to fill the space left beneath. The shallower bed provides less resistance to the downward flowing fluid and thus fluid is drawn from the shallower side through the hole to the deeper side. The fluid accelerates grains in the direction of the flow, from the shallower to the deeper column. As the beds begin to fall in the second half of the cycle an over-pressure develops beneath the beds and the

fluid flow is reversed. Fluid is forced upwards through the beds to fill the void above. Again the shallower bed provides less resistance to the upward moving fluid so fluid now flows through the channel from the deeper bed to the shallower bed. However, the shallower bed lands first, thus reducing the transfer of grains back from the deeper bed. Over a cycle there is a net transfer of grains from the shallower to the deeper column, hence the instability. The process is repeated and accelerates as the increasing Δh leads to less resistance to fluid flow through the shallower column and greater resistance through the deeper column. Eventually an equilibrium is established when as many grains move into the deeper column in the early part of the cycle as move back into the shallower column when the beds lands. At this stage the columns are in a dynamic equilibrium which usually occurs when the vast majority of grains reside in one column only.

5.8 Summary

We have investigated the water-driven partition instability, in which grains transfer from one side of a partitioned cell to the other through a lower connecting hole. We observed the instability effect in experiments and then used simulations which were able to accurately reproduce this process and provide insight into the instability mechanism. The transfer of grains results from the greater flow of fluid through the shallower column of grains as the beds are thrown by the vibration. The behaviour can be captured by a two-column coupled Kroll model.

This research has also shown that the Fluid Springs model is able to simulate systems of complex geometry with excellent accuracy. In the next chapter we use the FS model to simulate a large intruder within a system of dense particles in the fluid-enhanced Brazil nut effect.

Chapter 6

Fluid-Enhanced Brazil Nut Effect

A large dense intruder under suitable conditions will rise to the surface of a granular bed when vibrated vertically, the Brazil nut effect. In this chapter we study the fluid-enhanced Brazil nut effect in which the granular bed is immersed in a fluid. We initially observe and study the effect within experiments. Simulations are then used to reproduce the effect and study, in detail, the important fluid and grain motion around the intruder which are responsible for the rising mechanism. At the end of the chapter an analytical approach is proposed to model the rising mechanism of the Brazil nut.

6.1 Introduction

A large heavy object, often referred to as an "intruder", rises to the top of a bed of smaller particles under the influence of vertical vibration in what is known as the "Brazil nut effect" (BNE) (Harwood 1977; Williams 1976). Several competing mechanisms have been proposed to explain this behaviour. In one, known as "ratcheting" (Williams 1976; Bridgewater *et al.* 1969; Rosato *et al.* 1987), small grains fall beneath the large particle as the vibrated bed expands. When the bed settles to its rest state the intruder is elevated by these smaller particles which fell beneath it. In a second mechanism, often referred to as "convection-driven", the entire granular bed moves in vertical convection rolls, with broad upward moving regions at the centre of a shaken cell and narrow downward moving regions along the edges (Rátkai 1976; Knight *et al.* 1993; Cooke *et al.* 1996; Poschel and

Herrmann 1995; Gallas *et al.* 1996). In the convection-driven case, segregation occurs because the larger intruder particle cannot re-enter the downward flow and thus remains at the top of the bed. Both of these mechanisms tend to segregate large particles above smaller ones.

More recently the effects of interstitial air have been investigated and shown to dramatically influence the motion of the intruder through a fine granular bed (Möbius *et al.* 2001; Naylor *et al.* 2003; Yan *et al.* 2003). Möbius *et al.* (2001) showed that the presence of air strongly influences the rising of the intruder. Naylor *et al.* (2003) demonstrated that not only the presence of air but also the motion of air coupled to the granular bed plays a key role in the intruder's behaviour. The effects of air pressure have been investigated by Yan *et al.* (2003). A model to describe the air-driven BNE has been proposed (Möbius *et al.* 2005). This model treats the fluid as being compressible and ignores any direct interaction between the intruder and the bed during flight.

The influence of air on granular segregation has also been investigated both in experiment (Burtally *et al.* 2002) and simulation (Biswas *et al.* 2003; Zeilstra *et al.* 2008; Wylie *et al.* 2008). Under vertical vibration almost complete segregation occurs with one component rising to the top or forming a sandwich structure. Similar effects have also been observed for larger grains in water (Leaper *et al.* 2005). Under horizontal vibration, where the role of gravity can be ignored, segregation into a striped configuration occurs (Sánchez *et al.* 2004).

In all these cases the basic mechanism responsible for the BNE or segregation is the fact that the fluid provides a differential drag force which influences the two components differently. Indeed simulations which model the fluid as a drag force are able to reproduce segregation and single particle rising effects (Biswas *et al.* 2003; Wylie *et al.* 2008; Sánchez *et al.* 2004). More sophisticated techniques in which there is two-way coupling between the fluid and granular phases have also been used to investigate segregation effects (Zeilstra *et al.* 2008).

In this chapter we describe experiments and simulations carried out to investigate the behaviour of a large intruder in a shallow bed of smaller particles held in a vertically vibrated water-filled cell. We use the Fluid Springs model in which the fluid is resolved on a scale smaller than the host particles. Our key finding is

that the behaviour of the intruder is sensitive to the detailed fluid and particle flow in its vicinity. The use of such a microscopic fluid model allows us to accurately simulate the experimental system and to identify the principal physical mechanism that causes the intruder to rise. To our knowledge, no simulations of vibrated binary granular systems have been carried out in which the fluid is resolved on a scale that is smaller than the smallest particles. Indeed if the same system is simulated using the Simple Drag model in which the particle drag force is based on a bed equation, this form of rising does not occur.

6.2 Experimental Methods

All of our experiments were performed in collaboration with Hector Pacheco-Martinez, who is also studying within Nottingham University's Granular Dynamics Group. The experiments are conducted in a water-tight cell constructed from soda glass of dimensions 40 mm×10 mm in the horizontal plane and 43 mm tall. The bulk of the granular bed is made up of host glass spheres of density 2500 kg m^{-3} with mean radii of 1 mm and a spread of sizes in the range 0.85–1.15 mm to avoid gross crystallisation effects. We use a steel "Brazil nut" of density 7750 kg m^{-3} and radius 3.5 mm. The grains are inserted through one of two upper holes in the box until the bed has a height of 26mm. The cell is then filled with water of density 1000 kg m^{-3} and dynamic viscosity 1×10^{-3} kg m^{-1} s^{-1}. The cell is thin enough that we are able to view the steel intruder motion within the bed through the front wall. As we did with the partition instability experiments in section 5.2, the cell is shaken to remove any air bubbles trapped within the granular bed. More water is then added and the cell is sealed using bungs so that no visible air bubbles are contained within its volume. After each run the cell is removed from the vibratory apparatus and the steel ball is returned to the base of the cell. An image of the cell with the intruder half way up the bed is shown in Figure 6.1. The use of such a cell geometry allows for easy viewing of the intruder through the front glass surface.

During experiments the box is vibrated sinusoidally with frequency f in a direction within $\pm0.2^o$ of vertical in a manner which ensures accurate one-

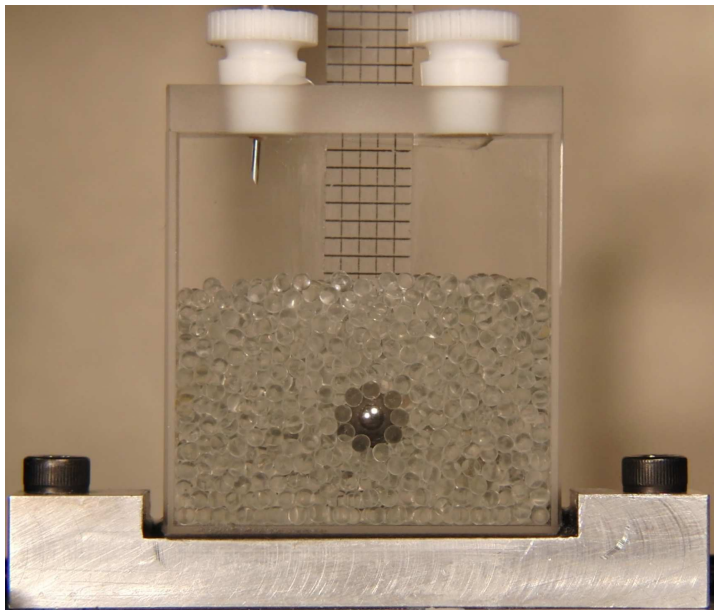

Fig. 6.1: Image of the experimental setup showing the water-filled cell, the glass granular bed and the steel Brazil nut. The intruder is positioned half way up the bed.

dimensional motion (Leaper *et al.* 2005). Again, as with the partition instability experiments, the vibration is monitored using cantilever capacitance accelerometers which display the dimensionless maximum acceleration Γ. The experiments are monitored through the use of a high speed camera, which allows the study of the intruder and surrounding granular motion within each cycle.

6.3 Experimental Results

Figure 6.2 illustrates how a steel Brazil nut rises through a fluid-immersed glass bed when vibrated with parameters $f = 15$ Hz and $\Gamma = 3.5$. The intruder initially begins on the cell base away from the front and back walls. On the application of vertical sinusoidal vibration the intruder rises rapidly through the bed until it eventually emerges through the bed surface. Once the Brazil nut reaches the top of the bed it does not then re-enter the granular bulk. We note that the Brazil nut remains away from the front and back walls during rising.

Figure 6.3 plots the gap between the lowest point of the intruder and the base of the cell, H, against time, t, for vibration parameters $f = 15$ Hz and $\Gamma = 3.5$, 4.0 and 4.5. H was measured at the beginning of each cycle when there is no gap

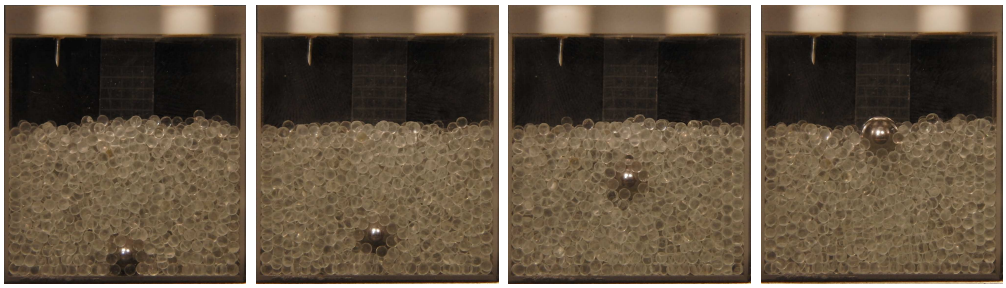

Fig. 6.2: Snapshots from experiments illustrating how a water-immersed steel Brazil nut rises through a glass granular bed when vibrated with parameters $f = 15$ Hz and $\Gamma = 3.5$. The intruder initially begins in the bottom of the bed away from the wall and remains so while rising through the bed.

between the cell base and the bottom of the bed and the cell is moving upwards with velocity $\dot{z}_c = A\omega$. We define this position of the cell to correspond to a phase angle $\theta = 0°$. The error bars were obtained from averaging the intruder trajectories over five independent runs.

Figure 6.3 shows that under vibration the large intruder will rise through the bed until it eventually breaks the bed surface. For all the vibratory conditions we have investigated we find that the vertical motion of the Brazil nut accelerates as it moves upwards through the bed. Figure 6.3 shows that as Γ is increased the speed with which the intruder rises increases due to the greater amount of energy input into the intruder and bed.

Under the vibratory conditions that we have investigated, there is very little convective motion of the bed in the absence of the intruder. With the intruder present, the upward motion of the Brazil nut drives two vertical convection rolls within the cell. This shows that, in our system, the intruder does not rise due to convective effects alone. We have also carried out experiments in the absence of the liquid. We find that, under the same vibratory conditions, the bed is highly fluidised and the intruder either rises slowly or remains within the bed. Clearly, the presence of the liquid has a strong effect on the intruder's behaviour.

We note that there is some dependence of intruder rise time on the position in the cell between the front and back faces. Intruders that are in contact with one of these faces rise typically about 15% faster than those initially positioned in the middle. In our experiments we try to start with the intruder away from

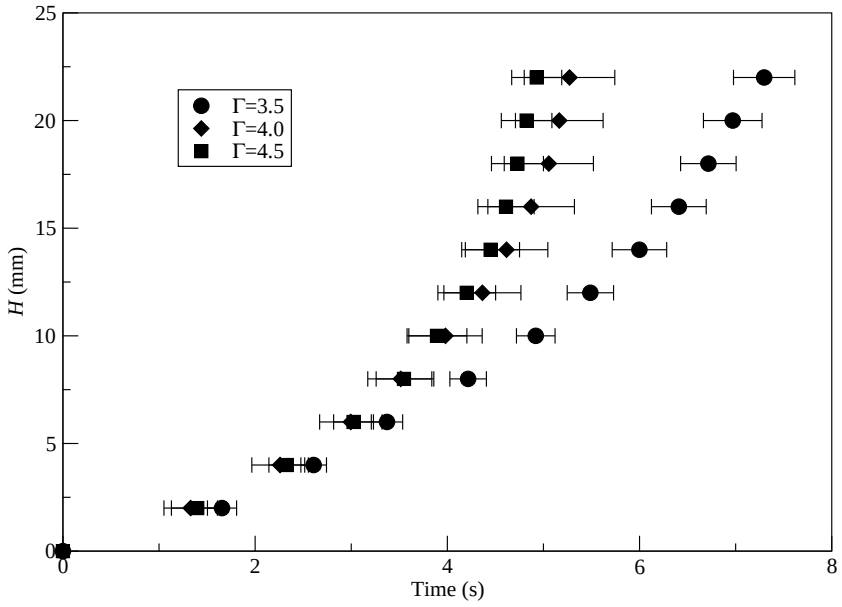

Fig. 6.3: Intruder gap H plotted against time, t, when vibrated vertically with parameters $f = 15$ Hz and $\Gamma = 3.5$ (circles), $\Gamma = 4.0$ (diamonds) and 4.5 (squares). The error bars correspond to the standard error calculated over five independent trajectories.

these walls.

We now perform numerical simulations of the experimental system. This allows us to obtain detailed information about the intruder mechanism that is otherwise unattainable from experiments.

6.4 Simulations

In this section we perform simulations, firstly using the Fluid Springs (FS) model and then using the Simple Drag (SD) model. These simulations attempt to reproduce the results obtained within experiments. These models are described in detail in Sections 2.5.2 and 2.4.1. We present results for particles that interact through the Damped Hertzian (DH) contact forces described in detail in Section 2.1.1. We have observed that the total time taken by the steel intruder to rise through the bed is greatly affected by the "hardness" of the spheres. Therefore we use real particle properties to model the granular interactions accurately. Within these collisions the damping parameter was chosen so that the coefficient of restitution is 0.2 for relative impact velocity of 0.25 m s^{-1}. However, we note that

Parameter	*Value*
Number of particles	1350
Host density ρ_H	2500 kg m^{-3}
Host Diameter d_H	2 mm
Host Young modulus E_H	7.02×10^{11} N m^{-2}
Host Poisson ratio σ_H	0.24
Intruder density ρ_I	7750 kg m^{-3}
Intruder diameter d_I	7 mm
Intruder Young modulus E_I	21.1×10^{11} N m^{-2}
Intruder Poisson ratio σ_I	0.30
e	0.2
μ, μ_W	0.25
Fluid density ρ	1000 kg m^{-3}
Dynamic viscosity η	10^{-3} kg m^{-1} s^{-1}
Time-step Δt	5×10^{-7} s
Cell size L_x (x–axis)	40 mm
Cell size L_y (y–axis)	10 mm
Cell size L_z (z–axis)	43 mm
f	15 Hz
Γ	3.5–4.5

Table 6.1: Parameters for Brazil nut simulations using the SD model.

the global behaviour is rather insensitive to this value due to lubrication effects, which are captured by the Fluid Springs model as demonstrated in Section 2.8.

Tangential frictional forces between the grains themselves and between the grains and the walls of the cell are also important to the BNE. Coulomb's friction between particles is also included using equation 2.3. Here the coefficient of friction μ was chosen to be 0.25 between particles and between particles and walls, a value that was found to best match simulation with experiment.

For both the FS and SD simulations we chose our parameters appropriate to model a steel intruder vibrated in a water-immersed glass bed. We use a system

Parameter	*Value*
Lattice spacing Δ	3.33×10^{-4} m
Fluid time-step Δt	1.0×10^{-4} s
Host C_s	0.6
Host n_r	3
Intruder C_s	0.5
Intruder n_r	10.5

Table 6.2: Parameters for Brazil nut simulations using the FS model. These are in addition to those shown in Table 6.1.

of 1350 spherical glass particles of equal radii, $r_H = 1$ mm, with a 10% variation in size to avoid crystallisation. The steel intruder has radius $r_I = 3.5$ mm. The density of the host material is $\rho_H = 2500$ kg m^{-3} and the density of the intruder is $\rho_I = 7750$ kg m^{-3}. The water has a density $\rho = 1000$ kg m^{-3} and viscosity $\eta = 1 \times 10^{-3}$ kg m^{-1} s^{-1}. The cell used has the same dimensions as those used in experiments.

To improve numerical efficiency within the FS model, we use time-steps of 5×10^{-7} s to resolve the particle motion and 1×10^{-4} s for the fluid motion. The simulation parameters for the SD and FS models are summarised in tables 6.1 and 6.2 respectively.

The simulation arrangements are set up in a similar way for both coupling techniques. The grains are randomly distributed throughout the cell and then allowed to settle onto the cell base until completely at rest. The grains settle under the influence of gravity only. In the FS model simulations the cell is then shaken with fluid drag acting upon the particles so that transient effects may be removed. During this time the large intruder is fixed to the cell base. After one second of vibration the intruder is released from the cell base at a time corresponding to a phase angle of $\theta = 0°$. The intruder is then allowed to rise through the bed and data is recorded. Within both simulation models the cell is vibrated at frequency $f = 15Hz$ for vibration amplitudes corresponding to $\Gamma =$ 3.5, 4.0 and 4.5.

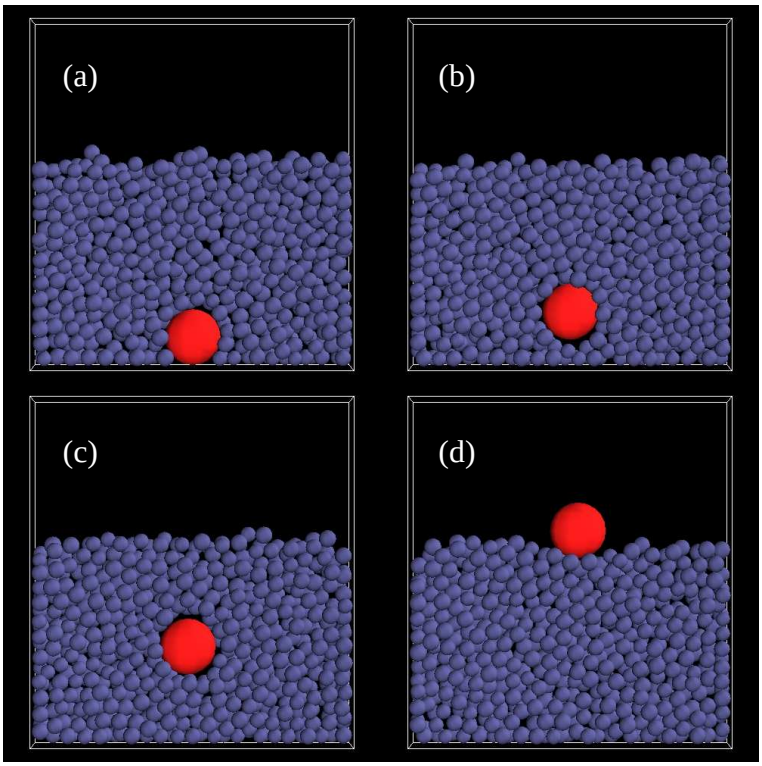

Fig. 6.4: A sequence of snapshots showing the time evolution of a large steel intruder within a glass bed immersed in fluid and vibrated vertically at $f = 15$ Hz and $\Gamma = 3.5$. The times, t, correspond to (a) 0 s, (b) 2 s, (c) 5 s and (d) 8 s.

6.4.1 Fluid Springs Model

Figure 6.4 shows the time-evolution of the large steel Brazil nut within the bed of glass particles, simulated using the Fluid Springs model. The images show vertical cross-sections through the centre of the bed. The bed is immersed in a water-filled cell with the steel sphere initially positioned in the middle of the cell base. The system is vibrated vertically at $f = 15$ Hz for $\Gamma = 3.5$. As the system evolves the steel sphere moves upwards through the bed until eventually it emerges through the bed surface. During the motion the intruder remains in the bulk of the bed, away from the front and back walls. Once reaching the surface, the particle remains there for timescales accessible to simulation.

Figure 6.5 shows the gap between the intruder's lower surface and the cell base, H, plotted against time, t, for vibration parameters $f = 15$ Hz and $\Gamma = 3.5$, 4.0 and 4.5. H is recorded at the beginning of each cycle of vibration when $\theta = 0°$. The simulation data presented in Figure 6.5 was averaged over five independent runs as in the experiments. Here we observe that the Brazil nut

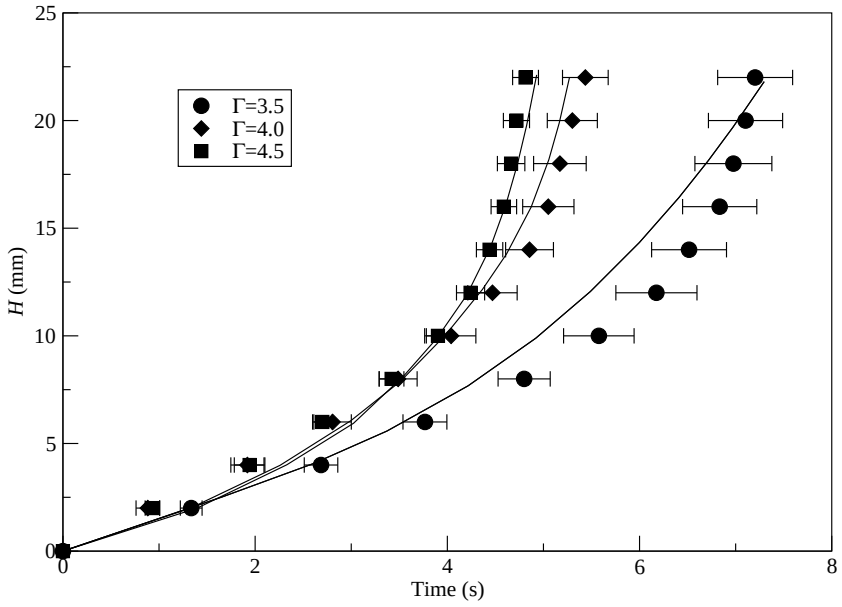

Fig. 6.5: Simulation results using the Fluid Springs model for the intruder gap H as a function of time, t, for a steel intruder in a water-immersed glass bed. The vibration parameters are $f = 15$ Hz and $\Gamma = 3.5$, 4.0 and 4.5. The error bars show the standard error calculated from five independent trajectories. The lines are polynomial fits to the corresponding experimental data, Figure 6.3, included here for comparison.

rises upwards through the bed for all of the vibration amplitudes considered. As in experiments, when Γ is increased the overall rise time of the intruder reduces. Figure 6.5 shows that the simulation results give very good agreement with those obtained in experiments.

We note that in the experiments, the rise times are sensitive to the cleanliness of the granular bed. Consequently, the grains and cell were cleaned prior to each experimental session. Similarly, the simulations are sensitive to the friction parameter μ.

As was noted within experiments, the Brazil nut rises at a faster rate when in contact with either the front or back cell wall. Figure 6.6 plots the gap, H, as a function of time, t, for the steel intruder when it is either fixed to the front wall or fixed in a plane half way between the front and back cell walls. The error bars again show the standard error calculated from five independent runs. Figure 6.6 shows that the Brazil nut rises considerably faster when fixed to the front wall. This is because the glass grains within the granular bed are able to move

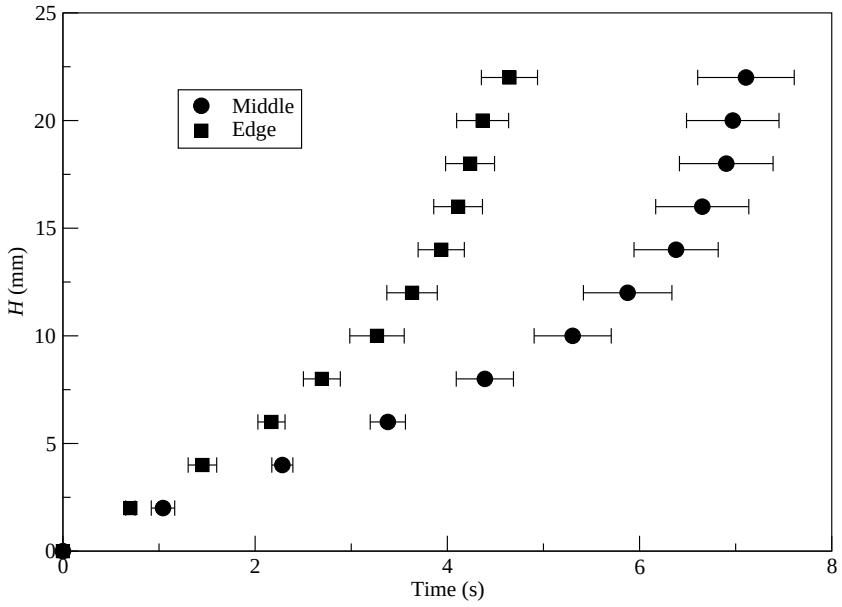

Fig. 6.6: Simulation results for the intruder gap H as a function of time, t, for a steel intruder fixed either on the front wall (squares) or half way between the front and back walls (circles). The vibration parameters are $f = 15$ Hz and $\Gamma = 3.5$. The error bars show the standard error calculated from five independent trajectories. The system is simulated using the Fluid Springs model.

downwards past the large intruder easier when the intruder is fixed to the front surface.

Figure 6.7 plots the normalised intruder position between the front and back walls, y_{norm}, against time, t. We evaluate the normalised position using $y_{norm} = (y_I - r_I) \,/\, (L_y - 2r_I)$, where y_I is the position of the intruder within the cell along the y–axis. Five runs are performed with the intruder initially positioned on the front wall and five runs are performed with the intruder initially placed in the centre of the cell base. The intruder trajectories have been plotted while the intruder is contained within the bed. When the Brazil nut reaches the surface of the bed we stop recording the intruder position as it is then free to move wherever within the cell. In both instances we observe that the intruder does not move far from its initial position. When the intruder begins on the front wall only once does the Brazil nut move towards the middle. Similarly when initially positioned in the middle of the cell the Brazil nut only once moves towards the front or back wall, which occurs very near the surface of the bed. As in Figure 6.6 we observe that the intruder emerges from the bed faster when initially positioned on the

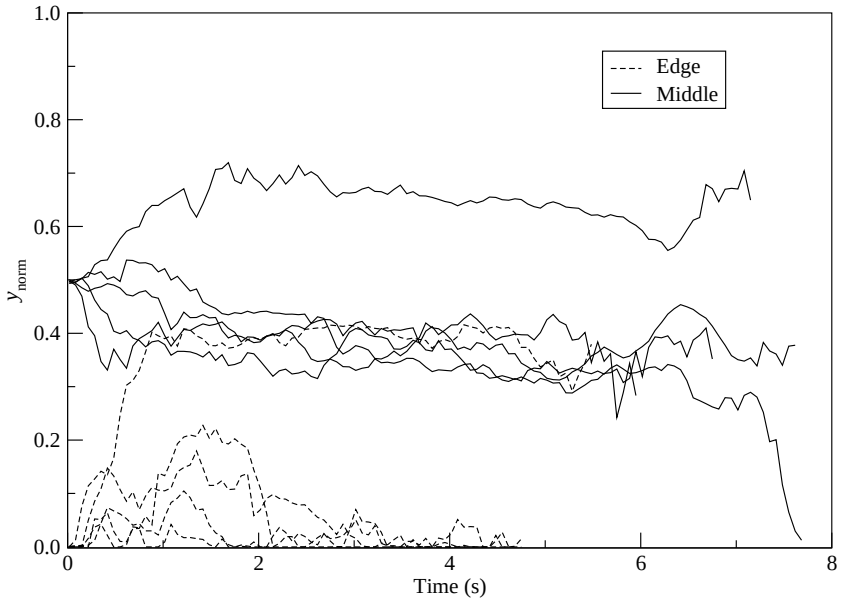

Fig. 6.7: Simulation results for the normalised position of the intruder between the front and back walls, $y_{norm} = (y_I - r_I) / (L_y - 2r_I)$, as a function of time, t, for a steel intruder in a water-immersed glass bed. The intruder is free to move within the cell and is initially placed either on the front wall (dashed-lines) or half way between the front and back walls (solid-lines). The vibration parameters are $f = 15$ Hz and $\Gamma = 3.5$. The system is simulated using the Fluid Springs model.

front wall. The movement of the intruder between the front and back walls may contribute to the standard error obtained within experiments and simulations, figures 6.3 and 6.4.

6.4.2 Simple Drag Model

The same system is now simulated using the SD model. This model couples the particles to the surrounding fluid using a drag force which is applied explicitly onto the particles in a manner which opposes the direction of motion of the particles. The strength of the drag force is determined using Ergun's empirical bed equation, equation 2.70. Note that in models of this type the fluid influences the particles, but the particles do not influence the fluid.

In these simulations we find that the Brazil nut does not rise from its initial starting position for all of the vibration amplitudes we study. The main difference between the FS and SD models is that, in the SD model, the fluid influences the particles but the particles do not influence the fluid. This difference in behaviour

suggests that the motion of the intruder is sensitive to details of the fluid flow. The fluid and grain motion around the intruder will be discussed in the following section.

6.4.3 Fluid-Enhancing Mechanism

Figure 6.8 shows the time-averaged fluid and granular flow around the Brazil nut when in flight for vibration parameters $f = 15$ Hz and $\Gamma = 3.5$. The flows were recorded once every vibration cycle at a phase angle of $\theta = 90°$. The results were averaged over 101 cycles of vibration, the duration for which the intruder remains within the bed.

Figure 6.8(a) shows the fluid flow while Figure 6.8(b) shows the corresponding granular flow. Figure 6.8(a) shows that as the intruder is thrown fluid is forced upwards and away from the space above the intruder while simultaneously being drawn towards the space beneath. Figure 6.8(b) shows that the grains are strongly influenced by the fluid and follow a similar trajectory. In particular the horizontal motion of the fluid below the intruder drags grains sideways eliminating any tendency for a void to develop beneath the intruder. It is this void-filling ratcheting mechanism that is responsible for the fluid-enhanced BNE.

Note that the sideways motion of the glass grains is substantially reduced in the SD model simulations because it is damped by the fluid as shown in Figure 6.9. Here we observe that no grains move horizontally towards the gap that develops beneath the intruder as it is thrown upwards. For this reason the intruder does not rise when using the SD model for the parameters which we have used.

We now propose an analytical approach which may be solved numerically to model the ascension of the Brazil nut.

6.5 Analytical Model

The connection between the Γ dependent rise times and the drag forces on the intruder as a result of the fluid and granular bed can be described by a simple analytical model. This model takes into account the interactions between the bed, the intruder and fluid flow during each cycle and enables us to deduce the

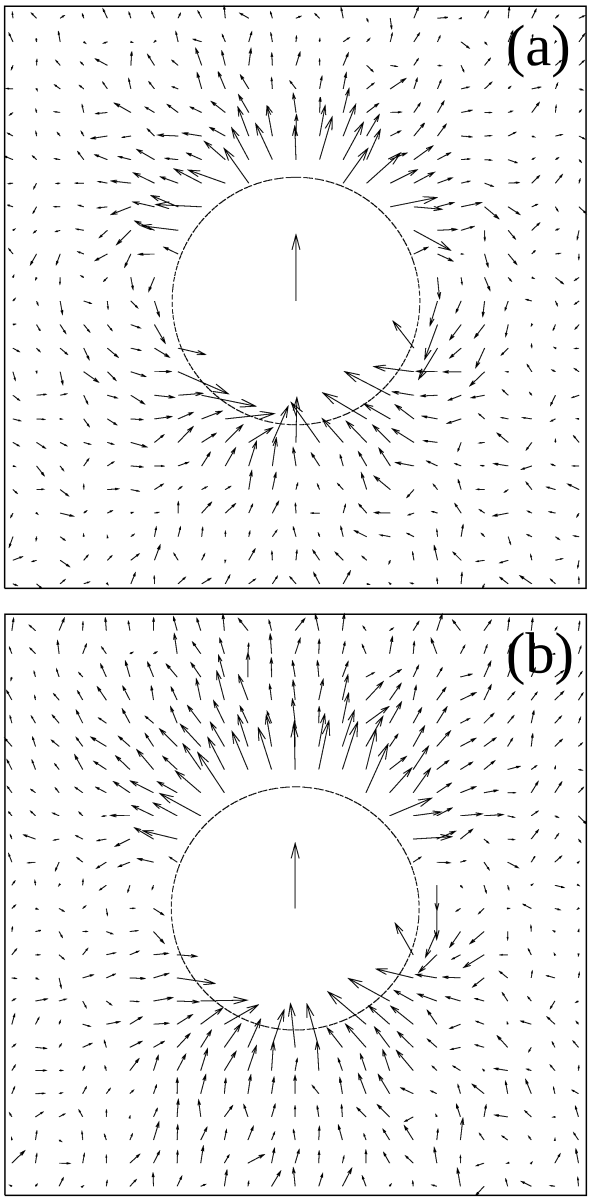

Fig. 6.8: Average (a) fluid and (b) grain motion relative to the centre of mass of the steel intruder using the Fluid Springs model. Both results were obtained at a phase angle of $\theta = 90°$ when the granular bed is moving upwards relative to the cell. The vibration parameters were $f = 15$ Hz and $\Gamma = 3.5$. The flows were averaged over 101 vibration cycles, the time taken for the intruder to reach the surface. The arrows in the centre of the Brazil nut shows the sphere velocity relative to the cell of 94 mm s^{-1} at this stage of the cycle. The magnitude of the fluid and grain velocity vectors are drawn to the same scale.

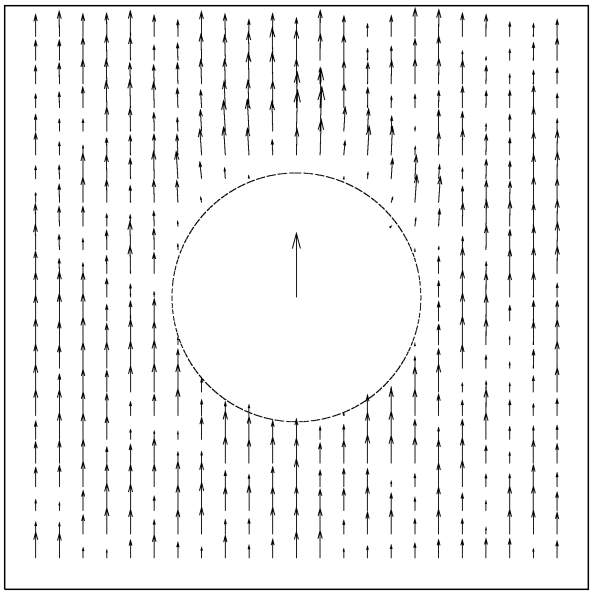

Fig. 6.9: Average grain motion relative to the centre of mass of the steel intruder using the Simple Drag model. The results were obtained at a phase angle of $\theta = 90°$ when the granular bed was moving upwards relative to the cell. The vibration parameters were $f = 15$ Hz and $\Gamma = 3.5$. The flow was averaged over 900 vibration cycles. The arrow in the centre of the Brazil nut shows the sphere velocity relative to the cell of 80 mm s^{-1} at this stage of the cycle. The magnitude of the grain velocity vectors are drawn to the same scale.

net displacement of the intruder. Our model differs from that of Möbius *et al.* (2005) as the fluid is treated as being incompressible and an explicit drag force is included to model the intruder-grain interactions during flight.

The model can be considered in two parts: during the first part we describe how we treat the granular bed and in the second part we describe how the Brazil nut's motion is coupled to that of the bed. Finally a quantitative comparison between the analytical results and those obtained through experiments is given.

In our simple model the bed is treated as a fluid-immersed porous medium which is thrown from the base during each vibration cycle; the trajectory is calculated using Newton's laws of motion. The intruder is modelled as a dense object which is allowed to move vertically through the bed in both an upwards and downwards direction.

If the glass granular bed and steel intruder are thrown independently from a surface they follow the same trajectories. When the granular bed and intruder

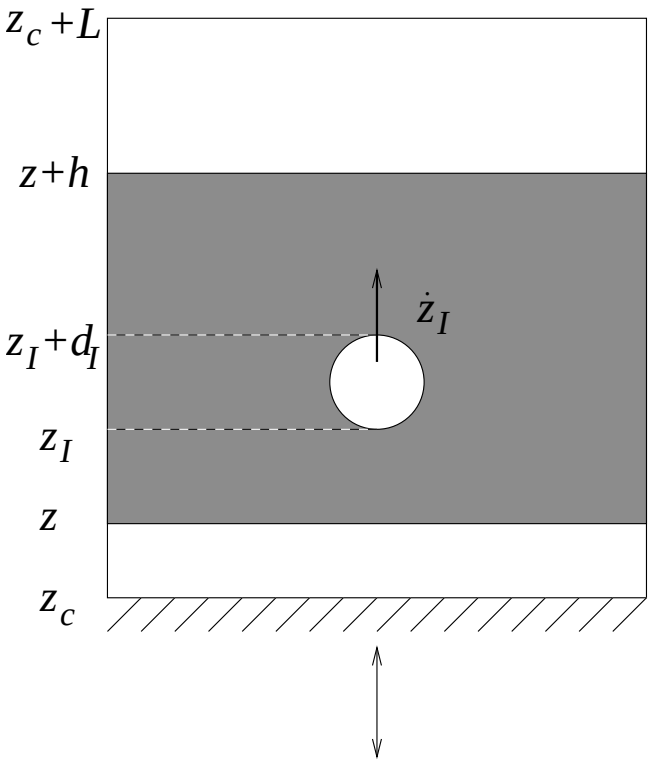

Fig. 6.10: Schematic diagram of a Brazil nut rising through a porous bed in a vibrating cell.

are then immersed in a fluid and thrown from the same surface the granular bed will land first as it experiences greater drag. The key finding of our simulations was that grains fill gaps beneath the intruder as it is thrown due to the two-dimensional fluid motion dragging grains into the gaps. To examine this motion a microscopic fluid model was necessary, however, this effect may be modelled in an analytical model by enforcing a condition so that gaps beneath and above the intruder are always filled. Thus when the intruder is immersed in the granular bed its flight is cut short and ends the moment the granular bed lands. This means that in each cycle the intruder is elevated by a small amount as it is unable to complete its trajectory. In addition a frictional drag force is applied explcitly on the intruder to couple the Brazil nut motion to the bed.

A schematic representation of the intruder immersed in the granular bed is shown in Figure 6.10. We now describe how the different parts of the model are constructed in more detail.

Granular Bed

Despite the presence of the large intruder the granular bed is treated as a single homogeneous porous medium which is made up of host particles of radii r_H. The bed is treated as being several orders of magnitude more massive than the intruder so that any momentum transfer from the intruder to the bed is considered to be negligible and can therefore be ignored. The granular bed is thrown and lands within each vibration cycle, without dilation, according to Newton's laws of motion. The fluid is treated as incompressible with density ρ and dynamic viscosity η so that as the cell is vibrated the bed lifts off from the cell base and fluid flows through the bed to occupy the space beneath. As the bed lands fluid flows in the opposite direction upwards through the bed providing drag to the granular bed motion. We use the Modified Kroll model, described in Section 2.4.1, to model the flight of the bed. The equation of motion of the bed may be given as

$$\dot{u}\left(1+\frac{\rho(1-\phi)}{\rho_H\phi}\right)+\frac{\rho_H-\rho}{\rho_H}\left(g+\ddot{z}_c\right)+\gamma u=0, \tag{6.1}$$

where $u=\dot{z}-\dot{z}_c$ is the rate of change of the gap between the cell base and the bottom edge of the porous bed. ϕ is the bed porosity, which for convenience is fixed to be the random packing fraction of $\phi=0.42$. Although in simulations there may be variations in the porosity with height we assume that these are small and ϕ is uniform across the bed. g and $\ddot{z}_c$ are the accelerations due to gravity and motion of the base, respectively. The drag parameter γ is related to the pressure gradient across the bed ∇P through the equation $\gamma u=-\nabla P/(1-\phi)\rho_H$. In our model $-\nabla P$ is determined using the empirical bed equation of Ergun

$$\nabla P=\left[\frac{37.5\eta\left(1-\phi\right)^2}{r_H^2\phi^3}+\frac{0.875\rho\left(1-\phi\right)|u|}{r_H\phi^3}\right]u. \tag{6.2}$$

Dense Intruder

The large intruder has density ρ_I and radius r_I and is restricted to only move upwards and downwards in a vertical direction within the bed. We have seen already that as the intruder is thrown and falls within each vibration cycle it drags host particles with it. Thus it is assumed that at the moment the granular bed lands the intruder also lands, but in a slightly elevated position. In the

simulations there is a small amount of downward penetration by the Brazil nut, however, this motion is ignored in the analytical model as it is difficult to capture accurately. The force within the analytical model is applied explicity to the Brazil nut and its equation of motion in the vertical direction, relative to the box, may be written in the general form

$$\rho_I V_I \frac{d^2 z_I}{dt^2} = -(\rho_I - \rho) V_I (g + \ddot{z}_c) + F_d. \tag{6.3}$$

Here M_I is the intruder mass and F_d is the drag force on the intruder due to presence of the fluid and the granular bed. The drag force is the sum of two further forces, $F_d = F_{fluid} + F_{bed}$. Here F_{fluid} is the drag on the intruder due to the presence of the fluid and F_{bed} is the drag due to the presence of the bed.

To determine the fluid drag on the intruder, F_{fluid}, a simple drag force of the form seen in Section 2.4.1 is used:

$$F_{fluid} = \frac{\frac{4}{3}\pi {r_I}^3 (-\nabla P)}{1 - \phi}. \tag{6.4}$$

The pressure gradient across the bed is again obtained using Ergun's empirical bed equation 6.2. This is a similar force to that experienced by the granular bed, however, a further force is required to model the collisions of the intruder with the host particles as it moves through the bed.

The force on the intruder due to the presence of the granular bed is dependent on many factors including relative velocity, material densities, packing fractions and friction. The motivation for our form of the force came from related experiments where dense spheres penetrate static beds of noncohesive granular spheres (Ambroso *et al.* 2005; Tsimring and Volfson 2003). Here it was experimentally determined that for low impact velocities the frictional force dominates and has a height dependence (Ambroso *et al.* 2005). In our model the intruder and granular bed always move in a similar direction so that the relative velocity is small and this approximation may be applied. Thus in our model we assume a frictional force F_{bed} which opposes the relative motion and is assumed to have a depth dependence of the form

$$F_{bed} = \alpha \left[1 - \exp\left(-\frac{h - (z_I - z + r_I)}{l} \right) \right] \frac{v}{|v|}. \tag{6.5}$$

Here $v = \dot{z}_I - \dot{z}$ is the relative velocity between the intruder and the distant bed particles, h is the height of the bed, α is the force strength and l is a length.

Both α and l are fitting parameters which we assume to be dependent on Γ. This variation of force with intruder depth is assumed to have the same form as the time-averaged density profile of host grains because, during flight, the intruder only interacts with grains locally. The density profile has been argued to be well approximated by a Fermi function (Hayakawa and Hong 1997) and the form used here is an expansion for agitated beds. The length l is a measure of the fluidisation of the bed and the force strength α is related to the weight of grains pushed by the intruder in the convection cycles. The bed force, F_{bed}, goes to zero as the intruder emerges from the bed.

We note that the form for F_{bed} that we have assumed is the same as that derived by Janssen (1895) for the depth dependence of the stress in a static granular bed. However, in the static case the length l is related to the saturation of the stress due to side-wall friction.

Analytical Model Results

In this section we compare results produced using the analytical model to those obtained from experiments.

Figure 6.11 plots the the intruder rise time curves, predicted by the analytical model, for vibration parameters $f = 15$ Hz with $\Gamma = 3.5$, 4.0 and 4.5. On the same graph we have plotted the experimental points for comparison. The best fit parameters used within the analytical model are as follows: for $\Gamma = 3.5$; $\alpha = 9.83\times10^{-3}$ N and $l = 4.0$ mm, for $\Gamma = 4.0$; $\alpha = 1.208\times10^{-2}$ N and $l = 4.2$ mm and for $\Gamma = 4.5$; $\alpha = 1.445\times10^{-2}$ N and $l = 4.5$ mm. In each case l is of the order of a few grain diameters and α is the same order of magnitude as the effective weight of grains pushed by the intruder. These values are consistent with the assumptions of the model. The force strength α increases with Γ due to the greater force experienced by the intruder as it is thrown and collides with the granular bed. The length-scale l increases with Γ also due to the greater fluidisation of the bed. Figure 6.11 shows that the analytical model is able to capture the intruder trajectories reasonably accurately.

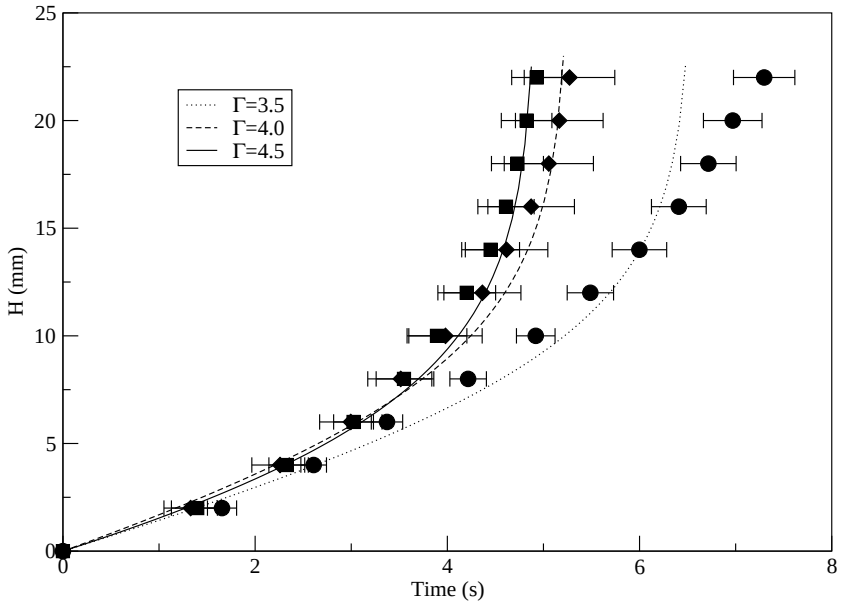

Fig. 6.11: The lines show the intruder gap H plotted against time, t, predicted by the analytical model. The experimental data points are also shown for comparison. The vibration parameters are $f = 15$ Hz and $\Gamma = 3.5$ (dotted-line and circles), 4.0 (dashed-line and diamonds) and 4.5 (solid-line and squares).

6.6 Summary

We have shown experimentally that the presence of a liquid can dramatically influence the behaviour of a dense intruder in a vibrated granular bed. Specifically, a large steel intruder was observed to rise rapidly to the surface of a bed of water-immersed glass particles when subjected to vertical vibration. To gain insight into this behaviour, we modelled the effect using simulations and found that a fluid-grain coupling technique based on a microscopic fluid-particle model was able to capture the process, both qualitatively and quantitatively. The simulations allowed a detailed investigation into the mechanism.

At the beginning of each vibration cycle the steel and glass particles are thrown upwards. Due to its larger mass and size, the steel intruder is slowed less by the fluid drag than the glass spheres. As the intruder is thrown upwards the void beneath it, that would be created due to the relative motion, is quickly filled with grains dragged by the fluid. Later in the cycle the intruder falls, reversing the direction of fluid flow, which in turn decelerates the motion of the grains beneath it. However, due to the grains' inertia, this flow is insufficient to return

them to their original position. This rearrangement is also strengthened as it is easier for the grains to move into a low density region, rather than in the opposite direction. The net result is that the intruder draws fluid and grains beneath it as it is thrown and later in the cycle lands on these particles increasing its vertical position. It is this fluid-enhanced ratcheting mechanism that causes the Brazil nut to rise rapidly through the bed.

Finally, a simple analytical approach to model the fluid-enhanced BNE was described. Our model introduces a drag force between the intruder and the bed which allow us to accurately predict the trajectories of the intruder.

Chapter 7

Zero-Gravity Fluid-Immersed Granular Suspensions

A system of fluid-immersed grains vibrated within a zero-gravity environment will form layers perpendicular to the cell oscillations. In this chapter we undertake a computational study reproducing effects observed in similar experiments performed within a magnet.

7.1 Introduction

In the last few years there has been a lot of interest in pattern formation involving granular materials (Aranson and Tsimring 2006). For example, dry granular beds under vibration have been found to form surface patterns (Melo *et al.* 1995) or stripes (Mullin 2000). If grains are immersed in a fluid they may exhibit a wide range of pattern formation behaviour due to the interaction between the particles and the fluid.

In experiments performed by Wunenburger *et al.* (2002) a system of spherical grains, vibrated horizontally on a surface within a water-filled cell, will align perpendicular to the direction of oscillation. The interaction leading to the alignment was suggested to occur due to the steady streaming effect induced by the oscillating motion of grains relative to the fluid (Riley 2001). Steady streaming is defined as the non-zero flow that results from calculating the time-average of a fluctuating flow for the non-linear terms in the Navier–Stokes equation. Such steady

streaming is a result of the viscous nature of fluid and the Reynolds stresses that occur in the main body of the fluid. In other experiments performed by Voth *et al.* (2002), at around the same time as Wunenburger's, it was found that fluid-immersed particles vibrated vertically on a horizontal surface form regular lattices. Voth et al. proposed a model based on steady streaming to explain the attractive part of the interaction which leads to the formation of the pattern. Klotsa *et al.* (2007) then examined a simpler system containing just two spheres in a fluid-filled cell under horizontal vibration. They studied how a pair of particles always align in a direction perpendicular to oscillation with the spheres separated by a well defined distance. More recently Klotsa *et al.* (2009) focused on chain formation within experiments and simulations. This study showed that the returning steady streaming flows perpendicular to the oscillations induces a strong attractive force towards the free ends of the chains. Thus, providing the vibrated cell is sufficiently wide, roaming single particles and short chains will be drawn into the free end of the chain enhancing its length.

Beysens *et al.* (2008) have observed ordering phenomena of bubbles within an oscillating fluid. Their experiments investigated the liquid-vapour phase transition of hydrogen during high frequency ($f = 10$–25 Hz) and low amplitude (0.3–0.47 mm) vibrations in a weightless environment. Gravity effects were negated using a strong magnetic-field gradient. The experiments were performed near the liquid-vapour critical point. It was observed that, as the system was vibrated, vapour bubbles nucleate and grow in the liquid phase. When these bubbles grew to a sufficient size the bubbles would move with a different velocity to the oscillating fluid. The bubbles then ordered themselves in planes perpendicular to the vibration motion.

Due to the moving fluid-vapour interfaces associated with these experiments it is difficult to recreate such a system within simulations. One possible solution is to shake fluid-immersed grains, instead of the vapour bubbles, in a system without gravity. Grains immersed in an oscillating fluid will move with a different velocity to the fluid. As there is no gravity the particles will be affected by the resulting streaming effects only.

Similar effects may be reproduced in experiments using fluid-immersed dia-

Fig. 7.1: Snapshot from experiments showing layer configuration of 50 μm diameter water-immersed bismuth particles when shaken within a magnetic field. The experiments were performed within an Oxford Instruments Minimum Condensed Volume (MCV) superconducting magnet with a maximum central field of 17 T and maximum field gradient of $BdB/dz = 1470$ T^2 m^{-1}. Here the oscillations are in a vertical direction perpendicular to the granular layers.

magnetic particles held within a strong inhomogeneous field. The magnetic field is tuned so that the particles are weightless at some height within the magnet. Thus, when the cell is shaken, the particles will experience drag relative to the fluid and streaming flows are formed. However, due to the magnetic field gradients there is only a small area over which the particles are weightless. Figure 7.1 shows a snapshot of shaken water-immersed bismuth particles within a strong magnetic field in experiments performed at Nottingham University. Here we see that the bismuth particles organise themselves into distinct layers perpendicular to the oscillation motion.

In the next section we detail results obtained from simulations studying pattern formation of fluid-immersed granular suspensions within a zero-gravity system.

Parameter	*Value*
Number of particles	720
Particle density	4000 kg m^{-3}
Particle diameter	2 mm
Spring constant k_n	3000 kg s^{-2}
e	0.2
μ, μ_W	0.2
Fluid density ρ	1000 kg m^{-3}
Dynamic viscosity η	4×10^{-3} kg m^{-1} s^{-1}
Lattice spacing Δ	3.33×10^{-4} m
Cell length L_X, L_Y, L_Z	33.3 mm
n_r	3
C_S	1.0
Δt	1×10^{-4} s
f	50 Hz
Γ	5.0

Table 7.1: Parameters for the zero-gravity fluid-immersed granular suspension simulations when using the Fluid Springs model.

7.2 Simulations

In order to study granular pattern formation in vibrated zero-gravity fields we perform simulations. We use 720 spherical particles of diameter 2 mm and density 4000 kg m^{-3}. The particles and fluid are held in a cubic cell of dimensions $L_X = L_Y = L_Z = 33.3$ mm, where L_i is the cell length along the i–axis. In these suspension simulations the inter-particle collisions are rare due to the fluid streaming flows holding particles apart. Hence realistic collisions dynamics are not necessary, so for computational efficiency the contact forces are modelled using the LSD collision scheme, described fully in section 2.1.1. We use a spring constant of $k_n = 3000$ kg s^{-2} in equation 2.1 and choose γ_n so that the coefficient of restitution e is equal to 0.2. Friction between particles, μ, and friction between particles and walls, μ_W, are both set to 0.2.

The fluid used has a viscosity four times that of water so that $\eta = 4{\times}10^{-3}$ kg m^{-1} s^{-1} whereas the fluid density is the same as water $\rho = 1000$ kg m^{-3}. The fluid-grain coupling model we use is the FS model, described comprehensively in Section 2.5.2. At all times there is no gravitational force acting upon the particles or fluid. The cell is shaken sinusoidally in the vertical direction with vibration parameters $f = 50$ Hz and $\Gamma = 5.0$. The simulation parameters are summarised in Table 7.1.

Figure 7.2 shows snapshots of the shaken particle system as it evolves with time. The particles are initially dispersed randomly within the cell, as shown in Figure 7.2(a). Soon after shaking starts the grains begin to converge and order themselves into "layers" perpendicular to the vibration motion as seen in Figure 7.2(b). After just 5 s the grains have ordered themselves into two distinguishable layers which span the entire cross-section of the box as seen in Figure 7.2(c). At 5 s the layers are still forming and there are a few free particles and smaller groups of particles which have not yet merged with a larger layer. We also observe that some parts of the layers are often two or more particles thick. These layer configurations are stable as we find that once the grains group into layers they remain so. However, after $t = 15$ s, we observe that the thicker parts of the layers are less stable. In Figure 7.2(d) we notice that the thick part of the top layer "forks" into two thinner layers on the right-hand edge of the cell. When a granular layer forks it means that it splits vertically into thinner layers which are still attached together. By $t = 75$ s all of the free particles have merged into the two layers. This configuration is stable for the timescales accessible to us.

Thus we see that there are behavioural similarities between the chains and the layers. We find that the layers position themselves a reasonable distance apart within the box perpendicular to the vibration motion as was observed in the chain simulations and experiments of Klotsa *et al.* (2009). Klotsa *et al.* noted that chains are highly unstable when they are more than one particle thick parallel to the oscillations. Any excess grains tend to be repelled due to the strong streaming flows perpendicular to the chain. This is very different to the behaviour exhibited by the layers in Figure 7.2 which are very often more than one particle in thickness. The layer configuration may not always be completely

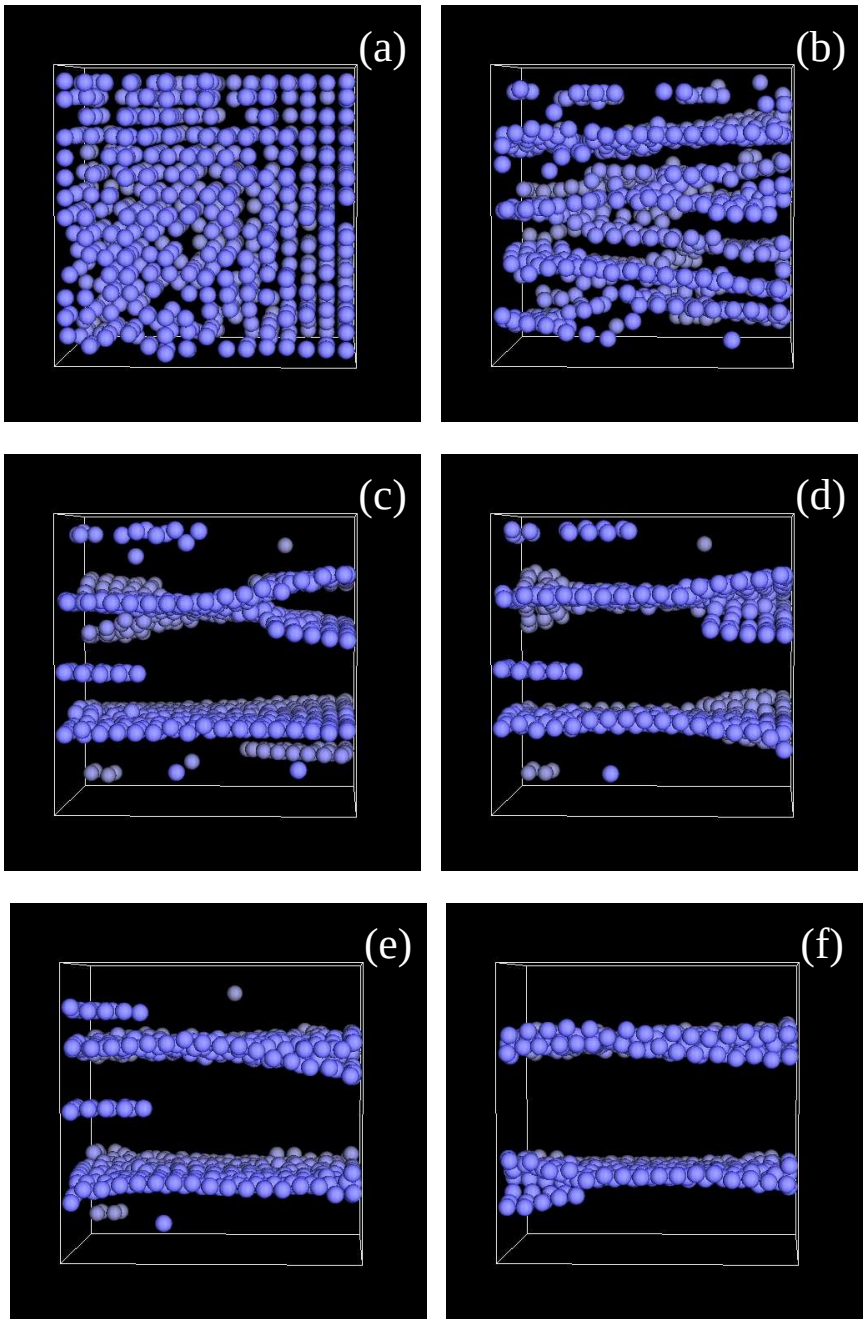

Fig. 7.2: Snapshots from simulation showing the time evolution of 720 fluid-immersed spheres of diameter 2 mm vertically vibrated within a cubic cell at $f = 50$ Hz and $\Gamma = 5.0$. The timings correspond to (a) $t = 0$ s, (b) $t = 1$ s, (c) $t = 5$ s, (d) $t = 15$ s, (e) $t = 40$ s and (f) $t = 75$ s.

stable, as evidenced by the layers forking, but once the grains are within the layers they remain so indefinitely.

We have performed some simulations which have allowed the study of the basic characteristics and behaviours of fluid-immersed granular beds shaken within a weightless environment. We summarise the main properties we observed in the next section.

7.3 Summary

In this section we make a note of the main characteristics we observed within the simulations and suggest where the studies of such systems may be taken in the future. The main behaviours that we observed were these:

a) The grains form layers perpendicular to the vibration motion after initially being positioned in a randomised state. The layers are the natural state for the particles to reside.

b) The layers will initially choose to be a single particle diameter in thickness. As grains are added to the layer it will grow until it spans the entire cell cross-section. On the addition of further grains the layer will grow in thickness so that it may be two or more grains thick in the direction normal to vibration. This configuration is also stable unlike that seen in the chains (Klotsa *et al.* 2009).

c) There is some level of repulsion between layers as the two thick layers are not attracted to one another within the cell.

d) The layers are stable as no particles leave the layer once they have merged with it.

e) If the layer becomes thick, i.e. more than a single particle deep, the layer is prone to "forking". Here the layer splits into two or more thinner layers which are still attached to the bulk of the bed. This behaviour may be seen in the later time periods of Figure 7.2 and tends to occur near the cell walls.

In this chapter we have observed some of the zero-gravity granular suspension characteristics, however, this study has been brief and there are many things which are not understood which would require attention in the future. We would want to study the flows around the layers and explain how it is possible for thick layers to be stable. We would also want to understand the attractive and repulsive forces between layers and why thick layers fork into thinner layers.

Chapter 8

Concluding Remarks

A brief review of the main findings of the research are presented in this chapter. We also include some suggestions for future work involving fluid-immersed granular systems.

8.1 Chapter Review

In the first chapter of this thesis we introduced the reader to the vast field that is granular dynamics. We underline the widespread occurrence of granular materials and their pervasiveness into many aspects of our daily lives. We emphasise the importance of these materials within many industries including the pharmaceutical, agricultural and construction-based industries as well as their complex and often counter-intuitive behaviours. The chapter finishes by introducing the reader to fluid-grain systems. The vast majority of granular systems, unless held within a vacuum, will in some way be affected by the interstitial fluid in which they are immersed. It is important to understand how and why granular materials are affected by fluid and it is these interactions in a range of systems that this thesis is concerned with.

In **Chapter 2** we described the simulation methods used to model our fluid-grain systems. The first part of the chapter was concerned with outlining the Molecular Dynamics (MD) technique used to model the grains. Within this section we described the contact forces used including the Linear Spring-Dashpot (LSD) and the Damped Hertzian (DH) collision schemes. We then performed

some comparisons to show under what conditions each model was best suited. We showed that the DH collision scheme allowed for the largest time-step and thus the best computational efficiency. If contact forces do not affect the system behaviour then LSD contact forces are suitable. We then briefly discussed the approach used to model the fluid. This approach was based on spatially discretising the governing equations of fluids, the Navier–Stokes equations, onto a staggered Marker-and-Cell mesh and solving using the projection method with suitable boundary conditions.

We then discussed several approaches in which we may couple these two phases. The first model we described was the analytical Kroll model. This model considers the forces experienced by a porous granular bed when shaken in an air-filled cell in order to determine an equation of motion for the flight of the bed. To determine the flight of a body within a dense fluid we introduce a modified version of the Kroll model, the MK model, which includes buoyancy effects that appear when fluid inertia is considered. Both of these models capture behaviour very accurately despite modelling the bed as a porous body. We then described two models which use empirical bed equations to couple the fluid and grain phases. The first model uses MD to determine the particle interactions and couples the fluid and grain phases using a drag force based on a bed equation. This force is applied explicitly onto the grains in such a manner that opposes the direction of particle motion. The model is appropriately named the Simple Drag (SD) model. The second model modifies the Navier–Stokes equations for incompressible fluids to include a term which estimates the momentum transfer between the fluid and grains using a bed equation. The resulting model, which is called the Navier–Stokes (NS) model, reproduces the effects of a fluid-immersed granular bed where the grains are individually modelled using MD.

We then introduced two models in which the fluid grid is small in relation to the particle size. These two models share common features as neither use bed equations to determine the momentum transfer between the fluid and grains. Instead the forces are determined through a template. The first model we described was the Particle Template (PT) model where the particles' motions are determined individually using MD and the fluid is solved using the Navier–Stokes

equations. In order to couple the fluid and grain motion the fluid lattice points immersed within the particle are forced to share the same velocity as the particle while the corresponding force on the particle is calculated by taking an integral over the template of the stress-tensor divergence. The second model we described was the Fluid Springs (FS) model. This model differs from the PT model in that on each grain we create a template of grid-points which moves with the particle. For each lattice point on the template, we predict the difference in the future fluid and grain paths and then correct the motion using an imaginary damped spring which forces the two phases to converge.

The second half of this chapter was concerned with making comparisons between the models and determining under which conditions they were most suitable. We found that in two dimensions the FS model was stable and able to achieve more accurate results with fewer lattice points contained within its volume than for the same parameters in the PT model. In the last part of the chapter we observed that the FS model is able to capture hydrodynamic lubrication effects that arise when fluid is squeezed from the space between two close surfaces.

In **Chapter 3** we studied fluid-immersed beds within oscillating systems in three dimensions. We found that the NS and FS models could capture the behaviour of a thrown porous bed accurately while the PT model was unable to do so for similar simulation parameters. We showed that the NS and FS models were able to model fluid flowing through packed beds in unsteady flow regimes.

In **Chapter 4** we studied heap formation in a three-dimensional system using the SD, NS and FS models. The first simulations we performed were using the SD model, where we found that a water-immersed granular bed in a vibrated cell forms a domed surface whose maximum height is in the centre of the cell. We observed that this piling was a result of friction-driven convection and that as the wall friction parameter was increased the granular convection increased also. We then performed simulations in a similar system using the NS and FS models. Here we found that the convection is primarily driven by fluid and is considerably stronger than the friction driven convection in the SD model simulations. In the NS and FS model simulations the granular bed forms a tilt which spans the

entire cell rather than forming a dome in the middle. In order to investigate the effect of walls on tilting within the FS and NS model simulations some further simulations were performed. We observed that convection is stronger, in the NS and FS model simulations, in the presence of some wall friction. The last simulations were performed in the absence of side walls with periodic boundary conditions which showed that a pile is maintained and strengthened because of the presence of fluid-driven convection. We concluded that "Faraday tilting" is a fluid-driven effect that may be enhanced by the presence of wall friction.

Studying Faraday tilting also allowed us to compare results obtained with the NS and FS models for a well-known effect. We observed that the two models achieved very comparable results and found that the FS model was able to capture all of the behaviours of the tilting simulations despite not requiring an empirical bed equation to couple the fluid-grain interactions. The advantage of the NS model over the FS model was that the results were obtained considerably faster. However, the NS model had some unrealistic boundary effects which were not observed within the FS model.

In **Chapter 5** we investigated the fluid-driven partition instability. Here we studied the behaviour of a water-immersed system of spherical barium titanate particles in a rectangular cell which was divided into two columns, linked by two connecting holes, one at the top and one at the bottom of the cell. Under vibration the grains spontaneously move into just one of the columns via a gradual transfer of grains through the connecting hole at the base of the cell. The effect was first studied within experiments. We then focused on developing simulations to accurately model this process and provide insight into the instability mechanism. The first model used to simulate the partition instability was the NS model which was unable to accurately capture the coupling between the fluid and grains within the bottom connecting channel. We later used the FS model which provided excellent agreement with experimental results. The transfer of grains was found to arise from the greater flow of fluid through the shallower column of grains as the beds are thrown during vibration. This leads to grains transferring at an accelerating rate as the height difference between the granular columns increases. At the end of the chapter we proposed a simple analytic model to describe the

fluid-driven partition instability based on two coupled granular beds vibrated within an incompressible fluid. This model was able to capture the instability process over a range of vibrational amplitudes using a single fitting parameter.

In **Chapter 6** we studied the fluid-enhanced "Brazil nut effect". Here a large heavy intruder held within a water-filled rectangular cell will rise through a bed of smaller host particles when a vertical oscillating force is applied. A detailed experimental investigation was carried out to investigate the behaviour of a large steel intruder in a shallow bed of smaller glass particles held in a vertically vibrated water-filled cell. As we did with the partition instability we performed simulations so that the rising mechanism may be studied in greater detail than is possible within experiments. The Brazil nut is thrown a greater height than the surrounding bed particles during each vibration cycle. In simulations performed with the FS model we showed that the role of an incompressible fluid is crucial to the rising mechanism. As the intruder is thrown it moves through the bed and drags fluid and hence particles behind it. When the intruder falls it lands on some of these dragged grains which elevates its original position by a small amount. In simulations performed using the SD model to couple the granular and fluid motion for the same parameters we found that the large intruder does not rise from its original position. The SD model simulations confirmed the role of fluid in the intruder rising process. At the end of the chapter we proposed an analytical approach to model the ascension of a large intruder held within a fluid immersed porous bed in a vibrating cell. The analytical model used the Modified Kroll model to determine the flight of the porous bed while the forces on the immersed intruder are made up from a fluid drag component and a force based on the vertical density profile of a granular bed. We then showed that an analytical model of this form was able to accurately model the fluid-enhanced Brazil nut effect.

In **Chapter 7** we conducted a brief theoretical study of zero-gravity fluid-immersed granular suspensions. These simulations were performed using the FS model for dense grains in a viscous fluid. After initially being positioned in a randomised state we showed that the natural state of grains is to form layers perpendicular to the vibration motion. We observed that layers are repulsive of

one another. We also found that, unlike the two-dimensional case of chains, layers more than a single particle thick are stable. The layers are stable as no particles shoot off and they do not break up into smaller layers. However, we observed that if the layer is thick, i.e. more than a single particle deep, the layer is prone to "forking". Here the layer splits into two or more thinner layers that are still attached to the bulk of the bed.

8.2 Future Work

Following the work presented in this thesis a number of possible research paths can be suggested.

In chapter 2 we introduced the FS model and later investigated the strength of the imaginary spring constant necessary to simulate the fluid-grain coupling accurately for various sets of parameters. We would want to further the investigation and find how the fluid springs constant varies with the number of fluid points contained within the particle in three-dimensional simulations. If possible an empirical relation could be determined.

In chapter 5 our investigation of the partition instability has been extensive, however, it could be further improved. We find that the instability occurs at certain vibrational parameters but not at others. We would suggest the investigation of when the instability onsets as vibration strength is increased.

In chapter 7 we investigated pattern formation of fluid-immersed grains vibrated in a cell held within a weightless environment. There were several behaviours of the patterns that we have been unable to explain due to the brief nature of our study. We would want to examine the flows around the layers and explain how it is possible for thick layers to be stable when parallel chains are unstable (Klotsa *et al.* 2009). We would also want to understand the forces between layers and why thick layers fork into thinner layers.

Throughout this thesis we have shown that the FS model may be used effectively to simulate a variety of fluid-immersed granular systems. Within chapter 2 we showed that the FS model was able to accurately simulate fluid-grain systems when held within oscillatory fluid flows. In chapters 4 and 5 we showed that

the model was able to simulate large vibrated granular systems to a high level of accuracy. Later in chapter 6 we used the FS model to simulate a bidisperse system and observe microscopic flow around a large rising intruder. Our thesis has shown a wide variety of systems that may be simulated with the FS model. Some suggestions for topics of further study would include sedimenting particles within magnetic fields and sand avalanches. We would also suggest studying two component particle separation using the FS model to see if a model which includes microscopic fluid flow affects the separation dynamics or can reveal more about the process. We would also suggest the study of tilt oscillations of two component granular mixtures when held within a small fluid-filled vibrated cell. Another interesting study would be whether the FS model may be extended to handle non-Newtonian fluids through the use of a shear thickening viscous term or another similar technique. Another area with a vast array of options for study would be the investigation of non-spherical objects within fluids using either the PT or FS models. We would be interested in whether the irregular particle shapes affect the dynamic behaviour of many of the phenomena already studied within granular dynamics.

Finally, due to the potential application of our research to the industrial processing of granular materials, we would encourage the reproduction of our experiments and simulations at an industrial scale. All of our simulations have been carried out in systems containing just a few thousand particles. To validate our findings, our simulations should be carried out in larger systems and our experiments should be carried out in larger cells.

Bibliography

Akiyama, T. and T. Shinomura (1991). Investigation of wall shear-stress in vibrating particle beds. *Powder Technology 66*, 243–247.

Akiyama, T. and T. Shinomura (1993). Measurements of wall shear stress in particle beds when vibrations are imposed vertically along the direction of shear. *Advanced Powder Technology 4*, 129–142.

Akiyama, T., T. Shinomura, S. Murakawa, and K. M. Aoki (2001). A surface instability of granules under vibration in partitioned containers. *Granular Matter 3*, 177–183.

Allen, M. P. and D. J. Tildesley (2000a). *Computer simulation of liquids*, pp. 78–82. Oxford University Press.

Allen, M. P. and D. J. Tildesley (2000b). *Computer simulation of liquids*, pp. 149–152. Oxford University Press.

Ambroso, M. A., R. D. Kamien, and D. J. Durian (2005). Dynamics of shallow impact cratering. *Physical Review E 72*, 041305.

Anderson, J. D. (1995). *Computational fluid dynamics*, pp. 153–161. McGraw Hill.

Aranson, I. S. and L. S. Tsimring (2006). Patterns and collective behaviour in granular media: Theoretical concepts. *Rev. Mod. Phys. 78*, 641.

Beysens, D., D. Chatain, P. Evesque, and Y. Garrabos (2008). Nucleation and growth of a bubble pattern under vibrations in weightlessness. *Europhysics Letters 82*, 36003.

Bird, G. A. (1994). *Molecular dynamics and the direct simulation of gas flow*. Oxford University Press.

Biswas, P., P. Sánchez, M. R. Swift, and P. King (2003). Numerical simulations of air-driven granular separation. *Physical Review E 68*, 050301.

Bridgewater, J., N. W. Sharpe, and D. C. Stocker (1969). Particle mixing by percolation. *Chemical Engineering Research and Design 47*, 114.

Burtally, N., P. J. King, and M. R. Swift (2002). Spontaneous air-driven separation in vertically vibrated fine granular mixtures. *Science 295*, 1877.

Chen, W., W. Pritchard, and S. Tavener (1995). Bifurcation for flow past a cylinder between parallel planes. *Journal of Fluid Mechanics 284*, 23.

Chen, W. and R. Wei (1998). A capillary-like phenomenon in granular material under vertical vibration. *Physical Review Letters A 244*, 389–393.

Chorin, A. J. (1968). Numerical solution of the navier-stokes equations. *Math. Comput. 22*, 745.

Cooke, W., S. Warr, J. M. Huntley, and R. C. Ball (1996). Particle size segregation in a two-dimensional bed undergoing vertical vibration. *Physics Review E 53*, 2812.

Coulomb, C. (1773). Memoir de mathematique et de physique. *Academie des Sciences L'Imprimerie Royale Paris 7*, 343.

Darcy, H. (1856). Les fontaines publiques de la ville de dijon.

Davis, R. H., J. Serayssol, and E. J. Hinch (1986). The elastohydrodynamic collision of two spheres. *Journal of Fluid Mechanics 163*, 479.

de Gennes, P. G. (1966). *Superconductivity of metals and alloys*, pp. 83. W. A. Benjamin, Inc., New York.

di Felice, R. (1994). The voidage function for fluid-particle interaction systems. *International journal of multiphase flow 20*, 153–159.

Eggers, J. (1999). Sand as maxwell's demon. *Physical Review Letters 83*, 5322.

Ennis, B. J., J. Green, and R. Davis (1994). The legacy of neglect in the united states. *Chemical Engineering Progress 90*, 32–43.

Ergun, S. (1952). Fluid flow through packed columns. *Chemical Engineering Programming 48*, 89.

Ertuck, E. (2005). Discussions on driven cavity flow and steady solutions at high reynolds numbers. *www.cavityflow.com*.

Faraday, M. (1831). On a peculiar class of acoustical figures; and on certain forms assumed by groups of particles upon vibrating elastic surfaces. *Philosophical Transactions of the Royal Society of London 52*, 299.

Fogelson, A. L. and C. S. Peskin (1988). A fast numerical method for solving the three-dimensional stokes equations in the presence of suspended particles. *Journal of Computational Physics 79*, 50–69.

Frigo, M. and S. G. Johnson (2005). The design and implementation of fftw3. *93*, 216–231.

Frigo, M. and S. G. Johnson (2006). Manual for fftw 3.2 online. *www.fftw.org*.

Gallas, J. A. C., H. J. Herrmann, T. Poschel, and S. Sokolowski (1996). Molecular dynamics simulations of size segregation in three dimensions. *Journal of Statistical Physics 82*, 443.

Gear, C. W. (1967). The automatic integration of ordinary differential equations. *Communications of the ACM 14*, 176–179.

Glowinski, R., T. Pan, T. I. Hesla, and D. D. Joseph (1999). A distributed lagrange multiplier/fictitious domain method for particulate flows. *International journal of multiphase flow 25*, 755–794.

Glowinski, R., T. Pan, T. I. Hesla, D. D. Joseph, and J. Periaux (1999). A distributed lagrange multiplier/fictitious domain method for flows around moving rigid bodies: application to particulate flow. *International journal of multiphase flow 30*, 1043–1066.

Glowinski, R., T. Pan, and J. Periaux (1999). A fictitious domain method for external incompressible viscous-flow modelled by navier–stokes equations. *Computer methods in applied mechanics and engineering 112*, 133–148.

Goldhirsch, I. and G. Zanetti (1993). Clustering instability in dissipative gases. *Physical Review Letters 70*, 1619.

Gondret, P., M. Lance, and L. Petit (2002). Bouncing motion of spherical particles in fluids. *Physics of Fluids 473*, 1–21.

Harlow, F. H. and J. E. Welch (1965). Numerical calculation of time-dependent viscous incompressible flow of fluid with free surface. *Physics of Fluids 8*, 2182.

Harwood, C. F. (1977). Powder segregation due to vibration. *Powder Technology 16*, 51.

Hayakawa, H. and D. C. Hong (1997). Thermodynamic theory of weakly excited granular systems. *Physical Review Letters 78*, 2764.

Herrmann, H. J. and S. Luding (1997). Modelling granular media on the computer. *Continuum Mechanics and Thermodynamics 10*, 189–231.

Höfler, K. and S. Schwarzer (2000). Navier–stokes simulation with constraint forces: Finite-difference method for particle-laden flows and complex geometries. *Physics Review E 61*, 7146–7160.

Hou, M. Y., H. N. Tu, R. Liu, Y. L. Li, K. Q. Lu, P. Y. Lai, and C. K. Chan (2008). Temperature oscillations in a compartmentalised bidisperse granular gas. *Physical Review Letters 100*, 068001.

Jaeger, H. M., S. R. Nagel, and R. P. Behringer (1996). Granular solids, liquids, and gases. *Reviews of Modern Physics 68*, 1259.

Janssen, H. A. (1895). Tests on grain pressure silos. *Zeits. Verien. Deutsche Ing.*.

Kalthoff, W., S. Schwarzer, and H. J. Herrmann (1997). Algorithm for the simulation of particle suspensions with inertia effects. *Physics Review E 56*, 2234.

Klotsa, D., M. R. Swift, R. M. Bowley, and P. J. King (2007). Interaction of spheres in oscillatory fluid flows. *Physics Review E 76*, 056314.

Klotsa, D., M. R. Swift, R. M. Bowley, and P. J. King (2009). Chain formation of spheres in oscillatory fluid flows. *Physics Review E 79*, 021302.

Knight, J. B., H. M. Jaeger, and S. R. Nagel (1993). Vibration-induced size separation in granular media - the convection connection. *Physical Review Letters 70*, 3728.

Kudrolli, A. (2004). Size separation in vibrated granular matter. *Reports on progress in Physics 67*, 209–247.

Kuipers, J. A. M., K. J. Vanduin, and F. P. H. van Beckum (1993). Computer-simulations of the hydrodynamics of a two-dimensional gas-fluidised bed. *Computational Chemical Engineering 17*, 839–858.

Kuusela, E. (2005). Steady-state sedimentation of non-brownian particles with finite reynolds number. *Ph.D. thesis, Laboratory of Physics, Helsinki University of Technology, Espoo, Finland*, 55.

Kuwabara, G. and K. Kono (1987). Restitution coefficient in a collision between two spheres. *Japanese journal of applied physics 26*, 1230–1233.

Lambiotte, R., J. M. Salazar, and L. Brenig (2005). From particle segregation to the granular clock. *Physical Review Letters A 343*, 224–230.

Leaper, M. C., A. J. Smith, M. R. Swift, P. J. King, H. E. Webster, N. J. Miles, and S. W. Kingman (2005). The behaviour of water-immersed glass-bronze particulate systems under vertical vibration. *Granular Matter 7*, 57–67.

Lian, G., X. Yong, W. Huang, and M. J. Adams (2001). On the squeeze flow of a power-law fluid between rigid spheres. *Journal of Non-Newtonian Fluid Mechanics 100*, 151–164.

López-Alcarez, P. (2007, January). *Controlling the fluid-driven separation of vertically vibrated granular mixtures*. Ph. D. thesis, University of Nottingham.

Lubachevsky, B. D. (1991). How to simulate billiards and similar systems. *Journal of computational physics 94*, 255–283.

Luding, S. (1995). Granular materials under vibration: Simulations of rotating spheres. *Physical Review E 52*, 4442.

Maeno, Y. (1996). Numerical investigation of surface level instability due to a tube in a vibrating bed of powder. *Physica A 232*, 27–29.

McNamara, S. and W. R. Young (1994). Inelastic collapse in 2 dimensions. *Physics Review E 50*, 28–31.

Melo, F., P. B. Umbanhowar, and H. L. Swinney (1995). Hexagons, kinks and disorders in oscillated granular layers. *Physical Review Letters 75*, 3838.

Milburn, R. J. (2006, January). *The dynamics of vibrated fluid-particle systems*. Ph. D. thesis, University of Nottingham.

Milburn, R. J., M. A. Naylor, A. J. Smith, M. C. Leaper, K. Good, M. R. Swift, and P. J. King (2005). Faraday tilting of water-immersed granular beds. *Physics Review E 71*, 011308.

Möbius, M. E., X. Cheng, P. Eshius, G. S. Karczmar, S. R. Nagel, and H. M. Jaeger (2005). Effect of air on granular size separation in a vibrated granular bed. *Physics Review E 72*, 011304.

Möbius, M. E., B. E. Lauderdale, S. R. Nagel, and H. M. Jaeger (2001). Brazil nut effect - size separation of granular particles. *Nature, London 414*, 270.

Mullin, T. (2000). Coarsening of self-organised clusters in binary mixtures of particles. *Physical Review Letters 84*, 4741.

Naylor, M. A., M. R. Swift, and P. J. King (2003). Air-driven brazil nut effect. *Physics Review E 68*, 012301.

Ohtsuki, T., D. Kinoshita, Y. Nakada, and A. Hayashi (1998). Surface level migration in vibrating beds of cohesionless granular materials. *Physics Review E 58*, 7650.

Pak, H. K., E. Vandoorn, and R. P. Behringer (1995). Effects of ambient gases on granular materials under vertical vibration. *Physical Review Letters 74*, 4643–4646.

Poschel, T. and H. J. Herrmann (1995). Size segregation and convection. *Europhysics Letters 29*, 123.

Rátkai, G. (1976). Particle flow and mixing in vertically vibrated beds. *Powder Technology 15*, 187.

Reynolds, O. (1885). On the dilatancy of media composed of rigid particles in contact. *Philos. Mag. 20*, 469.

Riley, N. (2001). Steady streaming. *Annual Review of Fluid Mechanics 33*, 43–65.

Ristow, G. H. (1996). Particles moving in spatially bounded, viscous fluids. *Computer Physics Communications 99*, 43–52.

Ristow, G. H. (1997). Wall correction factor for sinking cylinders in fluids. *Physics Review E 55*, 2808.

Rosato, A., K. J. Strandburg, F. Prinz, and R. H. Swendsen (1987). Why the brazil nuts are on top - size segregation of particulate matter by shaking. *Physical Review Letters 58*, 1038.

Sánchez, P., M. R. Swift, and P. J. King (2004). Stripe formulation in granular mixtures due to the differential influence of drag. *Physics Review Letters 93*, 184302.

Smith, A., M. C. Leaper, M. R. Swift, and P. J. King (2005). Travelling waves in a water-immersed binary granular system vibrated within an annular cell. *Physics Review E 71*, 031303.

Stevens, A. B. and C. M. Hrenya (2005). Comparison of soft-sphere models to measurements of collision properties during normal impacts. *Powder Technology 154*, 99–109.

Taguchi, Y. H. (1991). New origin of a convective motion: Elastically induced convection in granular materials. *Physical Review Letters 69*, 9.

Thomas, B., M. Mason, and A. Squires (2000). Some behaviours of shallow vibrated beds across a wide range in particle size and their implication for powder classification. *Powder Technology 111*, 34.

Thomas, B. and A. Squires (1998). Support for faraday's view of circulation in fine-powder chladni heap. *Physical Review Letters 81*, 574.

Tsimring, L. S. and D. Volfson (2003). Modeling of impact cratering in granular media. *Unpublished*.

van der Meer, D., P. Reimann, K. van der Weele, and D. Lohse (2002). Spontaneous ratchet effect in a granular gas. *Physical Review Letters 92*, 184301.

van der Weele, D., D. van der Meer, M. Versluis, and D. Lohse (2001). Hysteretic clustering in granular gas. *Europhysics Letters 53*, 328–334.

van der Weele, K. (2008). Granular gas dynamics: How maxwell's demon rules in a non-equilibrium system. *Contemporary Physics 49*, 157.

van Gerner, H. J., M. A. Hoef, D. van der Meer, and K. van der Weele (2007). Interplay of air and sand: Faraday heaping unravelled. *Physics Review E 76*, 51305.

Viridi, S., M. Schmick, and M. Markus (2006). Experimental observations of oscillations and segregation in a binary granular mixture. *Physics Review E 74*, 041301.

von Kroll, W. (1954). *Forsch. Gebiete Ingenieurwes 50*, 2.

Voth, G. A., B. Bigger, M. R. Buckley, W. Losert, M. P. Brenner, H. A. Stone, and J. P. Gollub (2002). Ordered clusters and dynamical states of particles in a vibrated fluid. *Physical Review Letters 88*, 234301.

Wen, C. Y. and Y. H. Yu (1966). Mechanics of fluidisation. *Chemical Engineering Program Symposium Series 62*, 100.

White, F. M. (1991). *Viscous fluid flow*, Chapter 3, pp. 182. McGraw-Hill, Inc.

Williams, J. C. (1976). Segregation of particulate materials - a review. *Powder Technology 15*, 245.

Wunenburger, R., V. Carrier, and Y. Garrabos (2002). Periodic order induced by horizontal vibrations in a two-dimensional assembly of heavy beads in water. *Physics of Fluids 14*, 2350.

Wylie, J. J., Q. Zhang, H. Y. Xu, and X. X. Sun (2008). Drag-induced particle segregation with vibrating boundaries. *Europhysics Letters 81*, 54001.

Yan, X., Q. Shi, M. Hou, and K. Lu (2003). Effects of air on the segregation of particles in a shaken granular bed. *Physical Review Letters 91*, 014302.

Zeilstra, C., M. A. van der Hoef, and J. A. M. Kuipers (2008). Simulations of density segregation in vibrated beds. *Physical Review E 77*, 031309.

Zhang, W., R. Noda, and M. Horio (2005). Evaluation of lubrication force on colliding particles for dem simulation of fluidised beds. *Powder Technology 158*, 92–101.

(Wunenburger *et al.* 2002) (Akiyama and Shinomura 1991) (Akiyama and Shinomura 1993) (Akiyama *et al.* 2001) (Allen and Tildesley 2000a) (Allen and Tildesley 2000b) (Anderson 1995) (Aranson and Tsimring 2006) (Beysens *et al.* 2008) (Bird 1994) (Biswas *et al.* 2003) (Chen and Wei 1998) (Coulomb 1773) (Darcy 1856) (Davis *et al.* 1986) (de Gennes 1966) (di Felice 1994) (Ennis *et al.* 1994) (Eggers 1999) (Ertuck 2005) (Faraday 1831) (Fogelson and Peskin 1988) (Frigo and Johnson 2005) (Frigo and Johnson 2006) (Gear 1967) (van Gerner *et al.* 2007) (Glowinski *et al.* 1999) (**?**) (Glowinski *et al.* 1999) (Goldhirsch and Zanetti 1993) (Gondret *et al.* 2002) (Harlow and Welch 1965) (Herrmann and Luding 1997) (Höfler and Schwarzer 2000) (Hou *et al.* 2008) (Jaeger *et al.* 1996) (Kalthoff *et al.* 1997) (Klotsa *et al.* 2007) (Klotsa *et al.* 2009) (Knight *et al.* 1993) (von Kroll 1954) (Kuipers *et al.* 1993) (Kuwabara and Kono 1987) (Kuusela 2005) (Lambiotte *et al.* 2005) (Leaper *et al.* 2005) (Lian *et al.* 2001) (López-Alcarez 2007) (Lubachevsky 1991) (Maeno 1996) (McNamara and Young 1994) (van der Meer *et al.* 2002) (Melo *et al.* 1995) (Milburn *et al.* 2005) (Möbius *et al.* 2001) (Möbius *et al.* 2005) (Mullin 2000) (Naylor *et al.* 2003) (Ohtsuki *et al.* 1998) (Pak *et al.* 1995) (Reynolds 1885) (Riley 2001) (Ristow 1996) (Ristow 1997) (Rosato *et al.* 1987) (Smith *et al.* 2005) (Stevens and Hrenya 2005) (Taguchi 1991) (Thomas *et al.* 2000) (Thomas and Squires 1998) (Viridi *et al.* 2006) (Voth *et al.* 2002) (van der Weele *et al.* 2001) (van der Weele 2008) (Wen and Yu 1966) (Williams 1976) (Bridgewater *et al.* 1969) (Harwood 1977) (Rátkai 1976) (Cooke *et al.* 1996) (Gallas *et al.* 1996) (Poschel and Herrmann 1995) (Burtally *et al.* 2002) (Wylie *et al.* 2008) (Sánchez *et al.* 2004) (Janssen 1895) (Yan *et al.* 2003) (Zeilstra *et al.* 2008) (Zhang *et al.* 2005) (Kudrolli 2004) (White 1991) (Hayakawa and Hong 1997)